UNIVERSIDADE ESTADUAL PAULISTA “JÚLIO DE MESQUITA FILHO”
FACULDADE DE ENGENHARIA
CÂMPUS DE ILHA SOLTEIRA

MAURICIO KIOTSUNE IWANAGA

INVESTIGATION OF GROUND SURFACE VIBRATION TO LOCATE LEAKS IN BURIED WATER PIPES

Ilha Solteira
2023

UNIVERSIDADE ESTADUAL PAULISTA
"JÚLIO DE MESQUITA FILHO"
Campus de Ilha Solteira

PROGRAMA DE PÓS-GRADUAÇÃO EM ENGENHARIA MECÂNICA

MAURICIO KIOTSUNE IWANAGA

INVESTIGATION OF GROUND SURFACE VIBRATION TO LOCATE LEAKS IN BURIED WATER PIPES

Thesis presented to the São Paulo State University – UNESP to obtain the degree of PhD in Mechanical Engineering.

Prof. Dr. Michael John Brennan
Advisor

Prof. Dr. Fabrício César Lobato de Almeida
Co-advisor

Ilha Solteira
2023

FICHA CATALOGRÁFICA

Desenvolvido pelo Serviço Técnico de Biblioteca e Documentação

Iwanaga, Mauricio Kiotsune.

I96i Investigation of ground surface vibration to locate leaks in buried water pipes / Mauricio Kiotsune Iwanaga. -- Ilha Solteira: [s.n.], 2023

196 f. : il.

Tese (doutorado) - Universidade Estadual Paulista. Faculdade de Engenharia de Ilha Solteira. Área de conhecimento: Mecânica dos Sólidos, 2023

Orientador: Michael John Brennan

Coorientador: Fabrício César Lobato de Almeida

Inclui bibliografia

1. Leak localization. 2. Buried pipe localization. 3. Ground surface vibration. 4. Unwrapped phase.

Raiane da Silva Santos

Raiane da Silva Santos

Supervisora Técnica de Seção

Seção Técnica de Referência, Atendimento ao usuário e Documentação

Diretoria Técnica de Biblioteca e Documentação

CRB/8 - 9999

UNIVERSIDADE ESTADUAL PAULISTA

Câmpus de Ilha Solteira

CERTIFICADO DE APROVAÇÃO

TÍTULO DA TESE: INVESTIGATION OF GROUND SURFACE VIBRATION TO LOCATE LEAKS IN BURIED WATER PIPES

AUTOR: MAURICIO KIOTSUNE IWANAGA
ORIENTADOR: MICHAEL JOHN BRENNAN

Aprovado como parte das exigências para obtenção do Título de Doutor em Engenharia Mecânica, área: Mecânica dos Sólidos pela Comissão Examinadora:

Prof. Dr. MICHAEL JOHN BRENNAN (Participaçao Virtual)
Departamento de engenharia mecânica / Faculdade de Engenharia de Ilha Solteira - UNESP

Prof. Dr. DOUGLAS DOMINGUES BUENO (Participaçao Virtual)
Departamento de Matemática / Faculdade de Engenharia de Ilha Solteira - UNESP

Prof. Dr. JOAO ANTONIO PEREIRA (Participaçao Virtual)
Departamento de Engenharia Mecânica / Faculdade de Engenharia de Ilha Solteira - UNESP

Prof. Dr. PAULO JOSÉ PAUPITZ GONÇALVES (Participaçao Virtual)
Departamento de Engenharia Mecânica / Faculdade de Engenharia de Bauru - UNESP

Prof. Dr. ADRIANO TODOROVIC FABRO (Participaçao Virtual)
Departamento de Engenharia Mecânica / Universidade de Brasília - UnB

Ilha Solteira, 21 de março de 2023

This work is dedicated to my parents Ricardo and Marinês, my beloved fiancée Carol, and all relatives and friends that supported me.

ACKNOWLEDGEMENTS

First of all, I would like to thank my parents Ricardo and Marinês, my fiancée Carol, my grandmother Geni, my mother-in-law Sueli, and my sisters-in-law Laís e Thais for providing me support and tenderness throughout these years. Without a doubt, I would not be able to accomplish this goal without their participation. I will always be grateful for the things they did to me, and the times they had to be stronger for me. As time passes by, I see how fortunate I am for having people like them in my life. Always teaching me the true meaning of family and love.

I would like to thank Prof. Mike Brennan, Prof. Fabrício Almeida and Dr. Oscar Scussel for being more than advisors to me. They are always concerned about my work and well-being, that now I have the feeling that they are like another family to me. Every single meeting that we got is an opportunity of exchanging experiences and ideas, that make me feel a better person and motivated to keep learning new things. I will always be grateful for their guidance, patience and motivation of keeping me doing my best. Always teaching me the true meaning of leadership and wisdom.

I would like to thank my friends Rafael Teloli, João Trentin, Lucas Chaim, Rafael Mattei, Vinicíus Cleante, Jean Carneiro, Vitor Girardi, João Brogin, Lucas Zanetti, Luis Villani, Marcus Yano and Gabriel Moimás for sharing ideas, discussions and opportunities that also make me feel with a better purpose in life. I will always be grateful for the good times we spend together making barbecues, drinking booze and talking about things of life. Always teaching me the true meaning of friendship and adulthood.

I would like to thank Prof. Emiliano Rustighi, Prof. Paulo Paupitz, Prof. Jennifer Muggleton, Prof. Phillip Joseph, Pedro Casado, Bruno Cavenaghi and Matheus Quartaroli for sharing ideas, discussions and data that help our research going forward.

I would like to thank UNESP and its staff for educating me since 2012. They are undoubtedly the foundation of who I became, and I will keep doing my work with seriousness and professionalism to honor their legacy.

I would like to thank SABESP and its staff, especially Marcelo Miki, Rosane Miki and Cícero Rocha, for the financial support to our research and the efforts of keeping our partnership.

This work was funded by the Ilha Solteira Research Foundation (FEPISA), project number 9.0005/2020.

“La semplicità è la suprema sofisticazione” - Leonardo da Vinci

RESUMO

O risco de escassez de água tem aumentado em muitas regiões do mundo. Uma vez que os vazamentos representam uma grande quantidade de desperdício, os setores de abastecimento dependem das tecnologias de localização de vazamentos. Uma situação comum encontrada na prática é quando uma tubulação enterrada não é acessível. Neste caso, são recomendadas as tecnologias que não requerem qualquer acesso. Entretanto, existem apenas algumas delas com desempenho muito limitado. Muitas pesquisas têm sido realizadas nos últimos anos, com foco na localização de objetos enterrados usando medidas de vibração da superfície do solo, devido às ondas que se propagam nele. Elas são consideradas soluções potenciais para as tecnologias de localização de vazamentos, já que o primeiro passo geralmente é localizar a tubulação. Além disso, algumas pesquisas também foram realizadas para localizar vazamentos sem conhecimento prévio do local onde a tubulação está enterrada. Embora sejam promissoras, a aplicação prática de tais técnicas pode ser bastante complicada e custosa, já que normalmente elas requerem uma estimativa da velocidade de onda no solo e um conjunto de sensores montados na superfície. A principal motivação para esta tese é apresentar uma técnica de localização de vazamento baseada em medições de vibração da superfície do solo, que não requer uma estimativa da velocidade de onda no solo, robusta à interferência do ruído de fundo, e com uma configuração simples. Para isso, o fenômeno de propagação de ondas no solo devido a um tubo enterrado com vazamento é introduzido através de um modelo analítico, cujos resultados são validados a partir de um modelo numérico e um experimento. As técnicas de localização são então apresentadas com base no contexto físico fornecido pelo modelo analítico. A técnica proposta, denominada técnica de dois sensores, é baseada na fase medida por um par de sensores móvel em diferentes posições na superfície do solo. A técnica usada como base de comparação, denominada técnica de um sensor, é baseada na diferença de amplitude medida por um único sensor móvel em diferentes posições na superfície do solo. A aplicação delas é ilustrada com os modelos analítico e numérico, e seus desempenhos são avaliados na prática com dados experimentais adquiridos em campos de testes. As contribuições da pesquisa são destacadas pelos resultados experimentais, nos quais a técnica de dois sensores pode localizar a tubulação para distâncias maiores em relação ao vazamento, e é mais robusta à interferência de fontes externas de ruído em relação à técnica de um sensor.

Palavras-chave: localização de vazamentos; localização de tubulações enterradas; vibração da superfície do solo; fase entre dois sensores.

ABSTRACT

The risk of water shortage has increased in many regions of the world. Since leaks represent a large amount of water waste, water supply sectors depend on leak localization technologies. A common situation found in practice is when a buried pipe is not accessible and, consequently, some technologies cannot be applied as the sensors cannot be attached directly to the pipe. For this type of situation, the technologies that do not require any access to the buried pipe are recommended. However, there are only a few of them with very limited performance. A large amount of research has been carried out in recent years, focusing on the location of buried objects using measurements of ground surface vibration, due to the waves that propagate in the soil. This research can provide potential solutions for leak localization technologies, since the first step is usually to locate the buried pipe. Furthermore, some research has also been conducted in the location of leaks without prior knowledge of where the pipe is buried. Although they are promising, the practical application of such techniques can be quite complicated and expensive as they usually require an estimate for the wave speed in the soil, and a set of sensors mounted on the ground surface. In this thesis, a leak localization technique is presented which is based on measurements of ground surface vibration. The technique does not require an estimate for the wave speed in the soil, is robust to the interference of background noise, and is simple to setup. To illustrate the method, the phenomenon of wave propagation in soil due to a leaking buried pipe is first introduced via an analytical model, which is validated with a numerical model and an experiment. The localization techniques are then presented using the analytical model. The proposed technique, which is named the two-sensor technique, is based on the unwrapped phase measured by a roving pair of sensors on different positions on the ground surface. The technique used as baseline, named one-sensor technique, is based on the amplitude difference measured by a single sensor on different positions on the ground surface. The application of both techniques is illustrated with the analytical and numerical models, and their performances are evaluated in the practice with experimental data acquired on test rigs. The research contributions are highlighted by the experimental results, in which the two-sensor technique can locate the pipe for longer distances relative to the leak, and is more robust to the interference of external sources of noise in relation to the one-sensor technique.

Keywords: leak localization; buried pipe localization; ground surface vibration; unwrapped phase.

LIST OF FIGURES

LIST OF TABLES

LIST OF SYMBOLS

Symbol	Name	Units
a	Pipe mean radius	m
b	Pipe-wall thickness	m
B_{soil}	Soil bulk modulus	N/m^2
B^*_{soil}	Soil complex bulk modulus	N/m^2
B_{water}	Water bulk modulus	N/m^2
c	Wave speed	m/s
c_d	Speed of the compressional wave in soil	m/s
c_f	Speed of the predominantly fluid-borne axisymmetric wave	m/s
c_s	Speed of the shear wave in soil	m/s
c_{water}	Wave speed in water	m/s
E_{pipe}	Pipe material Young's modulus	N/m^2
f	Frequency	Hz
G_{soil}	Soil shear modulus	N/m^2
G^*_{soil}	Soil complex shear modulus	N/m^2
h	Radial distance in soil relative to pipe center	m
k	Wavenumber	m^{-1}
k_d	Wavenumber of the compressional conical wave in soil	m^{-1}
k_d^R	Radial component of wavenumber of the compressional conical wave in soil	m^{-1}
k_f	Wavenumber of the predominantly fluid-borne axisymmetric wave	m^{-1}
k_s	Wavenumber of the shear wave in soil	m^{-1}
k_s^R	Radial component of wavenumber of the shear conical wave in soil	m^{-1}
k_{water}	Wavenumber in water	m^{-1}
k^R_{water}	Radial component of wavenumber in water	m^{-1}
$K^{(\text{pipe})}$	Wave dynamic stiffness of pipe-wall	N/m^3

$K^{(\text{pipe\_soil})}$	Wave dynamic stiffness of the interaction between pipe-wall and soil	N/m^3
$K^{(\text{soil})}$	Wave dynamic stiffness of soil	N/m^3
$\tilde{K}^{(\text{water})}$	Wave dynamic stiffness of water	N/m^3
$\mathbf{K}^{(\text{pipe})}$	Wave dynamic stiffness matrix of pipe-wall	N/m^3
$\mathbf{K}^{(\text{soil})}$	Wave dynamic stiffness matrix of soil	N/m^3
$\mathbf{K}^{(\text{water})}$	Wave dynamic stiffness matrix of water	N/m^3
P	Amplitude of acoustic pressure in water	N/m^2
r	Radial coordinate in relation to pipe center	m
$S_1(\omega)$	Spectral density of sensor 1	(m/s)^2/Hz, (m/s^2)^2/Hz
$S_2(\omega)$	Spectral density of sensor 2	(m/s)^2/Hz, (m/s^2)^2/Hz
$S_{1,2}(\omega)$	Cross-spectral density between sensors 1 and 2	(m/s)^2/Hz, (m/s^2)^2/Hz
t	Time coordinate	s
T	Period	s
u_a	Axial displacement at the interface between pipe-wall and soil	m
u_a	Vector of displacements at the interface between pipe-wall and soil	m
U_a	Amplitude of axial displacement at the interface between pipe-wall and soil	m
u_h	Axial displacement of soil	m
U_h	Amplitude of axial displacement of soil	m
v_a	Voltage generated by an accelerometer	V
V_a	Amplitude of voltage generated by an accelerometer	V
v_g	Voltage generated by a geophone	V
V_g	Amplitude of voltage generated by a geophone	V
w_a	Radial displacement at the interface between pipe-wall and soil	m
W_a	Amplitude of radial displacement at the interface between pipe-wall and soil	m
W_d	Complex amplitude of compressional wave in soil	m

w_h	Radial displacement of soil	m
W_h	Amplitude of radial displacement of soil	m
W_s	Complex amplitude of shear wave in soil	m
x	Spatial coordinate	m
x_1	Signal measured by sensor 1	m/s, m/s^2
x_2	Signal measured by sensor 2	m/s, m/s^2
x_l	Horizontal distance of a measurement position in relation to a leak	m
X	Amplitude of spatial coordinate	m
y	Vertical distance on ground surface in relation to pipe center	m
y_l	Vertical distance of a measurement position in relation to a leak	m
z	Distance between pipe center and ground surface	m
α_a	Sensitivity constant of an accelerometer	V/(m/s^2)
α_g	Sensitivity constant of a geophone	V/(m/s)
$\gamma_{1,2}^2$	Coherence between sensors 1 and 2	-
η_d	Soil bulk loss factor	-
η_{pipe}	Pipe material loss factor	-
η_s	Soil shear loss factor	-
θ_d	Angle of propagation of the compressional conical wave	rad
θ_s	Angle of propagation of the shear conical wave	rad
λ	Wavelength	m
ν_{pipe}	Pipe material Poisson's ratio	-
ρ_{pipe}	Pipe material density	kg/m^3
ρ_{soil}	Soil density	kg/m^3
ρ_{water}	Water density	kg/m^3
σ_a	Compressional stress at the interface between pipe and soil	N/m^2
$\boldsymbol{\sigma}_a$	Vector of stresses at the interface between pipe and soil	N/m^2
τ_a	Shear stress at the interface between pipe and soil	N/m^2
T_a	Amplitude of shear stress at the interface between pipe and soil	N/m^2

$\phi_{1,2}$	Unwrapped phase between sensors 1 and 2	rad
$\hat{\phi}_{1,2}$	Approximate line for the values of unwrapped phase between sensors 1 and 2	rad
Φ_a	Amplitude of compressional stress at the interface between pipe and soil	N/m^2
ψ	Plane wave	-
Ψ	Amplitude of plane wave	-
ω	Angular frequency	rad/s
ω_{low}	Inferior limit of the leak noise bandwidth	rad/s
ω_{high}	Superior limit of the leak noise bandwidth	rad/s

CONTENTS

1 INTRODUCTION

1.1 BACKGROUND

Water is essential for life. Globally, there is concern about water availability for the next decades due to the world demographic growth, unsustainable economic practices and rapid urbanization, which results in great pressure on water demand and infrastructure (ELIASSON, 2015). Food availability is also of great concern for the next decades because food production is strictly related to water availability (HANJRA; QURESHI, 2010), and the world climate change acts as an aggravating factor on both water and food availabilities since it interferes with rainfall patterns and occurrences of droughts (RAGAB; PRUDHOMME, 2002; BROWN; FUNK, 2008).

Burek *et al*. (2016) estimated the global water scarcity for 2010 and its progression up to 2050, as shown in Fig. 1. The classification of each region is based on the percentage of total annual water withdrawals for human use in relation to total available renewable surface water resources. A particular region is in water scarcity if the percentage is between 20-40%, or in severe water scarcity if exceeds 40%. Some regions, such as Northern and Southern Africa, Middle East, Central and Eastern Asia, are already undergoing severe water scarcity as can be seen in Fig. 1(a), and will likely have to cope with even more extreme conditions in the next decades as can be seen in Fig. 1(b). According to the estimation for 2010, about 1.9 billion people (which corresponded to 27% of the global population at that time) lived in potential severely water-scarce areas, and this could increase to approximately 2.7-3.2 billion according to the prediction for 2050.

Another important aggravating factor for water scarcity is the amount of non-revenue water, that corresponds to the difference between the volume of water that is inserted into a water distribution system and the volume of water that reaches customers. Such a difference can be caused by leakages, customer meter under-registration, data handling error, thefts, and unbilled authorized consumption (FRAUENDORFER; LIEMBERGER, 2010). According to a recent study carried out by Liemberger and Wyatt (2019), the global volume of non-revenue water is approximately 126 billion cubic meters per year. The same study also analyzed the volume of non-revenue water for individual regions around the world and concluded that some of them, such as Central Asia, North and South America, belong to the groups that contain the highest volumes of non-revenue water per capita per day. Note in Fig. 1 that the same regions have already faced problems related to water scarcity, and the respective amount of non-revenue water could be saved for shortage periods.

Figure 1 – Global water scarcity. (a) Estimation for 2010 and (b) projection for 2050 in relation to 2010.

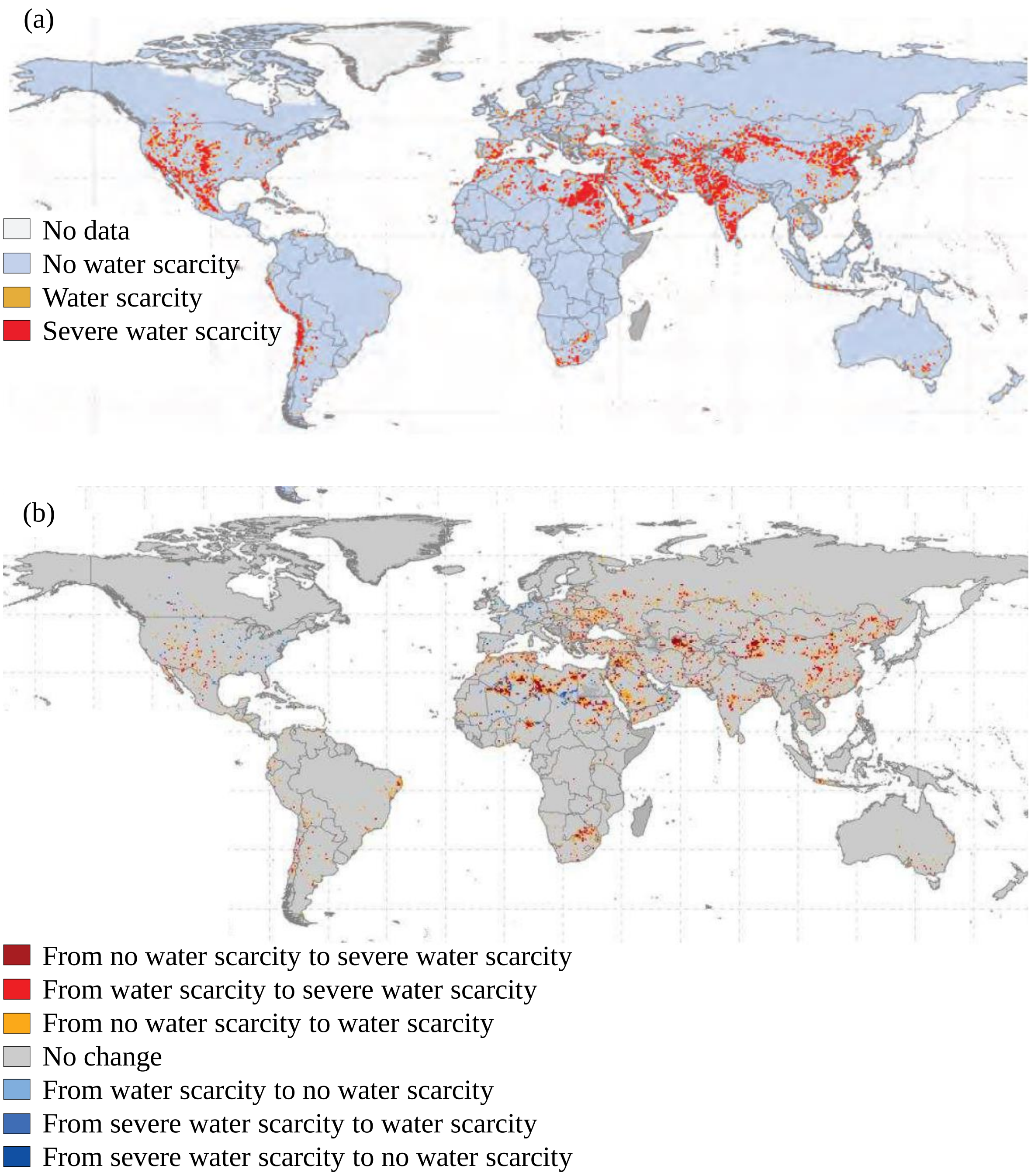

Source: adapted from Burek *et al*. (2016).

The study of Liemberger and Wyatt (2019) also estimated conservatively a cost of about USD 39 billion per year for the global volume of non-revenue water. Therefore, besides the risks for health and infrastructure of many countries, such a waste clearly represents an important financial problem for their water supply sector. In order to minimize these problems, water companies apply different solutions in which one of them is to decrease the number of leaks in their pipe networks (FRAUENDORFER; LIEMBERGER, 2010).

1.2 LITERATURE REVIEW ON CURRENT LEAK LOCALIZATION TECHNOLOGIES

The available leak localization technologies are classified according to Fig. 2. The classification adopted for them in this thesis is based on the criterium used by Islam *et al*. (2022), where they are divided into technologies that contain access to the buried pipe and technologies that do not contain access to the buried pipe. As shown in Fig. 2, the ones that have access to the buried pipe are subdivided into technologies that are applied inside the pipe and technologies that are applied outside the pipe. The ones that do not have access to buried pipe are subdivided into acoustic technologies and electromagnetic technologies.

Figure 2 – Classification of the available leak localization technologies.

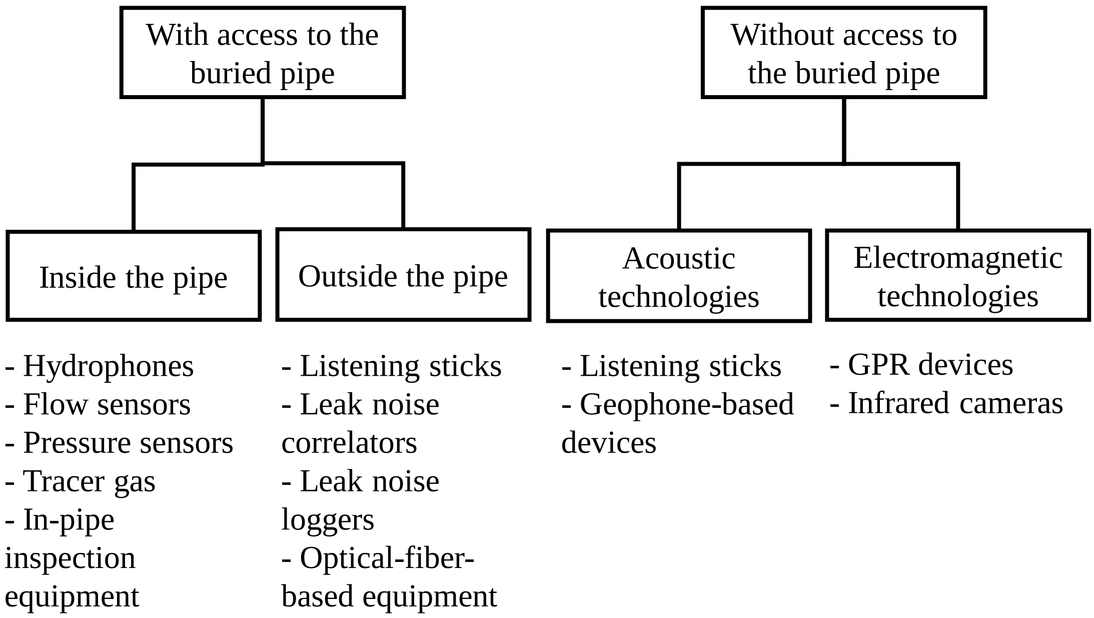

Source: elaborated by the author.

1.2.1 Leak localization technologies with access to the buried pipe

Pipe networks usually contain access points, such hydrants, standpipes, and underground valves, that are used for strategic water supply and maintenance. These access points can also be conveniently used to install devices to acquire measurements, or to monitor the conditions of specific sections of the pipe network. Each one of such devices that require a sort of access to the buried pipe is discussed as follows, in which a brief explanation is provided followed by the respective advantages and disadvantages.

- **Hydrophones:** sensors designed to listen to waterborne sound as microphones are designed to listen to airborne sound. Hydrophones are usually piezoelectric transducers containing a sensing element that generates an electrical potential in response to a change of the acoustic pressure in the water (AZO SENSORS, 2012). They are used to listen to the leak sound by introducing them into the pipe at convenient access points such as hydrants, as shown in Fig. 3(a), or manholes, as shown in Fig. 3(b).

Figure 3 – Examples for the application of hydrophones in a buried water pipe. (a) Hydrophone installed on a hydrant and (b) hydrophone installed directly in the pipe via a manhole.

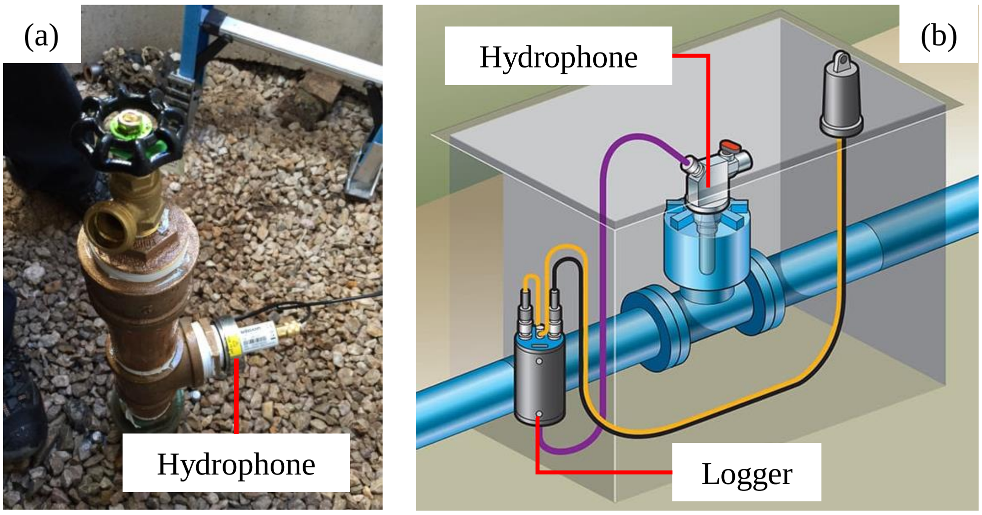

Source: adapted from (a) SebaKMT (2023) and (b) Primayer (2020).

The main advantage of hydrophones is that they can sense the acoustic pressure due to a leak for longer distances in relation to the leak-induced pipe-wall vibration, sensed by accelerometers placed on plastic pipes or pipes with large diameter (HAMILTON; CHARALAMBOUS, 2020). This characteristic makes hydrophones the most suitable sensor for locating leaks in situations where the pipe-wall vibration contains a small Signal-to-Noise Ratio (SNR) (GAO *et al*., 2005), such as when the background noise is high or the distance between the access points is relatively large (HAMILTON; CHARALAMBOUS, 2020).

The main disadvantage of hydrophones is that their application is limited to internal access to the pipe and, depending on the conditions of the pipe network, such an access is not possible or the corresponding access points are extremely far one from the other. Hence, hydrophones are not able to sense the leak-induced acoustic pressure due to the strong attenuation.

Figure 4 – Example for the application of flow sensors in a buried water pipe.

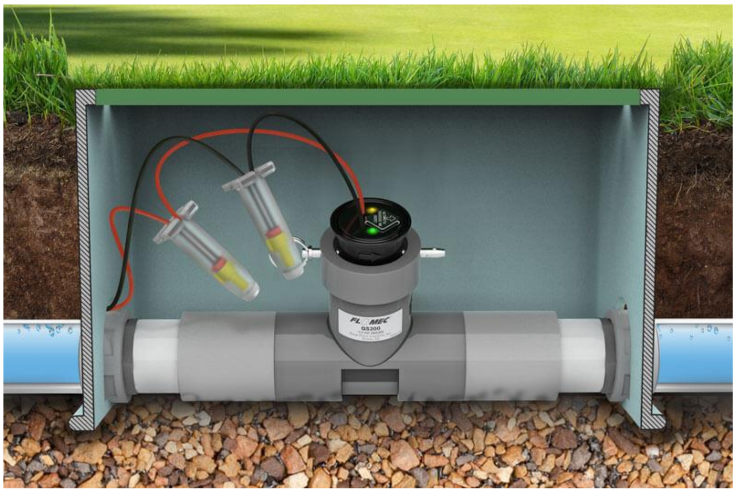

Source: Flomec (2023).

- **Flow sensors:** devices connected in series to the pipeline, as shown in Fig. 4, to measure the respective volumetric or mass flow. They are commonly used to detect leaks by comparing the input and output flows of a particular section of the pipe, in which a leak is detected if the output flow is minor than the input flow (ISLAM *et al*. 2022).

The main advantage of flow sensors is that background noise, such as road traffics, construction sites, seismic activities, etc., do not interfere considerably with their measurements as for the vibration sensors, such as accelerometers and geophones.

The main disadvantage of flow sensors is their measurements are prone to the interference caused by water household consumption. To mitigate such a problem, measurements are usually carried out at night when the demand is at its lowest and the leakages are at their highest percentage of the flow (ALKASSEH *et al*., 2013).

Figure 5 – Example for the application of pressure sensors in a buried water pipe.

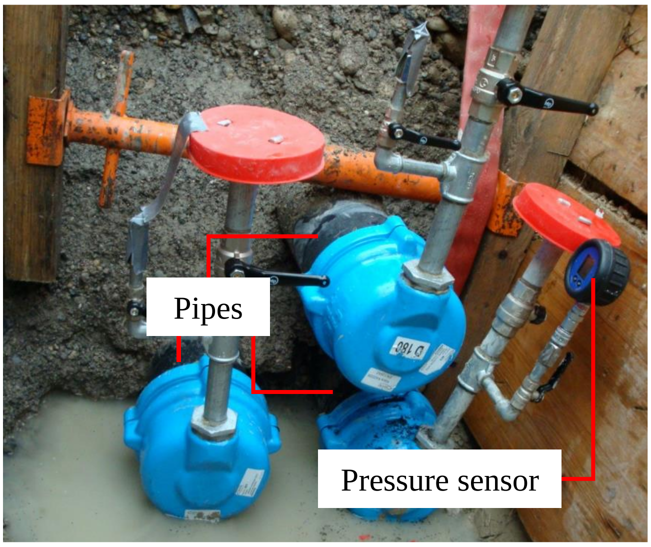

Source: adapted from Keller (2023).

- **Pressure sensors:** devices that measure the absolute or gauge pressure inside the pipe, as shown in Fig. 5. Note that these types of pressure are different from the acoustic pressure, measured by hydrophones for example, which is induced by small fluctuations of the fluid particles (KIM, 2010).

The main advantage of pressure sensors is background noise does not interfere considerably with their measurements. They can also be used to conveniently monitor high pressures inside the pipe to prevent bursts in the network, and low pressures inside the pipe to prevent problems with the supply for distant or elevated points along the network (ISLAM *et al*. 2022).

The main disadvantage of pressure sensors is that they are not able to detect minor leaks, as they generally do not cause considerable pressure changes inside the pipe (ISLAM *et al*. 2022).

- **Tracer gas detectors:** tracer gas is a leak localization technique in which the water-filled pipe network is pressurized with non-toxic and insoluble gases, that are basically composed by ammonia, halogens, and helium (EL-ZAHAB; ZAYED, 2019). If the network contains a crack or a fault in a particular section, the tracer gas escapes through it and reaches the ground surface as the gas is lighter than the air. Then, detectors are used to locate the position on the ground surface where the tracer gas is flowing through (EL-ZAHAB; ZAYED, 2019), as shown in Fig. 6.

Figure 6 – Example for the application of tracer gas detectors on a buried water pipe.

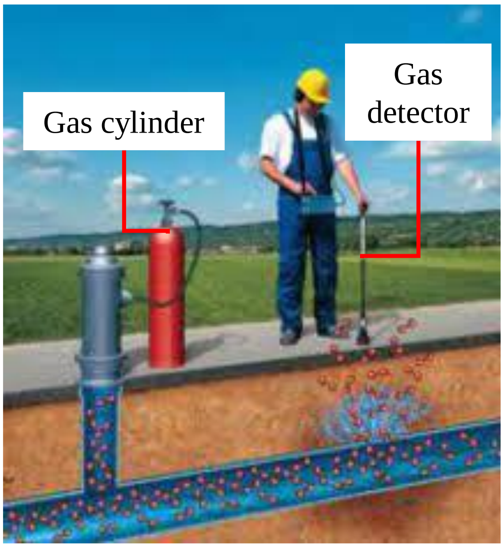

Source: adapted from Bavitech Corporation (2023).

The main advantage of the tracer gas technique is that its performance is independent from the pipe material and geometry, and from the layout of the pipe network. Furthermore, the environment has practically no interference on the respective localization procedure since the detectors are only sensitive to the tracer gas.

The main disadvantages of such a technique are that its application on pipes with large diameter is very expensive as a great amount of tracer gas is needed to pressurize it, and its method relies on knowing the waterflow direction and blocking alternative routes during the localization procedure. In addition, there is also a risk of the tracer gas flowing through a different location on the ground than that of the leak (KVS, 2023).

- **In-pipe inspection equipment:** moving devices that are introduced in the pipeline to check for leaks and pipe-wall conditions. The two most popular commercial examples are the SmartBall® and Sahara®, as shown in Figs. 7(a) and 1.7(b), respectively. SmartBall® is a sphere-shaped device that follows waterflow and has an acoustic sensor to measure the sound inside the pipe; an accelerometer and a gyroscope to map the device path underground; and a magnetometer to measure the magnetic field coming of the pipe-wall to identify joints and other features in the pipeline (XYLEM, 2023a). Sahara® is an inline tethered device that follows the waterflow via a parachute-like structure, and has an acoustic sensor to measure the sound inside the pipe and a camera with embedded light system for visual inspection (XYLEM, 2023b). In addition, research is currently being carried out to design in-pipe robots for leak localization in buried water pipes (CHATZIGEORGIOU *et al*., 2012; MOHAMED *et al*., 2021), and for leak localization in pipes with large diameter which are commonly used to transport gas and oil (WALEED *et al*., 2019; MOHAMED *et al*., 2021).

Figure 7 – Examples of commercial in-pipe inspection equipment. (a) SmartBall® and (b) Sahara®.

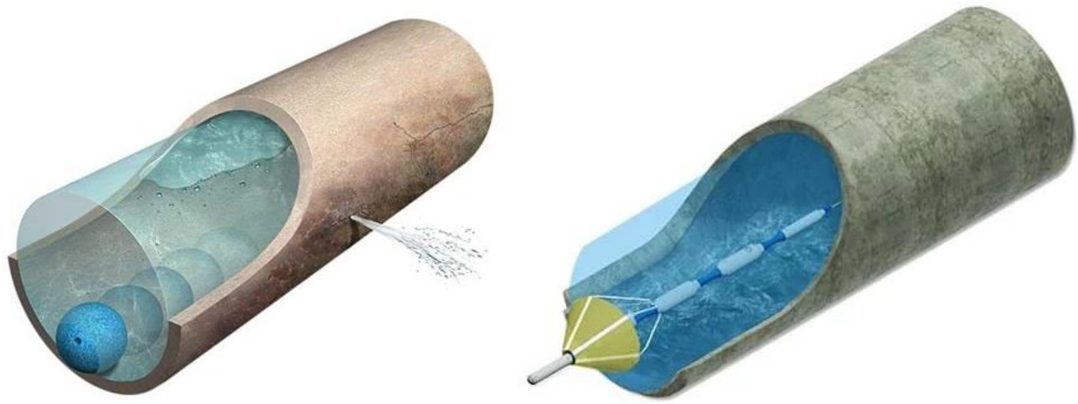

(a) (b)

Source: (a) Xylem (2023a) and (b) Xylem (2023b).

The main advantages of in-pipe inspection equipment are that they can be used to locate multiple leaks in only one application, and can also be used to monitor other defects in the pipe, such as blockages and corrosion of metallic pipes.

The main disadvantages of such an equipment are that their application is limited to a minimum pipe diameter so that the device can be inserted in the pipe, and can only be operated by the respective manufacturing company. Furthermore, there is a risk of the in-pipe device diverting from the correct path or getting stuck during the inspection.

- **Leak noise correlators:** computer-based devices that pinpoint the leak position along a straight section of the pipeline. The localization procedure is usually based on synchronized measurements of pipe-wall vibration using accelerometers, or leak sound using hydrophones, at two different positions along a straight section where the leak might be located as shown in Fig. 8. Then, the time delay between the two signals is estimated via cross-correlation. By combining the time delay with the leak noise velocity in the pipe and the distance between the two sensors, the leak position in relation to one of the sensors is estimated (FUCHS; RIEHLE, 1991; HUNAIDI *et al*., 2000; GLENTIS; ANGELOPOULOS, 2019).

Figure 8 – Example for the application of leak noise correlators on a buried water pipe.

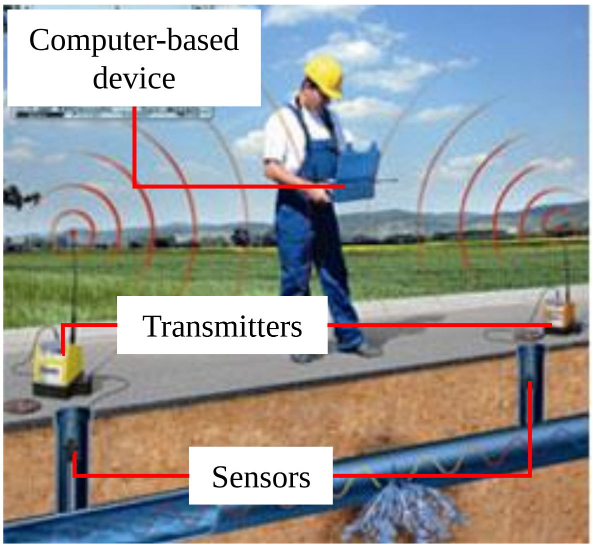

Source: adapted from Aquasave (2015).

The main advantage of leak noise correlators is that the signals can be passed through a bandpass filter directly in the computer-based device before calculating cross-correlation (FUCHS; RIEHLE, 1991; HUNAIDI *et al*., 2000). This procedure makes such devices quite robust to uncorrelated noise as the corresponding SNR is enhanced when the cut-off frequencies are correctly set for the bandpass filter (GAO *et al*. 2004). Historically, leak noise correlators are one of the most popular devices applied on leak surveys due to its effectiveness and simplicity in relation to other leak localization techniques (FUCHS; RIEHLE, 1991).

The main disadvantage of leak noise correlators is that the respective technique relies on knowing the velocity of leak noise propagation in the pipe to estimate the leak position. Usually, the values for such a velocity stored in the leak noise correlators are estimated empirically for different pipe diameters, pipe materials, and types of sensors, as shown in ADS (2010).

An assessment of the velocities provided by multiple leak noise correlators commercially available was carried out by Sewerin (2023a), showing that there is a great variability among them. Furthermore, experiments to measure the velocity of leak noise propagation were also performed by Sewerin (2023a), whose results show that the velocity may vary more than 100 m/s for a specific pipe diameter and material. According to the investigation, such a variation does not result in a relevant error for the leak noise position if the distance between the two sensors is not too long (< 30 m). To attend such a condition, operators change the position of the pair of sensors along the pipeline keeping a short space interval between them until the leak is pinpointed. An alternative solution adopted for some types of leak noise correlators, as the one shown in Gutermann (2023), is to synchronize multiple sensors so that multiple measurement points can be performed simultaneously along the pipeline. The condition of keeping a short distance between the sensors, however, might not be possible as the corresponding access points might be quite distant one from the other, and the leak noise propagating in the pipe cannot reach them due to the weak excitation combined with the strong attenuation. An alternative solution for this is to measure in-situ the velocity of leak noise propagation by exciting the pipe strongly with an actuator and estimating the interval that it takes to travel a particular section of the pipe, as discussed in Almeida *et al*. (2021).

- **Leak noise loggers:** programmable data loggers that can be combined with different types of sensors, such as accelerometers and hydrophones, to monitor leaks in a pipe network. The sensors are deployed in multiple access points, such as underground valves and hydrants, generally spaced 200 to 500 m apart (ISLAM *et al*. 2022). The localization procedure with leak noise loggers is usually carried out at night to minimize the interference of background noise (ISLAM *et al*. 2022; EL-ZAHAB; ZAYED, 2019).

Figure 9 – Example for the application of leak noise loggers on a buried water pipe. (a) Temporary leak survey and (b) logger permanently fixed to an access point.

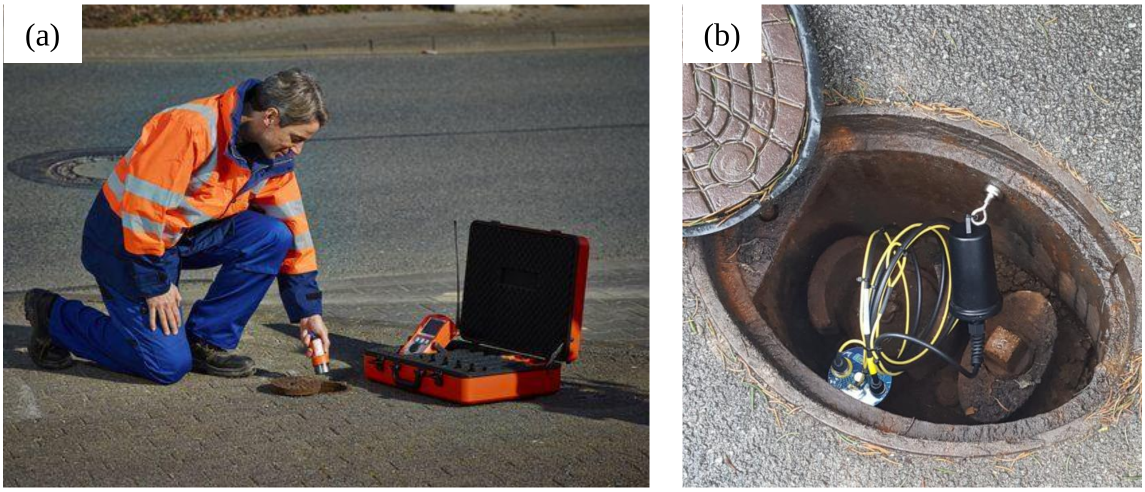

Source: (a) Sewerin (2023b) and (b) Esders (2020).

The main advantage of leak noise loggers is that they can be used to locate multiple leaks in a pipe network (EL-ZAHAB; ZAYED, 2019). They can also be used for temporary leak surveys, as shown in Fig. 9(a), or for permanent leak monitoring in which the loggers are fixed permanently to specific access points (EL-ZAHAB; ZAYED, 2019), as shown in Fig. 9(b). Note that the second type of operation is very convenient since it does not require a considerable workforce as many other leak localization techniques. It also enables leak localization at an early stage saving an important amount of water. Furthermore, as leak noise loggers can provide data on a regular basis, their localization procedure can be improved by using classification techniques, such as Naïve Bayes, decision tree, deep learning and support vector machine (EL-ZAHAB *et al.*, 2016; EL-ZAHAB; MOHAMMED ABDELKADER; ZAYED, 2018). It is also expected that the performance of such devices for online leak monitoring of complex pipe networks will improve over the next years due to their compatibility with wireless sensors and Internet of Things (IoT), together with the significant amount of research that has been conducted on such topics recently. (EL-ZAHAB; MOHAMMED ABDELKADER; ZAYED, 2018; RABEEK; BEIBEI; CHAI, 2019; GAUTAM *et al.*, 2020; ISLAM; ASLAN, 2021)

The main disadvantage of leak noise loggers is that they cannot precisely pinpoint the leak position. So, other technologies, such as leak noise correlators, listening sticks or geophone-based devices, are usually applied in the vicinities of the pipeline where the loggers pointed out a leak to enhance the localization procedure (DATAMATIC, 2023).

- **Optical-fiber-based equipment:** recent solutions for primarily permanent leak monitoring where an optical fiber wire is buried together with the pipe, as shown in Fig. 10, and one section end is connected to a computer-based device that generates the light waveforms and captures the portion that is scattered along the optical fiber, as shown in Joode (2021) for example. They operate based on the dilation and contraction of the optical fiber due to the local temperature change caused by a leak, depending upon the fluid temperature in relation to the fiber surroundings temperature. If a particular section of the fiber stretches or contracts, the respective density changes locally and, hence, the amount of light that is scattered changes as well (NIKLES *et al.*, 2004). Due to such a physical behavior, two phenomena with distinct spectral characteristics are explored in fiber optics: the Raman scattering and the Brillouin scattering.

Figure 10 – Example for the application of optical-fiber-based equipment on a buried water pipe.

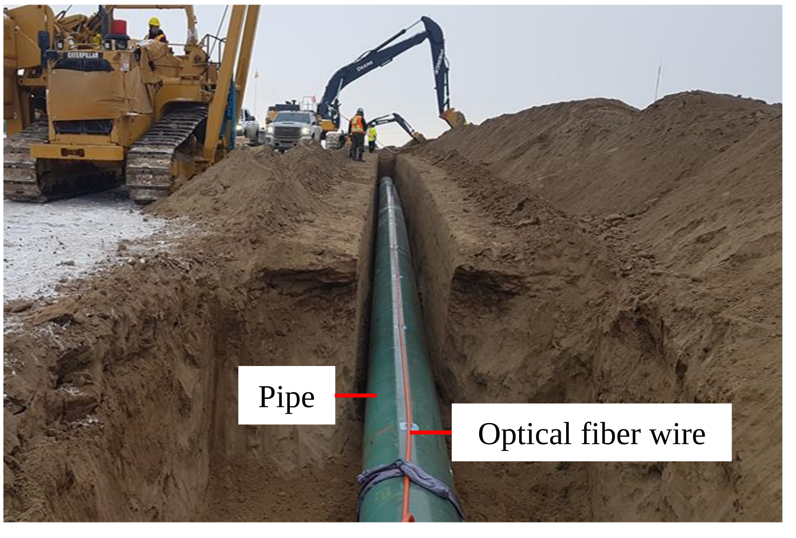

Source: adapted from Koles, Jalilian and Hull (2020).

Raman scattering is the occurrence of two frequency shifted components, named Stokes and Anti-Stokes, in the spectrum of the scattered light due to the fiber particle motion induced by temperature change. The amplitude of the Anti-Stokes component is strongly temperature dependent, whereas the amplitude of the Stokes component is not. After filtering the irrelevant frequency content, the ratio between the amplitudes of the Anti-Stoke and Stokes components provides the fiber temperature (NIKLES *et al.*, 2004).

Brillouin scattering is the occurrence of high-frequency shifted components (in the GHz range) in the spectrum of the scattered light, due to acoustic waves propagating in the fiber generated by temperature change. The acoustic waves create moving gratings where the incident light is diffracted. Then, the diffracted light experiences a Doppler shift as the moving gratings travel along the fiber at the velocity of the acoustic waves, which is directly related to the medium density and depends on both temperature and strain. So, the fiber temperature and strain can be extracted from the spectrum of the scattered light due to Brillouin scattering phenomenon (NIKLES *et al*., 2004; SHI *et al*., 2021). Brillouin-based sensing techniques are exploited more than Raman-based techniques because the former is based on measuring a frequency and the latter is based on measuring amplitudes. Therefore, Brillouin-based techniques tend to be more accurate than Raman-based techniques since amplitude usually suffers from higher sensitivity to drifts (NIKLES *et al*., 2004).

The main advantages of optical-fiber-based equipment are that they can be used to locate multiple leaks in a pipeline (YANG; GUO; GAO, 2020) and, once the optical fiber is buried with the pipe, it does not require a considerable workforce for the localization procedure. Furthermore, they also enable leak localization at an early stage saving an important amount of water.

The main disadvantages of the optical-fiber-based equipment are that they are quite expensive because of the optical fiber high cost (ISLAM *et al*. 2022), and require a lot of efforts and investments to deploy optical fiber on an entire pipe network.

1.2.2 Leak localization technologies without access to the buried pipe

Depending on the pipe network, there are some situations where the operators need to locate a leak without having access to the buried pipe, or the access points are excessively far one from the other and, hence, the leak noise propagating in the pipe is heavily attenuated before reaching the sensors. For these types of situations, operators have to apply leak localization technologies that do not require access to the buried pipe. Each one of them is discussed as follows, in which a brief explanation is provided followed by the respective advantages and disadvantages.

Figure 11 – Example for the application of listening sticks (a) on a buried water pipe and (b) on the soil.

Source: (a) Abdullah (2020) and (b) Atkins (2022).

- **Listening sticks:** devices used to hear the leak sound propagating in the buried pipe, as shown in Fig. 11(a), or in the soil, as shown in Fig. 11(b). The stick is made of a rigid material, such as steel or wood, to transmit the vibration to a membrane within a resonant cavity that amplifies the leak sound in mechanical listening sticks, such as the one shown in HWM (2023), or to an electro-mechanical transducer that digitally amplifies the leak sound in electronic listening sticks, such as the one shown in Envirotech Online (2013). The leak localization procedure with listening sticks generally starts with operators surveying for leaks by listening to the sound at multiple access points of a pipe network. Once they encounter a suspected leak, operators pinpoint it by listening on the ground surface directly above the pipe at short space intervals of about 1 m (HUNAIDI, 2000).

The main advantages of listening sticks are their simple setup and straightforward operation, as no equipment needs to be inserted in the pipe or buried in the soil. Furthermore, some modern electronic devices also contain built-in digital filters that improve the localization procedure (HUNAIDI, 2000).

The main disadvantages of listening sticks are that their performance relies on the operator expertise, which means that the same device might result in different locations for a particular leak if it is handled by different operators (ISLAM *et al.*, 2022; HAMILTON;

CHARALAMBOUS, 2020; EL-ZAHAB; ZAYED, 2019; HUNAIDI, 2000). Furthermore, the localization procedure with such devices is quite sensitive to external sources of noise (ISLAM *et al*., 2022; HAMILTON; CHARALAMBOUS, 2020; EL-ZAHAB; ZAYED, 2019), since they only measure the amplitude of leak sound propagating in the pipe or in the soil.

- **Geophone-based devices:** geophones are sensors designed to measure the ground motion in terms of displacement or velocity. They consist of a moving mass wrapped by a coil of wire, suspended by a spring over a magnet as shown in Fig. 12(a). When the mass moves, the interaction of the movement and the magnetic field induces an electrical current through the coil of wire resulting in an electrical signal read in terms of voltage (EARTH SCIENCES, 2021). Some geophone-based devices, such as the one shown in Heath Consultants (2001), are designed to work as microphones in which a rigid plate is placed on the ground surface and the device resonant chamber is placed on the plate to generate sound, that is converted to voltage by an electro-mechanical transducer. The leak localization procedure with geophone-based devices is similar to the one using listening sticks on the ground surface, where the operators pinpoint the leak by measuring ground motion directly above the pipe at short space intervals (HEATH CONSULTANTS, 2001), as shown in Fig. 12(b).

The main advantages of geophone-based devices are their simple setup and straightforward operation, as no equipment needs to be attached or inserted in the pipe and no equipment needs to be buried in the soil as well.

Figure 12 – Geophone-based devices. (a) Schematic diagram for a geophone and (b) example for the application of a geophone-based device for leak localization.

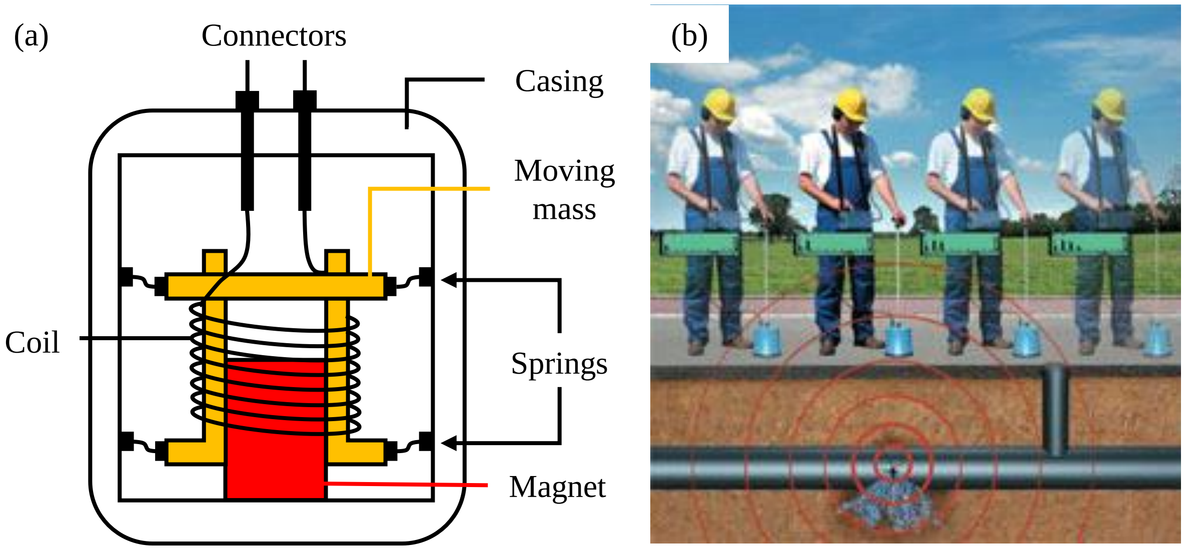

Source: adapted from (a) Guideline Geo (2021) and (b) Aquasave (2015).

The main disadvantages are their performance relies on the operator expertise (HEATH CONSULTANTS, 2001), and their localization procedures are quite sensitive to external sources of noise since they only measure amplitude of ground vibration.

- **GPR devices:** Ground Penetrating Radar (GPR) devices, such as the one shown in GeoScan (2023), operate by introducing high-frequency electromagnetic waves into the soil via a transmitting antenna. When the incident waves reach an object that has a different dielectric permittivity than for the soil, such as a buried pipe, a portion of the waves is reflected towards the ground surface and a receiving antenna captures them, as shown in Fig. 13, and the object is then located by analyzing the amplitude and time delay of such reflected waves for each position of the device on the ground surface (HUNAIDI *et al.*, 2000; ABOUHAMAD; ZAYED; MOSELHI, 2016). A leak, however, can be located by GPR devices due to two phenomena. One is the underground voids created by water that escapes from the leak and circulates near the pipe, creating a medium that contains a quite different dielectric permittivity in relation to the soil, which results reflections of the incident waves coming from the transmitting antenna. The other phenomenon is the soil saturation due to water that escapes from the leak, changing the respective dielectric permittivity that slows down the incident waves coming from the transmitting antenna. Since a particular frequency is set for the electromagnetic waves in the device, the location determined for the pipe is commonly deeper due to the decrease of the wave velocity in the saturated soil. (HUNAIDI *et al.*, 2000; ABOUHAMAD; ZAYED; MOSELHI, 2016)

Figure 13 – Example for the application of GPR devices for leak localization.

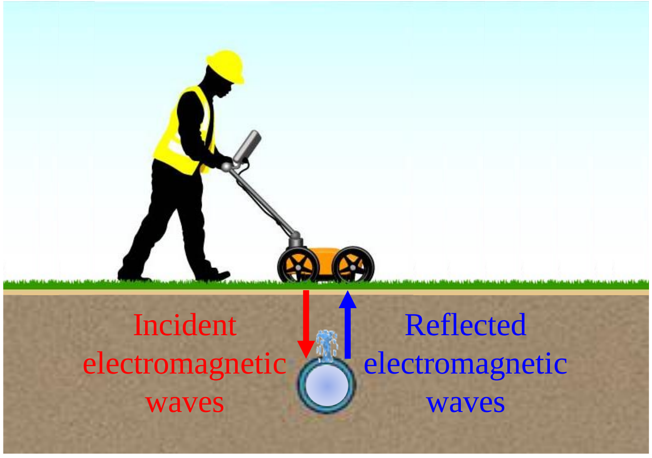

Source: adapted from Provac Australia Pty Ltd (2021).

The main advantages of GPR devices are their simple setup and straightforward operation, as no equipment needs to be attached or inserted in the pipe and no equipment needs to be buried in the soil as well. Furthermore, different frequencies can be set for most of GPR devices, such as the one shown in GeoScan (2023), to control the penetration depth and the resolution for the electromagnetic waves inserted in the soil. If a high frequency (in the MHz range) is set, the waves can reach deeper depths but cannot locate smaller objects due to the low spatial resolution. However, if a low frequency (in the GHz range) is set, the waves can only reach shallow depths but can locate smaller targets due to the high spatial resolution (ISLAM *et al.*, 2022; ABOUHAMAD; ZAYED; MOSELHI, 2016).

The main disadvantage of GPR devices is that their performance depends on the moisture content of the surrounding soil, as the electromagnetic energy is strongly attenuated by water (ABOUHAMAD; ZAYED; MOSELHI, 2016; METJE *et al.*, 2007). This means that if a buried pipe contains a leak running for a long period, a great portion of the surrounding soil becomes saturated and, hence, most of the wave energy is attenuated rather than be reflected. Furthermore, GPR devices are expensive solutions for leak detection, (ISLAM *et al.*, 2022; EL-ZAHAB; ZAYED, 2019) and the presence of other buried objects close to the pipe can also compromise their performance since they can reflect the incident waves coming from the transmitting antenna. (CATALDO *et al.*, 2014)

- **Infrared cameras:** devices that capture infrared radiation from a surface and display it as a visible image (HUNAIDI *et al.*, 2000). They are applied for leak detection assuming that the fluid contained inside the buried pipe has a different temperature in relation to the surrounding soil, so that the pipe and the leak can be located by analyzing the temperature gradient on the ground surface as shown in Fig. 14.

Figure 14 – Example for the application of infrared cameras for leak localization.

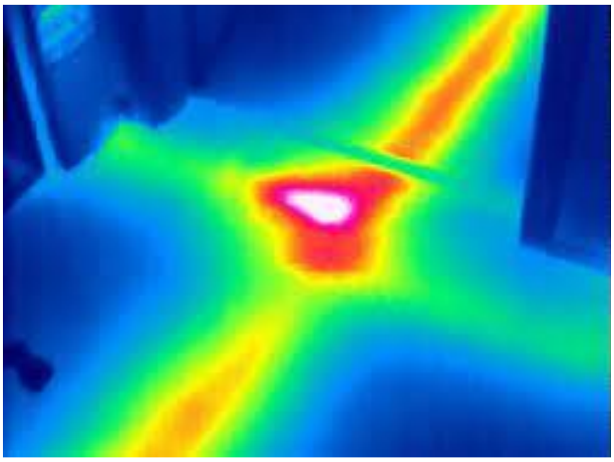

Source: adapted from InfraTec (2023).

The main advantage of infrared cameras is that they can be used to monitor large areas in less time in comparison with other leak localization techniques (FAHMY; MOSELHI, 2009). Furthermore, they have a simple setup and straightforward operation, as no equipment needs to be attached or inserted in the pipe, and no equipment needs to be buried in the soil as well.

The main disadvantage of infrared cameras is that their performance depends on a minimum difference between the fluid temperature and the soil temperature. Otherwise, it is not possible to differentiate the pipe and the leak from the background. In addition, the environment also must be carefully considered to minimize interferences when using infrared cameras, as the temperatures of the ground surface and pavement change throughout the day, and the respective mean daily temperature also changes throughout the seasons (HUNAIDI *et al.*, 2000; FAHMY; MOSELHI, 2009).

1.3 LITERATURE REVIEW ON PIPE AND LEAK LOCALIZATION TECHNIQUES BASED ON MEASUREMENTS OF GROUND SURFACE VIBRATION

According to the literature review on the available leak localization technologies presented previously, there are only a few techniques that do not require carrying out measurements on the buried pipe. As such technologies have limitations that can compromise their respective performance, and placing sensors directly on the buried pipe or on an access point might not be possible as well, investigations are being conducted to evaluate potential solutions that can improve leak localization technologies in which sensors are not in contact with the pipe. To do this, the first step is usually to locate the buried pipe and then the leak position, in which vibro-acoustic localization techniques have been already shown to be promising solutions to locate buried pipes (METJE, 2007; MUGGLETON; RUSTIGHI, 2013). This motivates a brief review for the state-of-the-art research on pipe and leak localization techniques based on measurements of ground surface vibration, to highlight the main contributions for the leak localization technologies and the main limitations that can be overcome with alternative approaches.

1.3.1 Pipe localization techniques based on measurements of ground surface vibration

The pipe localization techniques based on measurements of ground surface vibration are classified according to Fig. 15. The classification adopted for the pipe localization techniques in this thesis is based on the criterium used by Liu *et al*. (2020), in which they are divided into techniques with single access to the buried pipe and techniques without access to the buried pipe. Note that a single access only provides a contact point to the buried pipe, but not its location on the ground surface. As shown in Fig. 15, the pipe localization techniques that have single access to the buried pipe are subdivided into traditional acoustic transmission and improved acoustic transmission techniques, and the ones that do not have access to the buried pipe are subdivided into active seismic wave techniques and point vibration measurement technique. Each one of them is discussed as follows, in which a brief explanation is provided followed by the respective advantages and disadvantages.

Figure 15 – Classification of the pipe localization techniques based on measurements of ground surface vibration.

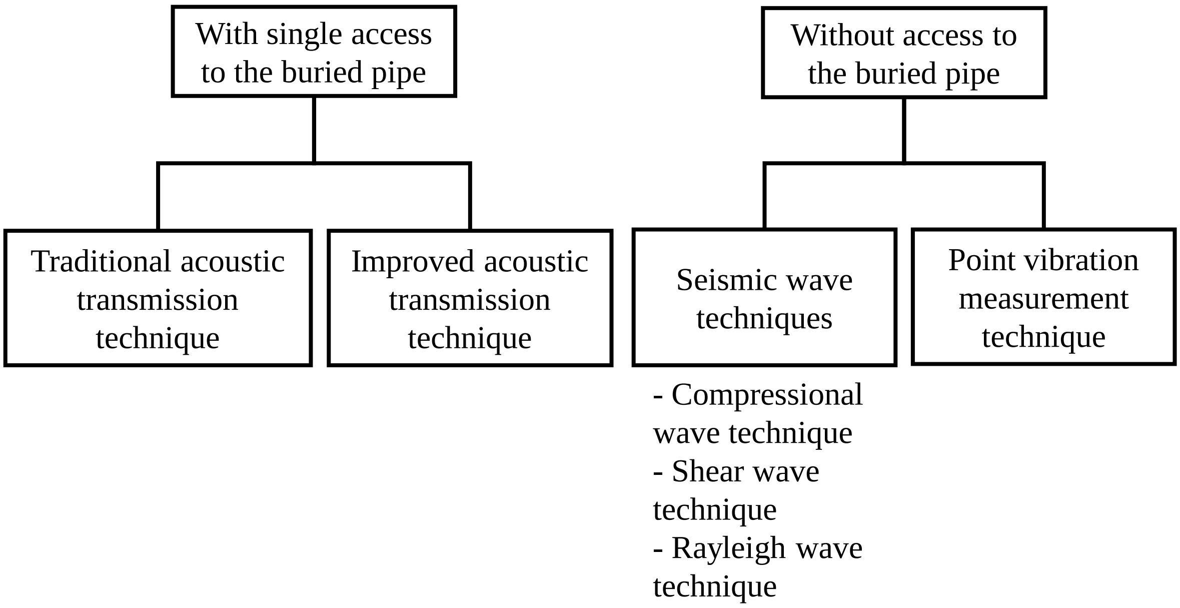

Source: elaborated by the author.

- **Traditional acoustic transmission technique:** pipe localization technique in which the buried pipe is excited actively by some mechanism attached to the pipe, or to an access point (STERLING *et al*., 2009), as shown in Fig. 16. The buried pipe can also be passively excited by opening a valve or a hydrant connected to it (STERLING *et al*., 2009). Such an excitation generates acoustic waves that travel along the buried pipe, and waves that radiate into the soil towards the ground surface. The vibration of the ground surface is measured by a single sensor, or a set of sensors, and the pipe location is then determined on the ground surface by the sensor position that contains the highest amplitude (STERLING *et al*., 2009; KATZ; KARAA; NIVER, 2011). This is because the distance directly above the pipe is the shortest one in relation to the ground surface and, hence, the waves radiating from the buried pipe suffer less attenuation (JETTE; PARKER, 1980).

The main advantages of the traditional acoustic transmission technique are its simple setup as it can be performed with just one excitation source and one sensor (KATZ; KARAA; NIVER, 2011), and its simple data analysis as only vibration amplitude is measured on the ground surface. This type of technique is already well stablished and is applied commercially with available devices for pipe localization, such as the ones shown in Fuji Tecom (2022) and Radiodetection (2023).

Figure 16 – Example for the application of acoustic transmission techniques for pipe localization. (a) Lateral and (b) front views showing the measurement setup.

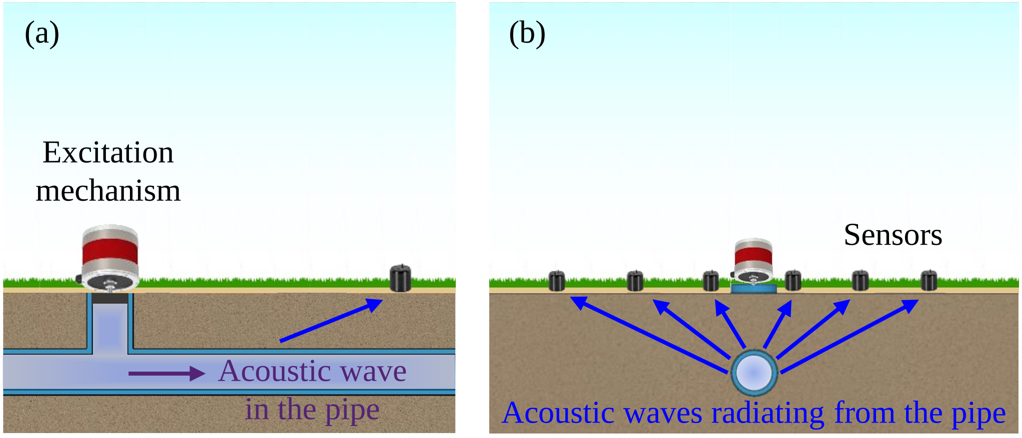

Source: elaborated by the author.

The main disadvantages of the traditional acoustic transmission technique are that it can only be applied if there is at least one access point to the buried pipe, and its performance is quite sensitive to background noise since it only measures amplitude of ground surface vibration (LIU *et al*., 2020).

- **Improved acoustic transmission technique:** pipe localization technique proposed by Muggleton, Brennan and Gao (2011) whose measurement setup is illustrated in Fig. 16, in which an inertial shaker is mounted on a plastic plate bolted to the flanged end of the pipe. Such a setup is performed to excite specifically the predominantly fluid borne-axisymmetric wave, which is well-coupled with the surrounding soil and effectively radiates waves into it (MUGGLETON; BRENNAN; PINNINGTON, 2002; MUGGLETON; BRENNAN; LINFORD, 2004). A set of sensors positioned inline is used to measure the vibration for a rectangular measurement grid on the ground surface. The frequency response functions between the signals measured for each position of the measurement grid, and the input voltage of the shaker are calculated. Then, the contour maps for the respective amplitude and spatially unwrapped phase are plotted for the entire measurement grid for a particular frequency. The results show that the unwrapped phase is a feature more reliable to extract the pipe location on the ground surface, because it is more robust to the interference of background noise. The amplitude, however, can be used as a supplementary feature to identify discontinuities where reflections can occur, such as a bend in the pipe or a change in the pipe material/dimensions, or even a leak.

The main advantage of the improved acoustic transmission technique is its robustness to background noise since the localization procedure is based on both amplitude and phase of the frequency response functions between each sensor on the ground surface and the shaker input.

The main disadvantage of this technique is that it can only be applied if there is at least one access point to the buried pipe, and the respective data analysis is more complex than for the traditional acoustic transmission technique because it requires the analysis of contour maps. Furthermore, their practical application can be complex and time-consuming, because a large number of measurement positions is usually required to perform a contour map.

Figure 17 – Example for the application of active seismic wave techniques for pipe localization. (a) Lateral and (b) front views showing the measurement setup.

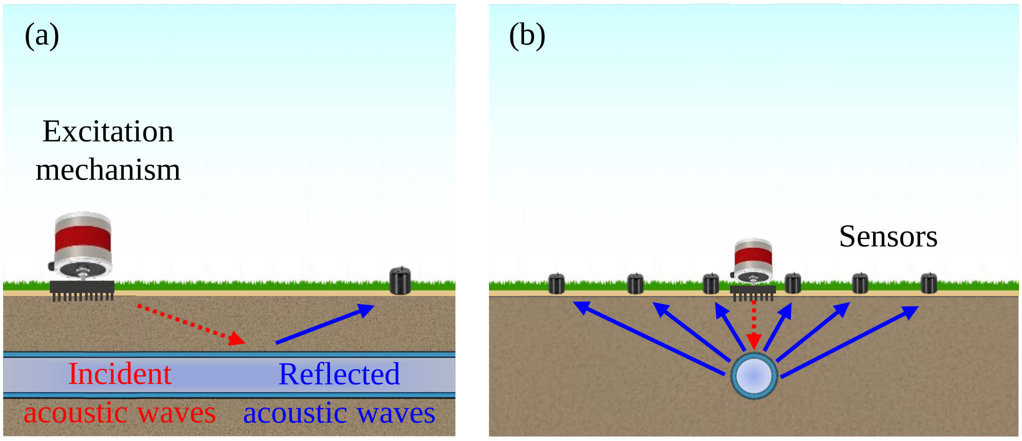

Source: elaborated by the author.

- **Active seismic wave techniques:** pipe localization techniques in which the soil is excited by some mechanism on the ground surface, as shown in Fig. 17. The excitation generates acoustic waves that propagate in the soil, which are reflected after reaching the buried pipe due to their different mechanical properties in relation to the soil (MUGGLETON; PAPANDREOU, 2014). After being reflected, the waves propagate towards the ground surface where they are captured by a set of sensors positioned inline.

These techniques are subdivided according to the type of wave that is predominantly generated in the soil by the excitation mechanism, i.e., compressional wave, shear wave and Rayleigh wave techniques (LIU *et al*., 2020). Papandreou, Brennan and Rustighi (2011) proposed an excitation mechanism composed by an inertial shaker and a platform that contains prongs to properly couple the mechanism with the ground. The inertial shaker is attached to the platform in a specific orientation to generate predominantly compressional waves (also known as longitudinal waves) in the soil, which are the ones whose particles move at the same direction that the disturbance is propagating in the medium (KIM, 2010). Muggleton and Papandreou (2014) proposed an excitation mechanism similar to previous one, but with a different platform in which the inertial shaker is attached in a specific orientation to generate predominantly shear waves (also known as transverse waves) in the soil, which are the ones whose particles move perpendicularly to the direction that the disturbance is propagating in the medium (KIM, 2010). Once the ground surface vibration is measured for the compressional wave and shear wave techniques, an underground cross-sectional image of the pipe in a plane perpendicular to the ground surface is elaborated, in which the region that contains strong reflection content corresponds to the pipe location. To elaborate such an image, the cross-sectional area of the soil covered by the image is first discretized in a specific number of pixels. By combining an estimation for the respective wave speed in the soil and the relative distance that the wave takes to propagate from the source, reflect on a buried object and reach a sensor on the ground surface, the time of flight for such a path is calculated for each pixel of the image. Then, the envelope of cross-correlation function between the vibration measured by each sensor on the ground surface and the excitation signal is calculated. The values of such envelopes that correspond to a particular time of flight are summed, and then plotted in the respective pixel of the image. So, if a pixel corresponds to a reflector, then its total sum is higher than for a pixel that does not correspond to a reflector (PAPANDREOU; BRENNAN; RUSTIGHI, 2011; MUGGLETON; PAPANDREOU, 2014).

A Rayleigh wave is a specific type of wave that propagates near the surface of solids (such as the ground surface), and contains both longitudinal and transverse motions with a phase difference (TELFORD; GELDART; SHERIFF, 1990). As performed by Phillips, Cascante and Hutchinson (2000), this particular type of wave can be generated by simply hitting the ground surface. After measuring the ground surface vibration with a set of sensors, an analysis is performed in both time and frequency domains for a case in which there is a buried object, and a case where there is none for the same soil. For the time domain analysis, the acceleration time series measured by each sensor are simply summed together and plotted on a plan, as a function of the timestamp and the distance in relation to the impact. For the frequency domain analysis, the power spectral density for each sensor is plotted on a plan as a function of the frequency and the distance in relation to the impact. In the time domain, the object location is given by the increase of the amplitude of late time responses, which is interpreted as an amplification of Rayleigh waves for the sensors located between the buried object and the source on the ground surface. In the frequency domain, the object location is given by the increase of the power spectral densities for sensors close to the buried object.

The main advantage of active seismic wave techniques is the convenience of not requiring any access to the buried pipe. The shear wave technique, in particular, has the advantage of resulting a better resolution for the pipe location than the compressional wave technique, because shear waves are slower than compressional waves and, consequently, the wavelength of shear waves is shorter than for the compressional waves (PAPANDREOU; BRENNAN; RUSTIGHI, 2011; MUGGLETON; PAPANDREOU, 2014). Furthermore, the Rayleigh wave technique is even more convenient than the other active seismic wave techniques, as the soil excitation can be performed by a simple impact rather than using a sophisticated mechanism to excite the soil.

The main disadvantage of compressional wave and shear wave techniques is they require an estimation for the wave speed in the soil, to elaborate the underground cross-sectional image to determine the pipe location (PAPANDREOU; BRENNAN; RUSTIGHI, 2011; MUGGLETON; PAPANDREOU, 2014). This can be quite problematic because more than one type of wave can propagate in the soil, and the corresponding wave speed might vary for different regions since the soil might not be homogenous. Furthermore, the performance of such techniques can also be affected by the reflections from objects buried in the vicinities of the pipe, and their application might be very cumbersome as the excitation mechanism can also generate surface waves that interfere with the particular wave considered for the technique (PAPANDREOU; BRENNAN; RUSTIGHI, 2011; MUGGLETON; PAPANDREOU, 2014). The main disadvantage of the Rayleigh wave technique is that it can only be used to locate objects buried at shallow depths, because the amplitude of Rayleigh waves decays exponentially with distance in relation to the ground surface (TELFORD; GELDART; SHERIFF, 1990).

- **Point vibration measurement technique:** technique for the detection of shallow-buried objects proposed by Muggleton, Brennan and Rogers (2014), in which an electrodynamic shaker with a built in impedance head is placed on the ground surface. The shaker is used to apply a harmonic force on the soil, and the impedance head is used to measure the point accelerance of the ground surface across a buried object. At low frequencies, the soil behaves as a single degree of freedom system with a well-defined resonance whose frequency is governed by the density and elastic properties of the soil locally. Since a shallow-buried object can alter the soil resonance measured directly above it on the ground surface, changes on the resonance frequency and the corresponding magnitude are observed to determine the object location (MUGGLETON; BRENNAN; ROGERS, 2014).

The main advantages of the point vibration measurement technique are the convenience of not requiring any access to the buried pipe, and not requiring any estimation for some wave speed propagating in the soil. Furthermore, this technique can be even more convenient than the active seismic wave techniques since it does not require a set of sensors placed on the ground surface.

The main disadvantage of the point vibration measurement technique is it can only be used to detect objects buried at shallow depths. Furthermore, it also requires an electromagnetic shaker with a special built-in sensor, which has the potential of increasing the cost for the application of such a technique.

1.3.2 Leak localization techniques based on measurements of ground surface vibration

Besides generating acoustic waves that travel along the buried pipe, a leak also radiates waves directly into the soil which can be sensed on the ground surface (ZHANG *et al*., 2022). Although the leak noise generation is a complex phenomenon that is still not fully understood, Burn *et al*. (1999) divided it into three types of sources depending on the different regions in which an acoustic wave can be generated. The first type of source is due to the water flowing through the leak orifice, which interacts strongly with the pipe wall generating acoustic waves that travel along the buried pipe. The second type of source is due to the impact of the water jet with the underground cavity wall, and the third type of source is due to the water that circulates inside the underground cavity, in which both sources generate waves that propagate into the soil. Since these waves are strongly attenuated with distance, leak localization techniques based on measurements of ground surface vibration are only applied for positions relatively close to the leak. They are basically divided in two classifications, named as image fusion technique and passive seismic wave technique. Each one of them is discussed as follows where a brief explanation is provided, followed by the respective advantages and disadvantages.

- **Image fusion technique:** leak localization technique proposed by Yan *et al*. (2020) whose measurement setup is illustrated in Fig. 18, in which a leak excites the buried pipe resulting in acoustic waves that travel along it, and acoustic waves that radiate into the soil as discussed previously. Like the improved acoustic transmission technique, a set of sensors positioned inline is used to measure the vibration for a rectangular measurement grid on the ground surface. Then, the contour map for the respective amplitude is plotted for multiple frequencies that correspond to the bandwidth in which the leak noise is predominant. The contour maps are then combined using an image fusion algorithm to generate an enhanced image, in which the leak position can be clearly located on the ground surface.

The main advantages of the image fusion technique are the convenience of not requiring any access to the buried pipe, and not requiring any estimation for some wave speed propagating in the soil. Furthermore, such a technique has the potential of being totally automated since the respective algorithm provides a result that does not require a sophisticated data analysis by the operator.

The main disadvantages of the image fusion technique are its performance can be sensitive to background noise because it only measures the amplitude of ground surface vibration, and their practical application can be complex and time-consuming since a large number of measurement positions is usually required to perform a contour map.

Figure 18 – Example for the application of leak localization techniques based on measurements of ground surface vibration. (a) Lateral and (b) front views showing the measurement setup.

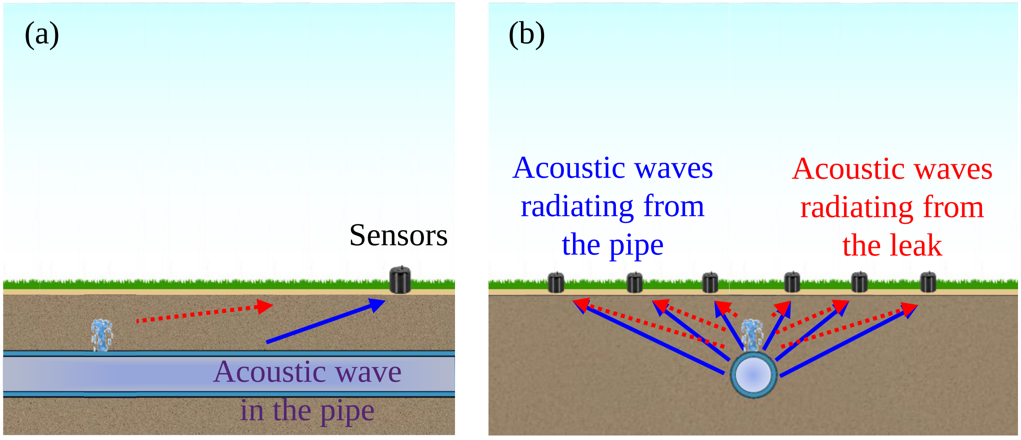

Source: elaborated by the author.

- **Passive seismic wave techniques:** leak localization technique initially proposed by Wang *et al*. (2017), in which the leak coordinates are provided on two-dimensional space, and then extended by Cheng *et al*. (2018), in which the leak coordinates are provided on three-dimensional space. Both of them are similar in principle to the compressional wave and shear wave techniques, but no excitation mechanism is used to generate waves in the soil. Instead, a leak in the buried pipe generates acoustic waves that propagate into the soil and then are captured on the ground surface by a set of sensors positioned inline, as shown in Fig. 18. The time difference between a pair of sensors along a line across the pipe is calculated by combining an estimation for the respective wave speed in the soil, and the relative distance that the wave takes to propagate from a leak to a sensor on the ground surface, on two-dimensional space or on three-dimensional space. Once the ground surface vibration is measured, the time difference between each pair of sensors is estimated via cross-correlation function. Both time differences are then used as arguments of an objective function which provides an estimation for the leak position on two-dimensional space, or on three-dimensional space, via an optimization algorithm.

The main advantages of the passive seismic wave techniques are the convenience of not requiring any access to the buried pipe, and not requiring any type of excitation mechanism to generate acoustic waves in the soil.

The main disadvantage of the passive seismic techniques is they require an estimation for the wave speed in the soil, to calculate the time difference between the ground surface vibration measured by a pair of sensors on the ground surface (WANG *et al.*, 2017; CHENG *et al.*; 2018). This can be quite problematic because more than one type of wave can propagate in the soil, and the corresponding wave speed might vary for different regions since the soil might not be homogenous.

1.4 MOTIVATION AND OBJECTIVES

As a great portion of world population is already facing problems related to water scarcity and is prone to turn into even more severe conditions in the next decades, saving non-revenue water by decreasing leakages in water distribution systems is an approach that must be adopted worldwide. Besides being the most suitable solution for water supply in shortage periods, reducing leakages can also provide important benefits for the global economy and ecosystems, since a great amount of energy and resources used for treatment and distribution of water would be saved.

Therefore, water supply sectors around the world depend on the available leak localization technologies to repair their distribution systems in order to decrease the amount of leaks. Based on the respective literature review, there are only a few techniques that can be applied without having access to buried pipes, which also contain limitations that can inhibit their application for some situations. Since not having access to buried pipes might be usual depending on the pipe network, vibro-acoustic techniques have been investigated to complement the available leak localization technologies applied on the ground surface. Based on the respective literature review, most of the proposed vibro-acoustic techniques require an estimation of the wave speed which can be very complicated since more than one wave can propagate simultaneously in the soil. Furthermore, some of them are only based on the amplitude of ground surface vibration and, consequently, the respective performance can be highly affected if SNR is low. Other ones require an excitation mechanism and a grid of sensors on the ground surface, whose setup can be quite complicated, and the cost can be high.

The main motivation of this thesis is to contribute with a new passive leak localization technique based on measurements of ground surface vibration. It does not require an estimate of a wave speed, is robust to interference of background noise, and has a simple and low-cost setup to improve the localization procedure when access to buried pipes is not possible. The proposed technique is composed by two sequential steps. The first step is to locate the pipe position and the second step is to locate the leak position. Based on the investigation carried out by Muggleton, Brennan and Gao (2011), the unwrapped phase is the main feature explored to extract evidence for pipe and leak locations on the ground surface, due to its robustness to the interference of background noise. The technique used by single-sensor roving devices, such as listening sticks and geophone-based devices, is also introduced as a baseline to evaluate the performance of the proposed technique. For this purpose, the objectives of this thesis are

1. To introduce the proposed localization technique which uses a pair of sensors, named two-sensor technique, and the technique used as baseline which uses only one sensor, named one-sensor technique. The phenomenon of wave propagation in soil due to a buried leaking pipe is used as theoretical background to introduce both techniques.

2. To illustrate the application for both localization techniques, by applying them on the theoretical data extracted from the analytical and numerical models of the buried pipe system.

3. To investigate and adjust features for practical application of the two-sensor technique, such as the most suitable domain (time or frequency) to extract the pipe location and the minimum distance between the pair of sensors.

4. To evaluate the performance for practical applications of the two-sensor technique in relation to the one-sensor technique, by applying them on the experimental data collected in test rigs.

5. To evaluate the limitations of the two-sensor technique when the pair of sensors is not positioned perpendicularly to the pipe direction.

1.5 CONTRIBUTIONS TO KNOWLEDGE

- A pipe and leak localization technique was developed based on the unwrapped phase of ground surface vibration. The technique is robust to the interference of background noise, requires no excitation mechanism or an estimation for the wave speed in the soil. Its main purpose is to complement the available leak localization technologies when access to buried pipes is not possible.

- The technique was validated by way of a detailed experimental investigation to evaluate the performance of the proposed localization technique, in relation to the technique used by single-sensor devices.

1.6 THESIS OUTLINE

This thesis consists of 7 chapters and 3 appendices. Chapter 1 presents the main purpose of this research, which is to assist worldwide water supply sectors to minimize non-revenue water by reducing leaks in their distribution systems. A brief literature review of the available leak localization techniques is provided where each one of them is discussed with their respective advantages and disadvantages, showing that only a few do not require access to buried pipes. Then, a brief literature review of pipe and leak localization techniques based on measurements of ground surface vibration is provided to evaluate their contributions to the available leak localization techniques without access to buried pipes, and limitations that can be overcome with alternative solutions. The objectives of the research are then presented, followed by the contributions to knowledge.

Chapter 2 begins with the definition of dispersion relation to explain how a wave propagates in time and space. Then, the phenomenon of wave propagation in soil due to a leaking buried pipe is introduced with an analytical model of the buried pipe system, together with some simplifying assumptions, to explain which types of waves radiate from the pipe into the soil and in which conditions they can do that. The analytical model is then validated qualitatively with the data extracted from a numerical model of the buried pipe system, and with the data extracted from an experiment carried out in a test rig.

Chapter 3 introduces the localization technique proposed in this thesis, named two-sensor technique, and the localization technique used by single-sensor roving devices, named one-sensor technique, in which the pipe localization procedure is detailed for each one followed by the corresponding leak localization procedure. The application of both techniques is also illustrated in this chapter by applying them on the theoretical data, extracted from the analytical and numerical models for the buried pipe system.

Chapter 4 presents an investigation for the features of the two-sensor technique, such as pipe location extraction in time domain or in frequency domain, and distance between the sensors on the ground surface. Such an investigation is performed to adjust each feature adequately, so that the technique presents a proper performance for practical applications.

Chapter 5 introduces the test rigs and the experiments that were carried out to measure ground surface vibration. The contour maps for amplitude and unwrapped phase are presented to investigate the spatial distribution of vibration amplitude and lines of constant phase on the ground surface due to a leaking buried pipe. The one-sensor and two-sensor techniques are then tested with the experimental data extracted from the test rigs, and their performances are compared and discussed based on the analysis carried out for the spatial distribution of the experimental data.

Chapter 6 presents a new experimental dataset which is used to evaluate the performance of the two-sensor technique when the necessary conditions are not fulfilled. Such an investigation is carried out to check limitations of the technique when the sensors are placed relatively far from the pipe, or from the leak, and when they are placed misaligned in relation to the buried pipe on the ground surface. Another experimental investigation is carried out to compare the performance for accelerometers and geophones applied with the two-sensor technique, to verify which type of sensor is more suitable.

Chapter 7 presents the summary of the thesis, the main conclusions for the research and the recommendations for further work.

Appendix A introduces the analytical model for the wavenumber in the pipe, which is used to explain the wave propagation in a buried pipe system in Chapter 2.

Appendix B contains the complementary results for the experimental investigations of the two-sensor technique presented in Chapters 5 and 6.

Appendix C presents the comparison between the sensitivities of geophones and accelerometers to support the discussions presented in Chapter 6.

2 WAVE PROPAGATION IN SOIL DUE TO A LEAKING WATER PIPE

2.1 INTRODUCTION

This chapter presents an analytical model for ground surface vibration due to waves that radiate from a leaking water pipe into the surrounding soil. The development of such a model started with Jette and Parker (1980) by modelling the ground surface vibration directly over a buried gas pipe. A couple of decades later, Gao *et al*. (2017) modified it to investigate the waves that can radiate from a buried water pipe depending on the type of soil, and then Muggleton *et al*. (2023) extended it to model the ground surface vibration for positions across the pipe. Currently, a simplified version for such an analytical model was developed and validated numerically and experimentally by the author advisors and colleagues. This version is presented in this chapter, whose main purpose together with the respective results is to explain the physics of wave propagation in soil due to a leaking water pipe. Such a explanation is then used as a theoretical background to introduce the one-sensor and two-sensor techniques, that correspond to the author main contribution.

The chapter begins with a simple explanation for the dispersion relation to introduce the concept of wavenumber, which is a physical quantity that describes the wave propagation for a system. Then, a brief introduction into the waves that can radiate into the soil from a leaking water pipe, together with the necessary conditions, is provided. This is followed by the respective analytical model for ground surface vibration, which is introduced as an extension of the one for wavenumber of the predominantly fluid-borne axisymmetric wave, presented in Appendix A. The analytical model presented in this chapter is based on the version proposed by Gao *et al*. (2017), but without considering the reflections of incident waves on the ground surface for simplicity. Although it is does not capture all phenomena occurring during wave propagation, the version presented in this chapter is sufficient to replicate the lines of constant phase that travels on the ground surface due to a leaking buried pipe, which are then used to explain the one-sensor and two-sensor techniques. A validation is then performed qualitatively via a numerical model for the buried pipe system and an experiment carried out on a test rig, in which the contour maps resulted for the analytical model are compared with the ones resulted for the numerical model and for the experiment.

2.2 DEFINITION OF THE DISPERSION RELATION

The dispersion relation describes the wave propagation in time and space for a system. A schematic diagram for the propagation of a plane wave $\psi(x,t)$, where t and x correspond to time and space coordinates respectively, is presented in Fig. 19. Plane waves correspond to the type of disturbance in which the motion of every particle along the plane perpendicular to the direction of propagation is the same (GRAFF, 1975), and they are only used in this section to provide a simple explanation for the dispersion relation. The variables T, λ and c correspond to period, wavelength and wave speed, respectively. Note in Fig. 19 that the wave takes a period T to travel a distance that corresponds to λ, so the respective speed is $c = \lambda/T$.

Figure 19 – Schematic diagram for the propagation of a plane wave $\psi(x,t)$ in time and space.

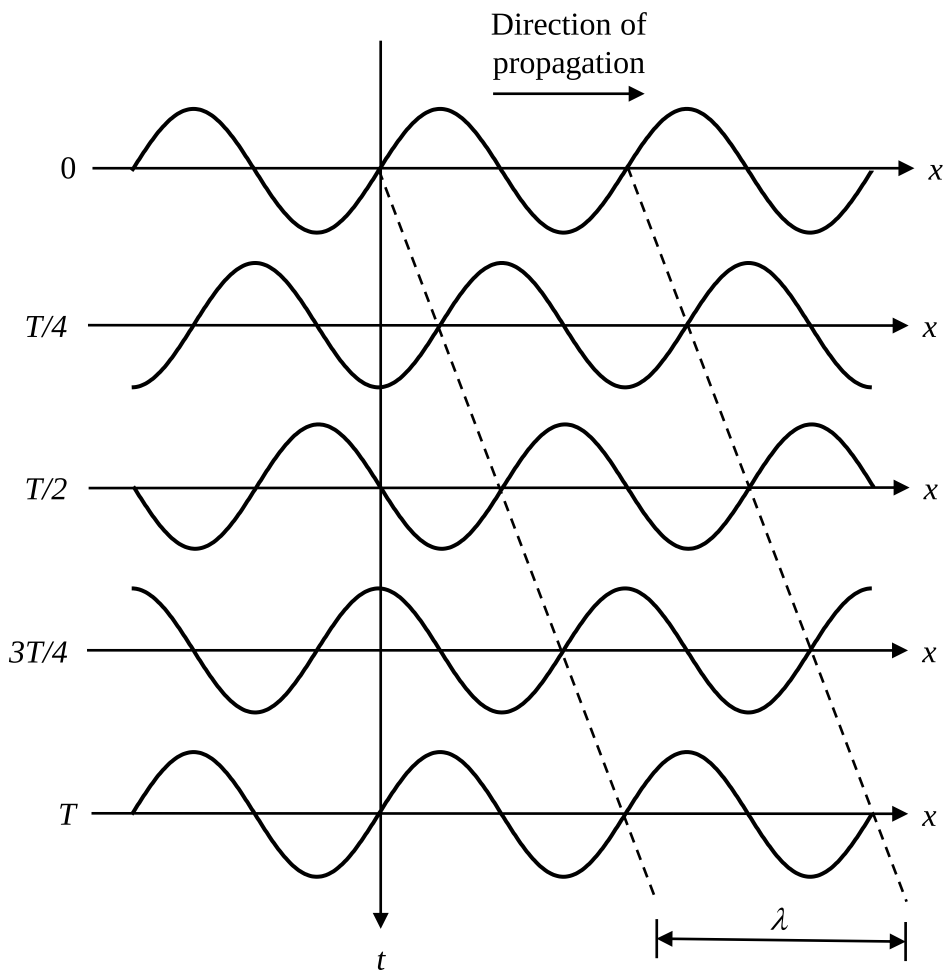

Source: adapted from Kim (2010).

As the frequency and the wavenumber are given by $f = 1/T$ and $k = 2\pi/\lambda$, respectively, the dispersion relation is defined as (KIM, 2010)

$$k = \omega/c\,, \tag{1}$$

where $\omega = 2\pi f$ is the angular frequency, and the plane wave is described as (KIM, 2010)

$$\psi(x,t) = \Psi e^{\mathrm{j}(\omega t - kx)}, \tag{2}$$

in which $\mathrm{j}=\sqrt{-1}$ and Ψ is the wave amplitude.

Therefore, as can be seen in Eq. (2), the frequency and the wavenumber are physical quantities that describe how a wave propagates in time and space for a system, and the respective speed of propagation is given by the dispersion relation represented by Eq. (1).

2.3 CONICAL WAVES RADIATING FROM A BURIED PIPE

A 3D schematic diagram for the body waves propagating in an infinite soil medium surrounding the pipe with infinite length is shown in Fig. 20. Note that, considering the simplifying assumptions given in Appendix A, the predominantly fluid-borne axisymmetric wave is the only wave propagating in the pipe, and the body waves that radiate from the pipe into the soil can be the shear and compressional conical waves (JETTE; PARKER, 1980; PINNINGTON; BRISCOE, 1994; GAO *et al*., 2016; GAO *et al*., 2017), as shown in Fig. 20(a).

The wavefront for each type of wave is illustrated in Fig. 20(b) separately with the respective wave speed. According to the dispersion relation, the speed of the predominantly fluid-borne axisymmetric wave is given by $c_f = \omega/\mathrm{Re}\{k_f\}$, where $\mathrm{Re}\{\bullet\}$ corresponds to the real part and k_f is the wavenumber of the predominantly fluid-borne axisymmetric wave, whose analytical model is presented in Appendix A. The speeds of the compressional and shear conical waves are given by $c_d = \omega/\mathrm{Re}\{k_d\}$ and $c_s = \omega/\mathrm{Re}\{k_s\}$, respectively, in which k_d is the compressional wavenumber and k_s is the shear wavenumber.

Figure 20 - Schematic diagram for wave propagation in a buried pipe system. (a) 3D view showing the wavefront for each wave propagating in the system separately, (b) lateral view showing each wavefront with the respective wave speed, and (c) diagrams showing the relation between the wavenumber k_f and the radial wavenumber components k_d^R and k_s^R, and the relation between the wavenumber k_f and the angles of propagation θ_d and θ_s.

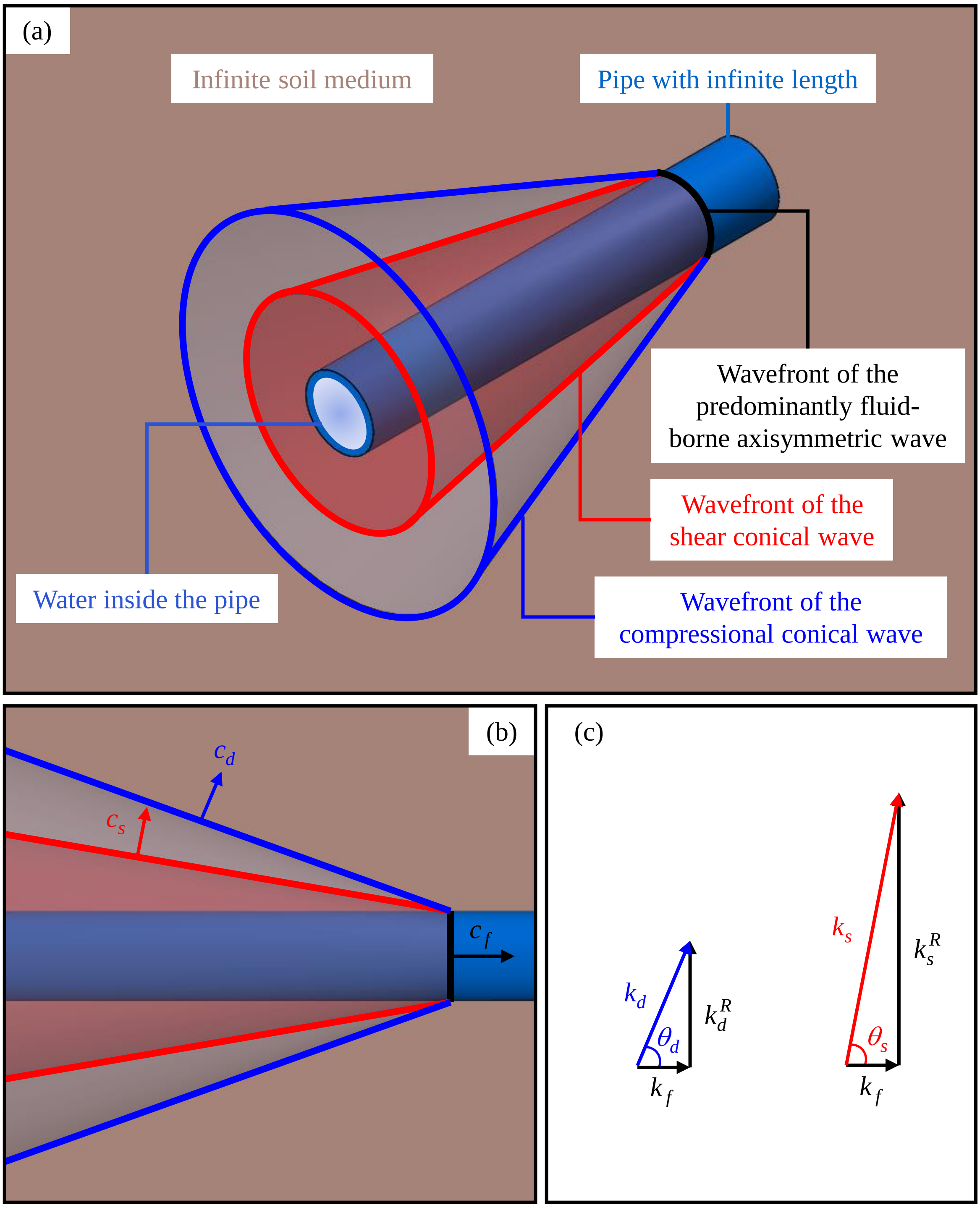

Source: elaborated by the author.

The wavefront for each conical wave has a certain angle of propagation, which is determined by the wavenumber (or the wave speed) in the soil compared to the wavenumber (or the wave speed) in the pipe. As shown in Fig. 20(c), the angles of propagation for the compressional and shear conical waves are given by (MUGGLETON *et al*., 2023)

$$\theta_d = \cos^{-1}\left(k_f / k_d\right) = \cos^{-1}\left(c_d / c_f\right), \; \theta_s = \cos^{-1}\left(k_f / k_s\right) = \cos^{-1}\left(c_s / c_f\right), \qquad \text{(3a,b)}$$

respectively, and the radial wavenumber components for the compressional and shear conical waves are related to the wavenumber k_f by $k_d^R = \sqrt{k_d^2 - k_f^2}$ and $k_s^R = \sqrt{k_s^2 - k_f^2}$, respectively (JETTE; PARKER, 1980; PINNINGTON; BRISCOE, 1994; MUGGLETON; BRENNAN; PINNINGTON, 2002; GAO *et al*., 2016, 2017; BRENNAN *et al*., 2017, 2018; MUGGLETON *et al*., 2023). Note in Eq. (3a,b) that

- If $c_d / c_f < 1$ then $\theta_d > 0$, and if $c_s / c_f < 1$ then $\theta_s > 0$. This means that, if the wave speed in the pipe is greater than a wave speed in the soil, then a conical wave radiates from the buried pipe into the soil with a certain angle of propagation.

- If $c_d / c_f > 1$ then no compressional conical wave radiates from the buried pipe, and if $c_s / c_f > 1$ then no shear conical wave radiates from the buried pipe. Instead, a wave with an exponential decay radiates from it towards the ground surface. Such a type of wave is known as evanescent wave (KIM, 2010; RUSSELL, 2014), and it can only be sensed in the vicinities of the pipe surface due to its exponential decay.

In addition, the wave speed in elastic media is a physical quantity governed by the relation between the medium resistance to a specific type of stress and the medium density, in which the wave speed is proportional to the medium resistance and inversely proportional to the medium density (GRAFF, 1975). For a soil medium, the compressional and shear wave speeds are given by (JETTE; PARKER, 1980; GAO *et al*., 2016; SCUSSEL *et al*., 2018, 2019)

$$c_d = \sqrt{\left(\mathrm{Re}\left\{B_{\mathrm{soil}}^*\right\} + 4\mathrm{Re}\left\{G_{\mathrm{soil}}^*\right\}/3\right)\Big/\rho_{\mathrm{soil}}}\,,\; c_s = \sqrt{\mathrm{Re}\left\{G_{\mathrm{soil}}^*\right\}\Big/\rho_{\mathrm{soil}}}\,, \tag{4a,b}$$

respectively, where ρ_{soil} is the soil density.

The term $B_{\mathrm{soil}}^* = B_{\mathrm{soil}}\left(1 + \mathrm{j}\,\eta_d\right)$ is the complex bulk modulus of the soil that describes the medium resistance to a change in volume (or dilatational disturbance) (GRAFF, 1975), in which B_{soil} and η_d are the bulk modulus and the bulk loss factor of the soil, respectively. The term $G_{\mathrm{soil}}^* = G_{\mathrm{soil}}\left(1 + \mathrm{j}\,\eta_s\right)$ is the complex shear modulus of the soil that describes the medium resistance to rotational disturbances (GRAFF, 1975), in which G_{soil} and η_s are the shear modulus and the shear loss factor of the soil, respectively.

Therefore, by comparing Eqs. (2.3a,b) with Eqs. (2.4a,b), a conical shear wave and a conical compressional wave can propagate into the soil depending on the respective properties. Note that, if the speed of the predominantly fluid-borne axisymmetric wave in the pipe exceeds a wave speed in the soil, then a conical wave radiates from the buried pipe. Otherwise, the wave is evanescent and cannot be sensed on the ground surface. For a typical sandy soil, it has been discovered that both compressional and shear conical waves radiate from the buried pipe. For a typical stiff clay soil, however, only shear conical wave radiates from the buried pipe (GAO *et al*., 2017). This behavior has been successfully demonstrated at test sites with different pipe materials/geometries and soil types in Brazil and in the UK (BRENNAN *et al*., 2018; SCUSSEL *et al*., 2018, 2019).

2.4 ANALYTICAL MODEL FOR GROUND SURFACE VIBRATION

The analytical model for ground surface vibration due to the conical waves that radiate from a leaking water pipe is an extension of the one presented in Appendix A. The same simplifying assumptions given in Appendix A are also considered for the derivation of the analytical model presented in this chapter. It is also assumed that $k_f < k_s$ and $k_f < k_d$, or $c_f > c_s$ and $c_f > c_d$, so that both shear and compressional conical waves radiate from the pipe into the surrounding soil, which are shown as a combined wave in Fig. 21.

Figure 21 - 3D view of the wave propagation in a buried pipe system, showing the wavefront of the combined compressional and shear conical waves.

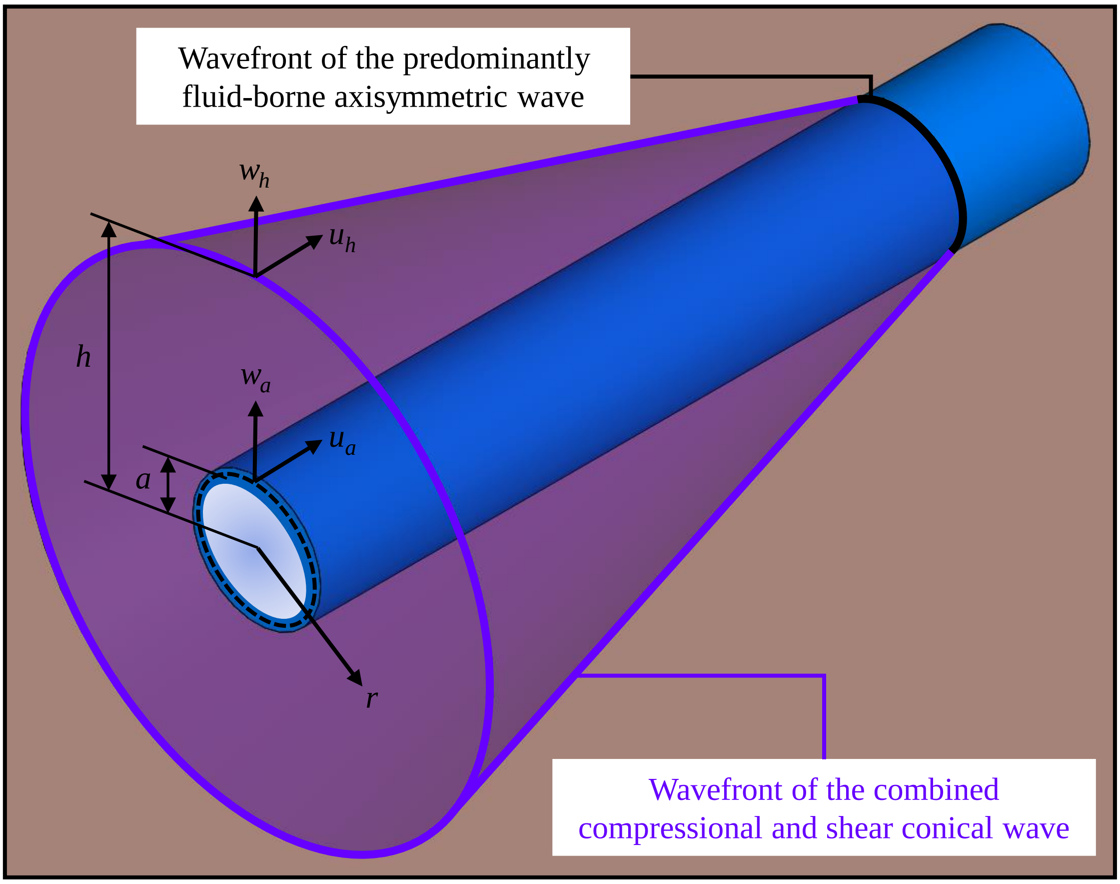

Source: elaborated by the author.

In the initial phase of the model development, only the vibration of the infinite soil medium at a radial distance h from the pipe center is considered as shown in Fig. 21. Assuming that the pipe and the soil are under compact contact, in which the stresses and displacements of the pipe-wall are equal to the stresses and displacements of the soil at the interface $r = a$ (also known as “no-slip” boundary condition) (JETTE; PARKER, 1980; GAO *et al*., 2016, 2017), the amplitudes of axial and radial displacements of the surrounding soil at a radial distance $r = h$, U_h and W_h, are related to the amplitude of axial and radial displacements of the pipe and soil interface, U_a and W_a, by (GAO *et al*., 2016, 2017)

$$\mathbf{u}_h = \mathbf{B}_{r=h}\mathbf{B}_{r=a}^{-1}\mathbf{u}_a, \tag{5}$$

where

$$\mathbf{B}_r = \begin{bmatrix} -\mathrm{j}k_f H_0\left(k_d^R r\right) & k_s^R H_0\left(k_s^R r\right) \\ k_d^R H_0'\left(k_d^R r\right) & -\mathrm{j}k_f H_0'\left(k_s^R r\right) \end{bmatrix},$$

in which $H_0\left(\bullet\right)$ is a Hankel function of the second kind and zero order, $\mathbf{u}_h = \{U_h \quad W_h\}^T$ and $\mathbf{u}_a = \{U_a \quad W_a\}^T$, where the superscript T denotes the transpose.

From Eq. (15) of Appendix A and assuming that there are only free waves in the buried pipe system, so that $\mathrm{T}_a = \Phi_a = 0$, the relationship between the amplitudes U_a and W_a is given by $U_a = \beta W_a$, where $\beta = -\left(K_{12}^{(\text{pipe})} + K_{12}^{(\text{soil})}\right) \Big/ \left(K_{11}^{(\text{pipe})} + K_{11}^{(\text{soil})}\right)$. Assuming that the analysis is restricted to low frequencies, where the acoustic wavelength in the water is much greater than the diameter of the pipe, the relationship between the amplitude W_a of radial displacement at the interface and the amplitude P of acoustic pressure in the pipe can be extracted from Eqs. (A.4), so that $W_a / P = 1 \big/ K^{(\text{water})} \approx \left(k_f^2 \big/ k_{\text{water}}^2 - 1\right) \Big/ \tilde{K}^{(\text{water})}$. Letting

$$\mathbf{B}_{r=a}^{-1} = \begin{bmatrix} A_{11} & A_{12} \\ A_{21} & A_{22} \end{bmatrix},$$

Eq. (5) can be written as

$$\begin{Bmatrix} U_h \\ W_h \end{Bmatrix} = \frac{P}{K^{(\text{water})}} \begin{bmatrix} -\mathrm{j}k_f H_0\left(k_d^R h\right) & k_s^R H_0\left(k_s^R h\right) \\ k_d^R H_0'\left(k_d^R h\right) & -\mathrm{j}k_f H_0'\left(k_s^R h\right) \end{bmatrix} \begin{bmatrix} A_{11} & A_{12} \\ A_{21} & A_{22} \end{bmatrix} \begin{Bmatrix} \beta \\ 1 \end{Bmatrix}. \tag{6}$$

Therefore, the relationship between the amplitude W_h of radial displacement of the soil and the amplitude P of acoustic pressure in the pipe is given by

$$W_h = \frac{P}{K^{(\text{water})}} \left[k_d^R \left(\beta A_{11} + A_{12}\right) H_0'\left(k_d^R h\right) - \mathrm{j}k_f \left(\beta A_{21} + A_{22}\right) H_0'\left(k_s^R h\right) \right]. \tag{7}$$

If $\left|k_d^R h\right| > 1$ and $\left|k_s^R h\right| > 1$, the Hankel functions can be approximated by complex exponential functions (JETTE; PARKER, 1980; GAO *et al.*, 2017), resulting in

$$w_h = W_h e^{\mathrm{j}\left(\omega t - k_f x\right)} = \left(W_d e^{-\mathrm{j}k_d^R h} + W_s e^{-\mathrm{j}k_s^R h}\right) e^{\mathrm{j}\left(\omega t - k_f x + \pi/4\right)}, \tag{8}$$

where $W_d = -\mathrm{j}\frac{\left(\beta A_{11} + A_{12}\right)P}{K^{(\text{water})}}\left(\frac{2k_d^R}{\pi h}\right)^{1/2}$ and $W_s = -\frac{k\left(\beta A_{21} + A_{22}\right)P}{K^{(\text{water})}}\left(\frac{2}{\pi k_s^R h}\right)^{1/2}$ are the complex amplitude functions of the compressional and shear waves, respectively.

To idealize the ground surface on the buried pipe system, an infinite plan parallel to the pipe direction is included at a distance z from the center of the pipe, as shown in Fig. 22. Note that the plan intersects the wavefront of the combined compressional and shear conical waves, in which the reflections of the incident conical waves on the surface are not considered for simplicity. Such an intersection results in a line of constant phase that travels at the same direction of the predominantly fluid-borne axisymmetric wave in the pipe, as shown in Fig. 22(a). Note that the shape of the line of constant phase changes with frequency because the complex amplitude of both compressional and shear waves are frequency dependent.

As shown in Fig. 22(b), to model the vibration sensed on the ground surface when the line of constant phase passes by, the radial displacement w_h is decomposed by the horizontal and vertical displacements, w_y and w_z, given by

$$w_y = \frac{y}{\sqrt{y^2 + z^2}} W_h e^{\mathrm{j}\left(\omega t - k_f x\right)} = \frac{y}{\sqrt{y^2 + z^2}}\left(W_d e^{-\mathrm{j}k_d^R \sqrt{y^2+z^2}} + W_s e^{-\mathrm{j}k_s^R \sqrt{y^2+z^2}}\right) e^{\mathrm{j}\left(\omega t - k_f x + \pi/4\right)}, \tag{9}$$

$$w_z = \frac{z}{\sqrt{y^2 + z^2}} W_h e^{\mathrm{j}\left(\omega t - k_f x\right)} = \frac{z}{\sqrt{y^2 + z^2}}\left(W_d e^{-\mathrm{j}k_d^R \sqrt{y^2+z^2}} + W_s e^{-\mathrm{j}k_s^R \sqrt{y^2+z^2}}\right) e^{\mathrm{j}\left(\omega t - k_f x + \pi/4\right)}, \tag{10}$$

respectively. Note that Eqs. (2.9) and (2.10) hold the conical spreading nature of the waves and the dominant phase dependence. Wave attenuation is encapsulated in the exponential terms in which the corresponding wavenumbers comprise both real and imaginary components.

Figure 22 - Inclusion of the ground surface on the buried pipe system. (a) 3D view of the wave propagation showing the line of constant phase on the ground surface, where the arrows indicate the corresponding direction of propagation. (b) Front view of the wave propagation showing the decomposition of the radial ground surface displacement w_h .

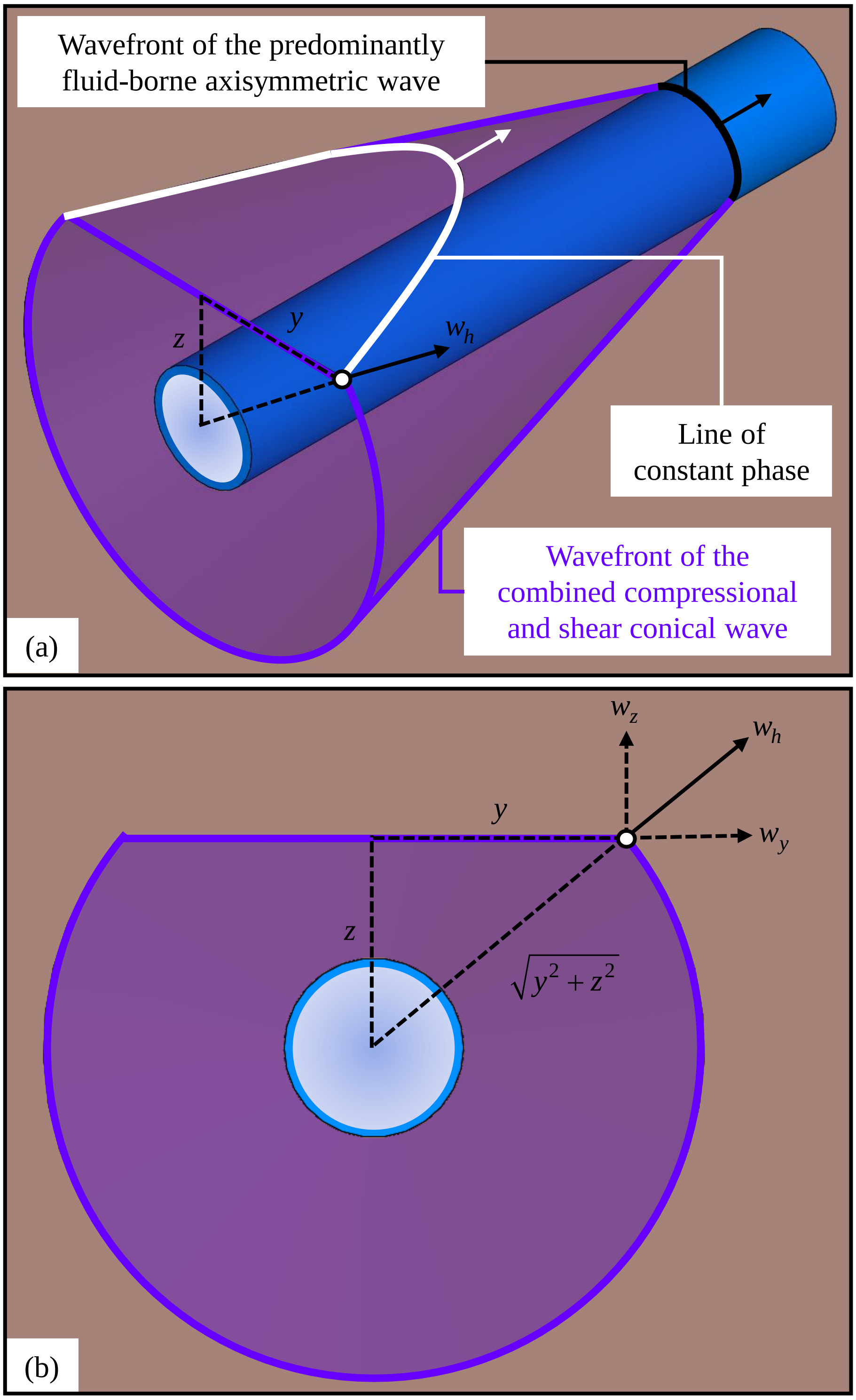

Source: elaborated by the author.

2.5 VALIDATION OF THE ANALYTICAL MODEL FOR GROUND SURFACE VIBRATION

The analytical model presented in the previous section is validated with data extracted from a numerical model of the buried pipe system, and from an experiment carried out in a test rig. The validation is performed qualitatively by comparing the contour maps for amplitude and unwrapped phase of the data extracted from both analytical and numerical models, and from the experiment.

2.5.1 Numerical model

The numerical model is an axisymmetric Finite Element Model (FEM) developed in the software COMSOL Multiphysics (v5.3), that describes a combined system composed by the water, the pipe, and the surrounding soil as shown in Fig. 23. Such a numerical model has been already used to validate an analytical model for the wavenumber in the pipe (BRENNAN *et al*. 2017; BRENNAN *et al*., 2018), to validate the analytical model for the ground surface vibration due to a leaking water pipe (MUGGLETON *et al*., 2023), and to test a pipe localization technique based on measurements of ground surface vibration (IWANAGA *et al*., 2023). The model discretization was carried out with a fine mesh of triangular elements, in which the water was modelled as a fluid with the COMSOL Pressure Acoustic module, and the pipe and soil were modelled as a linear elastic medium with the Solid Mechanics module. The external boundaries of the numerical model are Perfectly Matched Layers (PMLs) to simulate that the pipe has infinite length in the axial direction, and the surrounding soil has infinite length in both axial and radial directions, as shown in Fig. 23(a). A monopole source is positioned in the middle of the pipe for excitation. The ground surface is represented by a plane parallel to the pipe direction and 1 m above the pipe center, as shown in Fig. 23(a), where the reflections of the incident waves are not considered for simplicity. The measurement positions on the ground surface are within a grid with sides 15.5 m and 3 m, where the leak position is 1 m away from one of the sides as shown in Fig. 23(b). The x_l-axis is parallel to the pipe direction and corresponds to the distance relative to the leak position, and the y_l-axis is perpendicular to the pipe direction and corresponds to the distance relative to the pipe. The positions in the measurement grid are 0.5 m apart from each other, along both x_l-axis and y_l-axis.

Figure 23 - Schematic diagram for the numerical model of the buried pipe system (not to scale). (a) 3D view showing the components of the numerical model, and (b) top view showing the measurement grid on the ground surface with the corresponding coordinate system and distances.

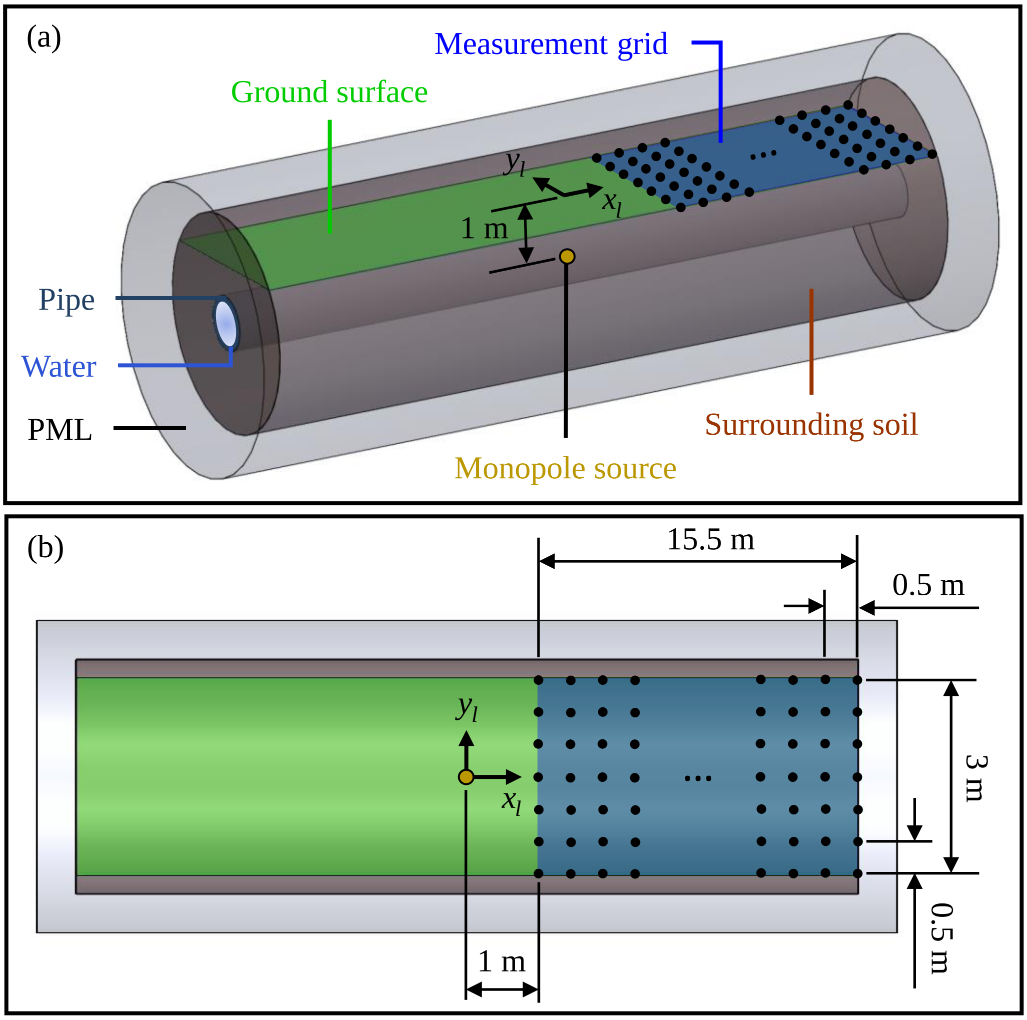

Source: elaborated by the author.

2.5.2 Experiment

The test rig with the corresponding experimental setup used to extract data for validation is presented in Fig. 24. Like the numerical model, the data extracted from such an experiment has been already used to test a pipe localization technique based on measurements of ground surface vibration (IWANAGA *et al.*, 2023). The test rig is located in Blithfield, UK, and is pressurized by the mains water distribution pipe as shown in Fig. 24(a). The leak was created through a standpipe connected to the main pipe at the leak position, in which a small valve attached to the standpipe is used to control the leak strength. The experiment was performed with seven I/O SM-24 geophones, a Brüel & Kjaer 4383 accelerometer and a Prosig DATS data acquisition system, as shown in Fig. 24(b). The same coordinate system adopted for the numerical model is also adopted for the experiment, in which x_l-axis is parallel to the pipe direction and y_l-axis is perpendicular to the pipe direction as shown in Fig. 24(c). The geophones were placed in line, 0.5 m apart and parallel to y_l-axis. Then, the line of geophones was moved 0.5 m along x_l-axis, while the accelerometer remained fixed at the leak position for all measurements. A total of 32 measurements were carried out resulting in a rectangular measurement grid with sides 15.5 m and 3 m, where the leak position is 1 m away from one of the sides (the same measurement grid adopted for the numerical model). The measurements consist of 130-s long velocity and acceleration time histories, sampled at a frequency of 1 kHz.

Figure 24 - British test rig and experimental setup. (a) Overview of the test rig showing the location of measurement grid (not to scale) and the leak mechanism, (b) photograph showing the experimental setup, and (c) schematic diagram for the measurement grid showing the corresponding coordinate system and distances (not to scale). The dashed blue lines correspond to the buried pipe.

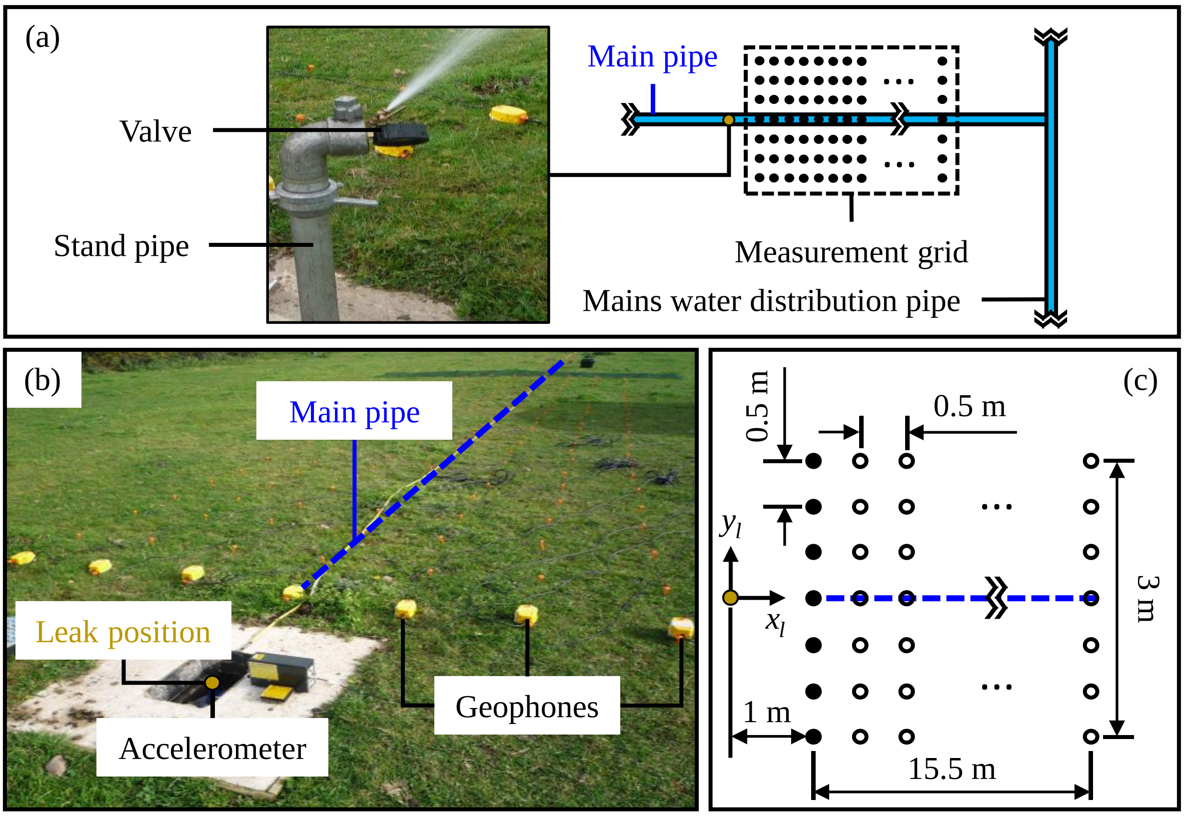

Source: elaborated by the author.

2.5.3 Contour maps

Since geophones were used to measure ground surface vibration in the experiment, vertical ground surface velocities were collected in the measurement grid. To be consistent on the comparison between the data provided by both analytical and numerical models and the experiment, the models are used to generate vertical ground surface velocities as well. The vertical ground surface velocities were generated via analytical model by differentiating Eq. (10) together with the parameters of Tab. 1, and via the numerical model using the FEM presented in subsection 2.5.1 together with the parameters of Tab. 1. For both models, the frequency response was calculated from 35 up to 60 Hz, using a frequency resolution of 1 Hz. For the experiment, the cross-spectral density between each geophone and the accelerometer fixed at the leak position was calculated with a 1,000-point fast Fourier transform and a Hanning window with 50% overlap, resulting in a frequency resolution of 1 Hz.

Table 1 - Parameters for the plastic pipe, soil and water used to generate data with the analytical and numerical models for ground surface vibration.

Parameters	Pipe	Soil	Water
Burial depth [m]	-	$z = 1$	-
Mean radius [mm]	$a = 80$	-	-
Pipe-wall thickness [mm]	$b = 9.85$	-	-
Young's modulus [GN/m^2]	$E_{\text{pipe}} = 1.9$	-	-
Bulk modulus [GN/m^2]	-	$B_{\text{soil}} = 0.13$	$B_{\text{water}} = 2.25$
Shear modulus [GN/m^2]	-	$G_{\text{soil}} = 0.025$	-
Density [kg/m^3]	$\rho_{\text{pipe}} = 900$	$\rho_{\text{soil}} = 1{,}850$	$\rho_{\text{water}} = 1{,}000$
Poisson's ratio	$\upsilon_{\text{pipe}} = 0.4$	-	-
Material loss factor	$\eta_{\text{pipe}} = 0.06$	$\eta_d = \eta_s = 0$	-
Wave speed [m/s]	$c_f = 334$	$c_d = 297,\ c_s = 116$	$c_{\text{water}} = 1{,}500$

Source: elaborated by the author.

The contour maps for the normalized amplitude of vertical ground surface velocities are shown in Fig. 25. The normalized amplitude of frequency response for the analytical and numerical models are shown in Fig. 25(a,b) for a frequency of 45 Hz, and the normalized

RMS values for the experimental data are shown in Fig. 25(c). The particular frequency of 45 Hz was selected to show the contour maps for the normalized amplitude of frequency response for the analytical and numerical models, to be consistent with the frequency selected to show the respective contour maps for the spatially unwrapped phase as follows.

The phase for each data was spatially unwrapped with the algorithm proposed by Herráez *et al*. (2002), to present the lines of constant phase travelling on the ground surface. The contour maps for the spatially unwrapped phase for the analytical, numerical, and experimental data are shown in Fig. 26 for a frequency of 45 Hz. Note that, to prevent phase distortions caused by spatial aliasing when plotting a contour map for phase, the spatial interval d within the measurement grid must be less than a half of the wavelength λ, i.e., $d < \lambda/2$ (GLEGG; DEVENPORT, 2019). Since $\lambda = c/f$, then the maximum frequency on which a contour map for phase can be plotted for a particular wavelength without spatial aliasing is given by

$$f < c/(2d). \tag{11}$$

For the data acquired with the theoretical and numerical models and with the experiment carried out in the British test rig, the minimum wave speed corresponds to the shear wave $(c_S = 116 \text{ m/s})$, as shown in Tab. 1, and the spatial interval corresponds to 0.5 m. According to Eq. (11), the maximum frequency on which a contour map for phase can be plotted without spatial aliasing is 116 Hz. Therefore, the frequency of 45 Hz was selected to plot the contour maps for spatially unwrapped phase in this case, because it is below 116 Hz and the respective leak position was found to be more evident.

Note in Fig. 25(b,c) that the amplitude is higher for positions close to the source, forming an approximate circular pattern from 1 m up to approximately 3 m along the x_l-axis, due to the spherical waves that radiate from the source (leak). In Fig. 25(a), although the amplitude is higher for positions close to the origin, the circular pattern is not present because the analytical model does not contain the source. Note that for distances longer than 3 m along the x_l-axis of Figs. 25(a,b), the analytical and numerical models contain approximately the same pattern in which the amplitude is higher for positions close to the pipe along the y_l-axis. In Fig. 25(c), however, the pattern for amplitude is not regular as for Figs. 25(a,b) since there are some regions away from the main pipe where the amplitude is slightly higher. This is due to background noise that becomes more dominant for longer distances in relation to the leak position, because of the geometrical spreading and attenuation experienced by the waves that propagate in the soil.

Figure 25 - Contour maps for the normalized amplitude of vertical ground surface velocities. Normalized ampltidue of frequency response for the data extracted from the (a) analytical model, and from the (b) numerical model for a frequency of 45 Hz. (c) Normalized RMS values for the data extracted from the experiment. The dashed blue lines correspond to the buried pipe.

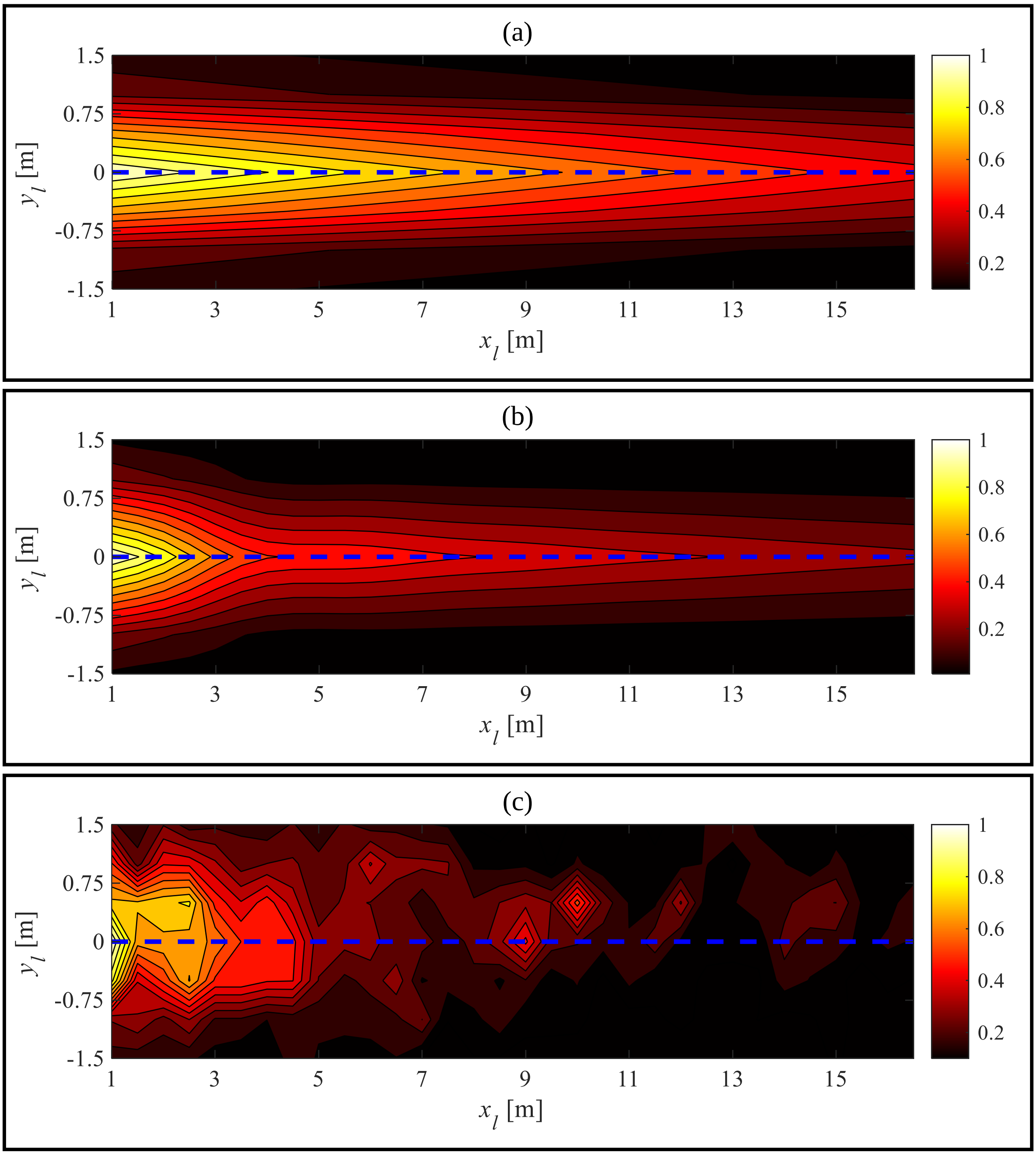

Source: elaborated by the author.

Figure 26 - Contour maps for the spatially unwrapped phase of vertical ground surface velocities for a frequency of 45 Hz. Spatially unwrapped phase for the data extracted from the (a) analytical model, (b) numerical model and (c) experiment. The dashed blue lines correspond to the buried pipe.

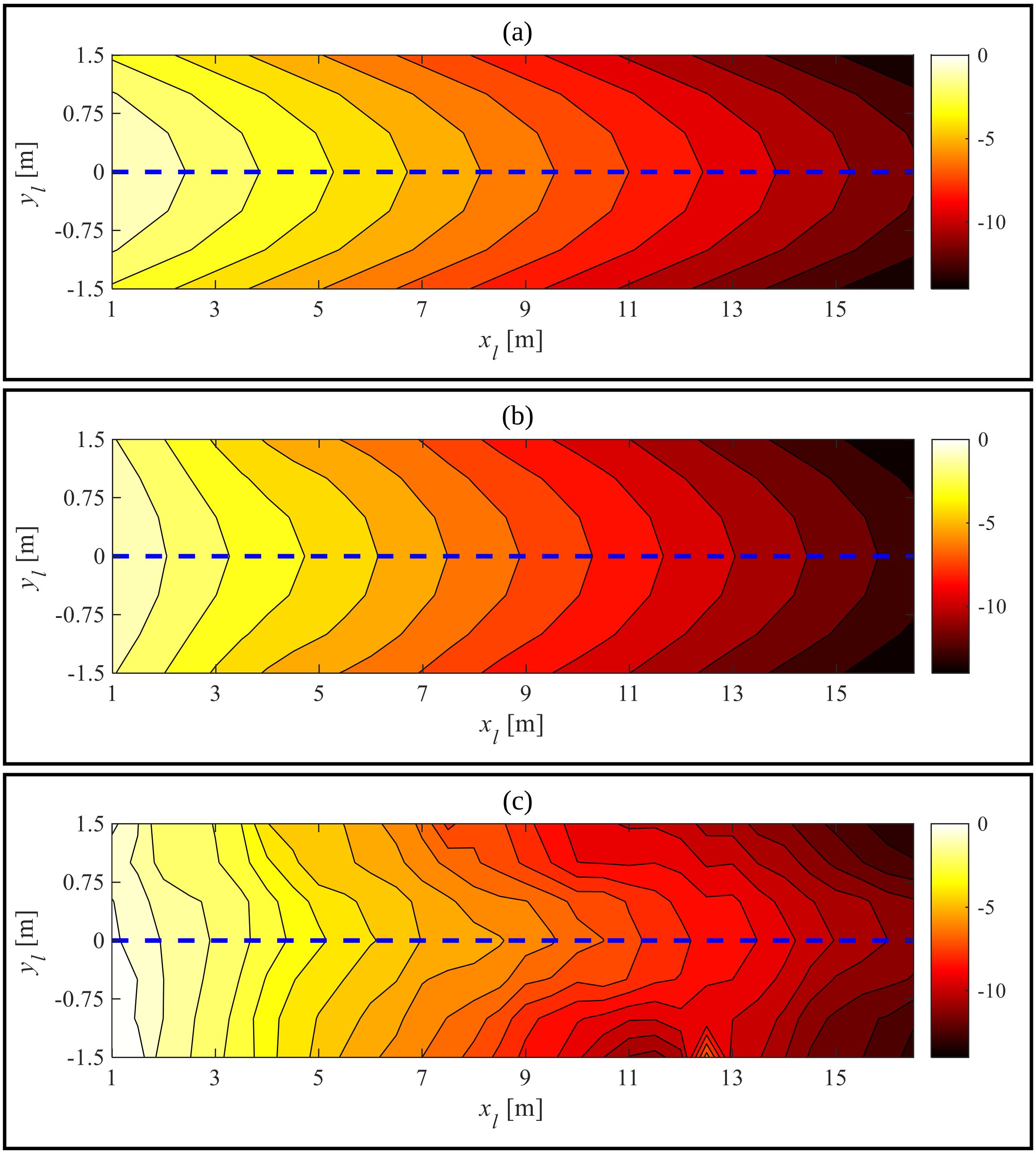

Source: elaborated by the author.

Note that, from 1 m up to approximately 3 m along the x_l-axis in Fig. 26(b,c), the lines of constant phase have approximated circular pattern due to the spherical waves that propagate from the source (leak). As the analytical model does not contain the source, the circular pattern is not present in Fig. 26(a). For distances longer than 3 m along the x_l-axis of Figs. 26(a-c), approximate hyperbolas of constant phase propagate on the ground surface due to the conical waves that radiate from the pipe. Note that, as the analytical model does not replicate the source and the background noise and does not consider reflections of the incident waves on the surface, it does not replicate the amplitude of ground surface vibration faithfully as can be seen by the results of Fig. 25. However, although the amplitude is affected by the absence of these considerations, the analytical model still can replicate with remarkable precision the lines of constant phase that travel on the ground surface for positions relatively far from the source (leak). This is because phase is less affected by uncorrelated noise than amplitude, as pointed out by Muggleton, Brennan and Gao (2011).

2.6 CONCLUSIONS

This chapter presents an analytical model for ground surface vibration due to a leaking water pipe. It has been shown that compressional and shear conical waves can propagate into the soil depending on the soil properties. Therefore, if a wave speed in the pipe is higher than a wave speed in the soil, then a conical wave radiates from the pipe into the soil. Otherwise, the wave will be evanescent and cannot be sensed on the ground surface. The derivation of the analytical model considers that the speed of the predominantly fluid-borne axisymmetric wave in the pipe is higher than both compressional and shear wave speeds in the soil, so that both compressional and shear conical waves radiate from the pipe. The analytical model is then validated qualitatively with a numerical model and an experiment carried out in a test rig, by comparing the corresponding contour maps for amplitude and unwrapped phase of ground surface vibration. The results highlight that, although the analytical model does not replicate the amplitude faithfully, it can predict with remarkable precision the lines of constant phase that travel on the ground surface for positions relatively far from the leak. This is because the analytical model does not contain the source of excitation for the buried pipe as the numerical model, neither considers the background noise and the reflections of incident waves on the ground surface as presented in the experimental data. The shape and direction of propagation for the lines of constant phase are used to explain the one-sensor and two-sensor techniques in the next chapter.

3 PIPE AND LEAK LOCALIZATION TECHNIQUES USING VIBRATION MEASURED ON THE GROUND SURFACE

3.1 INTRODUCTION

Leaks in buried pipes are precisely pinpointed by leak noise correlators, which are devices whose sensors are place on the pipe surface or some rigid structure attached to it (HUNAIDI *et al*., 2000; AL QAHTANI *et al*., 2020; ZAMAN *et al*., 2020). There are some situations, however, where access to the buried pipe is not possible and operators have to locate the pipe and the leak by measuring on the ground surface. As introduced in Chapter 2, a leak behaves as a source that excites the pipe resulting in waves which propagate along it, and conical waves that radiate into the surrounding soil. Therefore, depending on the excitation level resulted by the leak, it is possible to hear noise or to sense vibration on the ground surface resulted by the waves that radiate from the leak and the pipe. Usually, operators use listening sticks or some kind of single-sensor-roving device to hear leak noise, or to measure vibration on the ground surface. Although they perform well when leak noise is hearable, locating a leak with such devices might be troublesome for some conditions as they only sense sound or vibration amplitude, which is highly affected by uncorrelated noise. Furthermore, the process of tracking the direction to spot a buried pipe or a leak might be time-consuming, since it is based on amplitude difference that is only possible to estimate by measuring, at least, on two different positions on the ground surface.

Sophisticated techniques are currently being investigated for acoustic (CHEN; YAO; HUDSON, 2003; KUNDU, 2014; COBOS *et al*., 2017) and microseismic (ZOU *et al*., 2019) source localization, in which arrays of sensors are used to acquire the spatial distribution of sound or vibration for an environment. Although such techniques can also be used to locate buried pipes (XERRI *et al*., 2022) and leaks (WANG *et al*., 2017; CHENG *et al*., 2018) with measurements of ground surface vibration, their performance depends on a prior condition in which the wave speed must be known. In addition, since more than one type of wave may radiate from the buried pipe depending on the soil properties as explained in Chapter 2, the application of these techniques might be quite challenging as their algorithms have also to consider situations where more than one type of wave is propagating in the soil. The main purpose of this chapter is to introduce a simple technique that uses vibration measurements of a roving pair of sensors placed on the ground surface. Such a technique, named two-sensor technique, locates a leak on the ground surface by estimating the unwrapped phase for the pair of sensors to first locate the buried pipe, and then the leak position. The localization technique proposed in this thesis is designed to be robust to the interference of background noise to overcome the main limitations of those single-sensor-roving devices, and to avoid the complexity of arranging an array of sensors on the ground surface and estimating a speed for each wave propagating in the soil, as for the majority of the localization techniques available in the literature. To evaluate the performance of the proposed technique, the one-sensor technique is used as a baseline in this thesis and both of them are applied separately to locate a pipe and a leak with measurements of ground surface vibration in the following chapters. To do so, the working principles for the one-sensor and two-sensor techniques are first introduced in this chapter, and then their applications with corresponding limitations are illustrated by testing them on some samples of the theoretical data, provided by the analytical and numerical models of wave propagation in a buried pipe system presented in Chapter 2.

3.2 ONE-SENSOR TECHNIQUE

The technique used with single-sensor-roving devices to locate leaks in buried water pipes are based on amplitude difference of sound or vibration measured on the ground surface. Therefore, these devices can be used to pinpoint the leak position without first locating the buried pipe, by just following the direction that contains the highest amplitude. However, the localization procedure of the one-sensor technique is divided into two stages in this thesis where the first one, named pipe localization, is to locate the pipe position and the second one, named leak localization, is to locate the leak position on the ground surface. Such a procedure is established as mentioned for convenience, so the performance of both techniques can be properly compared for each individual stage.

An example for pipe localization with the one-sensor technique is illustrated in Fig. 27, where the sensor is moved along the measurement line perpendicular to the buried pipe, as shown in Figs. 27(a.i-iv), and the amplitude in terms of RMS value is measured for each position on the ground surface, as shown in Figs. 27(b.i-iv). As explained in Chapter 2, the RMS value is higher above the buried pipe and decreases for farther positions along the measurement line. The pair of measurement positions that contains the highest RMS value is marked on the ground surface, and two lines parallel to pipe direction are traced passing through the marks to circumscribe the pipe region as shown in Fig. 27(a.v).

Figure 27 - Pipe localization with one-sensor technique. (a.i) 1st, (a.ii) 2nd, (a.iii) 3rd, (a.iv) 4th measurement positions, and (a.v) pipe region resulted from one-sensor technique. (b.i) RMS value for (b.i) 1st, (b.ii) 2nd, (b.iii) 3rd and (b.iv) 4th measurement positions.

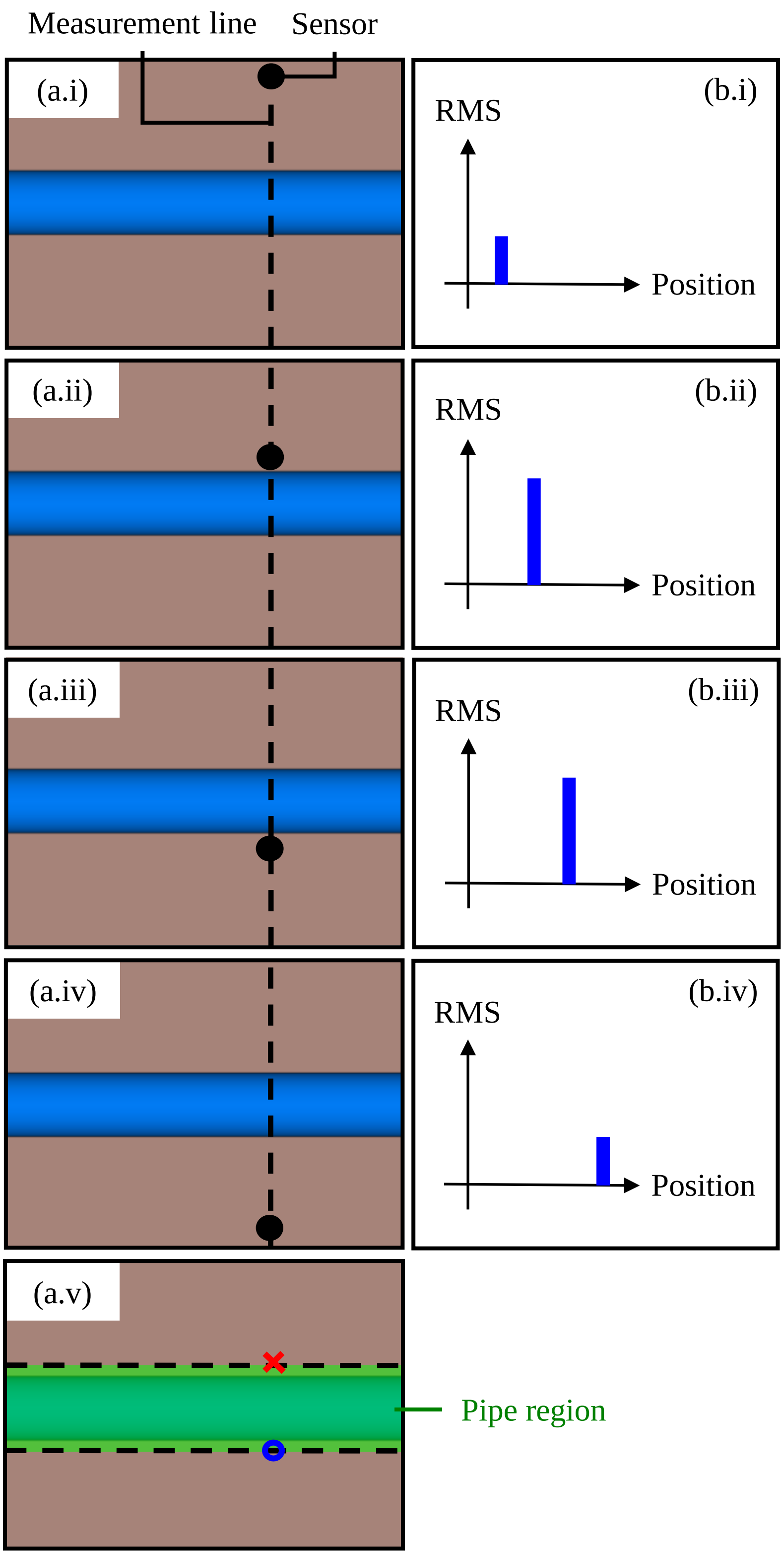

Source: elaborated by the author.

Figure 28 - Leak localization with one-sensor technique. (a.i) 1st, (a.ii) 2nd, (a.iii) 3rd, (a.iv) 4th measurement positions, and (a.v) pipe region resulted from one-sensor technique. (b.i) RMS value for (b.i) 1st, (b.ii) 2nd, (b.iii) 3rd and (b.iv) 4th measurement positions.

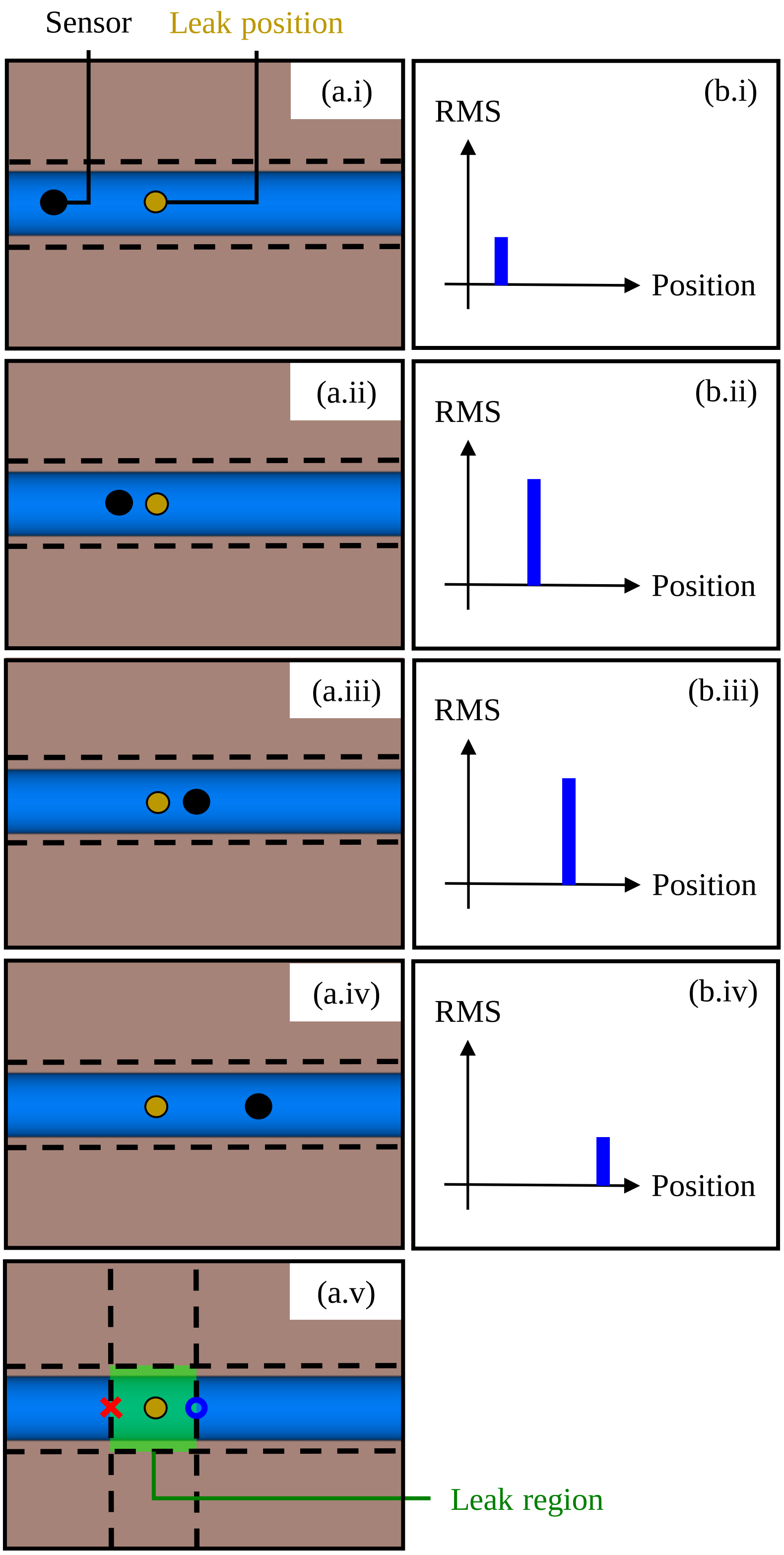

Source: elaborated by the author.

Once the pipe region is determined, leak localization is performed as illustrated in the example of Fig. 28 where the sensor is moved along pipe region, as shown in Figs. 28(a.i-iv), and the RMS value is measured for each measurement position, as shown in Figs. 28(b.i-iv). Note that the RMS values is higher above the leak and decreases for farther positions along pipe region. The pair of measurement positions that contains the highest RMS values is marked on ground surface, and two lines perpendicular to pipe direction are traced passing through the marks as shown in Fig. 28(a.v). The leak region is then determined by the intersection of the four lines.

3.3 TWO-SENSOR TECHNIQUE

The two-sensor technique is based on the slope of unwrapped phase measured by a pair of sensors on ground surface. As explained for the one-sensor technique, the localization procedure of two-sensor technique is divided into two stages, where the first one is pipe localization in which the pipe position is determined on ground surface, and the second one is leak localization in which the leak position is determined on ground surface.

An example for pipe localization with the two-sensor technique is illustrated in Fig. 29, where the measurement line is assumed to be perpendicular to pipe direction and the sensors 1 and 2 are moved along it as shown in Figs. 29(a.i-iii). The unwrapped phase $\phi_{1,2}(\omega) = -\omega\tau$ between the sensors is determined for each measurement position, as shown in Figs. 29(b.i-iii), where τ is the time difference between the vibration from the pipe reaching each of the sensors. Although the shape of the line of constant phase is frequency dependent as explained in Section 2.4, it is only used to explain the time difference between the pair of sensors of the two-sensor technique, without focusing on its exact representation on the ground surface. Note in Figs. 29(b.i-iii) that the slope $d\phi_{1,2}(\omega)/d\omega$ is negative, zero, or positive because it is governed by τ, and the arrival times for the line of constant phase depends on the position of the pair of sensors in relation to pipe. The algorithm of two-sensor technique checks the sign of $d\phi_{1,2}(\omega)/d\omega$ for each position along the measurement line. If the sign of $d\phi_{1,2}(\omega)/d\omega$ changes, the algorithm perceives that the pair of sensors crossed the buried pipe on the ground surface and marks the position where $d\phi_{1,2}(\omega)/d\omega$ is closer to zero as illustrated in Fig. 29(a.iv). Then, two lines parallel to the pipe region are traced passing through the marks and the pipe region is circumscribed on ground surface.

Analogously, the two-sensor technique can also be implemented by calculating cross-correlation in the time domain, rather than unwrapped phase in the frequency domain for each measurement position. The differences between implementation of the two-sensor technique in the time and frequency domains are investigated in the following chapter.

Figure 29 - Pipe localization with two-sensor technique. (a.i) 1st, (a.ii) 2nd, (a.iii) 3rd measurement positions, and (a.iv) pipe region resulted from two-sensor technique. (b.i) Unwrapped phase $\phi_{1,2}(\omega)$ of 1st, (b.ii) 2nd and (b.iii) 3rd measurement positions.

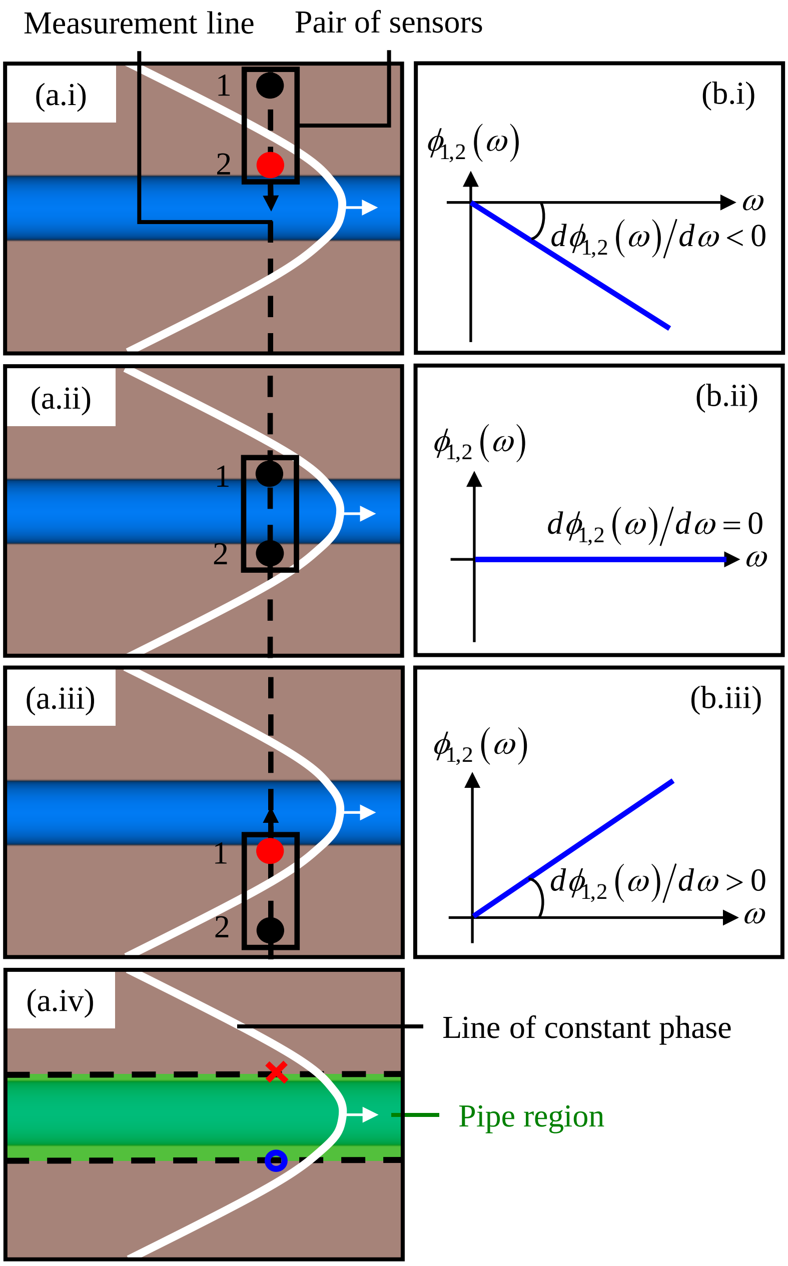

Source: elaborated by the author.

Figure 30 - Leak localization with two-sensor technique. (a.i) 1st, (a.ii) 2nd, (a.iii) 3rd measurement positions, and (a.iv) leak region resulted from two-sensor technique. (b.i) Unwrapped phase $\phi_{1,2}(\omega)$ of 1st, (b.ii) 2nd and (b.iii) 3rd measurement positions.

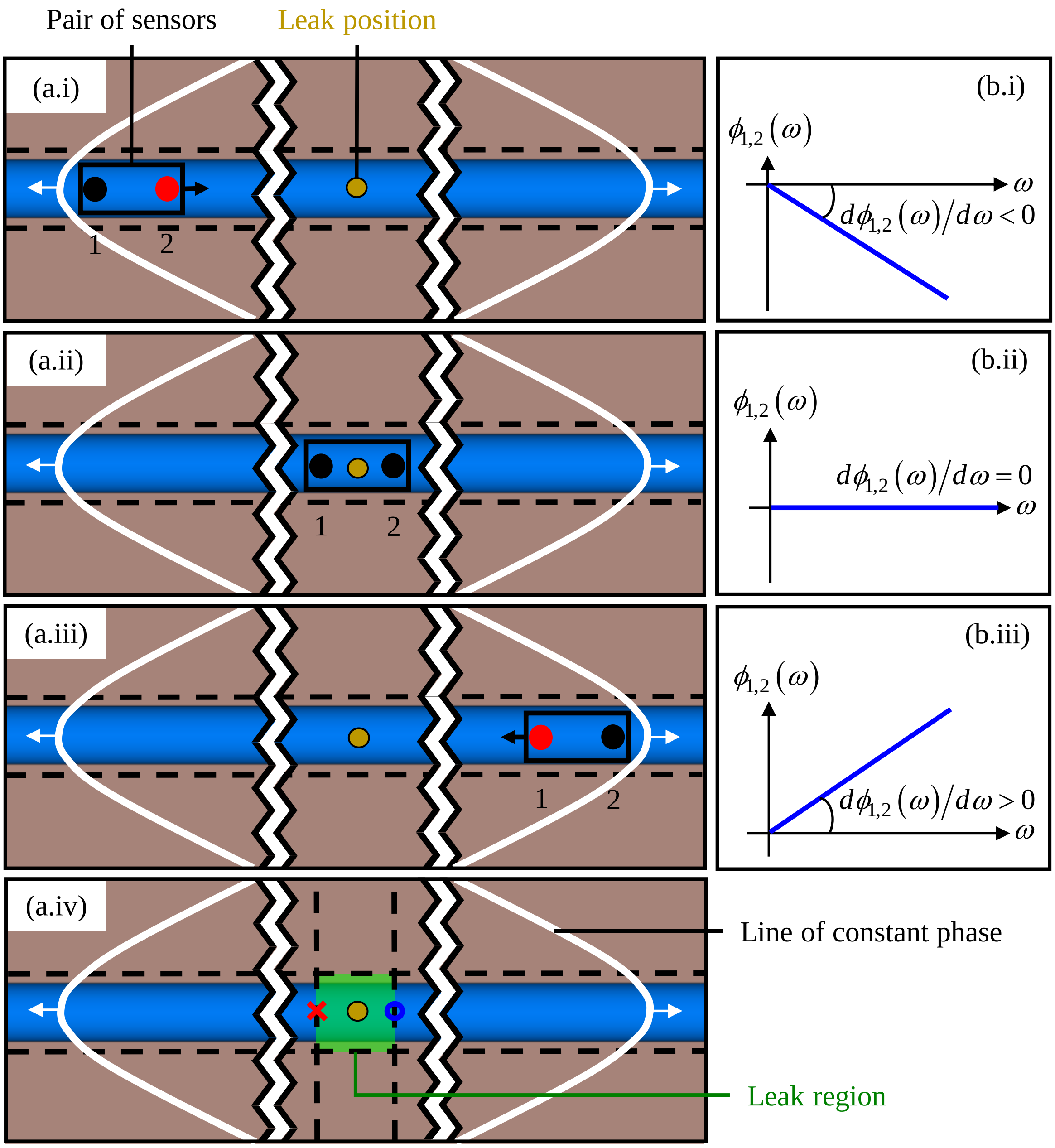

Source: elaborated by the author.

Once the pipe region is determined, leak localization is performed as illustrated in the example of Fig. 30 where sensors l and 2 are moved along the pipe region, as shown in Figs. 30(a.i-iii), and the unwrapped phase $\phi_{1,2}(\omega)$ is determined for each measurement position, as shown in Fig. 30(b.i-iii). Note that the slope $d\phi_{1,2}(\omega)/d\omega$ is negative, zero, or positive because it is governed by τ, and the arrival times for the line of constant phase depends on the position of the pair of sensors in relation to leak. The algorithm of two-sensor technique checks the sign of $d\phi_{1,2}(\omega)/d\omega$ for each position along the pipe region. If the sign of $d\phi_{1,2}(\omega)/d\omega$ changes, the algorithm perceives that the pair of sensors crossed the leak on ground surface and marks the position where $d\phi_{1,2}(\omega)/d\omega$ is closer to zero, as illustrated in Fig. 30(a.iv). Then, two lines perpendicular to pipe region are traced passing through the marks, as shown in Fig. 30(a.iv), and the leak region is then determined by intersection of the four lines. The black arrows in Figs. 29(a.i-iii) and 30(a.i-iii) represent the direction resulted from the tracking algorithm and this is detailed as follows.

3.3.1 Tracking algorithm

The tracking algorithm indicates the direction for pair of sensors to cross the buried pipe or the leak position on ground surface. The main purpose of this algorithm is to speed up localization procedure by determining the direction to cross them on ground surface with only one measurement (note that the same information is only possible with one-sensor technique by carrying out at least two measurements). The direction pointed by the tracking algorithm is resulted from the comparison between the direction informed by amplitude, and the direction informed by phase of pair of sensors. The direction informed by amplitude is given by the sensor that contains the highest RMS value for the pair, as represented by the red dot in Figs. 29(a.i-iii) and 30(a.i-iii). The direction informed by phase is given by the sign of $d\phi_{1,2}(\omega)/d\omega$. As illustrated in Figs. 29(a.i-iii) and 30(a.i-iii), the tracking algorithm only provides the direction for the pair of sensors if both amplitude and phase indicate the same direction as follows:

- If $d\phi_{1,2}(\omega)/d\omega \leq 0$ and $\mathrm{RMS}_1 \leq \mathrm{RMS}_2$, the algorithm points to the side of sensor 2.
- If $d\phi_{1,2}(\omega)/d\omega > 0$ and $\mathrm{RMS}_1 \geq \mathrm{RMS}_2$, the algorithm points to the side of sensor 1.
- Otherwise, the algorithm does not point to any side.

The terms RMS_1 and RMS_2 correspond to the RMS values for sensors 1 and 2, respectively.

3.3.2 Dependence of two-sensor technique on the angle between measurement line and pipe direction

Note from previous explanation that both localization techniques can only determine the leak region correctly if the pipe region is correctly determined first on ground surface. For the two-sensor technique specifically, the procedure of pipe localization requires that the measurement lines are set perpendicular to pipe direction so that the sign of $d\phi_{1,2}(\omega)/d\omega$ changes when the pair of sensors crosses the pipe on ground surface. This occurs because the arrival times for a line of constant phase depends on the position of each sensor along the measurement line in relation to pipe. Therefore, pipe direction is a condition assumed to be known prior to the application of two-sensor technique, so that it can estimate the pipe location on ground surface properly. However, this is a condition that might not be fulfilled depending on the situation on which the technique is applied and, consequently, measurement lines are set on ground surface misaligned in relation to pipe direction. Therefore, it is necessary to investigate which kind of results and limitations are expected when such a condition is not fulfilled.

As explained previously, the two-sensor technique can only determine the pipe region correctly if the sign of $d\phi_{1,2}(\omega)/d\omega$ changes when the pair of sensors crosses the pipe on ground surface. Therefore, the two-sensor technique is still able to locate a pipe when the measurement line is not perpendicular to pipe direction, only if the corresponding angle does not exceed a critical value in which a line of constant phase reaches one sensor before the other when they are at one side of the pipe, and then swaps when they are at the other side of the pipe, as shown in Fig. 31. Note that such a critical angle depends on the angles of propagation for the conical waves, given by Eq. (3a,b), and the burial depth as the shape of line of constant phase is governed by these parameters. Although the critical angle is used to explain the dependence of the two-sensor technique on the alignment between measurement line and pipe direction, an analytical model for it is beyond the scope of this thesis and is recommended as a future work.

If the angle between measurement line and pipe direction exceeds the critical value, then the line of constant phase always reaches one sensor before the other even if the pair of sensors crosses the pipe on ground surface. Consequently, the sign of $d\phi_{1,2}(\omega)/d\omega$ does not change and the two-sensor technique is not able to determine the pipe region correctly, as shown in Fig. 32, since the algorithm does not perceive that the pair of sensors has crossed the pipe on ground surface.

Figure 31 - Pipe localization with two-sensor technique when the angle between measurement line and pipe direction does not exceed the critical value. (a.i) 1st, (a.ii) 2nd, (a.iii) 3rd measurement positions, and (a.iv) pipe region resulted from two-sensor technique. (b.i) Unwrapped phase $\phi_{1,2}(\omega)$ of 1st, (b.ii) 2nd and (b.iii) 3rd measurement positions.

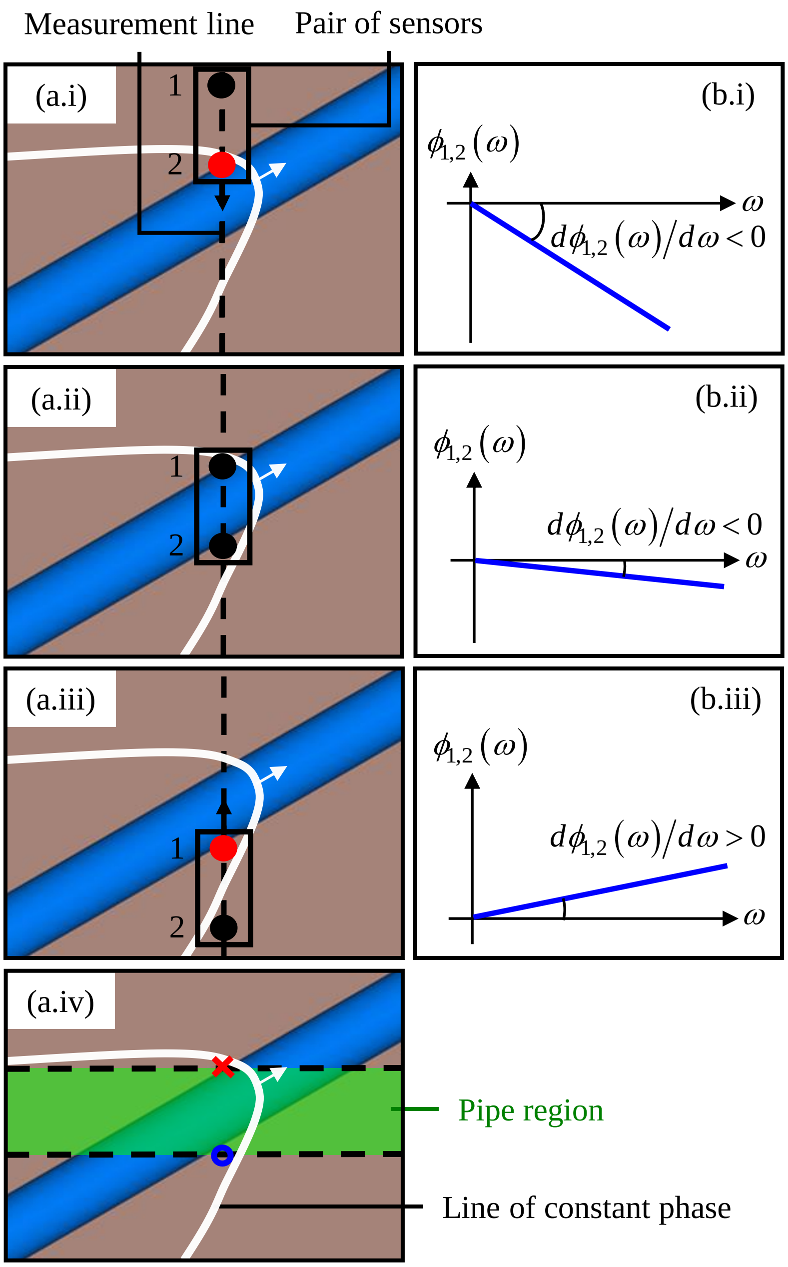

Source: elaborated by the author.

Figure 32 - Pipe localization with two-sensor technique when the angle between measurement line and pipe direction exceeds the critical value. (a.i) 1st, (a.ii) 2nd, (a.iii) 3rd measurement positions, and (a.iv) pipe region resulted from two-sensor technique. (b.i) Unwrapped phase $\phi_{1,2}(\omega)$ of 1st, (b.ii) 2nd and (b.iii) 3rd measurement positions.

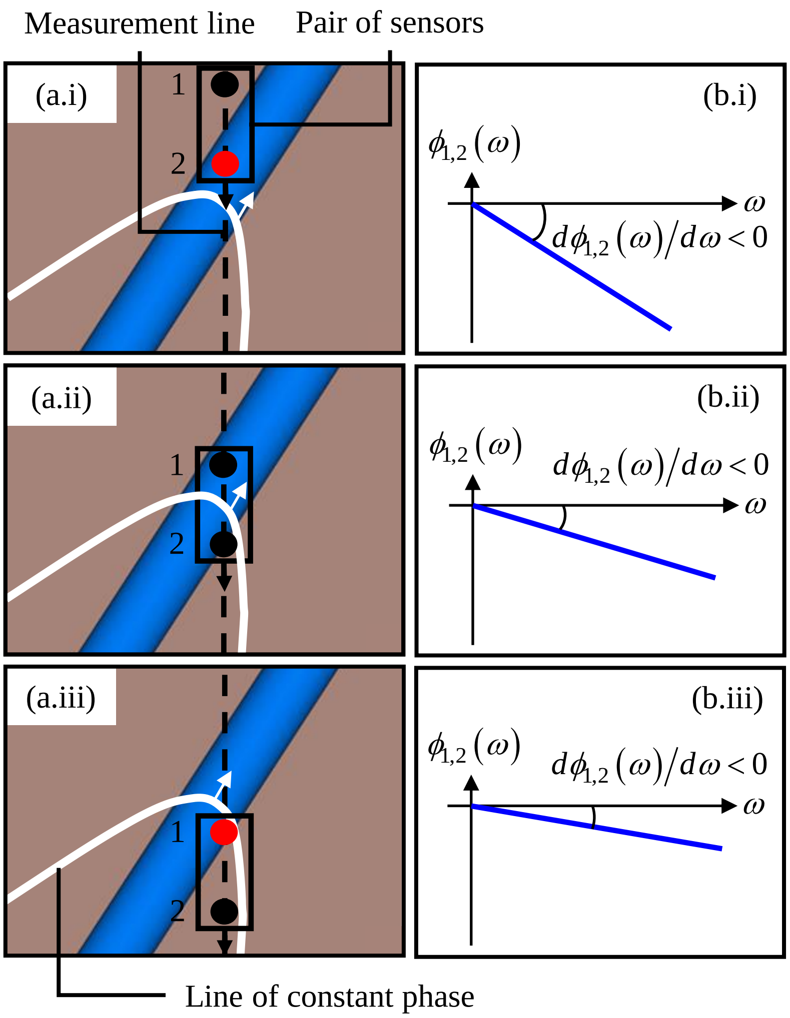

Source: elaborated by the author.

3.4 APPLICATION OF LOCALIZATION TECHNIQUES ON THE THEORETICAL DATA

The application of one-sensor and two-sensor techniques is demonstrated by testing them on the theoretical data provided by the analytical and numerical models presented in Chapter 2. For the first investigation, the measurement lines are set perpendicular to pipe direction and both techniques are applied to determine the pipe location for different positions in relation to the leak on ground surface. For the second investigation, the measurement lines are set misaligned in relation to pipe direction and both techniques are applied to determine the pipe location for different angles between measurement line and pipe direction.

3.4.1 Measurement lines perpendicular to pipe direction

Three different positions for the measurement line are considered for this analysis: 2 m, 8 m and 14 m away from the leak position along x_l-axis. The sensor positions on each measurement line are -1.5 m, -0.5 m, 0.5 m and 1.5 m away from the buried pipe along y_l-axis.

In the application of one-sensor technique, the normalized amplitude of vertical ground surface velocities for each sensor position is extracted from the contour map of Fig. 25(a) for the analytical model, and from the contour map of Fig. 25(b) for the numerical model. The results for pipe localization with one-sensor technique applied on the analytical and numerical data are tabulated in Tab. 2. The values highlighted in each column indicate the pair of positions that contains the highest amplitude for each measurement line.

In the application of two-sensor technique, the unwrapped phase of frequency response between the sensor positions along each measurement line was calculated from 35 up to 60 Hz, for both analytical and numerical models. The results for pipe localization with two-sensor technique applied on the analytical and numerical data, in which the measurement line is at 2 m, 8 m and 14 m away from the leak position are shown in Figs. 33, 34 and 35 respectively.

Table 2. Normalized amplitude of vertical ground surface velocities at 2 m, 8 m and 14 m away from the leak position, extracted from contour maps of the analytical and numerical data shown in Fig. 25(a,b).

		x_l [m]					
		2		**8**		**14**	
		Analytic.	**Numeric.**	**Analytic.**	**Numeric.**	**Analytic.**	**Numeric.**
y_l [m]	**1.5**	0.32	0.25	0.28	0.13	0.25	0.10
	0.5	0.82	0.74	0.72	0.50	0.63	0.43
	-0.5	0.82	0.74	0.72	0.50	0.63	0.43
	-1.5	0.32	0.25	0.28	0.13	0.25	0.10

Source: elaborated by the author.

Figure 33 - Pipe localization with two-sensor technique applied on the analytical and numerical data, 2 m away from the leak position. (a.i-iii) 1st, 2nd, 3rd positions of the pair of sensors and (a.iv) pipe location estimate, where the dashed blue lines correspond to the buried pipe. (b.i-iii) Unwrapped phase $\phi_{1,2}(\omega)$ for 1st, 2nd and 3rd positions, where the solid black line corresponds to the analytical data and the dotted blue line corresponds to the numerical data.

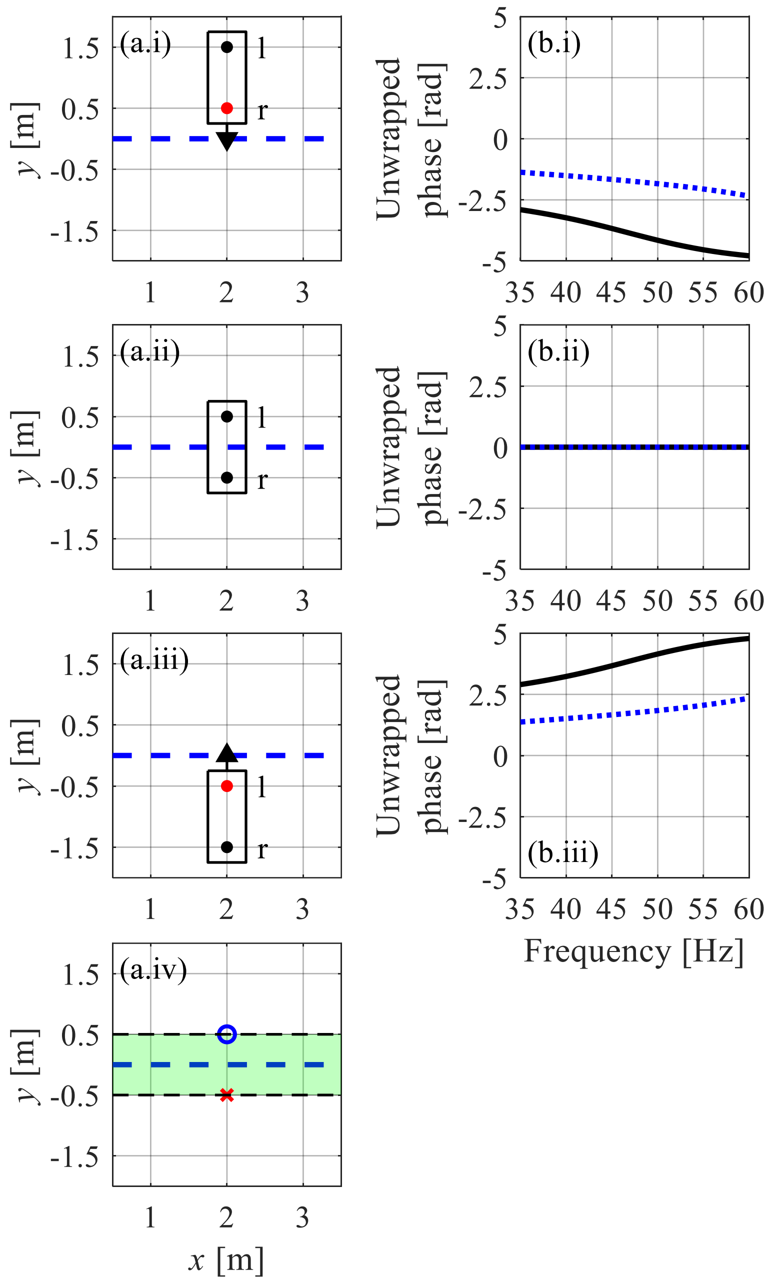

Source: elaborated by the author.

Figure 34 - Pipe localization with two-sensor technique applied on the analytical and numerical data, 8 m away from the leak position. (a.i-iii) 1st, 2nd, 3rd positions of the pair of sensors and (a.iv) pipe location estimate, where the dashed blue lines correspond to the buried pipe. (b.i-iii) Unwrapped phase $\phi_{1,2}(\omega)$ for 1st, 2nd and 3rd positions, where the solid black line corresponds to the analytical data and the dotted blue line corresponds to the numerical data.

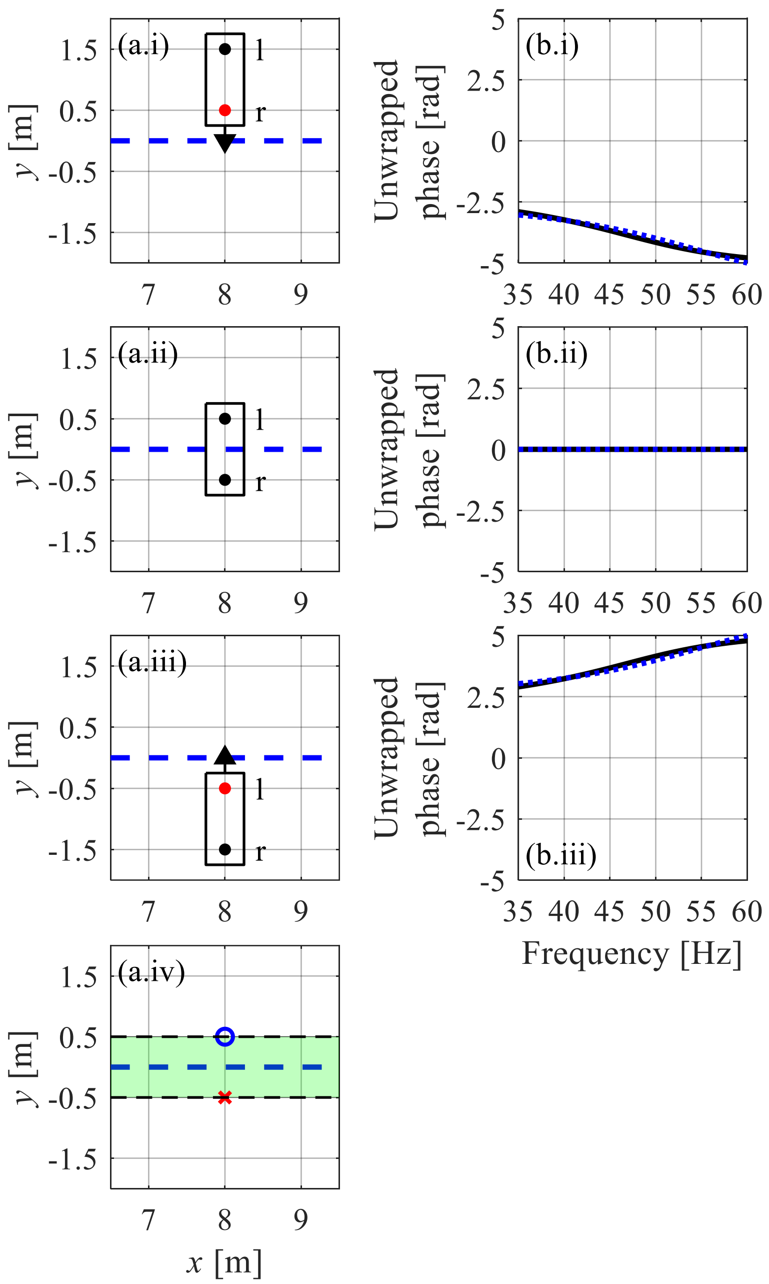

Source: elaborated by the author.

Figure 35 - Pipe localization with two-sensor technique applied on the analytical and numerical data, 14 m away from the leak position. (a.i-iii) 1st, 2nd, 3rd positions of the pair of sensors and (a.iv) pipe location estimate, where the dashed blue lines correspond to the buried pipe. (b.i-iii) Unwrapped phase $\phi_{1,2}(\omega)$ for 1st, 2nd and 3rd positions, where the solid black line corresponds to the analytical data and the dotted blue line corresponds to the numerical data.

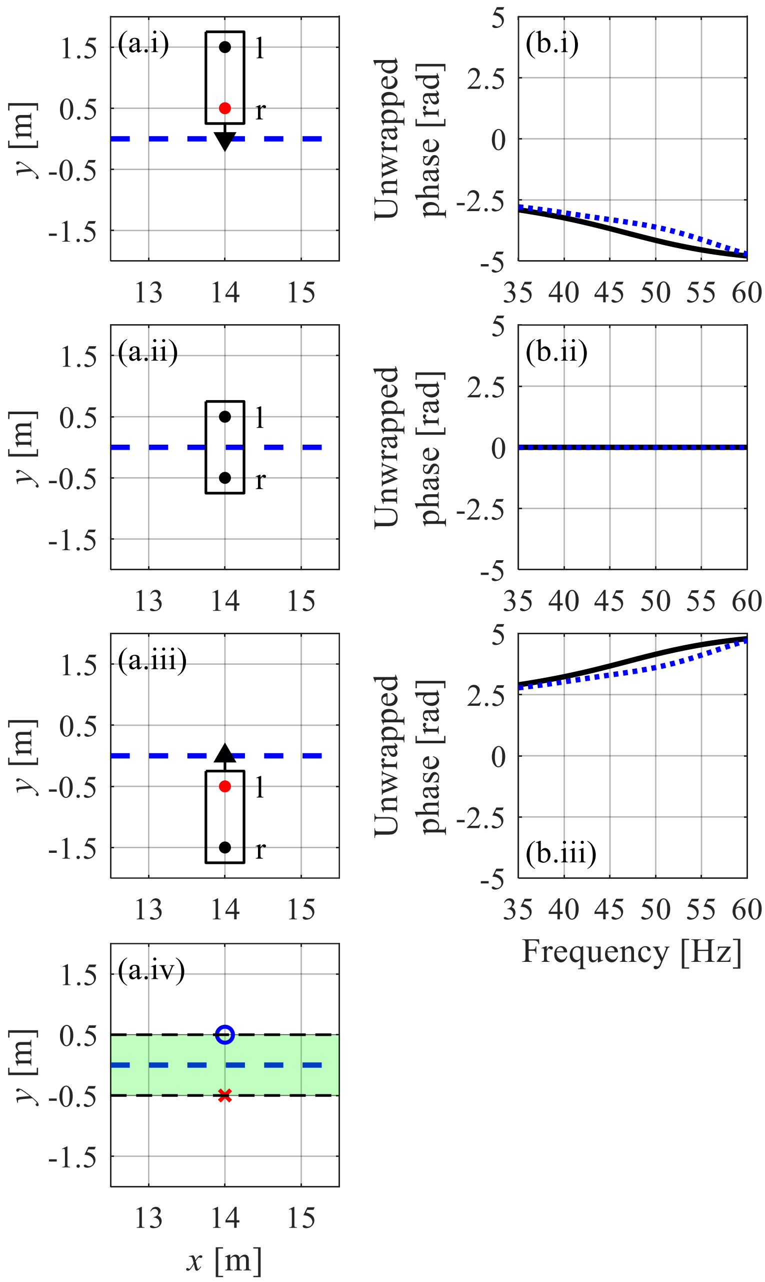

Source: elaborated by the author.

Note in Tab. 2 that the one-sensor technique correctly estimates the pipe location for all measurement line positions on ground surface. This is expected as amplitude of ground surface vibration is higher for positions close to the pipe along y_l-axis, as shown in Figs. 25(a-b), for the analytical and numerical models. The differences between the values for analytical and numerical data of Tab. 2, for each measurement line position, are due to the absence of source in the analytical model. Note that the difference between the normalized amplitude of analytical data and the normalized amplitude of numerical data is even higher for positions farther from the source, because of the contribution of spherical waves on the numerical model especially for positions close to the monopole source.

Note in Figs. 33, 34 and 35 that the two-sensor technique also correctly estimates the pipe location for all measurement lines on ground surface. The unwrapped phases for the analytical and numerical data do not overlay perfectly due to the absence of source in the analytical model. This difference is quite evident for the results shown in Fig. 33, where the corresponding measurement line is closest to the source (leak) position. Although their unwrapped phases do not overlay perfectly, both analytical and numerical data replicates successfully the theory presented in Fig. 29, in which the sign of $d\phi_{1,2}(\omega)/d\omega$ changes depending on the position of pair of sensors along the measurement line in relation to the pipe. This emphasizes that, although an approximate hyperbola of constant phase cannot be assumed for positions closer to the leak, as demonstrated in Fig. 25(b), the two-sensor technique still can locate a pipe on ground surface. Therefore, the performance of such a technique does not depend on an exact representation of the real phase between the pair of sensors, or on the exact representation of the lines of constant phase that travel on ground surface. The only condition that has to be fulfilled is the change on the sign of slope of unwrapped phase when the roving pair of sensors crosses the pipe on ground surface. Note also in Figs. 33, 34 and 35 that the direction provided by the tracking algorithm to cross the buried pipe on ground surface is correct for all measurement positions, emphasizing that both amplitude and phase of ground surface vibration are important for pipe localization, as pointed out by Muggleton *et al*. (2011).

3.4.2 Measurement lines misaligned with pipe direction

For this investigation, the measurement line positioned 8 m away from the leak is considered with three different angles between measurement line and pipe direction: 90°, 52° and 36°. Such angles were conveniently selected by rotating the pipe of Fig. 34 counter-clockwise, whose rotation axis corresponds to the point where the measurement line intersects the pipe on ground surface. The sensor positions on the measurement line are -1.5 m, -0.5 m, 0.5 m and 1.5 m away from the intersection point along y_l-axis.

In the application of one-sensor technique, the normalized amplitude of vertical ground surface velocities for each sensor position is extracted from the contour map of Fig. 25(a) for the analytical model, and from the contour map of Fig. 25(b) for the numerical model, considering the angle between measurement line and pipe direction. The results for pipe localization with one-sensor technique applied on the analytical and numerical data are tabulated in Tab. 3, following the same arrangement adopted in Tab. 2.

Table 3. Normalized amplitude of vertical ground surface velocities extracted from the analytical and numerical data, considering an angle between measurement line and pipe direction of 90°, 52° and 36°.

		x_l [m]					
		0°		**52°**		**36°**	
		Analytic.	**Numeric.**	**Analytic.**	**Numeric.**	**Analytic.**	**Numeric.**
y_l [m]	**1.5**	0.28	0.13	0.27	0.11	0.24	0.10
	0.5	0.72	0.50	0.71	0.48	0.67	0.47
	-0.5	0.72	0.50	0.73	0.51	0.75	0.52
	-1.5	0.28	0.13	0.29	0.12	0.33	0.29

Source: elaborated by the author.

In the application of two-sensor technique, the frequency response between the sensor positions along the measurement line was calculated from 35 up to 60 Hz, for both analytical and numerical models. The results for pipe localization with two-sensor technique for an angle between measurement line and pipe direction of 90°, 52° and 36° are shown in Figs. 34, 36 and 37 respectively.

Figure 36 - Pipe localization with two-sensor technique applied on the analytical and numerical data, 8 m away from the leak position and an angle between measurement line and pipe direction of 52°. (a.i-iii) 1st, 2nd, 3rd positions of the pair of sensors and (a.iv) pipe location estimate, where the dashed blue lines correspond to the buried pipe. (b.i-iii) Unwrapped phase $\phi_{1,2}(\omega)$ for 1st, 2nd and 3rd positions, where the solid black line corresponds to the analytical data and the dotted blue line corresponds to the numerical data.

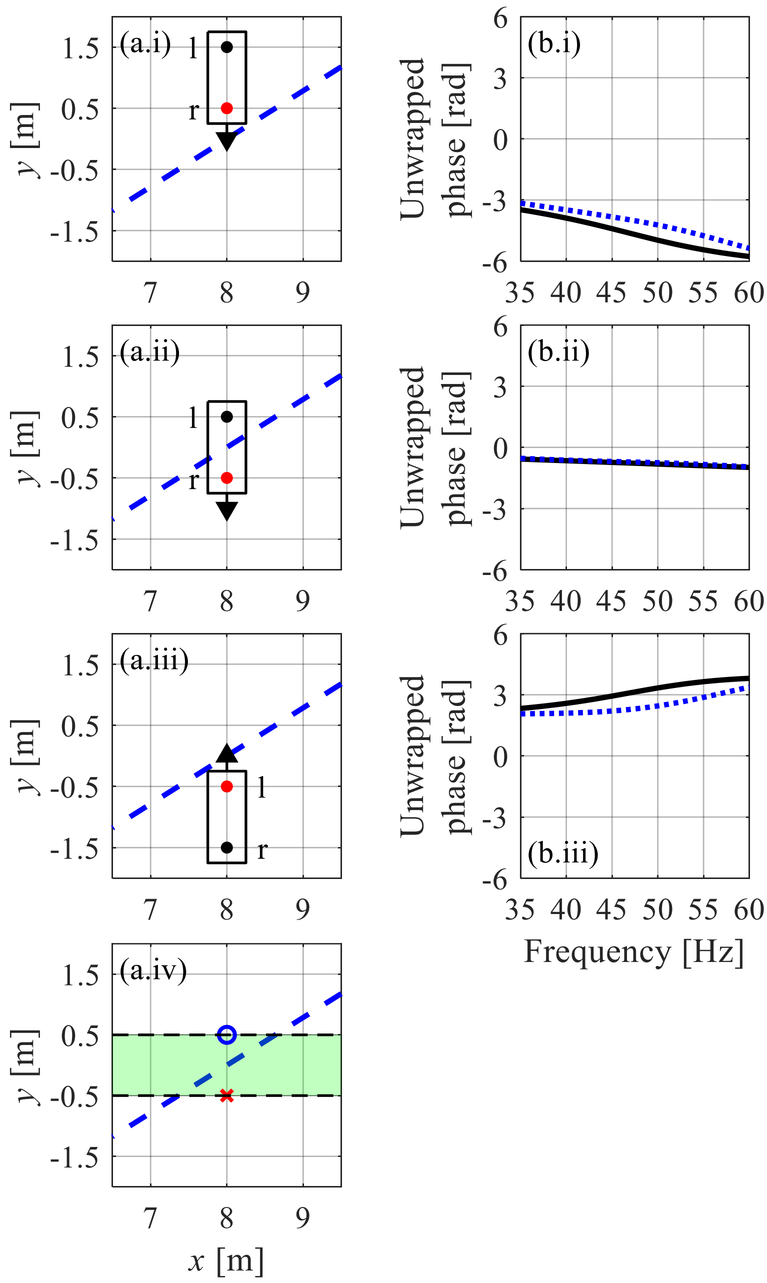

Source: elaborated by the author.

Figure 37 - Pipe localization with two-sensor technique applied on the analytical and numerical data, 8 m away from the leak position and an angle between measurement line and pipe direction of 36°. (a.i-iii) 1st, 2nd, 3rd positions of the pair of sensors and (a.iv) pipe location estimate, where the dashed blue lines correspond to the buried pipe. (b.i-iii) Unwrapped phase $\phi_{1,2}(\omega)$ for 1st, 2nd and 3rd positions, where the solid black line corresponds to the analytical data and the dotted blue line corresponds to the numerical data.

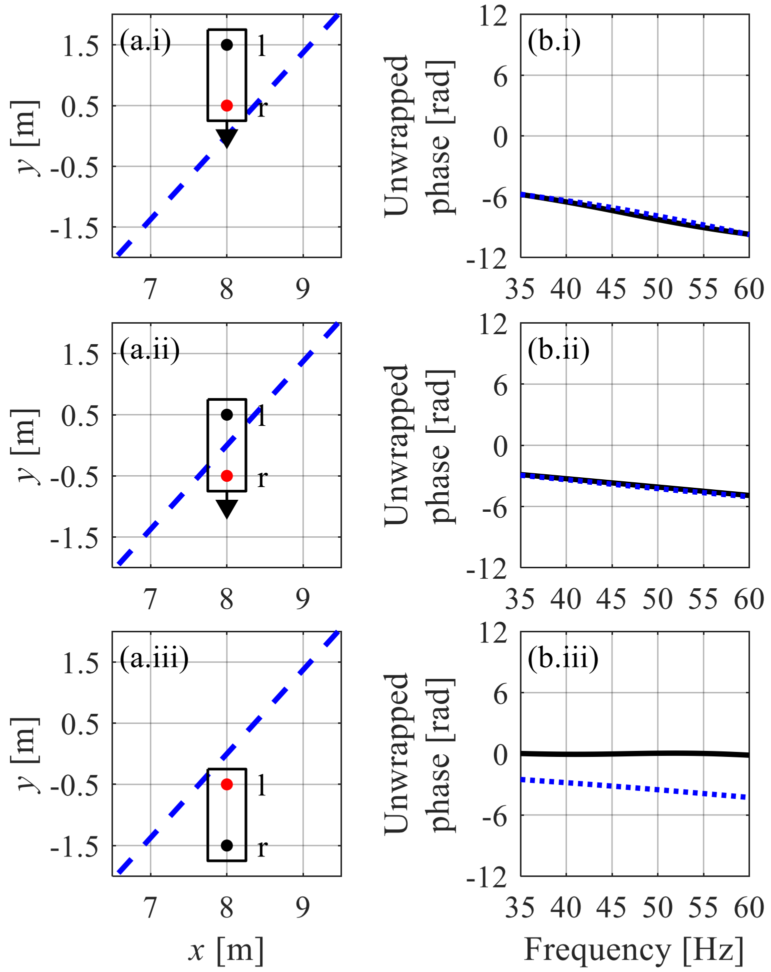

Source: elaborated by the author.

Note in Tab. 3 that the one-sensor technique estimates a pair of positions that encompass the leak along y_l-axis for all angles considered in the investigation. Note also that the columns for 52° and 36° do not keep the symmetry for 0° along y_l-axis in Tab. 3, because the measurement line is not perpendicular to pipe direction. Although the region resulted by the pair of positions highlighted in Tab. 3 does not encompass the pipe completely as the example shown in Fig. 27, the one-sensor technique can be applied to pinpoint the leak position as shown in Fig. 28 since the same region encompass the leak position on ground surface. Therefore, these results show that the one-sensor technique does not depend on knowing an approximation for the pipe direction.

By comparing Figs. 34(b.i-iii) and 36(b.i-iii), it can be seen that the unwrapped phase along the measurement line with 52° does not keep the symmetry for the unwrapped phase along the one with 0°, in which $d\phi_{1,2}(\omega)/d\omega = 0$ when the sensors are equidistant from the pipe as shown in Fig. 29. However, the two-sensor technique still results a pair of positions that encompass the leak along y_l-axis, since the sign of $d\phi_{1,2}(\omega)/d\omega$ changes when the pair of sensors crosses the pipe on ground surface. This is because the lines of constant phase still reach one sensor before the other when they are at one side of the pipe, and then swaps when they are at the other side of the pipe, as explained previously with Fig. 31. By analyzing Fig. 37(b.i-iii), however, it can be seen that the sign of $d\phi_{1,2}(\omega)/d\omega$ does not change along the measurement line with 36° and, consequently, the algorithm of two-sensor technique does not perceive that the pair of sensors has crossed the pipe on ground surface. This is because the angle exceeds the critical value in which lines of constant phase always reach one sensor before the other, regardless of their positions along the measurement line. Therefore, these results show that the two-sensor technique can locate a pipe on ground surface even when measurement lines are not perpendicular to pipe direction. However, the angle between them must be close as possible to 90°.

3.5 CONCLUSIONS

This chapter introduces the one-sensor and two-sensor techniques for pipe and leak localization. The one-sensor technique is based on the amplitude difference of a roving single sensor on ground surface, and the two-sensor technique is based on the unwrapped phase of a roving pair of sensors on ground surface, which contains a tracking algorithm to speed up the localization procedure. Both techniques are divided into two consecutive stages, in which the buried pipe is located in the first one and the leak in the second one. Due to the dependence of the two-sensor technique on the alignment between measurement lines and pipe direction, the application of the one-sensor and two-sensor techniques is illustrated by applying them on the theoretical data extracted from the analytical and numerical models for a buried pipe system, considering two investigations: measurement lines perpendicular to pipe direction and measurement lines misaligned to pipe direction.

The results for the first investigation show that the physics of wave propagation is not faithfully described by the analytical model for positions close to the leak on ground surface, since it does not replicate the source exciting the pipe as the numerical model. Although the one-sensor and two-sensor techniques are introduced based on the physics described by the analytical model, the results indicate that both techniques can be used for pipe localization, even for positions close to the leak (source), because they correctly estimated the pipe location for all measurement lines of both analytical and numerical models. This is because the localization techniques do not depend on an exact representation of the physics happening on ground surface. Instead, an amplitude difference must be measured so that a pipe can be located with the one-sensor technique, and the sign of the slope of unwrapped phase must be measured by a roving pair of sensors so that a pipe can be located with the two-sensor technique.

The results for the second investigation show that the one-sensor technique does not require that measurement lines are perpendicular to pipe direction, since it correctly estimated the pipe location for all different angles between them. The results also show that the two-sensor technique can locate a pipe when the measurement lines are not perpendicular to pipe direction. However, the angle between them must be as close as possible to 90° so that the algorithm can perceive that the pair of sensors has crossed the pipe on the ground surface, based on the change of the sign of slope of unwrapped phase.

The theoretical investigations presented in this chapter motivate the application of both localization techniques on experimental data of ground surface vibration, to check their performance on practical situations. Prior to this, the next chapter presents an investigation for the features of the two-sensor technique, so that they can be properly assessed before applying it on experimental data.

4 INVESTIGATION OF THE FEATURES FOR PRACTICAL APPLICATION OF TWO-SENSOR TECHNIQUE

4.1 INTRODUCTION

The concepts of wave propagation in a buried pipe system introduced in Chapter 2 are used to explain the lines of constant phase, on which the two-sensor technique is designed for pipe and leak localization using measurements of ground surface vibration. As explained in Chapter 3, the technique uses the slope of unwrapped phase between the pair of sensors as an indication for the localization procedure, which is governed by the respective time delay. This indication can also be extracted by simply calculating cross-correlation between the signals measured by the pair of sensors, and then checking the sign of the time delay that corresponds to the maximum absolute value. In practical situations, however, the presence of external phenomena can interfere with the extraction of such an indication in both time and frequency domains. Since the theoretical models presented in Chapter 2 do not consider external phenomena, it is necessary to verify on a real dataset which domain the two-sensor technique is less affected by these interferences, so the corresponding localization procedure can be set to be as much robust as possible. Furthermore, the sensors must be placed at different distances so that the technique is able to measure some time delay, and the area circumscribed on the ground surface to access the leak depends on the distance set for the pair of sensors. Therefore, it is also necessary to verify the minimum distance in which the sensors are still able to capture the indication for pipe location, even with the interference of external phenomena. This chapter presents two investigations, in which the first one is to evaluate if the time domain or the frequency domain is more suitable to extract the indication for pipe location, and the second one is to evaluate the minimum distance in which the pair of sensors can capture it. Both investigations are conducted on the experimental data measured in the British test rig.

4.2 EXTRACTING THE INDICATION OF PIPE LOCATION WITH TWO-SENSOR TECHNIQUE IN THE TIME AND FREQUENCY DOMAINS

A portion of the measurement grid set on the British test rig was used to verify if the extraction of the indication of pipe location with the two-sensor technique is more suitable in the time domain, or in the frequency domain. To carry out such an investigation, the technique is used in both domains to estimate the pipe location with measurements of ground surface vibration by calculating cross-correlation coefficient and phase of cross-spectrum density for each pair of 1 m spaced positions, along each of the 32 measurement lines across the pipe on the ground surface, as shown in Fig. 38. The coherence was also determined for each pair of positions to set the limits in the frequency domain that the function is greater than 10^{-2}, to guarantee that the phase is properly unwrapped (MUGGLETON; BRENNAN; GAO, 2011). Then, a line is approximated for the values of unwrapped phase within this bandwidth to estimate the respective slope in the frequency domain, and the same limits are also used to set the bandpass filter that the pair of signals are passed through before calculating cross-correlation coefficient in the time domain. The functions in the frequency domain were determined by averaging the time-series using segment averaging (SHIN; HAMMOND, 2008) with 32 averages, 1,000-point fast Fourier transform and a Hanning window with 50% overlap, resulting a frequency resolution of 1 Hz.

Figure 38 - Schematic diagram for measurement grid of the British test rig used to extract the indication of pipe location with the two-sensor technique in the time and frequency domains.

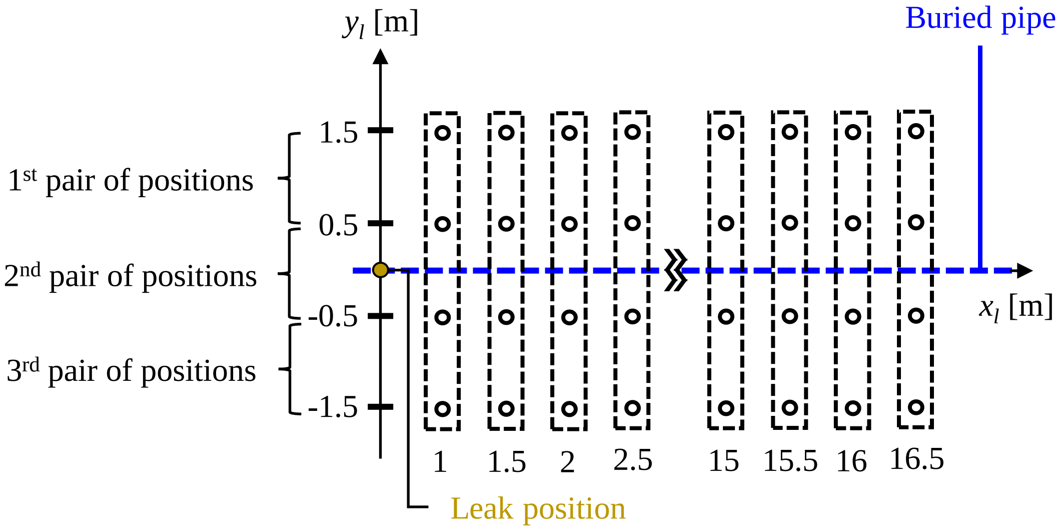

Source: elaborated by the author.

As explained for the frequency domain in Fig. 29, the pair of positions whose slope is closer to zero is marked on the ground surface if the sign of the slope of unwrapped phase changes along a measurement line. Similarly for the time domain, if the sign of the time delay that corresponds to the maximum absolute cross-correlation coefficient changes along a measurement line, then the pair of positions that contains the time delay closer to zero is marked on the ground surface. The results for the extraction of the indication of pipe location with the two-sensor technique is presented in Fig. 39, in which Fig. 39(a) shows the estimates of pipe localization using slope of unwrapped phase and Fig. 39(b) shows the estimates of pipe localization using maximum absolute cross-correlation coefficient. An estimate for each measurement line of Figs. 39(a) and 39(b) corresponds to a pair of 1 m spaced blue-circle and red-cross marks, in which a wrong estimate is defined when the pair of marks does not encompass the pipe, when the algorithm does not provide a pair of marks, or when it provides two or more pair of marks for the same measurement line. Note in Fig. 39(a) that there is a total of 4 wrong estimates using slope of unwrapped phase, for the measurement lines specifically located at x_l = 1.5, 2, 2.5 and 11 m. In Fig. 39(b), there is a total of 9 wrong estimates using maximum absolute cross-correlation coefficient, for the measurement lines specifically located at x_l = 2.5, 3, 3.5, 4, 6, 6.5, 9, 10.5 and 13.5 m.

Figure 39 - Results for the extraction of the indication of pipe location with the two-sensor technique in the time and frequency domains. (a) Estimates of pipe localization using slope of unwrapped phase, and (b) estimates of pipe localization using maximum absolute cross-correlation coefficient. The dashed blue lines correspond to the buried pipe.

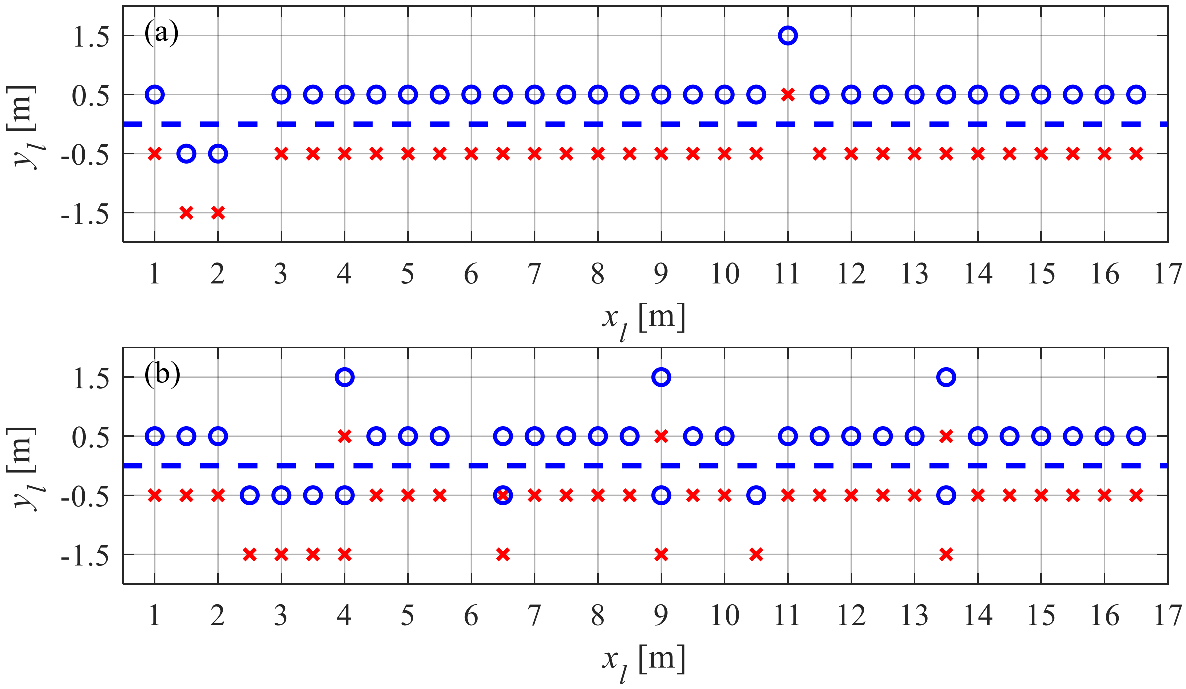

Source: elaborated by the author.

By comparing the results of Fig. 39(a) with the ones of Fig. 39(b), it is evident that extracting the indication of pipe location with the two-sensor technique in the frequency domain is more reliable than extracting it in the time domain. To present a detailed discussion for the different performances, an example for each type of wrong estimate for pipe localization using maximum absolute cross-correlation coefficient is presented. An example when the pair of marks does not encompass the pipe is shown in Fig. 40, an example when the algorithm does not provide a pair of marks is shown in Fig. 41, and an example when the algorithm provides two pair of marks for the same measurement line is shown in Fig. 42. By comparing Figs. 40(b.i-iii), 41(b.i-iii) and 42(b.i-iii) with 40(c.i-iii), 41(c.i-iii) and 42(c.i-iii), respectively, it can be seen that the approximate slope of unwrapped phase is more reliable than cross-correlation coefficient to extract an indication of when the pair of sensors crosses the pipe on the ground surface. Note that an evident change on the approximate slope of unwrapped phase can be identified when the pair of sensors crosses the pipe on the ground surface, while the time delay provided by the maximum absolute cross-correlation coefficient does not vary considerably. Note also that the cross-correlation coefficient does not contain an evident peak in Figs. 40(c.i-iii), 41(c.i-iii) and 42(c.i-iii), making the process of extracting the indication of pipe location in the time domain even more unreliable, and this is probably due to two reasons. The first one is the narrow bandwidth estimated from the coherences, as shown by the light green zones of Figs. 40(a.i-iii), 41(a.i-iii) and 42(a.i-iii), that is used to filter the signals before calculating cross-correlation coefficient. The second one is the interference of external phenomena, such as reflections of the wave in the pipe (GAO *et al*., 2009), resonances of the buried pipe system (ALMEIDA *et al*., 2018), and even other types of waves captured during the experiment. Note that these reasons are just conjectures, so they require further research to be properly assessed.

Although the system dispersion relation and the presence of reflections, resonances and other types of waves must be carefully considered when estimating a precise time delay between two sensors, the approximation of a straight line for the unwrapped phase is adopted only to capture a robust indication of when the pair of sensors crosses the pipe on the ground surface. Such a procedure improves the performance of the two-sensor technique in estimating an approximate pipe location, as can be seen by comparing Figs. 40(b.iv), 41(b.iv) and 42(b.iv) with Figs. 40(c.iv), 41(c.iv) and 42(c.iv), respectively. Therefore, the approximate slope of unwrapped phase in the frequency domain is more reliable for practical application of the two-sensor technique, than cross-correlation in the time domain.

Figure 40 - Example of when the pair of marks does not encompass the pipe, using the two-sensor technique with cross-correlation. (a.i-iii) Coherences, (b.i-iii) unwrapped phases (solid black line), approximated lines (dotted red line) and (c.i-iii) cross-correlation coefficients (solid black line) for 1st, 2nd and 3rd positions of the pair of sensors. (b.iv) Estimate of pipe localization using the slope of unwrapped phase, and (c.iv) estimate of pipe localization using the maximum absolute cross-correlation coefficient (red circle). The dashed blue lines correspond to the buried pipe.

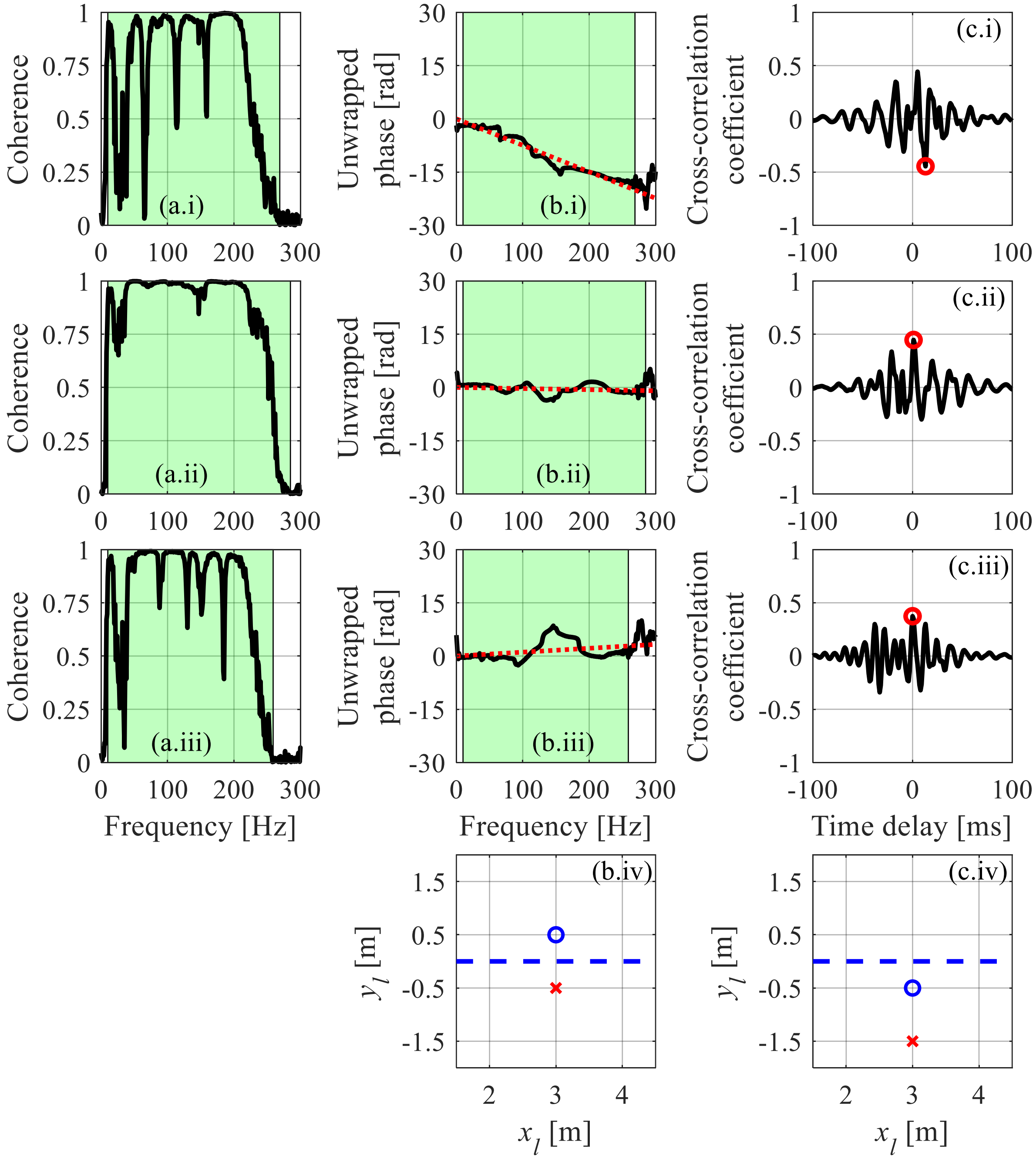

Source: elaborated by the author.

Figure 41 - Example of when the algorithm provides no pair marks for the same measurement line, using the two-sensor technique with cross-correlation. (a.i-iii) Coherences, (b.i-iii) unwrapped phases (solid black line), approximated lines (dotted red line) and (c.i-iii) cross-correlation coefficients (solid black line) for 1st, 2nd and 3rd positions of the pair of sensors. (b.iv) Estimate of pipe localization using the slope of unwrapped phase, and (c.iv) estimate of pipe localization using the maximum absolute cross-correlation coefficient (red circle). The dashed blue lines correspond to the buried pipe.

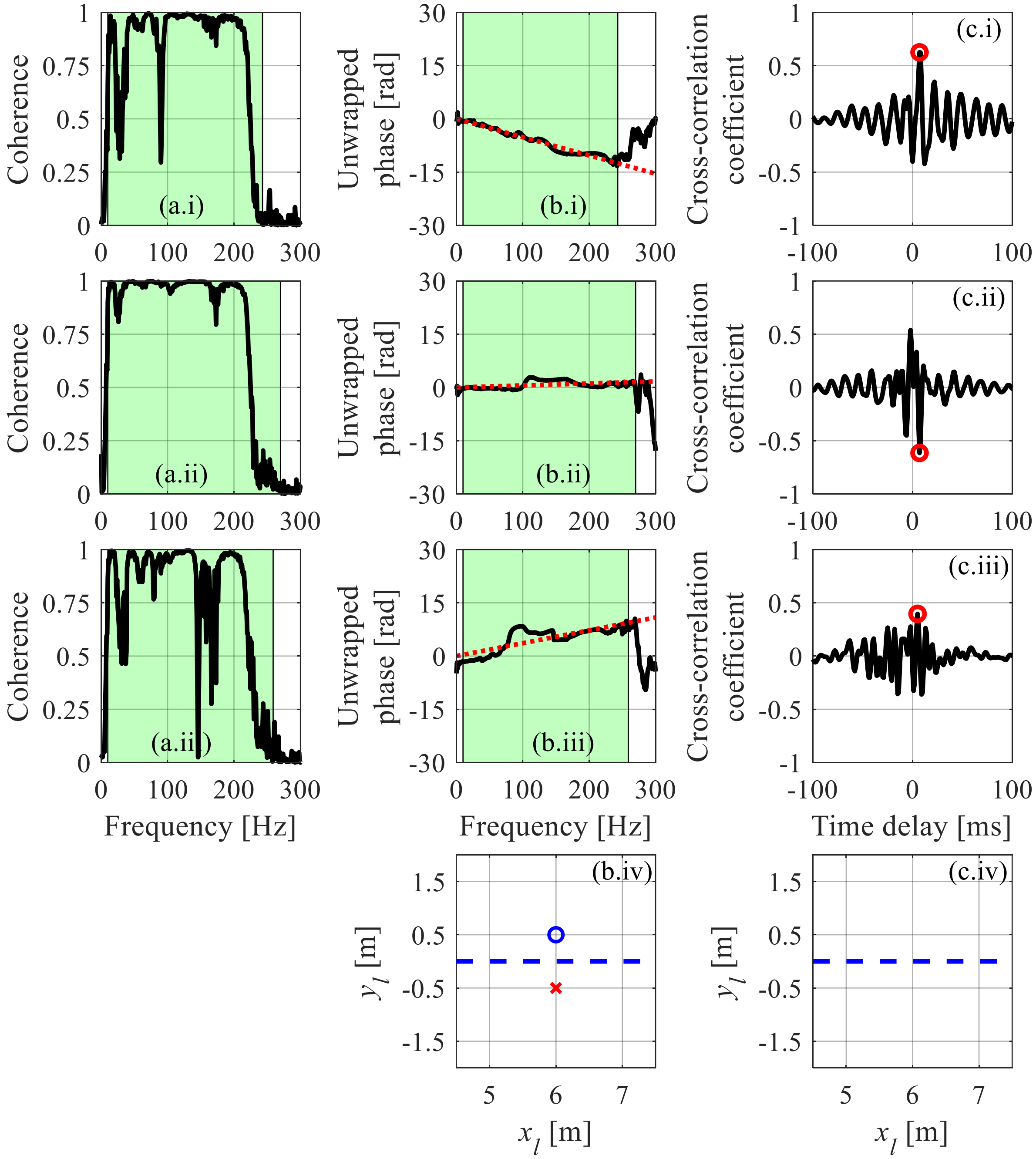

Source: elaborated by the author.

Figure 42 - Example of when the algorithm provides two pair marks for the same measurement line, using the two-sensor technique with cross-correlation. (a.i-iii) Coherences, (b.i-iii) unwrapped phases (solid black line), approximated lines (dotted red line) and (c.i-iii) cross-correlation functions (solid black line) for 1st, 2nd and 3rd positions of the pair of sensors. (b.iv) Estimate of pipe localization using the slope of unwrapped phase, and (c.iv) estimate of pipe localization using the maximum absolute cross-correlation coefficient (red circle). The dashed blue lines correspond to the buried pipe.

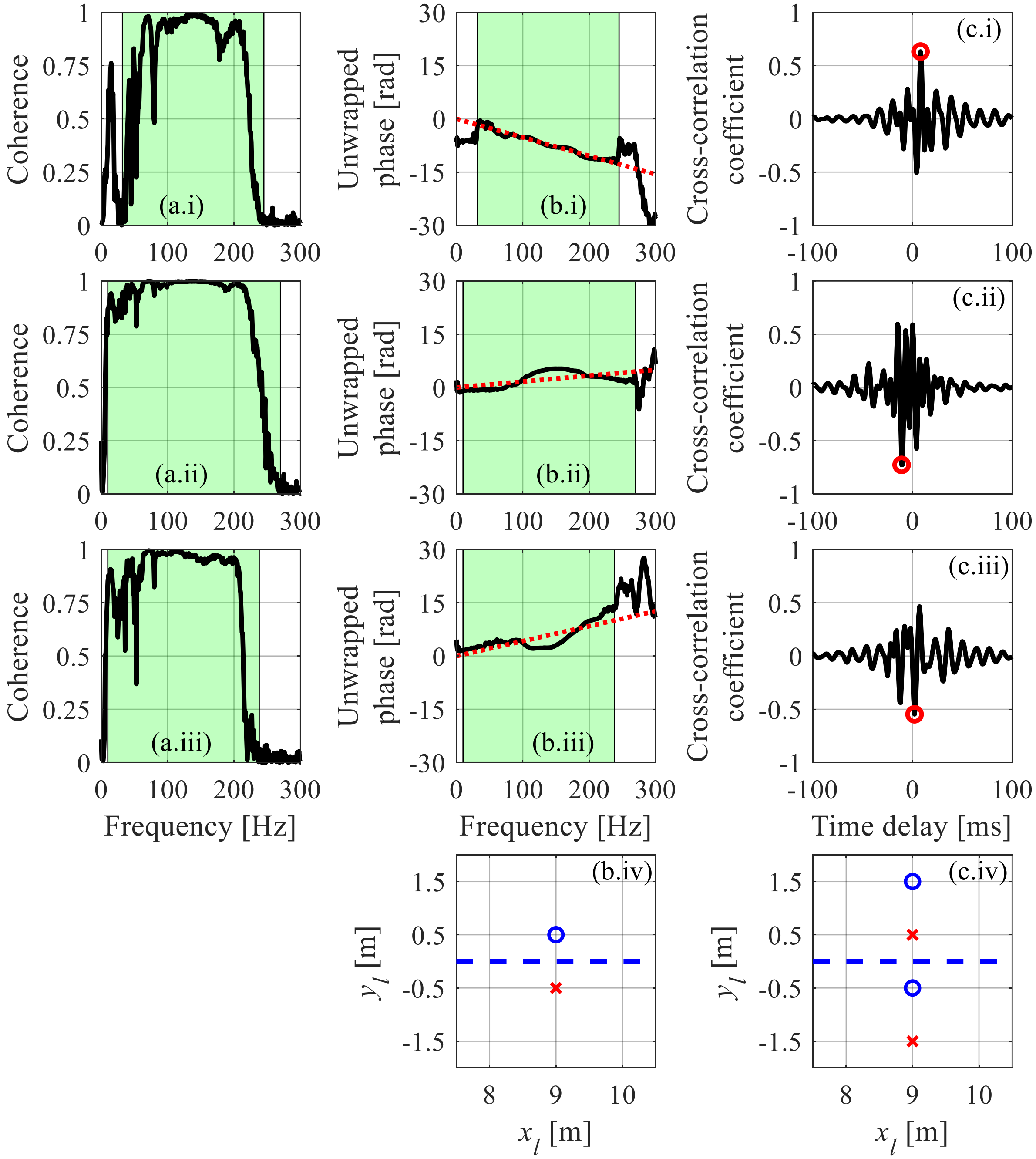

Source: elaborated by the author.

4.3 MINIMUM DISTANCE BETWEEN THE PAIR OF SENSORS FOR THE TWO-SENSOR TECHNIQUE

After verifying which domain is more suitable, a second investigation is carried out to check the minimum distance between the pair of sensors on the ground surface that the two-sensor technique is still able to extract the indication pipe location. To do so, the technique was applied on the complete measurement grid of the British test rig to estimate pipe location by calculating phase of cross-spectrum density for each pair of 0.5 m spaced positions, along each of the 32 measurement lines as shown in Fig. 43. Like the previous investigation, the coherence was determined for each pair of positions to set the limits in the frequency domain, in which the line is approximated for the values of unwrapped phase to estimate the respective slope. These limits were determined by selecting the bandwidth where the coherence is greater than 10^{-2}, to guarantee that the phase is properly unwrapped. Both coherence and cross-spectrum density were determined for each pair of positions by averaging the time-series, using segment averaging (SHIN; HAMMOND, 2008) with the same parameters used for the previous investigation. Then, the results obtained for 0.5 m between the pair of sensors are compared with the ones obtained for 1 m, presented in the previous section.

Figure 43 - Schematic diagram for measurement grid of the British test rig used to investigate the minimum distance between the pair of sensors of the two-sensor technique.

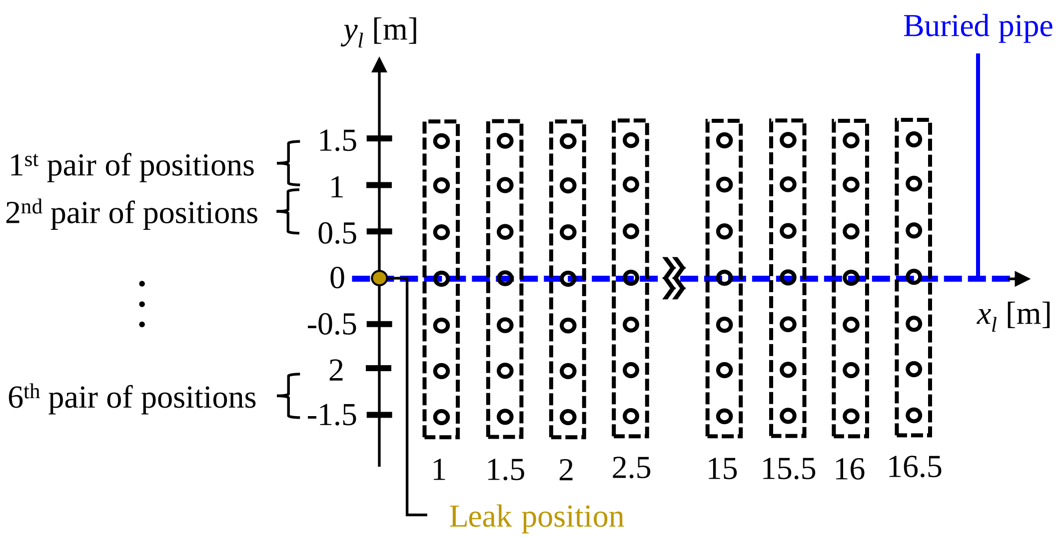

Source: elaborated by the author.

The results for the minimum distance between the pair of sensors of the two-sensor technique is presented in Fig. 44, in which Fig. 44(a) shows the estimates of pipe localization for 1 m between the sensors (which correspond to the same results shown in Fig. 39(a) and are shown again for convenience), and Fig. 44(b) shows the estimates of pipe localization for 0.5 m between the sensors. As explained for the previous investigation, an estimate corresponds to a pair of red-cross and blue-circle marks on each measurement line of Figs. 44(a) and 44(b), in which a wrong estimate is defined when the pair of marks does not encompass the pipe, when the algorithm does not provide a pair of marks, or when it provides two or more pair of marks for the same measurement line. Note in Fig. 44(a) that there is a total of 4 wrong estimates when the sensors are 1 m spaced, and a total of 22 wrong estimates when the sensors are 0.5 m spaced as shown in Fig. 44(b).

Figure 44 - Results for the investigation of minimum distance between pair of sensors for the two-sensor technique. (a) Estimates of pipe localization for 1 m between the sensors and (b) estimates of pipe localization for 0.5 m between the sensors. The dashed blue lines correspond to the buried pipe.

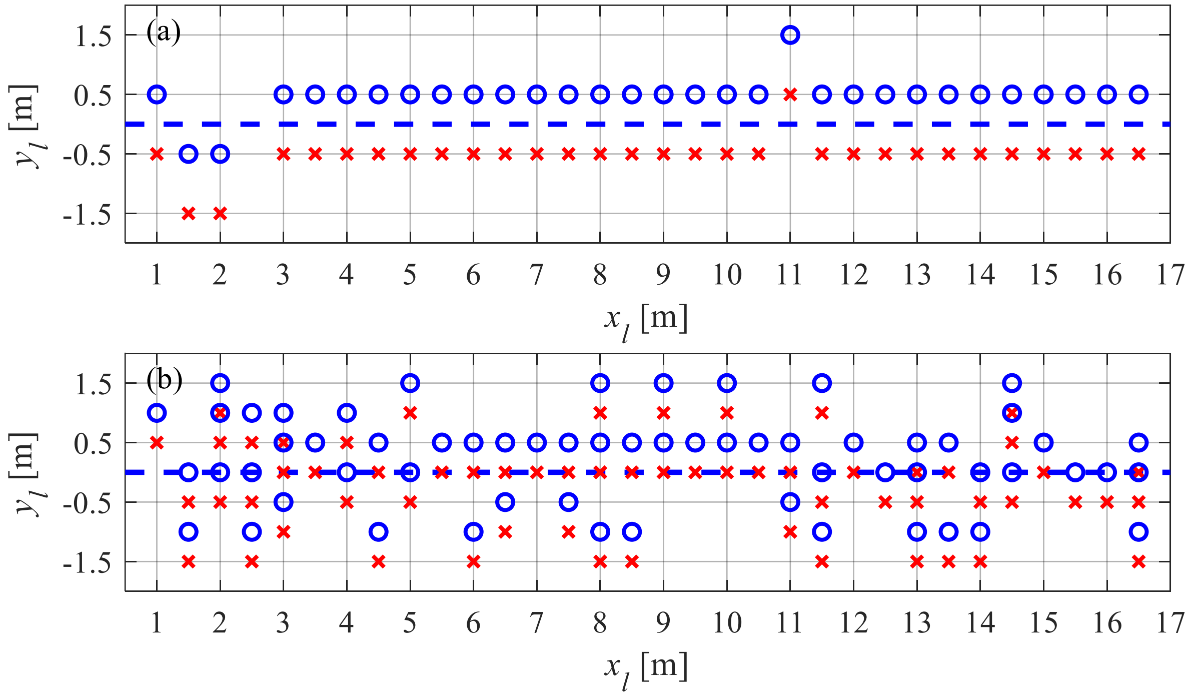

Source: elaborated by the author.

Figure 45 - Pipe localization with the two-sensor technique when the pair of sensors are 0.5 m spaced, applied on the measurement line 9 m away from the leak position of the British test rig – Part 1. (a.i-iii) Coherences, (b.i-iii) unwrapped phases (solid black line) and approximated lines (dotted red line), and (c.i-iii) CCCs (solid black line) for 1st, 2nd and 3rd positions of the pair of sensors. (b.iv) Estimate of pipe localization using the slope of unwrapped phase, and (c.iv) estimate of pipe localization using the maximum absolute CCC (red circle).

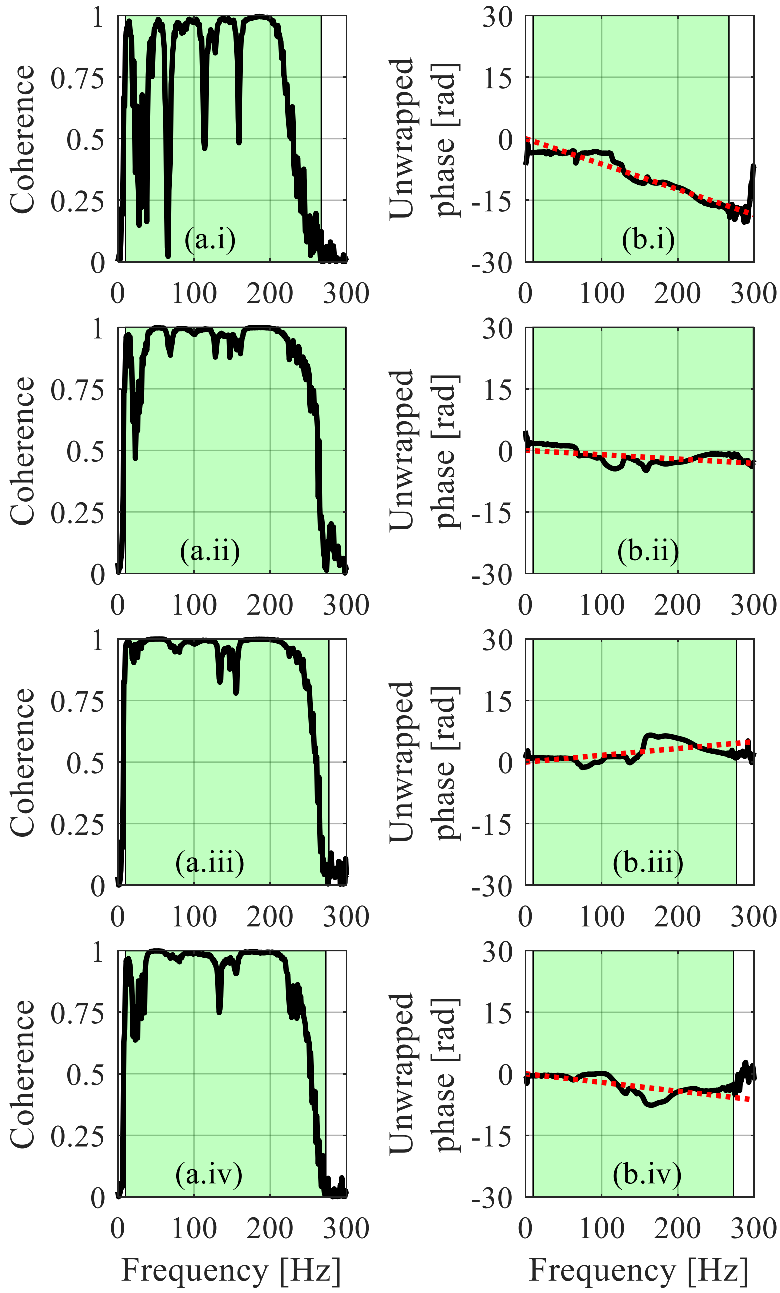

Source: elaborated by the author.

Figure 46 - Pipe localization with the two-sensor technique when the pair of sensors are 0.5 m spaced, applied on the measurement line 9 m away from the leak position of the British test rig – Part 2. (a.i-iii) Coherences, (b.i-iii) unwrapped phases (solid black line) and approximated lines (dotted red line), and (c.i-iii) CCCs (solid black line) for 1st, 2nd and 3rd positions of the pair of sensors. (b.iv) Estimate of pipe localization using the slope of unwrapped phase, and (c.iv) estimate of pipe localization using the maximum absolute CCC (red circle). The dashed blue lines correspond to the buried pipe.

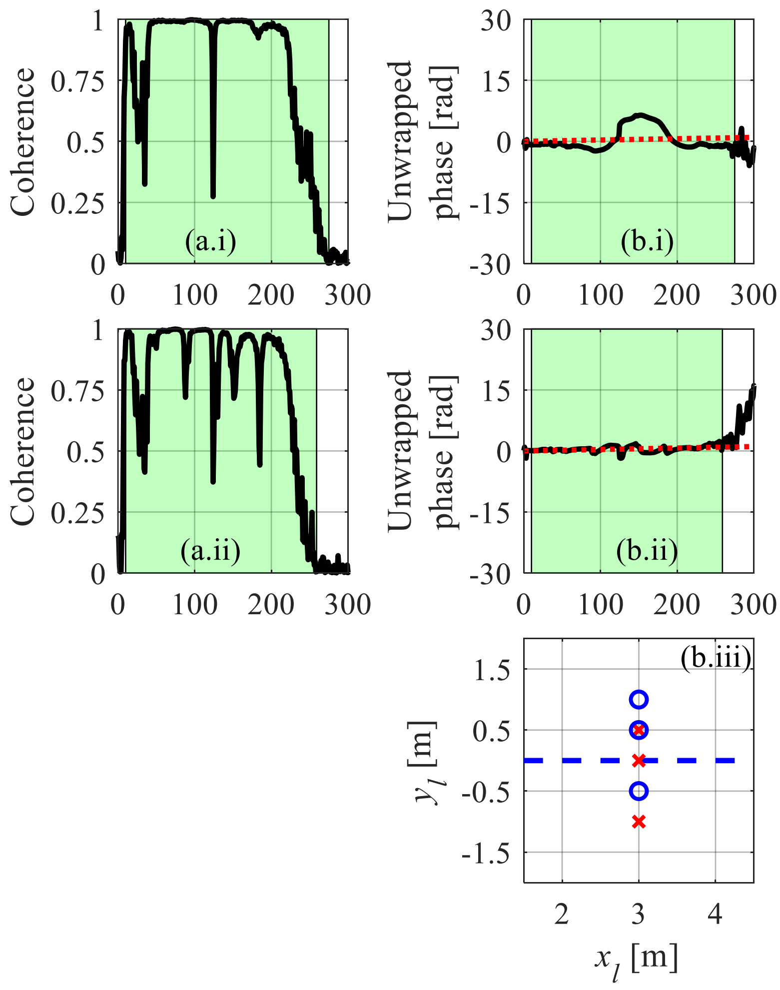

Source: elaborated by the author.

By checking the results of Fig. 44, it is evident that placing the pair of sensor 1 m apart is more reliable than placing them 0.5 m apart for the two-sensor technique. An example for a wrong estimate resulted for the distance of 0.5 m between the sensors is presented, to provide a detailed discussion for the different performances without extending unnecessarily. The results for all 6 pair of positions of the measurement line 3 m away from the leak position (which corresponds to the same measurement line of Fig. 40) are presented in Figs. 45 and 46.

By analysing Figs. 40(a.i-iii), 45(a.i-iv) and 46(a.i-iii), it can be seen that the coherences result approximately the same limits in the frequency domain for all pair of positions along the measurement line. By analysing Figs. 40(b.i-iii), 45(b.i-iv) and 46(b.i-iii), it can be seen that the unwrapped phase is strongly affected by the distance between the pair of sensors. Note in Figs. 45(b.i-iv) and 46(b.i-iii) that the slope of unwrapped phase does not change significantly for different positions in relation to the pipe, when the sensors are 0.5 m apart on the ground surface. This is because the distance that the wavefront travels from one sensor to the other is too short and, hence, the time difference between them is also too short because of the rapid phase velocity. Furthermore, since the slope of unwrapped phase is governed by the time delay between the pair of sensors, as explained in Chapter 3, the approximate line cannot effectively capture the change of such a slope because phase changes caused by external phenomena become more dominant. However, by analysing Figs. 40(b.i-iii), 41(b.i-iii) and 42(b.i-iii), it can be seen that the approximate line can effectively capture the change of the slope of unwrapped phase, when the sensors are 1m apart on the ground surface. This is because a longer distance between the sensors increases the slope of unwrapped phase and compensates for the phase changes caused by external phenomena. Therefore, the minimum distance between the pair of sensors must not be less than 1 m, so they can effectively extract the indication of pipe and leak location for the two-sensor technique.

4.4 CONCLUSIONS

This chapter presented investigations for two features for practical application of the two-sensor technique, where the first one corresponds to the extraction of the indication of pipe location in the time and frequency domains, and the second one corresponds to the minimum distance between the pair of sensors of the two-sensor technique. The results for the first investigation have shown that extracting the indication for pipe location with the maximum absolute cross-correlation is more likely to result in a wrong estimate, than using the slope of unwrapped phase. This is because the technique is not designed to precisely estimate time delay between the pair of sensors on which it is expected that cross-correlation would be more straightforward than phase, but it is a kind of estimation that might be strongly affected by narrow-band signals and external phenomena. To compensate for such interferences on the localization procedure, the two-sensor technique is designed to extract the indication of pipe and leak locations, based on the different times of arrival for the lines of constant phase that reach both sensors, which depend on the corresponding position in relation to the pipe, or the leak, on the ground surface. Since the results have shown that approximating a line for the values of unwrapped phase reduces the wrong estimates than finding the maximum absolute cross-correlation for the pair of sensors, it is concluded that the first procedure is more suitable for the practical application of the two-sensor technique.

The second investigation has shown that, although a minimum distance between the pair of sensors must be set for the two-sensor technique so that the resulted area to access the leak is not too large, it also must attend the condition that the line approximated for the values of unwrapped phase has to capture the indication of when the pair of sensors crosses the pipe, or the leak, on the ground surface. By using the complete measurement grid deployed on the British test rig, the results have shown that the minimum distance must not be minor than 1 m, otherwise the phase changes caused by external phenomena become more dominant as the slope of unwrapped phase decreases due to the rapid phase velocity and, hence, the two-sensor technique is more likely to provide a wrong estimate for pipe location. Note that, as the phase velocity measured by the pair of sensors is governed by the soil properties, as explained in Chapter 2, a faster line of constant phase might travel on the ground surface depending on the type of soil, resulting in an approximate slope of unwrapped phase too short. Therefore, the sensors must be placed farther from each other for systems with high phase velocity, so that the two-sensor technique can properly compensate for the phase changes caused by external phenomena.

Since the features for practical application of the two-sensor technique are properly assessed, the next chapters will present a comparison for the performance of the one-sensor and two-sensor techniques on experimental data.

5 EXPERIMENTAL INVESTIGATION OF THE LOCALIZATION TECHNIQUES - MEASUREMENT LINES PERPENDICULAR TO PIPE DIRECTION

5.1 INTRODUCTION

The application of one-sensor and two-sensor techniques was illustrated in Chapter 3, by testing them on the theoretical data extracted from the analytical and numerical models of ground surface vibration due to a leaking buried pipe. The results obtained for both localization techniques in Chapter 3, together with the ones obtained for the investigation of the features for practical application of the two-sensor technique in Chapter 4, motivate the application of both techniques on experimental data to evaluate their performance in the practice.

As discussed in Chapter 3, the two-sensor technique requires that the measurement lines have to be positioned as close as possible to 90° in relation to pipe direction, so that the algorithm can perceive that the pair of sensors has crossed the pipe on ground surface. To check implications of such a consideration on practical applications of the proposed technique, the experimental investigation presented in this thesis is divided into two parts. The first one is to evaluate the performance of the one-sensor and two-sensors techniques when the measurement lines are perpendicular to pipe direction, and the second one is to evaluate their performance when the measurement lines are misaligned with pipe direction.

This chapter presents the results for the first experimental investigation, in which the improvements for the two-sensor technique tracking algorithm are presented first to adapt it for application on experimental data, and a new experimental dataset measured on a test rig situated in São Paulo, Brazil, is introduced. Then, a new investigation similar to the one for the British test rig is performed to evaluate the patterns for vibration amplitude and lines of constant phase on the Brazilian test rig ground surface. At the end of this chapter, the performance of both localization techniques is compared by testing them on the experimental data measured on both test rigs.

5.2 MODIFIED TRACKING ALGORITHM

As presented in Chapter 3, the two-sensor technique tracking algorithm provides the direction for the pair of sensors to cross the pipe on the ground surface. Although its original version works for theoretical data, a more robust approach is necessary for applications on experimental datasets as real measurements contain environmental noise and other external sources. Therefore, depending on the SNR between the ground surface vibration due to a leaking buried pipe and the noise measured by the sensors, determining an exact slope for unwrapped phase, as shown in Figs. 29 and 30, is not possible.

To extract an approximate slope, a line has to be approximated for the values of unwrapped phase. To do so, the tracking algorithm is modified according to the flowchart of Fig. 47, where the signals $x_1(t)$ and $x_2(t)$ are measured by sensors 1 and 2, respectively, and are the algorithm input. The consecutive steps for the modified tracking algorithm are detailed as follows:

1st step: the spectral densities $S_1(\omega)$ and $S_2(\omega)$, and the cross-spectral density $S_{1,2}(\omega)$ are calculated via segment averaging, in which (SHIN; HAMMOND, 2008)

$$S_{1,2}(\omega) = \left|S_{1,2}(\omega)\right| e^{\mathrm{j}\phi_{1,2}(\omega)}, \tag{12}$$

where $\left|S_{1,2}(\omega)\right|$ and $\phi_{1,2}(\omega)$ are the modulus and phase of $S_{1,2}(\omega)$, respectively.

2nd step: the coherence $\gamma_{1,2}^2(\omega)$ is also calculated via segment averaging, in which (SHIN; HAMMOND, 2008)

$$\gamma_{1,2}^2(\omega) = \frac{\left|S_{1,2}(\omega)\right|^2}{S_1(\omega) S_2(\omega)}. \tag{13}$$

3rd step: $\phi_{1,2}(\omega)$ is extracted from $S_{1,2}(\omega)$ and the bandwidth dominated by leak noise content is estimated from $\gamma_{1,2}^2(\omega)$. The limits ω_{low} and ω_{high} of such a bandwidth are determined via a modified version of the algorithm proposed by Almeida (2013). In the modified version, the maximum value of $\gamma_{1,2}^2(\omega)$ is first found for frequencies greater than 10 Hz to neglect low frequency noise. Then, the frequencies ω_{low} and ω_{high} that encompass the maximum value of $\gamma_{1,2}^2(\omega)$ are determined, in which $\gamma_{1,2}^2(\omega_{\mathrm{low}}) \geq 10^{-2}$ and

$\gamma_{1,2}^2(\omega_{\text{high}}) \geq 10^{-2}$, to ensure that the phase $\phi_{1,2}(\omega)$ is properly unwrapped (MUGGLETON; BRENNAN; GAO, 2011).

Figure 47 - Flowchart of the modified tracking algorithm.

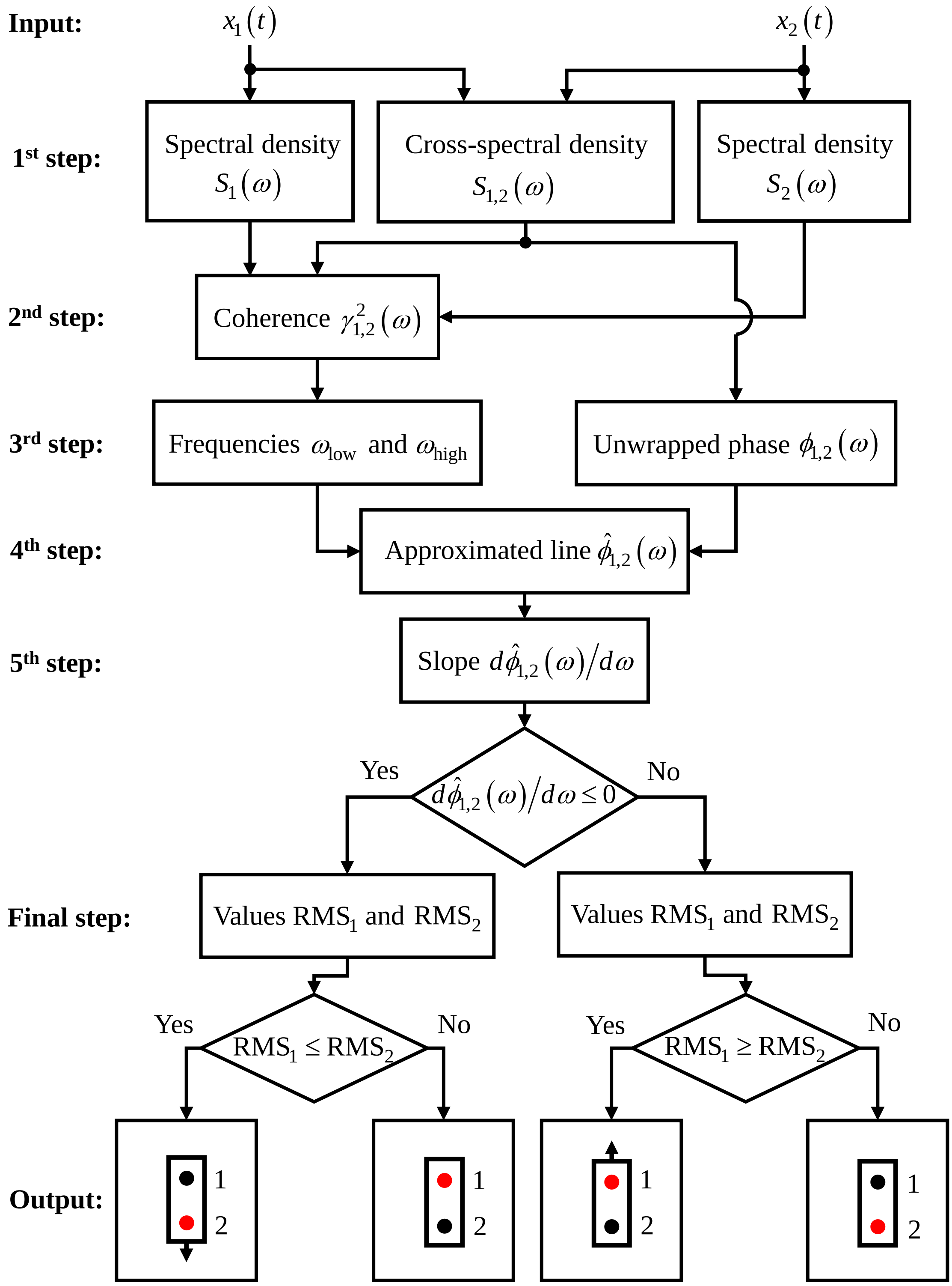

Source: elaborated by the author.

4th step: the line $\hat{\phi}_{1,2}(\omega)$ is determined for values of $\phi_{1,2}(\omega)$ between ω_{low} and ω_{high} via least squares fit, and the offset of $\hat{\phi}_{1,2}(\omega)$ is removed so that $\hat{\phi}_{1,2}(\omega)=0$ when $\omega=0$ (ALMEIDA, 2013).

5th step: the slope $d\hat{\phi}_{1,2}(\omega)/d\omega$ is extracted from $\hat{\phi}_{1,2}(\omega)$.

Final step: the values RMS_1 and RMS_2 are calculated for signals $x_1(t)$ and $x_2(t)$, respectively, and the sensor that contains the highest RMS value for the pair is shown in red, as illustrated in Fig. 47.

The approximate slope $d\hat{\phi}_{1,2}(\omega)/d\omega$ resulting from the modified tracking algorithm is used to locate the pipe and the leak as illustrated in Figs. 29 and 30, respectively. Substituting $d\phi_{1,2}(\omega)/d\omega$ for $d\hat{\phi}_{1,2}(\omega)/d\omega$ in the theory presented in Subsection 3.3.1, the direction pointed by the modified tracking algorithm results from the comparison between the direction informed by amplitude, and the direction informed by phase of the pair of sensors as follows:

- If $d\hat{\phi}_{1,2}(\omega)/d\omega \le 0$ and $\text{RMS}_1 \le \text{RMS}_2$, the algorithm points to the side of sensor 2.
- If $d\hat{\phi}_{1,2}(\omega)/d\omega > 0$ and $\text{RMS}_1 \ge \text{RMS}_2$, the algorithm points to the side of sensor 1.
- Otherwise, the algorithm does not point to any side.

5.3 TEST RIGS AND DESCRIPTION OF EXPERIMENTAL DATA

The one-sensor technique and the two-sensor technique, with the modified tracking algorithm, are tested with the experimental data measured on the British test rig presented in Chapter 2, and on the Brazilian test rig presented in this chapter. The schematic diagram and experimental setup for the Brazilian test rig are shown in Fig. 48.

Figure 48 - Brazilian test rig and experimental setup. (a) Overview of the test rig showing the measurement grid location (not to scale), (b) photograph showing the experimental setup, and (c) schematic diagram for the measurement grid showing the corresponding coordinate system and distances (not to scale).

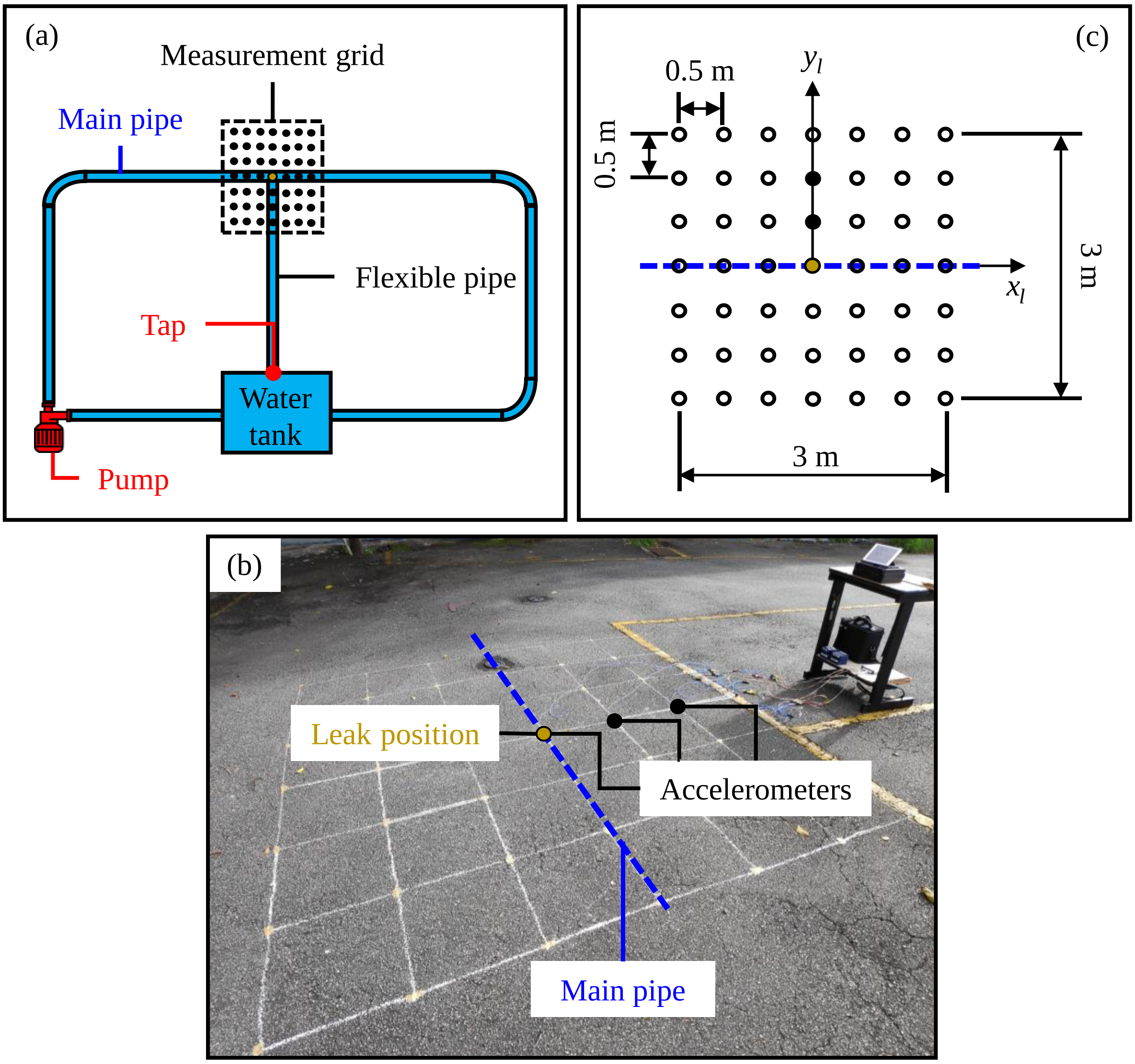

Source: elaborated by the author.

The respective pipe network is a closed circuit pressurized by a centrifugal pump, in which the leak is created through a hole in the main pipe and a portion of the waterflow is drained by a flexible pipe connected at the leak position, as shown in Fig. 48(a). A tap is attached to the other end of the flexible pipe, so that the drained water can be returned to a water tank and the leak strength controlled by opening/closing such a tap. The experiment was performed with 3 PCB 333B40 accelerometers and an LMS SCADAS data acquisition system, as shown in Fig. 48(b). The same coordinate system adopted for the British test rig is also adopted for the Brazilian test rig, in which the origin corresponds to the leak position as shown in Fig. 48(c). During the measurements, one accelerometer remained fixed at the leak position and the other two were placed 0.5 m apart for both directions in sorted positions, resulting in a squared measurement grid with sides 3 m. The measurements consist of 60 s long acceleration time histories, sampled at a frequency of 12.8 kHz.

As carried out for the British test rig, the patterns of vibration amplitude and lines of constant phase on the Brazilian test rig ground surface are also investigated. Such an experimental analysis supports the discussion on the performance of both localization techniques. To do so, the contour maps for RMS values and for spatially unwrapped phase of the Brazilian test rig are plotted. To extract the unwrapped phase, the cross-spectral density between each roving accelerometer and the one fixed at the leak position was calculated with 12,800-point fast Fourier transform and a Hanning window with 50% overlap, resulting in a frequency resolution of 1 Hz. Then, the phase of cross-spectral density was spatially unwrapped with the algorithm of Herráez *et al*. (2002), to present the lines of constant phase traveling on the ground surface.

The contour maps for the British and Brazilian test rigs are presented in Fig. 49. Specifically, the contour maps for RMS values, and spatially unwrapped phase for a frequency of 45 Hz are shown in Figs. 49(a.i) and 49(a.ii) for the British test rig, respectively, and the contour maps for RMS values, and spatially unwrapped phase for a frequency of 200 Hz are shown in Figs. 49(b.i) and 49(b.ii) for the Brazilian test rig, respectively. Note that the contour maps of Figs. 49(a.i) and 49(a.ii) are the same ones shown in Figs. 25(c) and 26(c) of Chapter 2, and are presented again in this chapter for convenience.

As explained in Section 2.5.3, each particular frequency was selected to present the contour map for spatially unwrapped phase for each test rig, because the respective leak position was found to be more evident on such frequencies and to prevent spatial aliasing as well. Note in Eq. (11), that the contour map for spatially unwrapped phase can be shown for the British test rig up to approximately 116 Hz, due to the spatial interval of 0.5 m and a shear wave speed of approximately 116 m/s. For the Brazilian test rig, the same contour map can be shown up to approximately 220 Hz, due to the spatial interval of 0.5 m and a shear wave speed of approximately 220 m/s (SCUSSEL, 2019).

Figure 49 - Contour maps for vertical ground surface vibration measured on the British and Brazilian test rigs. (a.i) Normalized RMS values and (a.ii) spatially unwrapped phase for a frequency of 45 Hz for the British test rig. (a.i) Normalized RMS values and (a.ii) spatially unwrapped phase for a frequency of 200 Hz for the Brazilian test rig. The dashed blue lines correspond to the buried pipe.

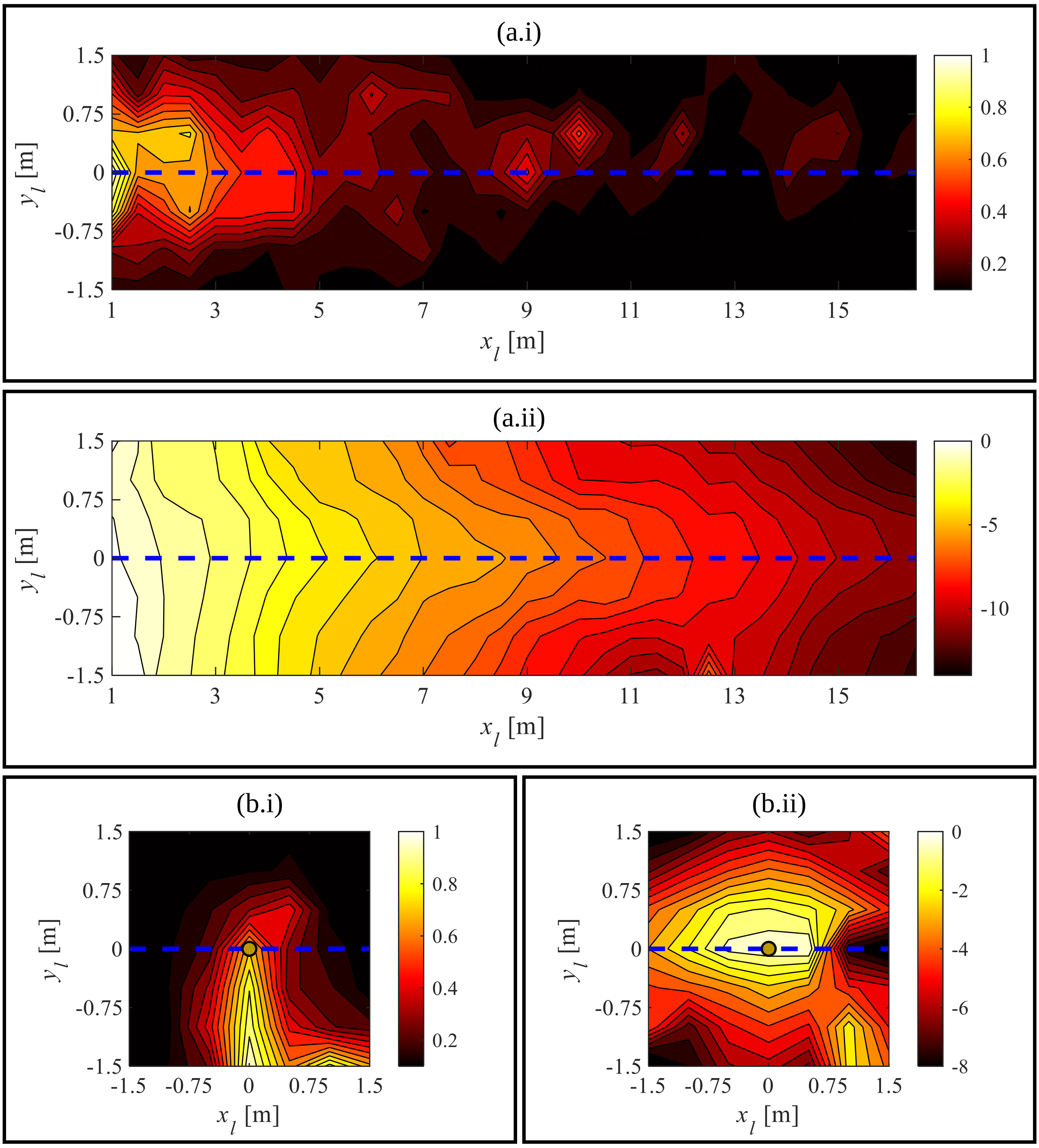

Source: elaborated by the author.

By comparing the results for the British and Brazilian test rigs shown in Figs. 49(a.i) and 49(b.i), respectively, a different pattern is observed between the contour maps for RMS values. As discussed in Subsection 2.5.3, the amplitude is higher for positions close to the leak (x_l = 0 m, y_l = 0 m) along the x_l-axis of the British test rig. However, for the Brazilian test rig, the amplitude is higher for positions along the y_l-axis towards the tap position (x_l = 0 m, y_l = -1.5 m). This difference is probably due to the different leak mechanisms that excites the main pipe of each test rig, where a rigid standpipe with no contact with the soil is used for the British test rig and a buried flexible pipe is used for the Brazilian test rig. By analyzing Figs. 48(a) and 49(b.i), the flexible pipe is probably excited by the strong jet from the tap located in the water tank. The amplitude of the waves that radiate from the flexible pipe is much higher than the amplitude of the ones that radiate from the main pipe, where the leak position is actually located in the test rig. Therefore, this comparison suggests that further research on mechanisms that can effectively replicate leak excitation is necessary, though it is beyond the scope of this thesis.

By comparing the contour maps of Figs. 49(a.ii) and 49(b.ii), a different pattern is also observed for the spatially unwrapped phase measured on the British and Brazilian test rigs. As discussed for the British test rig in Subsection 2.5.3, from 1 m up to approximately 3 m along the x_l-axis of Fig. 49(a.ii), the lines of constant phase have approximated circular pattern due to the spherical waves that propagate from the source (leak), and for distances longer than 3 m along the same axis, approximate hyperbolas of constant phase propagate on the ground surface due to the conical waves that radiate from the pipe. For the Brazilian test rig, however, the lines of constant phase only have approximated circular pattern because the measurement grid is much minor than the one for the British test rig, and the leak position is located at the middle.

Note for the contour maps for the Brazilian test rig that, although the amplitude of the waves that radiate from the main pipe and the leak are extremely low in relation to the amplitude of the ones that radiate from the flexible pipe, the sensors still capture circles of constant phase due to the spherical waves that radiate from the leak position in the main pipe, as can be seen in Fig. 49(b.ii). Therefore, this result indicates that phase is more reliable than amplitude of ground surface vibration to extract the indication of leak position for this situation.

5.4 APPLICATION OF LOCALIZATION TECHNIQUES ON THE EXPERIMENTAL DATA

The performance of the two-sensor technique in relation to the one-sensor technique is evaluated in this section, by applying them separately on the experimental data collected on the British and Brazilian test rigs. Both techniques are used to locate the main pipe of the British test rig, as the corresponding leak position is outside the measurement grid, and to locate the main pipe and leak of the Brazilian test rig, as the corresponding leak position is inside the measurement grid. The experimental data of each test rig is arranged in measurement lines to allow application of both localization techniques. Then, they are applied individually to mark the pipe and leak position estimates for each measurement line as explained in Chapter 3. Once estimates are done for all measurement lines, the pipe and leak regions are circumscribed on the ground surface by tracing the horizontal and vertical lines in relation to the pipe direction, passing through most of the marks in each application.

5.4.1 Results for the British test rig

The British test rig experimental data is divided into 3 zones, named A, B and C as shown in Fig. 50, to evaluate the performance of both techniques for different distances in relation to leak position along the pipe. The first measurement line of zones A, B and C are at 1 m, 7 m and 13 m away from the leak position, respectively. The corresponding 2nd and 3rd measurement lines are 1 m apart from each other along x_l-axis, and the position of the sensors are at -1.5 m, -0.5 m, 0.5 m and 1.5 m along each measurement line as illustrated in Fig. 50.

Figure 50 - Schematic diagram for measurement lines of the British test rig.

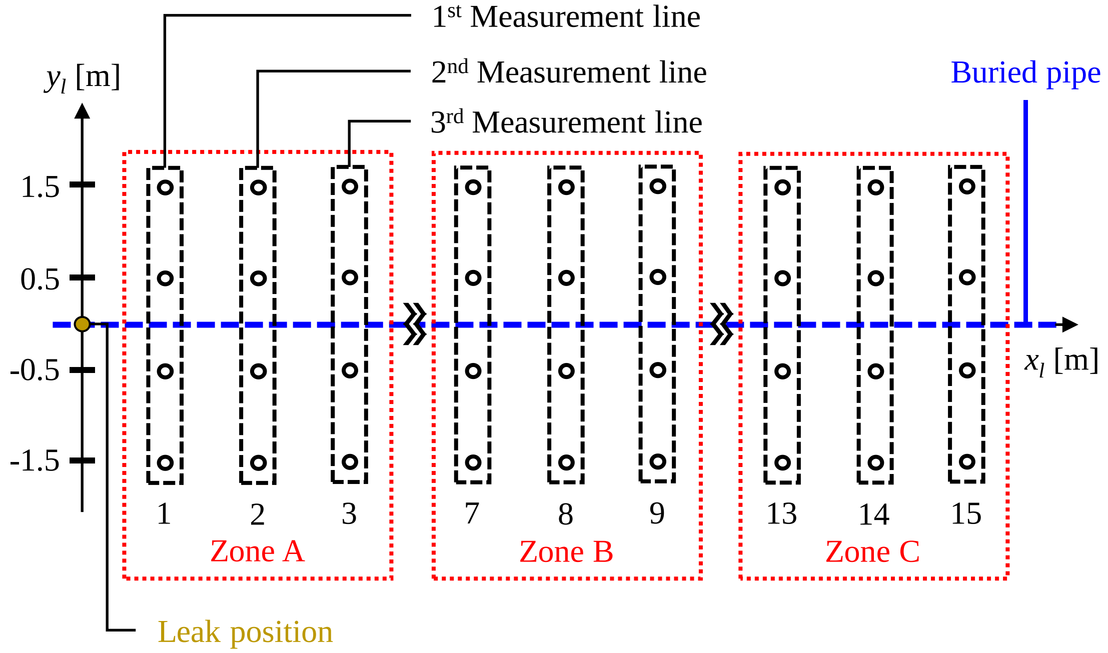

Source: elaborated by the author.

As discussed for the experimental results in Chapter 2, environmental noise becomes more dominant for longer distances in relation to the leak position due to geometrical spreading and attenuation experienced by waves that propagate in the soil. Therefore, the localization techniques are more likely to fail when applied on measurement positions relatively distant from the leak, because SNR between the ground surface vibration due to the leaking buried pipe, and the environmental noise decreases with distance. To focus the analysis on this kind of extreme condition, the results for pipe localization with the two-sensor technique on each measurement line of zone C are presented in this chapter, as it is the farthest zone from the leak position. The results for the two-sensor technique applied on each measurement line of zones A and B are presented separately in Appendix B.

The RMS velocities for each British test rig measurement line are tabulated in Tab. 4. The values highlighted in each column indicate the pair of positions which contains the highest pair of RMS values for each measurement line shown in Fig. 50. Note that the results of Tab. 4 are consistent with the contour map of Fig. 49(a.i), where RMS values are higher for positions close to the leak along the x_l-axis. For positions farther from the leak in which zones B and C are situated, the difference for RMS values in Tab. 4 decreases significantly along y_l-axis, and the algorithm fails to select the pair of positions that embraces the buried pipe.

Table 4 - RMS velocities [$\times 10^{-6}$ m/s] for measurement lines of the British test rig, shown in Fig. 50.

		x_l [m]								
		1	**2**	**3**	**7**	**8**	**9**	**13**	**14**	**15**
y_l [m]	**1.5**	2.00	2.38	1.78	1.43	0.82	1.05	1.92	1.12	1.08
	0.5	6.18	6.43	4.30	1.54	1.98	2.77	1.34	1.69	2.42
	-0.5	7.25	4.63	4.39	1.32	1.78	1.85	0.59	1.66	1.04
	-1.5	1.64	1.41	1.16	0.82	0.84	0.68	0.38	0.47	1.01

Source: elaborated by the author.

The results for pipe localization with the two-sensor technique applied on 1st, 2nd and 3rd measurement lines of zone C are shown in Figs. 51, 52 and 53, respectively, in which the green-shaded areas represent the bandwidth in which $\hat{\phi}_{1,2}(\omega)$ is approximated via least square fit with the modified tracking algorithm. As can be seen in the coherences of Figs. 51(b.i-iii), 52(b.i-iii) and 53(b.i-iii), the leak noise content is predominantly comprehended between approximately 10 and 250 Hz, where the approximated line $\hat{\phi}_{1,2}(\omega)$ captures a clear tendency for the slope of unwrapped phase as shown in Figs. 51(c.i-iii), 52(c.i-iii) and 53(c.i-iii).

Figure 51 - Pipe localization with the two-sensor technique applied on 1st measurement line of zone C of the British test rig. (a.i-iii) 1st, 2nd and 3rd positions of the pair of sensors, (b.i-iii) coherence $\gamma_{1,2}^2(\omega)$ for 1st, 2nd and 3rd positions, (c.i-iii) unwrapped phase $\phi_{1,2}(\omega)$ and approximated line $\hat{\phi}_{1,2}(\omega)$ for 1st, 2nd and 3rd positions, where the solid black line corresponds to $\phi_{1,2}(\omega)$ and the dashed red line corresponds to $\hat{\phi}_{1,2}(\omega)$, and (a.iv) estimate of pipe localization. The dashed blue lines correspond to the buried pipe.

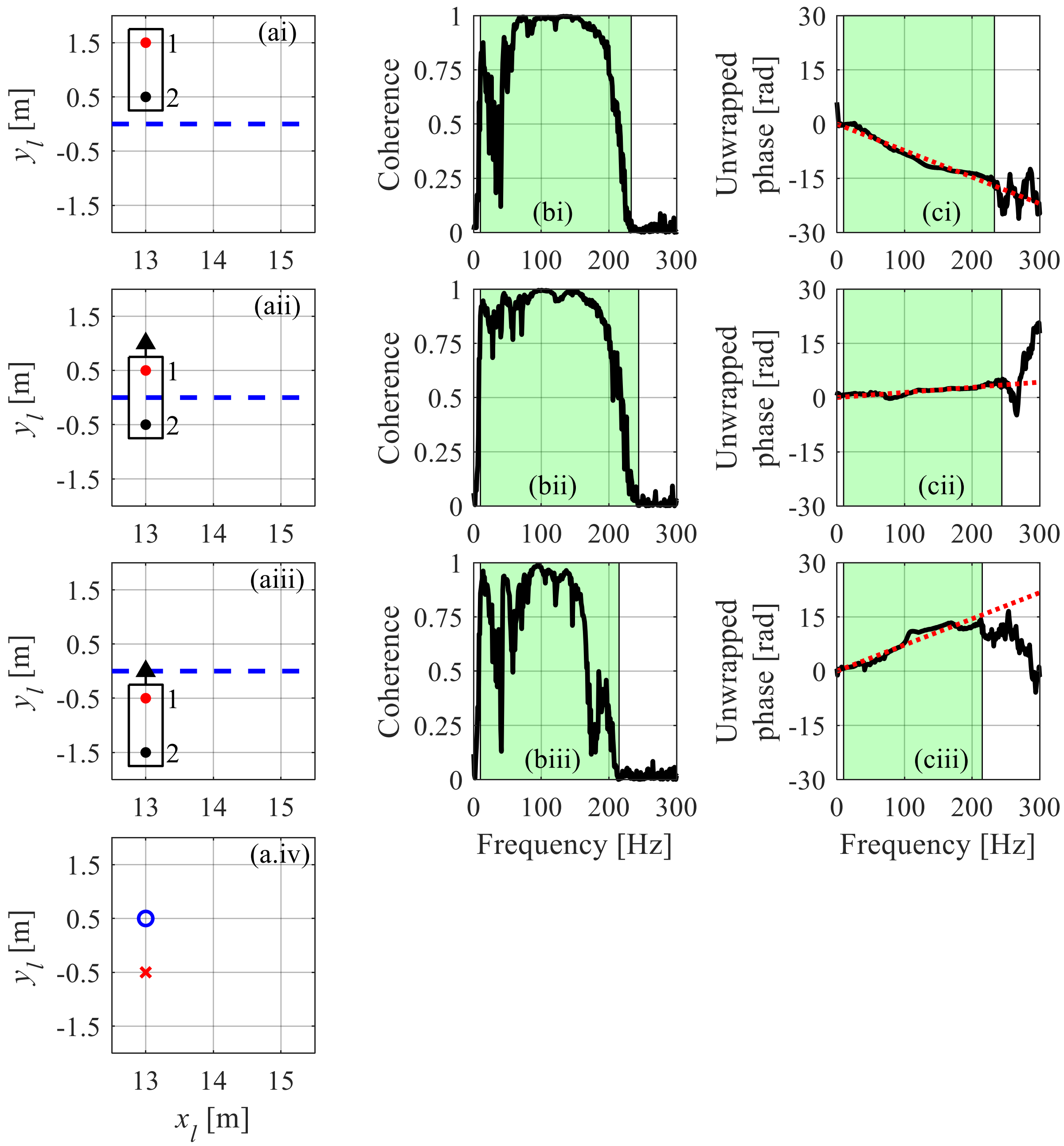

Source: elaborated by the author.

Figure 52 - Pipe localization with the two-sensor technique applied on 2nd measurement line of zone C of the British test rig. (a.i-iii) 1st, 2nd and 3rd positions of the pair of sensors, (b.i-iii) coherence $\gamma_{1,2}^2(\omega)$ for 1st, 2nd and 3rd positions, (c.i-iii) unwrapped phase $\phi_{1,2}(\omega)$ and approximated line $\hat{\phi}_{1,2}(\omega)$ for 1st, 2nd and 3rd positions, where the solid black line corresponds to $\phi_{1,2}(\omega)$ and the dashed red line corresponds to $\hat{\phi}_{1,2}(\omega)$, and (a.iv) estimate of pipe localization. The dashed blue lines correspond to the buried pipe.

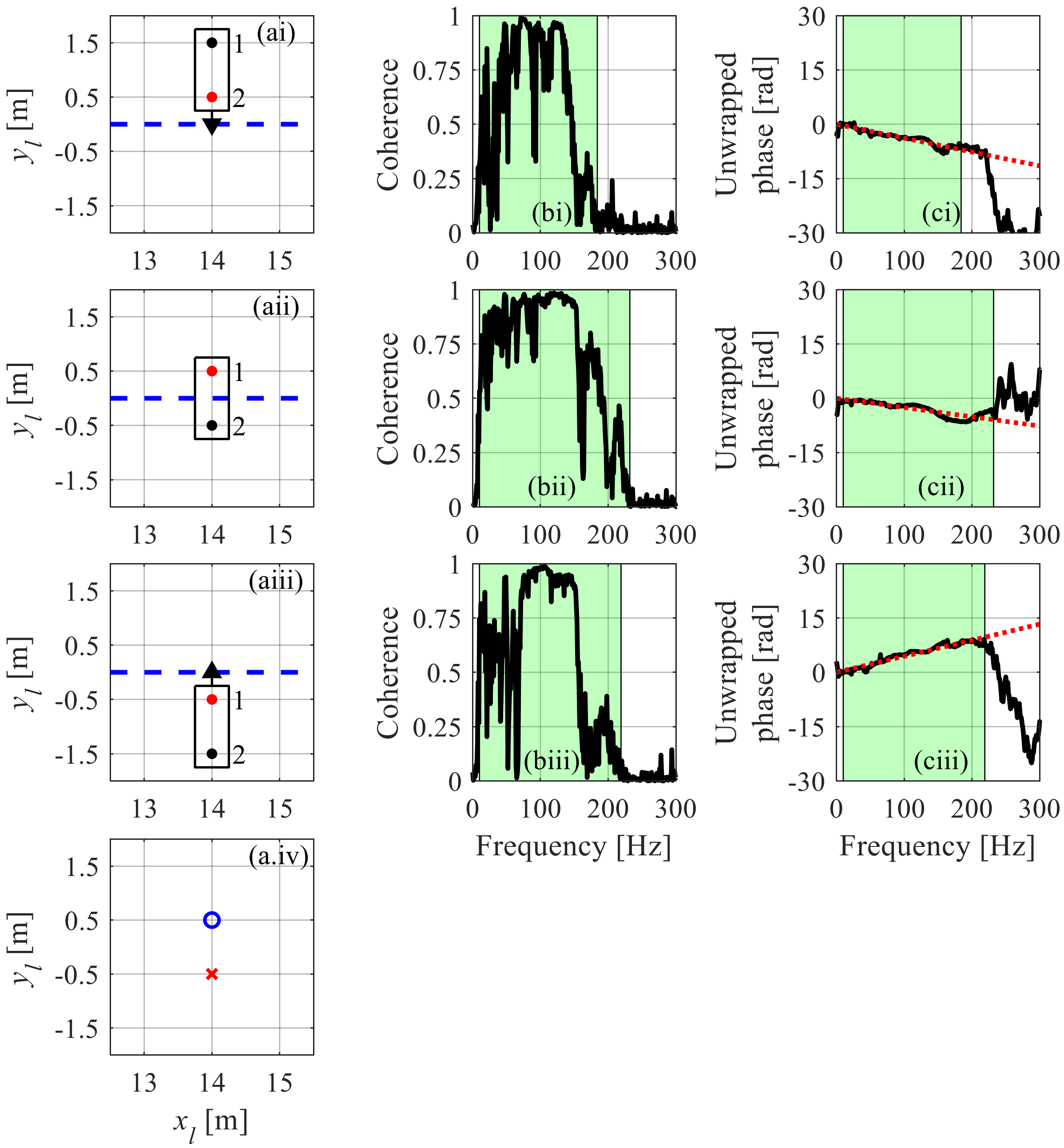

Source: elaborated by the author.

Figure 53 - Pipe localization with the two-sensor technique applied on 3rd measurement line of zone C of the British test rig. (a.i-iii) 1st, 2nd and 3rd positions of the pair of sensors, (b.i-iii) coherence $\gamma_{1,2}^{2}(\omega)$ for 1st, 2nd and 3rd positions, (c.i-iii) unwrapped phase $\phi_{1,2}(\omega)$ and approximated line $\hat{\phi}_{1,2}(\omega)$ for 1st, 2nd and 3rd positions, where the solid black line corresponds to $\phi_{1,2}(\omega)$ and the dashed red line corresponds to $\hat{\phi}_{1,2}(\omega)$, and (a.iv) estimate of pipe localization. The dashed blue lines correspond to the buried pipe.

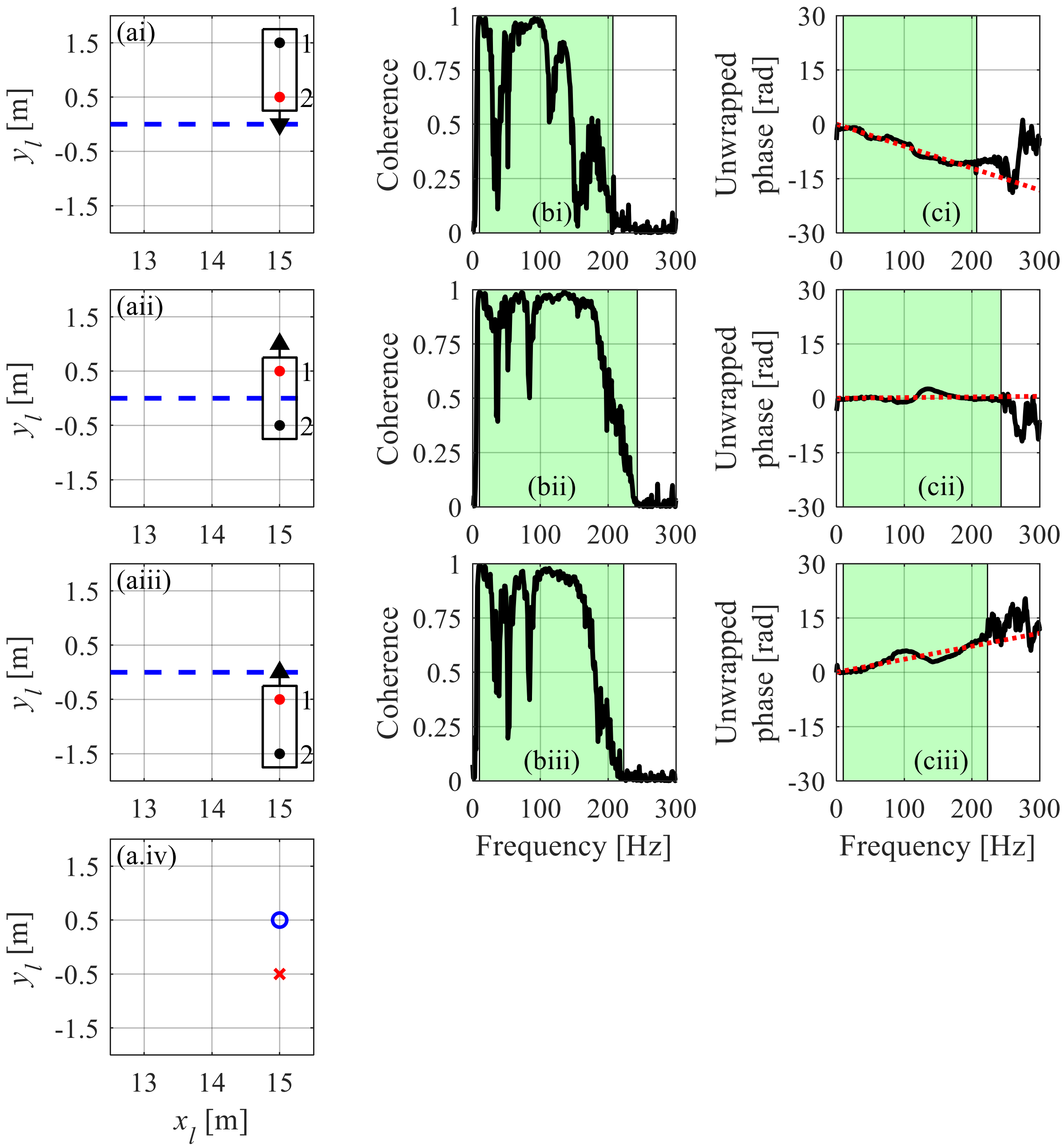

Source: elaborated by the author.

Note that $d\hat{\phi}_{1,2}(\omega)/d\omega < 0$, $d\hat{\phi}_{1,2}(\omega)/d\omega > 0$ and $d\hat{\phi}_{1,2}(\omega)/d\omega > 0$ for the 1st, 2nd and 3rd positions in Figs. 51(c.i-iii), respectively; $d\hat{\phi}_{1,2}(\omega)/d\omega < 0$, $d\hat{\phi}_{1,2}(\omega)/d\omega < 0$ and $d\hat{\phi}_{1,2}(\omega)/d\omega > 0$ for the 1st, 2nd and 3rd positions in Figs. 52(c.i-iii), respectively; and $d\hat{\phi}_{1,2}(\omega)/d\omega < 0$, $d\hat{\phi}_{1,2}(\omega)/d\omega > 0$ and $d\hat{\phi}_{1,2}(\omega)/d\omega > 0$ for the 1st, 2nd and 3rd positions in Figs. 53(c.i-iii), respectively. Therefore, the two-sensor technique algorithm detects the sign of $d\hat{\phi}_{1,2}(\omega)/d\omega$ changes between the 1st and 3rd positions for all measurement lines of zone C, and marks the 2nd one as shown in Figs. 51(a.iv), 52(a.iv) and 53(a.iv), since the corresponding $d\hat{\phi}_{1,2}(\omega)/d\omega$ is closer to zero. Note that these results are consistent with the theory presented in Fig. 29 and also with the contour map of Fig. 49(a.ii), as all of them indicates that the time difference between the signals measured by the pair of sensors tends to zero, when it is equidistant from the buried pipe on the ground surface.

Figure 54 - Results for pipe localization with (a.i-iii) one-sensor and (b.i-iii) two-sensor techniques applied on zones A, B and C of the British test rig. The dashed blue lines correspond to the buried pipe.

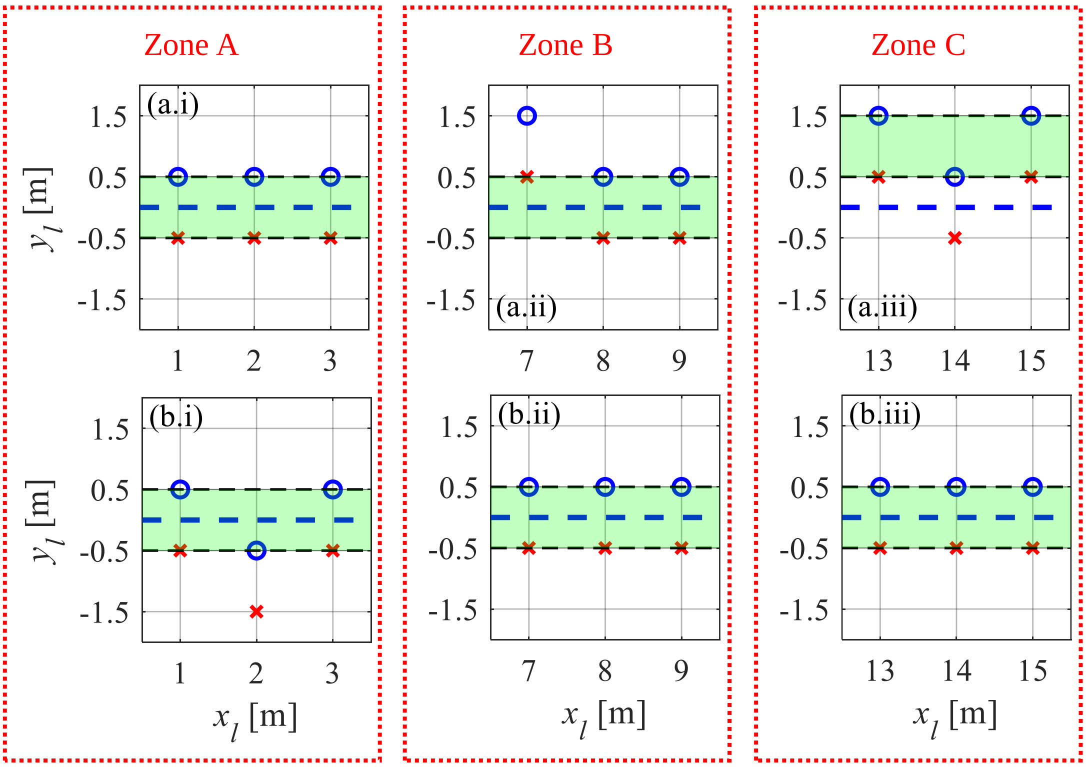

Source: elaborated by the author.

The results for pipe localization applied on regions A, B and C of the British test rig are presented in Fig. 54. Each pair of marks in Figs. 54(a.i-iii) corresponds to the estimate of pipe localization with the one-sensor technique applied on each measurement line, as indicated by the values highlighted in Tab. 4. Each pair of marks in Figs. 54(b.i-iii) corresponds to the estimate of pipe localization with two-sensor technique applied on each measurement line. Note that the estimates of pipe localization for the measurement lines of zone C, shown in Figs. 51(a.iv), 52(a.iv) and 53(a.iv), are grouped together in Fig. 54(b.iii). Similarly, the estimates of pipe localization for the measurement lines of zones A and B, presented in Appendix B, are grouped together in Figs. 54(b.i) and 54(b.ii), respectively. The pipe region for each zone is determined by tracing two lines parallel to the pipe direction, in which one passes through most of the blue-circle marks and the other passes through most of the red-cross marks. As it can be seen in Figs. 54(a.i-iii), the one-sensor technique estimates correctly for zones A and B, and fails for zone C. The two-sensor technique, however, correctly estimates the pipe location for all zones of the British test rig as shown in Figs. 54(b.i-iii). Such a difference between the performance of both techniques is consistent with the discussion provided by Muggleton, Brennan and Gao (2011), where unwrapped phase is less affected by uncorrelated noise than amplitude. Therefore, the two-sensor technique is more suitable for positions farther from the leak on the ground surface than the one-sensor technique, as environmental noise becomes more dominant in such conditions.

5.4.2 Results for application on the Brazilian test rig

The performance of both localization techniques is tested on a single zone of the Brazilian test rig, whose 1st measurement line is at -1.5 m away from the leak position. The corresponding 2nd and 3rd measurement lines are 1 m apart from each other along the x_l -axis, and the position of the sensors are at -1.5 m, -0.5 m, 0.5 m and 1.5 m along each measurement line as illustrated in Fig. 55.

Figure 55 - Schematic diagram for measurement lines of the Brazilian test rig.

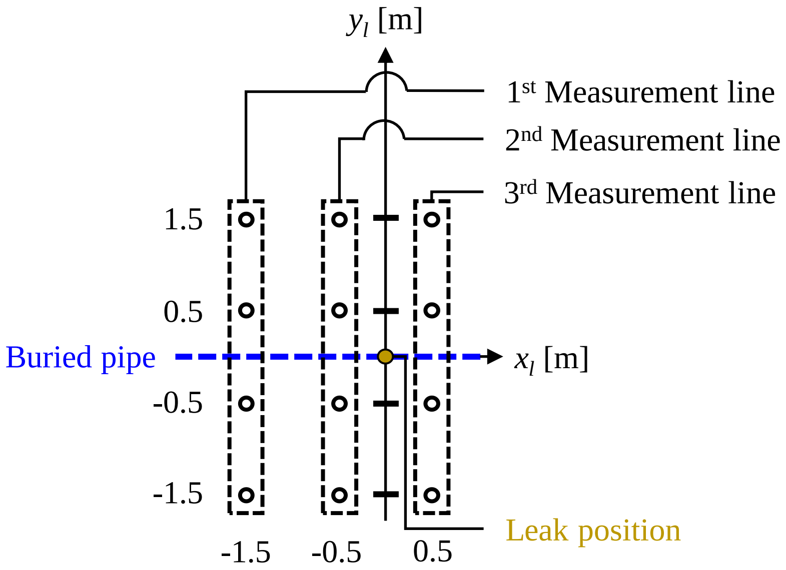

Source: elaborated by the author.

For the application of both localization techniques, the flexible pipe is assumed to be a high-level source of noise in the experiment, since the main pipe is the one that actually contains the leak in the test rig as discussed in Section 5.3. The RMS accelerations for each Brazilian test rig measurement line are tabulated in Tab. 5, following the same arrangement adopted for Tab. 4. The values highlighted in each column indicate the pair of positions which contains the highest pair of RMS values for each measurement line shown in Fig. 55. Note that the results of Tab. 5 are also consistent with the contour map of Fig. 49(b.i), where RMS values are higher for positions along the y_l-axis towards the tap position (x_l = 0 m, y_l = -1.5 m). Hence, the algorithm fails to select the pair of positions that encompasses the main pipe for all measurement lines.

Table 5 - RMS accelerations [$\times 10^{-4}$ m/s^2] for measurement lines of the Brazilian test rig, shown in Fig. 55.

		x_l [m]		
		-1.5	**-0.5**	**0.5**
y_l [m]	**1.5**	0.64	0.89	0.96
	0.5	0.60	1.43	3.25
	-0.5	0.67	2.55	2.10
	-1.5	0.72	2.04	4.52

Source: elaborated by the author.

The pipe localization with the two-sensor technique applied on 1st, 2nd and 3rd measurement lines of the Brazilian test rig are shown in Figs. 56, 57 and 58, respectively, following the same arrangement adopted for Figs. 56, 57 and 58. Unlike the results for the British test rig, the coherence and bandwidth of leak noise content for the Brazilian test rig are quite sensitive to measurement positions on the ground surface in relation to the leak. As can be seen in Figs. 56(b.i-iii), 57(b.i-iii) and 58(b.i-iii), the bandwidth of leak noise content for positions of measurement lines close to the leak ($|x_l| < 1$ m) is much wider than the one for positions farther from the leak; and the coherence for positions of measurement lines close to the leak is much greater than the one for positions farther from the leak. These are indications that the vibration measured on the ground surface due to the leak (source) is predominant in relation to the vibration due to the main pipe (note that the bandwidth of leak noise content for zone C of the British test rig is practically invariant for different positions of the measurement line along x_l-axis). Therefore, for this particular test rig, it is expected that the two-sensor technique will fail to locate the main pipe if measurement lines are relatively distant from the leak position, as they are in the investigation carried out on the British test rig. The reasons for such a limitation will be discussed later in next chapter.

Figure 56 - Pipe localization with the two-sensor technique applied on 1st measurement line of the Brazilian test rig. (a.i-iii) 1st, 2nd and 3rd positions of the pair of sensors, (b.i-iii) coherence $\gamma_{1,2}^2(\omega)$ for 1st, 2nd and 3rd positions, (c.i-iii) unwrapped phase $\phi_{1,2}(\omega)$ and approximated line $\hat{\phi}_{1,2}(\omega)$ for 1st, 2nd and 3rd positions, where the solid black line corresponds to $\phi_{1,2}(\omega)$ and the dashed red line corresponds to $\hat{\phi}_{1,2}(\omega)$, and (a.iv) estimate of pipe localization. The dashed blue lines correspond to the buried pipe and the dark yellow dots correspond to the leak position.

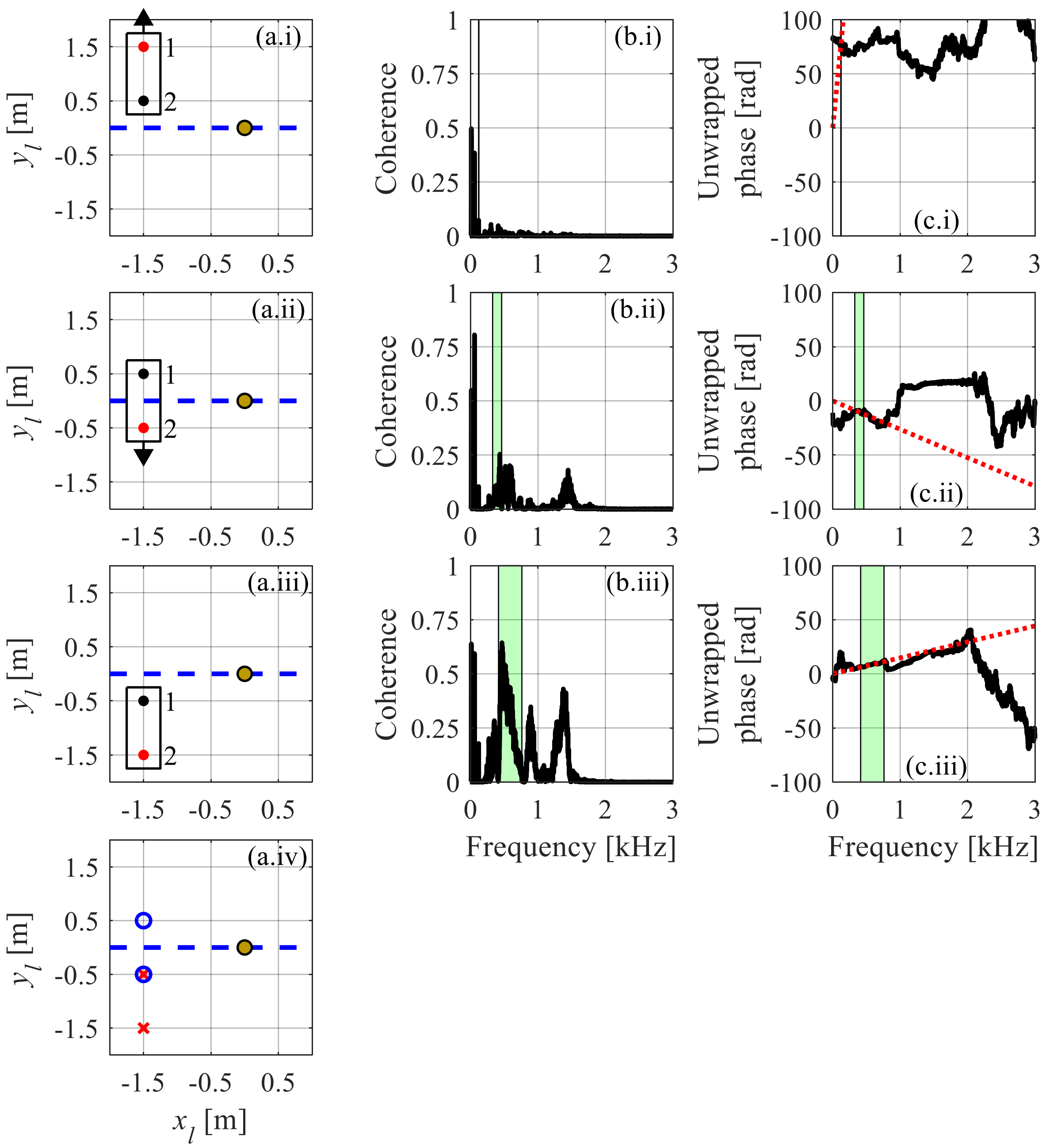

Source: elaborated by the author.

Figure 57 - Pipe localization with the two-sensor technique applied on 2nd measurement line of the Brazilian test rig. (a.i-iii) 1st, 2nd and 3rd positions of the pair of sensors, (b.i-iii) coherence $\gamma_{1,2}^{2}(\omega)$ for 1st, 2nd and 3rd positions, (c.i-iii) unwrapped phase $\phi_{1,2}(\omega)$ and approximated line $\hat{\phi}_{1,2}(\omega)$ for 1st, 2nd and 3rd positions, where the solid black line corresponds to $\phi_{1,2}(\omega)$ and the dashed red line corresponds to $\hat{\phi}_{1,2}(\omega)$, and (a.iv) estimate of pipe localization. The dashed blue lines correspond to the buried pipe and the dark yellow dots correspond to the leak position.

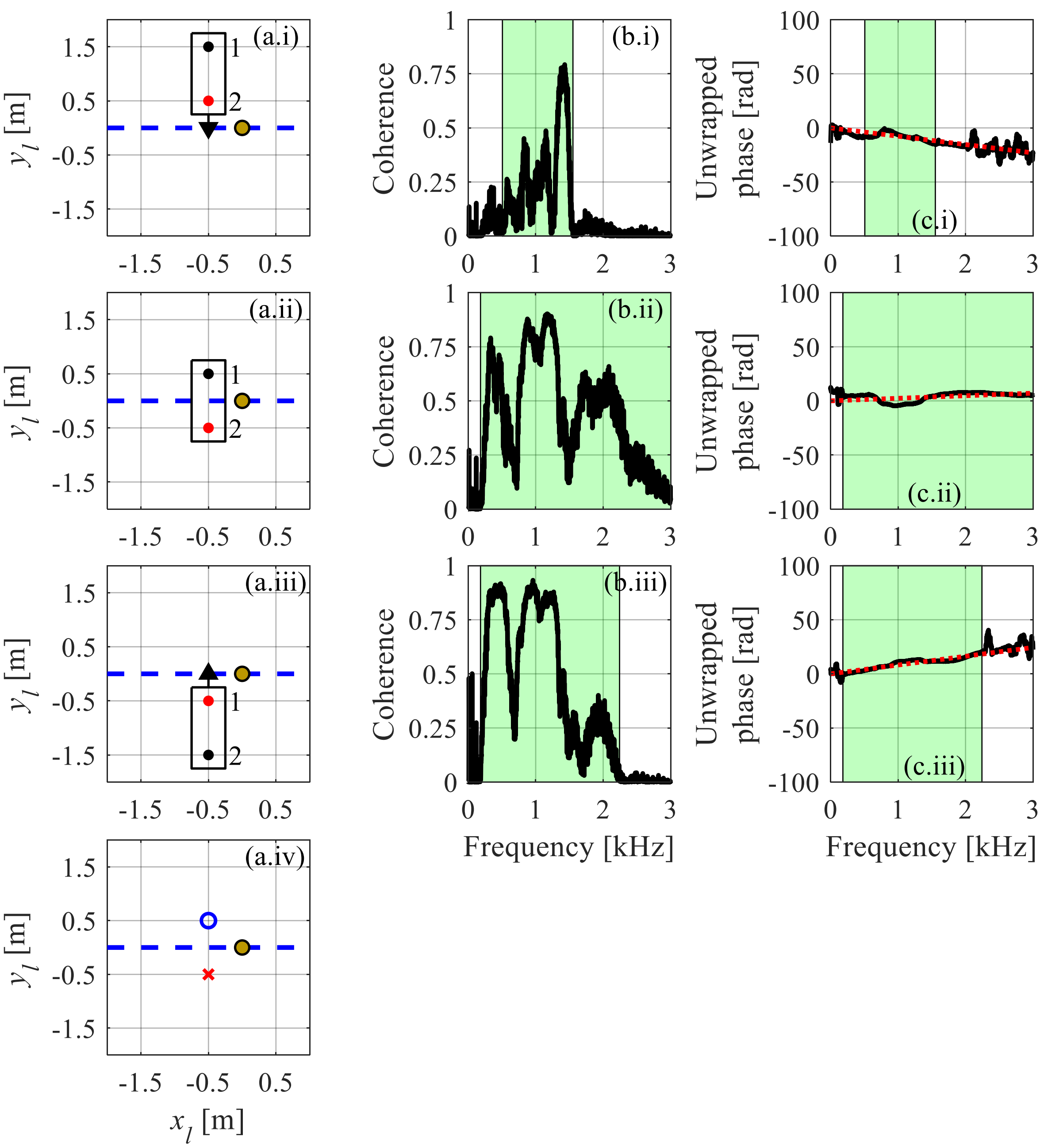

Source: elaborated by the author.

Figure 58 - Pipe localization with the two-sensor technique applied on 3rd measurement line of the Brazilian test rig. (a.i-iii) 1st, 2nd and 3rd positions of the pair of sensors, (b.i-iii) coherence $\gamma_{1,2}^{2}(\omega)$ for 1st, 2nd and 3rd positions, (c.i-iii) unwrapped phase $\phi_{1,2}(\omega)$ and approximated line $\hat{\phi}_{1,2}(\omega)$ for 1st, 2nd and 3rd positions, where the solid black line corresponds to $\phi_{1,2}(\omega)$ and the dashed red line corresponds to $\hat{\phi}_{1,2}(\omega)$, and (a.iv) estimate of pipe localization. The dashed blue lines correspond to the buried pipe and the dark yellow dots correspond to the leak position.

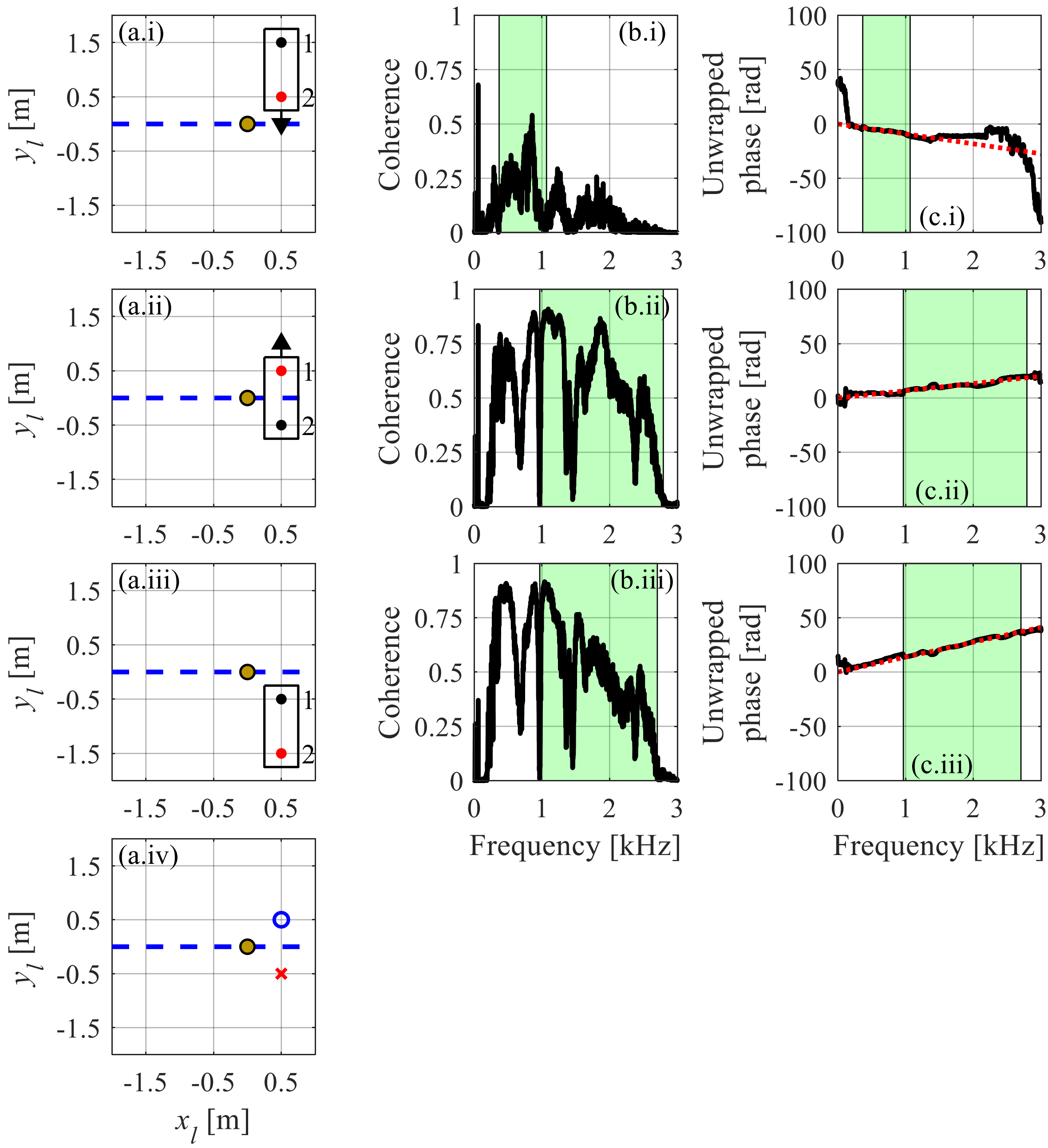

Source: elaborated by the author.

Note in Figs. 56(c.i-iii), that $d\hat{\phi}_{1,2}(\omega)/d\omega > 0$, $d\hat{\phi}_{1,2}(\omega)/d\omega < 0$ and $d\hat{\phi}_{1,2}(\omega)/d\omega > 0$ for the 1st, 2nd and 3rd positions, respectively, of the 1st measurement line. The two-sensor technique algorithm detects the sign of $d\hat{\phi}_{1,2}(\omega)/d\omega$ changes between the 1st and 2nd positions, and between the 2nd and 3rd positions. Since the sign of $d\hat{\phi}_{1,2}(\omega)/d\omega$ changes twice along the measurement line, the algorithm marks the 2nd and 3rd positions as shown in Fig. 56(a.iv). In Figs. 57(c.i-iii) and 58(c.i-iii), $d\hat{\phi}_{1,2}(\omega)/d\omega < 0$, $d\hat{\phi}_{1,2}(\omega)/d\omega > 0$ and $d\hat{\phi}_{1,2}(\omega)/d\omega > 0$ for the 1st, 2nd and 3rd positions, respectively, of the 2nd and 3rd measurement lines. The algorithm detects the sign of $d\hat{\phi}_{1,2}(\omega)/d\omega$ changes between the 1st and 3rd positions and marks the 2nd one as shown in Figs. 57(a.iv) and 58(a.iv), since the corresponding $d\hat{\phi}_{1,2}(\omega)/d\omega$ is closer to zero.

The results for pipe localization applied on the Brazilian test rig are presented in Fig. 59. Each pair of marks in Fig. 59(a) corresponds to the estimate of pipe localization with the one-sensor technique applied on each measurement line, as indicated by the values highlighted in Tab. 5. In Fig. 59(b), each pair of marks corresponds to the estimate of pipe localization with the two-sensor technique applied on each measurement line. The estimates for measurement lines of the Brazilian test rig, shown in Figs. 56(a.iv), 57(a.iv) and 58(a.iv), are grouped together in Fig. 59(b). Note that the one-sensor technique fails to estimate the pipe location, while the two-sensor technique correctly estimates it for the Brazilian test rig.

Figure 59 - Results for pipe localization with (a) one-sensor and (b) two-sensor techniques applied on the Brazilian test rig. The dashed blue lines correspond to the buried pipe and the dark yellow dots correspond to the leak position.

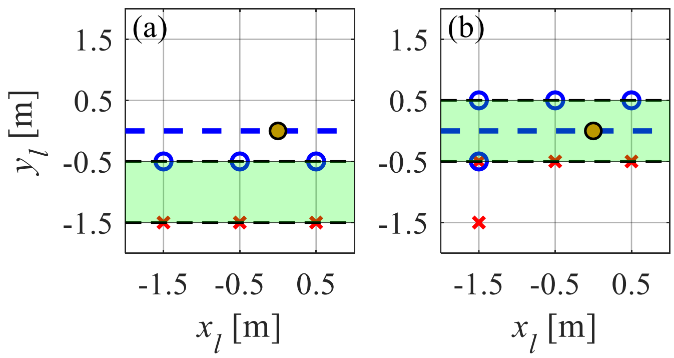

Source: elaborated by the author.

Once the pipe region is determined, the localization techniques are used to elaborate the leak region for the Brazilian test rig, in which the pair of sensors is moved along the pipe region on the positions -1.5 m, -0.5 m and 0.5 m. The leak localization with two-sensor technique applied on the Brazilian test rig is shown in Fig. 60, where the 1st and 2nd positions of the pair of sensors are shown in Figs. 60(a.i-ii), respectively, the coherence $\gamma_{1,2}^2(\omega)$ for the 1st and 2nd positions is shown in Figs. 60(b.i-ii), respectively, and the unwrapped phase $\phi_{1,2}(\omega)$ with the approximated line $\hat{\phi}_{1,2}(\omega)$ for the 1st and 2nd positions are shown in Figs. 60(c.i-ii), respectively. Note that $d\hat{\phi}_{1,2}(\omega)/d\omega < 0$ and $d\hat{\phi}_{1,2}(\omega)/d\omega > 0$ for the 1st and 2nd positions, respectively. The two-sensor technique algorithm detects the sign of $d\hat{\phi}_{1,2}(\omega)/d\omega$ changes between the two positions and marks the 2nd one, as shown in Fig. 60(a.iii), since the corresponding $d\hat{\phi}_{1,2}(\omega)/d\omega$ is closer to zero. Note that these results are consistent with the theory presented in Fig. 30 and also with the contour map of Fig. 49(b.ii).

Table 6 - RMS accelerations [$\times 10^{-4}$ m/s^2] for the positions in the pipe region elaborated for the Brazilian test rig with one-sensor technique.

		x_l [m]		
		-1.5	**-0.5**	**0.5**
y_l [m]	**-1.0**	0.65	3.16	3.26

Source: elaborated by the author.

The results of leak localization applied on the Brazilian test rig are shown in Fig. 61, where the pair of marks in Fig. 61(a) corresponds to the estimate of leak localization with the one-sensor technique, as indicated by the values highlighted in Tab. 6. In Fig. 61(b), the pair of marks corresponds to the estimate of leak localization with the two-sensor technique, which corresponds to the position marked in Fig. 60(a.iii). Two lines perpendicular to the pipe direction are traced passing through the pair of marks, and the leak region is determined by the intersection of the four lines. Note that the one-sensor technique fails to estimate the leak position as it failed to locate the buried pipe first, while the two-sensor technique correctly estimates it for the Brazilian test rig. Such a difference between the performance of both techniques is consistent with the contour maps of Figs. 49(b.i) and 49(b.ii), where they show that the sensors still capture the circles of constant phase due to the leak in the main pipe, although the amplitude of the waves that radiate from the flexible pipe is much higher than the amplitude of the waves that radiate from the main pipe and the leak. Therefore, these results indicate that the two-sensor technique is more suitable for environments that contain high-level source of noise than the one-sensor technique.

Figure 60 - Leak localization with two-sensor technique applied on the Brazilian test rig. (a.i-ii) 1st and 2nd positions of the pair of sensors, (b.i-ii) coherence $\gamma_{1,2}^{2}(\omega)$ for 1st and 2nd positions, (c.i-iii) unwrapped phase $\phi_{1,2}(\omega)$ and approximated line $\hat{\phi}_{1,2}(\omega)$ for 1st and 2nd positions, where the solid black line corresponds to $\phi_{1,2}(\omega)$ and the dashed red line corresponds to $\hat{\phi}_{1,2}(\omega)$, and (a.iii) estimate of leak localization. The dashed blue lines correspond to the buried pipe and the dark yellow dots correspond to the leak position.

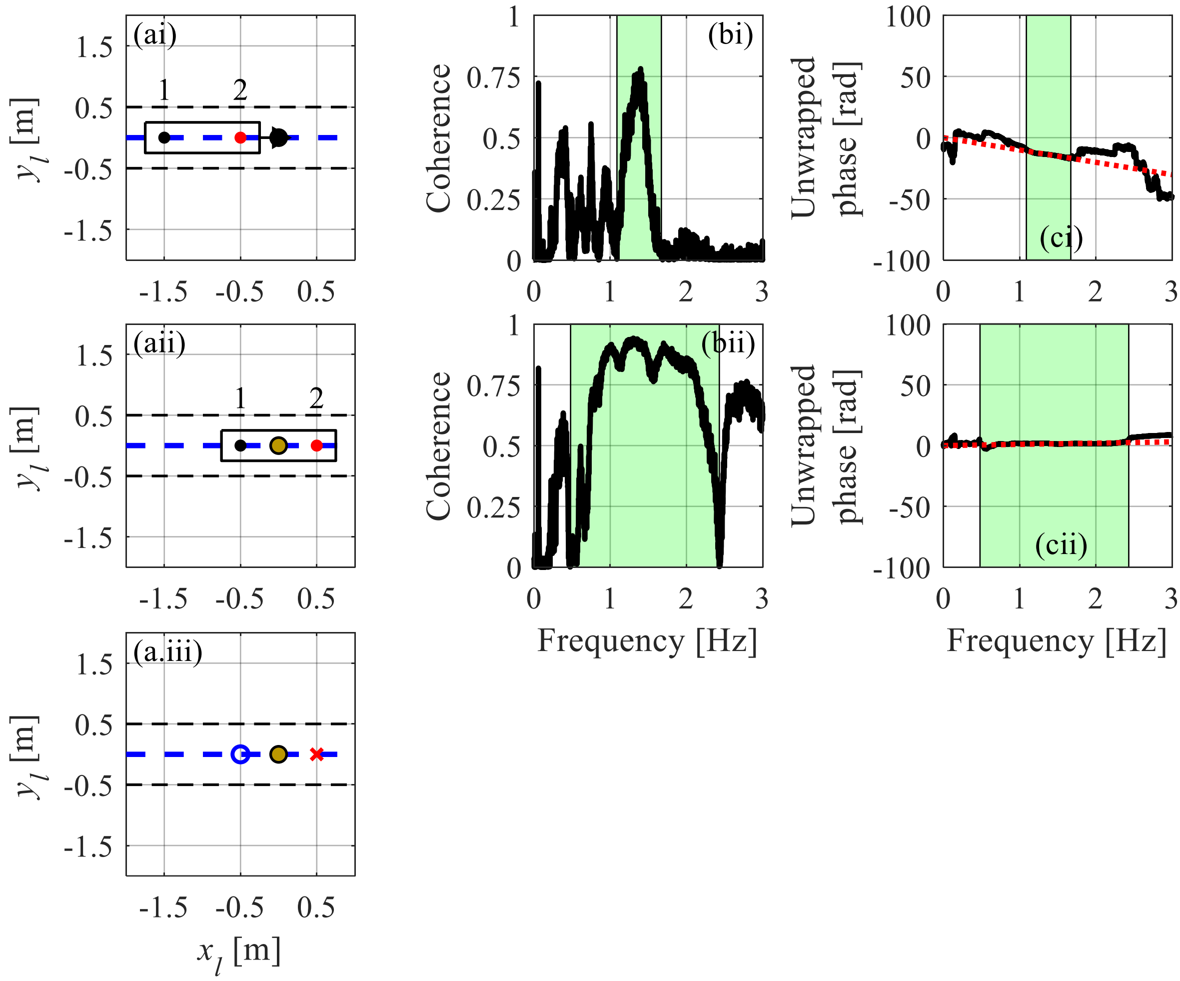

Source: elaborated by the author.

Figure 61 - Results of leak localization with (a) one-sensor and (b) two-sensor techniques applied on the Brazilian test rig. The dashed blue lines correspond to the buried pipe and the dark yellow dots correspond to the leak position.

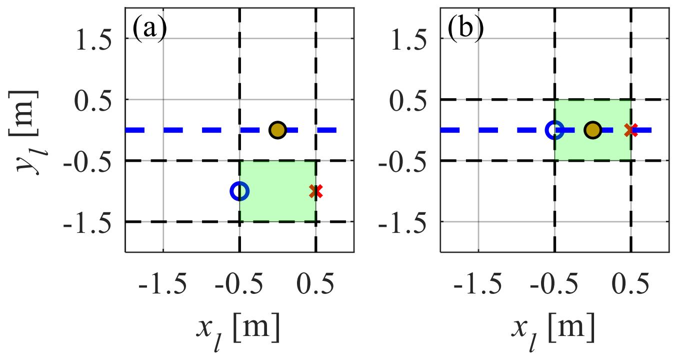

Source: elaborated by the author.

5.5 CONCLUSIONS

This chapter has presented the practical application of the one-sensor and two-sensor techniques by testing them on the experimental data collected on two test rigs, one located in Blithfield, UK, and the other in São Paulo, Brazil. The two-sensor technique tracking algorithm was modified to extract an approximate slope of unwrapped phase, as it is not possible to obtain an exact value due to the interference of environmental noise and other external sources. Then, an investigation on the patterns of amplitude and phase of ground surface vibration has been carried out for the Brazilian test rig, similar to the one conducted on the British test rig in Chapter 2, to support discussion on the performance of both localization techniques.

By comparing the corresponding contour maps obtained for both experimental data, a distinct pattern was observed on the Brazilian test rig where the amplitude is higher for positions perpendicular to the main pipe. This is probably due to the waves that radiate from the flexible pipe, whose amplitude is much higher than the amplitude of the waves that radiate from the main pipe and from the leak. After the experimental investigation, the one-sensor and two-sensor techniques were applied to locate the main pipe of the British test rig, and to locate the main pipe and leak of the Brazilian test rig, assuming that the flexible pipe is an external source of noise. The results for the British test rig indicate that both localization techniques can locate a leaking buried pipe for positions close to the leak on the ground surface if there is not a high-level source of noise close to measurement positions. For positions farther from the leak, however, the results indicate the two-sensor technique is more able to locate a leaking buried pipe than the one-sensor technique. This is because the two-sensor technique uses phase to locate the pipe, which is robust to the interference of uncorrelated noise. In addition, the results for the Brazilian test rig indicate that the two-sensor technique is more able to locate the buried pipe and the leak in an environment that contains a high-level source of noise than the one-sensor technique. This is because sensors can capture circles of constant phase that travel on the ground surface due to a leak in the main pipe, even with interference of the waves that radiate from the flexible pipe.

Assuming that the pipe direction is known, it is expected that the performance of the two-sensor technique is better than the one of the on-sensor technique for measurement positions far from the leak on the ground surface, as indicated by the results for the British test rig, and for an environment that contains a high-level source of noise, as indicated by the results for the Brazilian test rig. To check the sensitivity of both localization techniques on this condition and their performance for further distances in relation to the buried pipe, a new investigation will be presented in the next chapter where the techniques are tested on an experimental setup in which the measurement lines are misaligned in relation to pipe direction, and the distances in relation to the buried pipe are longer. Furthermore, the two-sensor technique is also tested on an experimental dataset acquired with geophones, to check if it is possible to improve its performance in relation to conventional accelerometers.

6 EXPERIMENTAL INVESTIGATION OF THE LOCALIZATION TECHNIQUES - MEASUREMENT LINES MISALIGNED WITH PIPE DIRECTION AND FEASIBILITY STUDY WITH GEOPHONES

6.1 INTRODUCTION

The previous chapter presented the results for application of the localization techniques assuming that the measurement lines are perpendicular to pipe direction. The comparison between their performances indicates that the two-sensor technique is more suitable for measurement positions farther from the leak, as demonstrated by the results for the British test rig, and also for environments that contain high-level source of noise, as demonstrated by the results for the Brazilian test rig. Although such results are encouraging for the application of the proposed technique, the investigation was limited to the condition of setting the measurement lines perpendicular to pipe direction, and the distances between sensors and buried pipe were relatively short, as measurements for longer distances might be carried out in the practice and the attenuation becomes even more dominant.

To evaluate the performance of the two-sensor technique in relation to the one-sensor technique on a more challenging situation, where the measurement lines are not perpendicular to the pipe direction and the distances between sensors and buried pipe are longer, a new experimental dataset is required. Furthermore, since the attenuation becomes more dominant for longer distances in relation to the buried pipe and also in relation to the leak, this motivates a new investigation to check if a sensor with higher SNR can improve the performance of the proposed technique.

This chapter presents the results for a second experimental investigation carried out on the Brazilian test rig, where wider measurement grids with different misalignment angles in relation to the pipe direction are elaborated to assess the main limitations of the one-sensor and two-sensor techniques on challenging situations that might occur in the practice. A third experimental investigation was also conducted on the Brazilian test rig to check if geophones can improve the performance of the two-sensor technique in relation to accelerometers, as geophones usually have higher sensitivity than accelerometers at low frequencies.

6.2 INVESTIGATION OF MISALIGNMENT ANGLE ON THE PERFORMANCE OF THE LOCALIZATION TECHNIQUES

6.2.1 Description of experimental data

The schematic diagram and setup for the second experiment on the Brazilian test rig are presented in Fig. 62, and the description for test rig components shown in Fig. 62(a) is given in Section 5.3. A total of 3 measurement grids was elaborated in the test rig, where the accelerometers were positioned on the ground surface at different angles in relation to the main pipe. In this case, 2 PCB 333B40 accelerometers and 3 PCB 356A17 triaxial accelerometers were used to measure vibration only in the vertical direction in relation to the ground surface. During the measurements, one accelerometer remained fixed at the leak position and the other four were placed in-line, 1 m apart and parallel to y_l-axis. Then, the line of accelerometers was moved to the opposite direction of y_l-axis to acquire for the other four positions. This procedure was repeated along x_l-axis and a total of nine measurement lines was elaborated, resulting in a rectangular measurement grid with sides 8 m and 7 m, where the leak position is located at the middle as shown in Fig. 62(c). Note that only the schematic diagram for the measurement grid with 0° misalignment is shown in Fig. 62. An LMS SCADAS data acquisition system was used to store the measurements, which consist of 60 s long acceleration time histories sampled at a frequency of 12.8 kHz.

As carried out for the experimental data presented in Chapter 5, the patterns of vibration amplitude for the second experiment are also investigated to support the discussion on the performance of both localization techniques, in which wider measurement grids are used as shown in Fig. 63. Note in Eq. (11) that the contour maps for spatially unwrapped phase can be shown up to approximately 110 Hz without spatial aliasing, due to the spatial interval of 1 m and assuming a shear wave speed of approximately 220 m/s (SCUSSEL, 2019). Therefore, the contour maps for spatially unwrapped phase are not presented for this case to be consistent with the analysis in the frequency domain, in which the leak noise content is predominantly contained at frequencies higher than 110 Hz.

Figure 62 - Second experimental setup on the Brazilian test rig. (a) Overview of the test rig showing the measurement grid location (not to scale), (b) photograph showing the experimental setup, and (c) schematic diagram for the measurement grid showing the corresponding coordinate system and distances (not to scale).

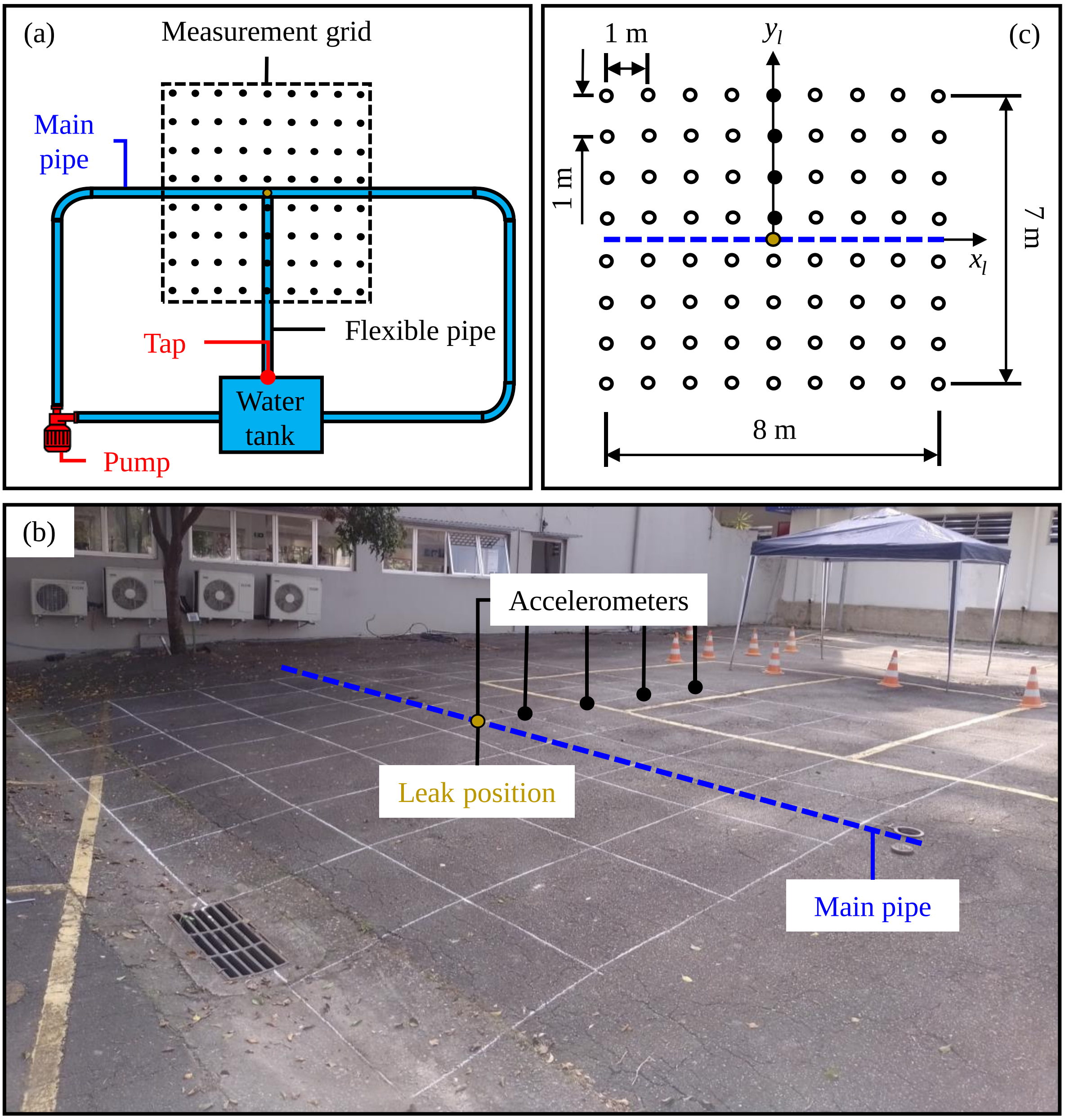

Source: elaborated by the author.

Figure 63 - Contour maps for vertical ground surface accelerations measured on the Brazilian test rig second experiment. Normalized RMS values for the measurement grids with (a) 0°, (b) 30° and (c) 60° misalignment.

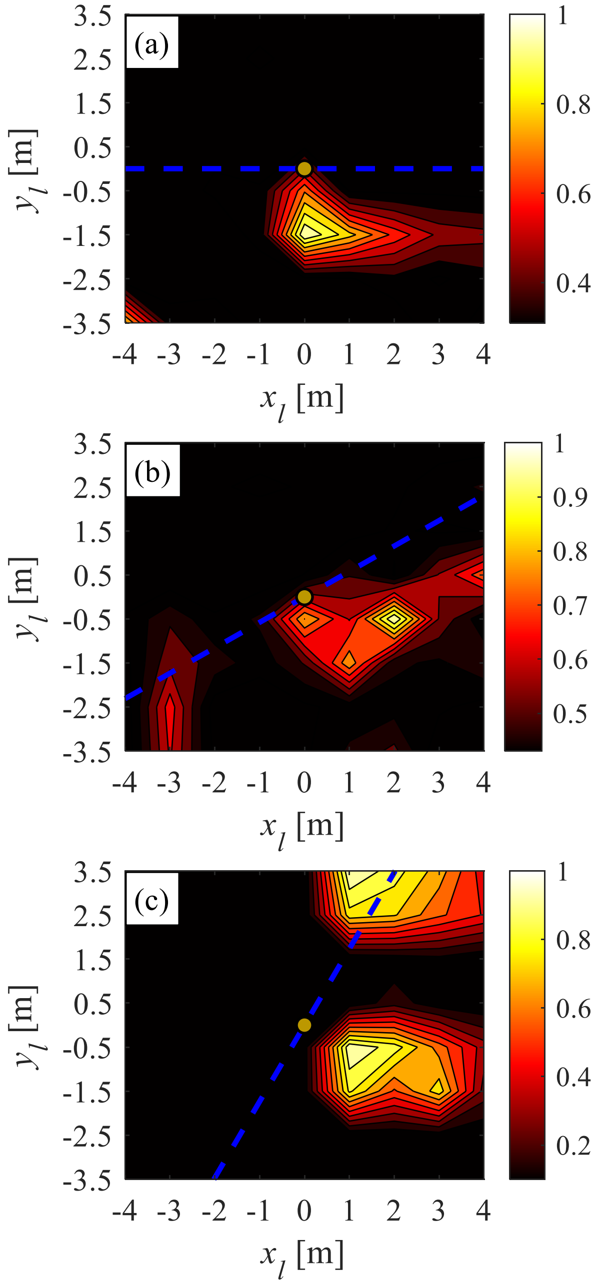

Source: elaborated by the author.

By comparing the results for the first and second experiments on the Brazilian test rig presented in Figs. 49(b.i) and 63(a), respectively, both patterns show that the vibration amplitude is higher for positions on the ground surface above the flexible pipe, as shown in Fig. 62(a). This is expected as the amplitude of the waves that radiate from the flexible pipe is much higher than the amplitude of the waves that radiate from the main pipe, as explained in Chapter 5, and the measurement grid of both experiments are aligned with the pipe direction on the ground surface, i.e., 0° misalignment. By comparing Figs. 63(b) and 63(c) with Fig. 63(a), it can be seen that the results are consistent as the patterns of vibration amplitude follows the orientation given by the angle between the pipe direction and the measurement grids axes. Note also in Figs. 63(b) and 63(c) that there are some regions distant from the leak position and close to the ends of the measurement grids, where the amplitude is significantly high. Such regions are probably due to some external sources of noise situated close to the test site.

6.2.2 Description of measurement lines

As carried out for the experimental data presented in Chapter 5, the performance of the two-sensor technique in relation to the one-sensor technique is evaluated in this chapter by applying them on the second experimental data collected in the Brazilian test rig. For the measurement grid with 0° misalignment, the one-sensor and two-sensor techniques are applied to circumscribe the pipe region on ground surface, as the measurement lines are perpendicular to the pipe direction. For the measurement grids with 30° and 60° misalignment, however, the localization techniques cannot be used to locate the buried pipe because the measurement lines are not perpendicular to the pipe direction. For these situations, they are only used to circumscribe a region on the ground surface that encompasses the leak position along y_l-axis of the measurement grid, as discussed in Subsection 3.3.2. If the region circumscribed on the ground surface encompasses the leak position, the localization techniques are then applied along it to circumscribe the leak region, as illustrated in Figs. 28 and 30.

To evaluate the performance of both localization techniques for different distances in relation to leak position, the data acquired on each measurement grid of the second experiment is divided into 3 zones, named A, B and C as shown in Fig. 64. The schematic diagrams for the experiments with 0°, 30° and 60° misalignment are illustrated in Figs. 64(a), 6.3(b) and 6.3(c), respectively. The first measurement line of zones A, B and C for each measurement grid is at -4 m, -1 m, and 2 m away from the leak position, respectively. The corresponding 2nd and 3rd measurement lines are 1 m apart from each other along x_l-axis, and the positions of the sensors are at -3.5 m up to 3.5 m, 1 m spaced along each measurement line.

6.2.3 Results for one-sensor technique

Before applying the localization techniques, the experimental data were passed through a bandpass filter with cutoff frequencies of 130 Hz and 1,000 Hz, to remove low-frequency noise and to prevent aliasing. After filtering the experimental data, the RMS accelerations for each position of the measurement grids with 0°, 30° and 60° misalignment were calculated, and the respective results are tabulated in Tabs. 7, 8 and 9, respectively. Following the same arrangement adopted for Tabs. 5 and 6, the values highlighted in each column of Tabs. 7, 8 and 9 indicate the pair of positions that contains the highest pair of RMS values for each measurement line shown in Figs. 64(a), 64(b) and 64(c), respectively. Note that the results of Tabs. 7, 8 and 9 are consistent with the contour maps of Figs. 63(a), 63(b) and 63(c) respectively, in which the coordinates of the highest RMS values for each table corresponds to the regions for each contour map where the vibration amplitude is higher.

Figure 64 - Schematic diagram for measurement lines of the second experiment in the Brazilian test rig. Measurement grids with (a) 0°, (b) 30° and (c) 60° misalignment.

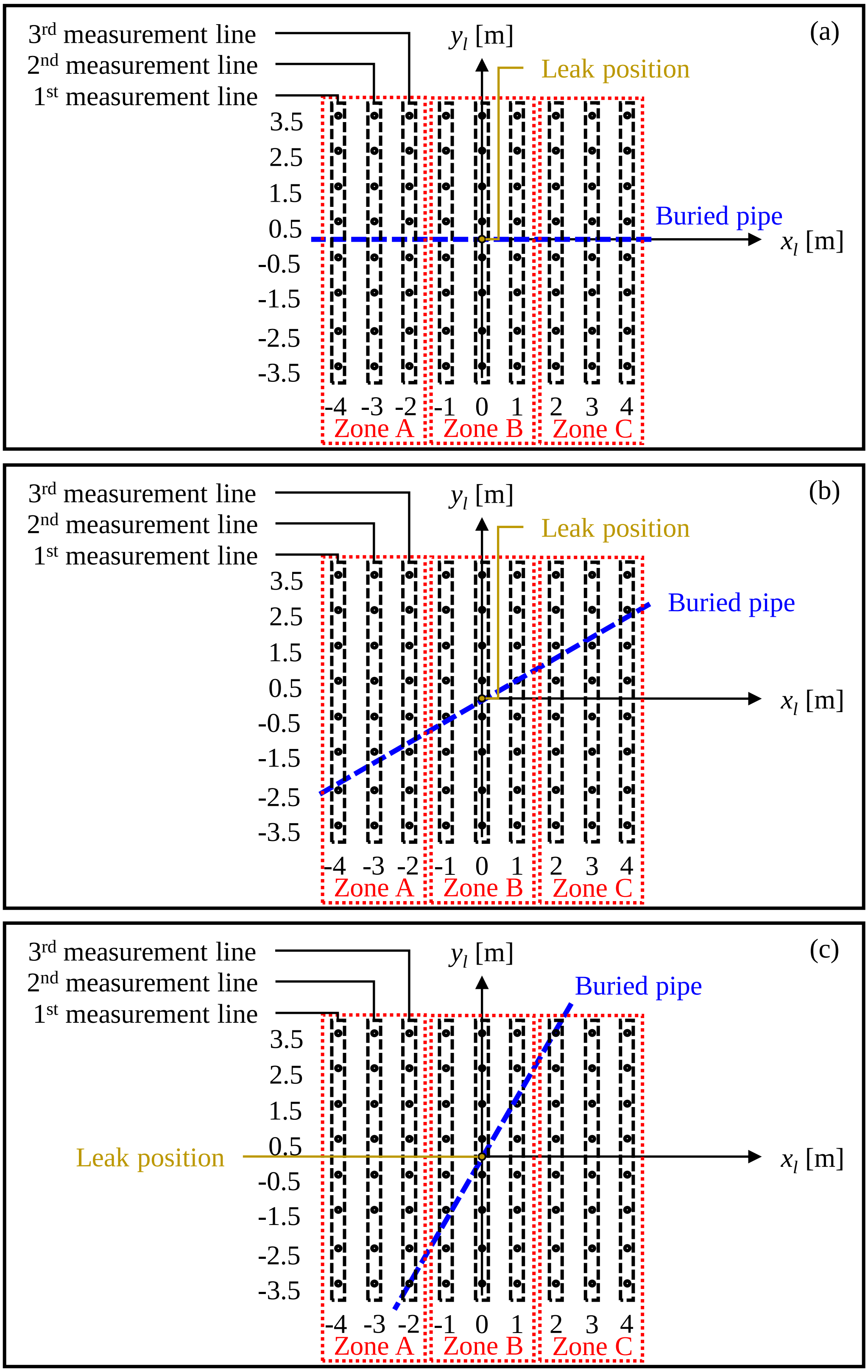

Source: elaborated by the author.

Table 7 - RMS accelerations [$\times 10^{-4}$ m/s²] for the measurement grid with 0° misalignment, shown in Fig. 64(a).

		x_l [m]								
		-4	**-3**	**-2**	**-1**	**0**	**1**	**2**	**3**	**4**
y_l [m]	**3.5**	6.02	6.69	6.35	6.22	6.20	6.06	6.34	5.98	5.97
	2.5	6.40	6.69	6.31	7.77	6.44	6.33	6.31	6.30	6.25
	1.5	5.76	6.00	5.88	5.98	5.88	5.82	5.69	5.69	5.70
	0.5	6.01	6.01	7.14	6.77	6.97	6.22	6.39	5.92	5.80
	-0.5	7.10	6.91	7.49	7.44	17.04	7.11	6.90	6.91	6.60
	-1.5	6.65	6.99	6.63	7.72	23.87	19.55	15.10	11.89	11.24
	-2.5	5.96	6.27	5.96	6.68	6.96	7.17	8.49	7.04	8.29
	-3.5	19.31	8.17	9.08	6.12	5.84	6.71	5.98	8.99	6.43

Source: elaborated by the author.

Table 8 - RMS accelerations [$\times 10^{-4}$ m/s²] for the measurement grid with 30° misalignment, shown in Fig. 64(b).

		x_l [m]								
		-4	**-3**	**-2**	**-1**	**0**	**1**	**2**	**3**	**4**
y_l [m]	**3.5**	6.85	6.12	6.08	6.01	6.05	5.97	6.07	6.16	6.22
	2.5	6.61	6.57	6.58	7.06	6.63	6.46	6.48	7.40	7.97
	1.5	5.74	5.70	5.76	5.71	5.80	6.23	6.90	6.60	6.79
	0.5	5.97	5.73	5.82	5.92	6.79	8.79	6.69	10.02	12.82
	-0.5	6.86	8.71	6.92	8.05	14.17	10.87	17.31	9.82	6.98
	-1.5	6.39	9.62	8.45	7.15	8.97	13.95	8.04	7.61	8.67
	-2.5	6.04	11.57	6.12	5.94	6.55	7.16	7.35	6.95	6.33
	-3.5	5.92	11.16	6.45	6.02	6.56	8.00	9.17	5.94	6.63

Source: elaborated by the author.

Table 9 - RMS accelerations [$\times 10^{-4}$ m/s²] for the measurement grid with 60° misalignment, shown in Fig. 64(c).

		x_l [m]								
		-4	**-3**	**-2**	**-1**	**0**	**1**	**2**	**3**	**4**
y_l [m]	**3.5**	6.05	6.58	5.98	6.04	6.83	94.02	81.78	66.02	41.20
	2.5	6.53	7.23	6.39	6.33	6.65	74.88	70.84	55.54	45.09
	1.5	5.68	6.17	5.73	5.67	6.26	7.11	8.61	11.14	6.61
	0.5	5.74	6.00	5.82	5.79	7.32	7.32	18.07	8.26	6.35
	-0.5	6.24	6.08	6.00	6.58	9.54	92.31	82.50	58.24	33.87
	-1.5	7.88	6.70	6.49	8.26	9.97	79.69	52.46	74.57	26.57
	-2.5	6.00	6.16	6.32	6.94	6.55	6.07	7.26	9.29	6.10
	-3.5	5.77	5.66	6.22	7.15	8.08	6.25	6.23	7.94	7.42

Source: elaborated by the author.

6.2.4 Results for two-sensor technique

After filtering the experimental data with the bandpass filter described in the previous subsection, the cross-spectral densities and coherences were calculated via Eqs. (5.1) and (5.2), respectively, for each pair of positions along each measurement line of zones A, B and C shown in Fig. 64. Both functions were determined by averaging the time-series using segment averaging (SHIN; HAMMOND, 2008) with 64 averages, 12,800-point fast Fourier transform and a Hanning window with 50% overlap, resulting in a frequency resolution of 1 Hz. The modified tracking algorithm of the two-sensor technique is then applied to estimate the limits of the leak noise bandwidth, and to calculate the approximate slope of unwrapped phase for each pair of positions.

As the application of the two-sensor technique is performed for a pair of positions along each measurement line, a great amount of results is generated during the process and, hence, presenting the results for all measurement lines is not practical. Instead, only the results for the two-sensor technique applied on the 2nd measurement line of zone B for each measurement grid are presented in this thesis. This particular measurement line was selected for each measurement grid because it is the line that passes exactly above the leak (source), where the attenuation is slower, corresponding to the best-case scenario for the application of both localization technique. Then, a detailed explanation on the performance of the two-sensor technique in relation to the one-sensor technique is provided without expanding unnecessarily. The results for the two-sensor technique applied on 1st, 2nd, 3rd and 4th positions of the 2nd measurement line of zone B, for the measurement grid with 0° misalignment are presented in Fig. 65, and the results for the respective 5th, 6th and 7th positions are presented in Fig. 66. The results for two-sensor technique applied on the measurement grids with 30º and 60° misalignment are presented in Appendix B for ease of reference.

To check the influence of the distance between buried pipe and sensors on the ground surface, the results for the measurement grid with 0° misalignment are analyzed first separately from the other measurement grids. As can be seen in Figs. 65(b.i-iv) and 66(b.i-iii), the coherence is practically zero and the estimated leak noise bandwidth is extremely narrow for positions farther than 2.5 m from the pipe along the measurement line. Furthermore, as can be seen in Figs. 65(c.i-iv) and 66(c.i-iii), the phase is not unwrapped adequately for positions farther than 2.5 m along y_l-axis. Consequently, the modified tracking algorithm provides a poor estimate for the corresponding slope of unwrapped phase, as shown by $\hat{\phi}_{1,2}(\omega)$ in Figs. 65(c.i) and 66(c.iii), which can lead to a false perception that the sign of the slope has changed and the algorithm marks a wrong estimate for the pipe position, as shown by the blue-circle and red-cross marks situated at $[x_l, y_l] = [0, \text{-}1.5]$ and $[x_l, y_l] = [0, \text{-}2.5]$, respectively, in Fig. 66(a.iv). For positions near than 2.5 m along y_l-axis, the phase is unwrapped adequately and the modified tracking algorithm successfully estimates the corresponding slope by approximating the line $\hat{\phi}_{1,2}(\omega)$. Therefore, it is evident that the distance between buried pipe and sensors on the ground surface has an important influence on the performance of the technique.

Figure 65 - Pipe localization with the two-sensor technique applied on the 2nd measurement line of zone B of the measurement grid with 0° misalignment - Part 1. (a.i-iv) 1st, 2nd, 3rd and 4th positions of the pair of sensors, (b.i-iv) coherence $\gamma_{1,2}^{2}(\omega)$ for 1st, 2nd, 3rd and 4th positions, (c.i-iii) unwrapped phase $\phi_{1,2}(\omega)$ (solid black line) and approximated line $\hat{\phi}_{1,2}(\omega)$ (dashed red line) for 1st, 2nd, 3rd and 4th positions. The dashed blue lines correspond to the buried pipe and the dark yellow dots correspond to the leak position.

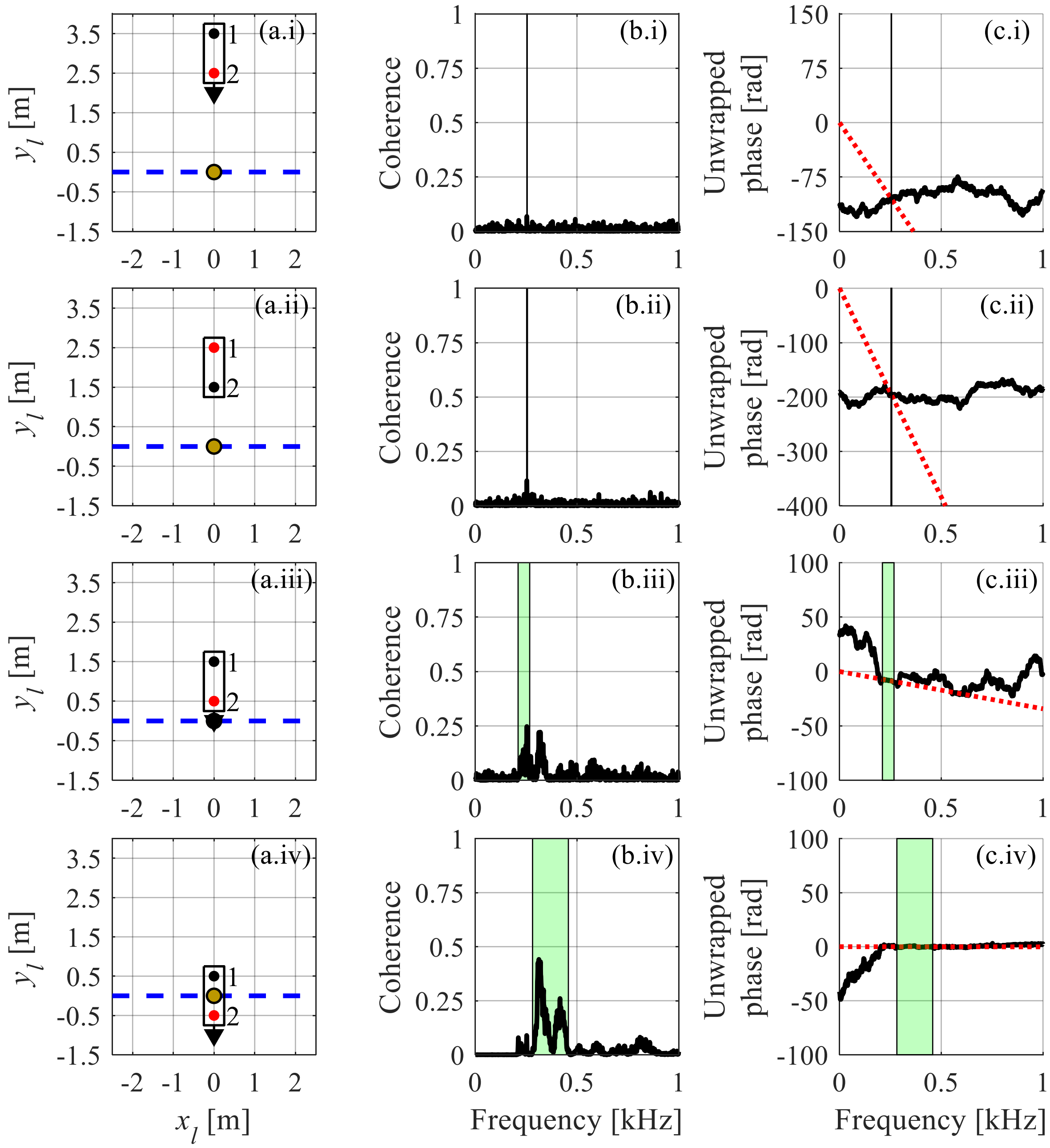

Source: elaborated by the author.

Figure 66 - Pipe localization with the two-sensor technique applied on the 2nd measurement line of zone B of the measurement grid with 0° misalignment - Part 2. (a.i-iv) 5th, 6th and 7th positions of the pair of sensors, (b.i-iv) coherence $\gamma_{1,2}^{2}(\omega)$ for 5th, 6th and 7th positions, (c.i-iii) unwrapped phase $\phi_{1,2}(\omega)$ (solid black line) and approximated line $\hat{\phi}_{1,2}(\omega)$ (dashed red line) for 5th, 6th and 7th positions, and (a.iv) estimate of pipe localization.

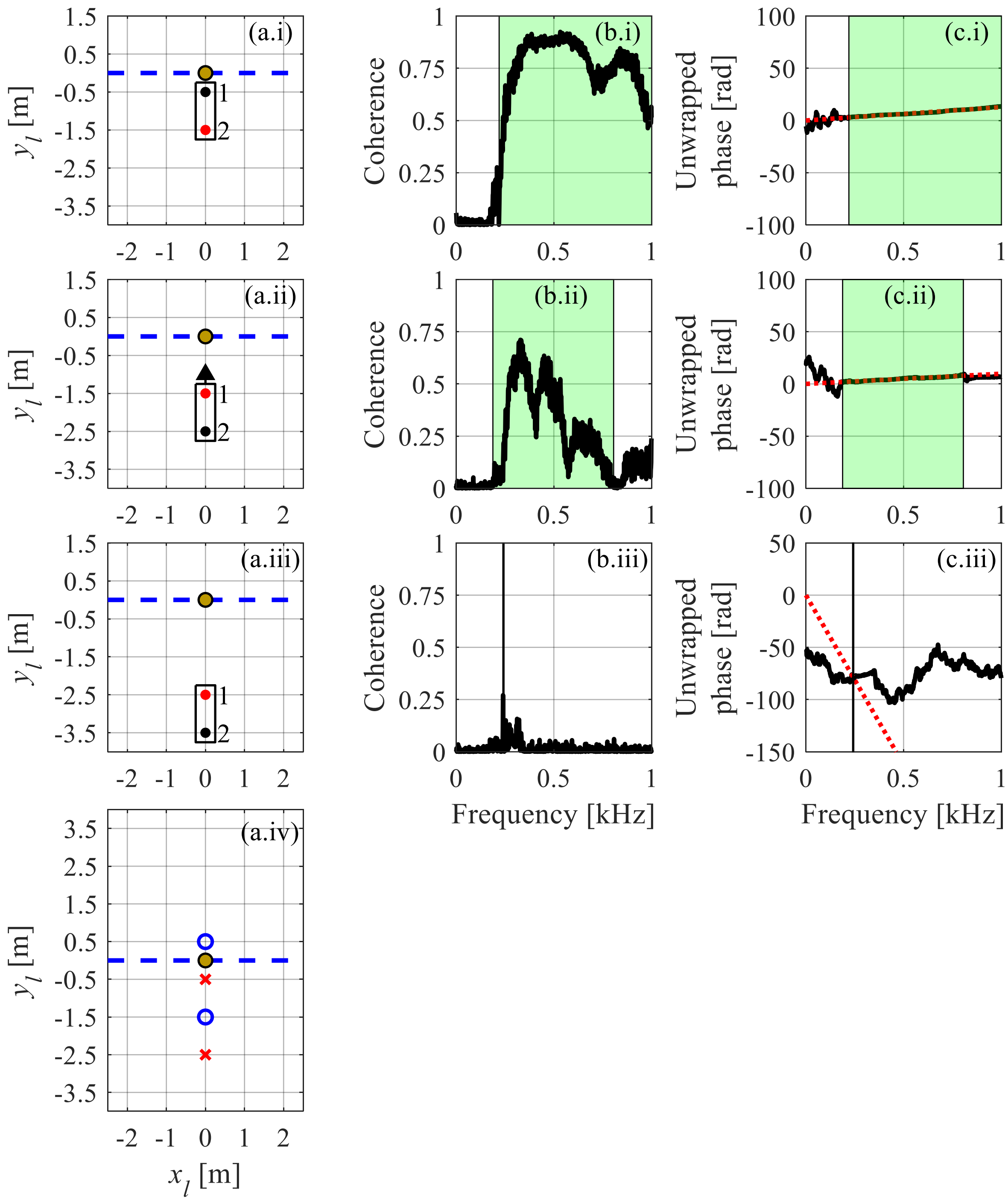

Source: elaborated by the author.

To investigate the influence of the misalignment between buried pipe and measurement lines on the performance of the two-sensor technique, the results for the measurement grids with 30° and 60°, presented in Appendix B, are compared with the ones for the measurement grid with 0° misalignment. By comparing the coherences for the same position in relation to the leak along each corresponding measurement line, for example Figs. 66(b.i), 85(b.i) and 87(b.i), it can be seen that the coherence decreases and the estimated leak noise bandwidth gets narrower with the increase of misalignment angle. Furthermore, by comparing the unwrapped phase for the same position in relation to the leak along each corresponding measurement line, for example Figs. 66(c.i), 85(c.i) and 87(c.i), it can be seen that the phase is unwrapped adequately for higher frequencies with the decrease of misalignment angle.

6.2.5 Comparison between the performances of one-sensor and two-sensor techniques

The performance of the two-sensor technique is compared with the performance of the one-sensor technique by applying them to locate the buried pipe for each zone of the measurement grid with 0° misalignment, and to trace the region on the ground surface that encompasses the leak position for each zone of the measurement grids with 30° and 60° misalignment. If one of them estimates the corresponding region correctly, then the localization technique is applied along it to circumscribe the leak region.

The results for the application of both localization techniques on the measurement grids with 0°, 30° and 60° misalignment are presented in Figs. 67, 68 and 69, respectively. Note that the region is only circumscribed on ground surface if both horizontal lines pass through most of the marks in a unique way. Therefore, if there is another way of tracing such horizontal lines passing through the same amount of blue-circle and red-cross marks, the algorithm does not circumscribe the region on ground surface, as shown in Figs. 67(a.ii) where there are 3 different ways of tracing the horizontal lines, and 69(b.i) where there are 2 different ways of tracing the horizontal lines, and hence the region is not circumscribed on ground surface.

By comparing the results of the one-sensor and two-sensor techniques for each application shown in Figs. 67, 68 and 69, the two-sensor technique has a better performance than the one-sensor technique when the measurement lines have 0° and 30° misalignment in relation to pipe direction. Note that the pipe region was correctly determined by the two-sensor technique for zone B of the measurement grid with 0° misalignment, as shown in Fig.

67(b.ii). The region that encompasses the leak position was correctly determined by the one-sensor technique for zone C of the measurement grid with 30° misalignment, as shown in Fig. 68(a.iii), and by the two-sensor technique for zone B of the same measurement grid, as shown in Fig. 68(b.ii). For the measurement grid with 60° misalignment, however, both localization techniques did not determine the respective region correctly.

Figure 67 - Results for pipe localization with (a) one-sensor and (b) two-sensor techniques applied on the measurement grid with 0° misalignment in relation to the pipe direction. The dashed blue lines correspond to the buried pipe and the dark yellow dots correspond to the leak position.

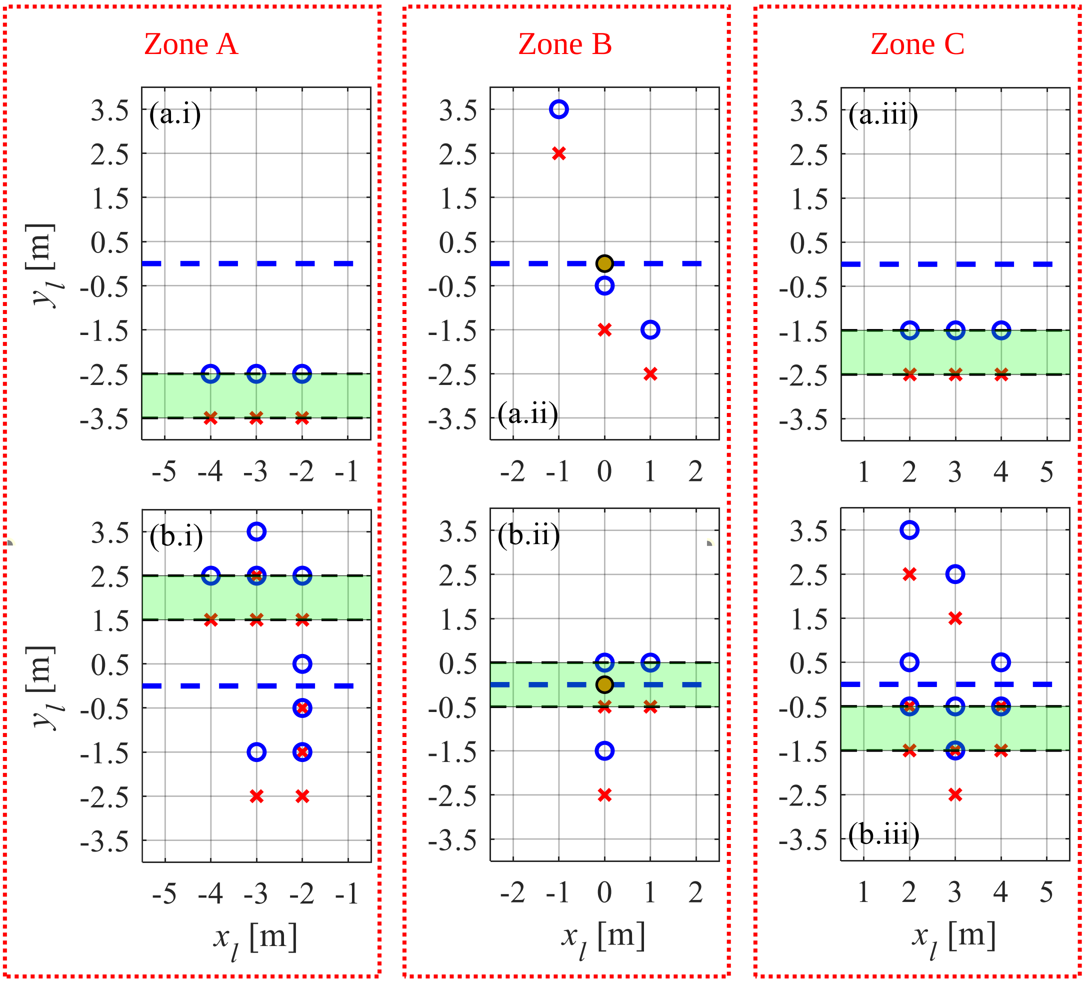

Source: elaborated by the author.

Figure 68 - Results for pipe localization with (a) one-sensor and (b) two-sensor techniques applied on the measurement grid with 30° misalignment in relation to the pipe direction. The dashed blue lines correspond to the buried pipe and the dark yellow dots correspond to the leak position.

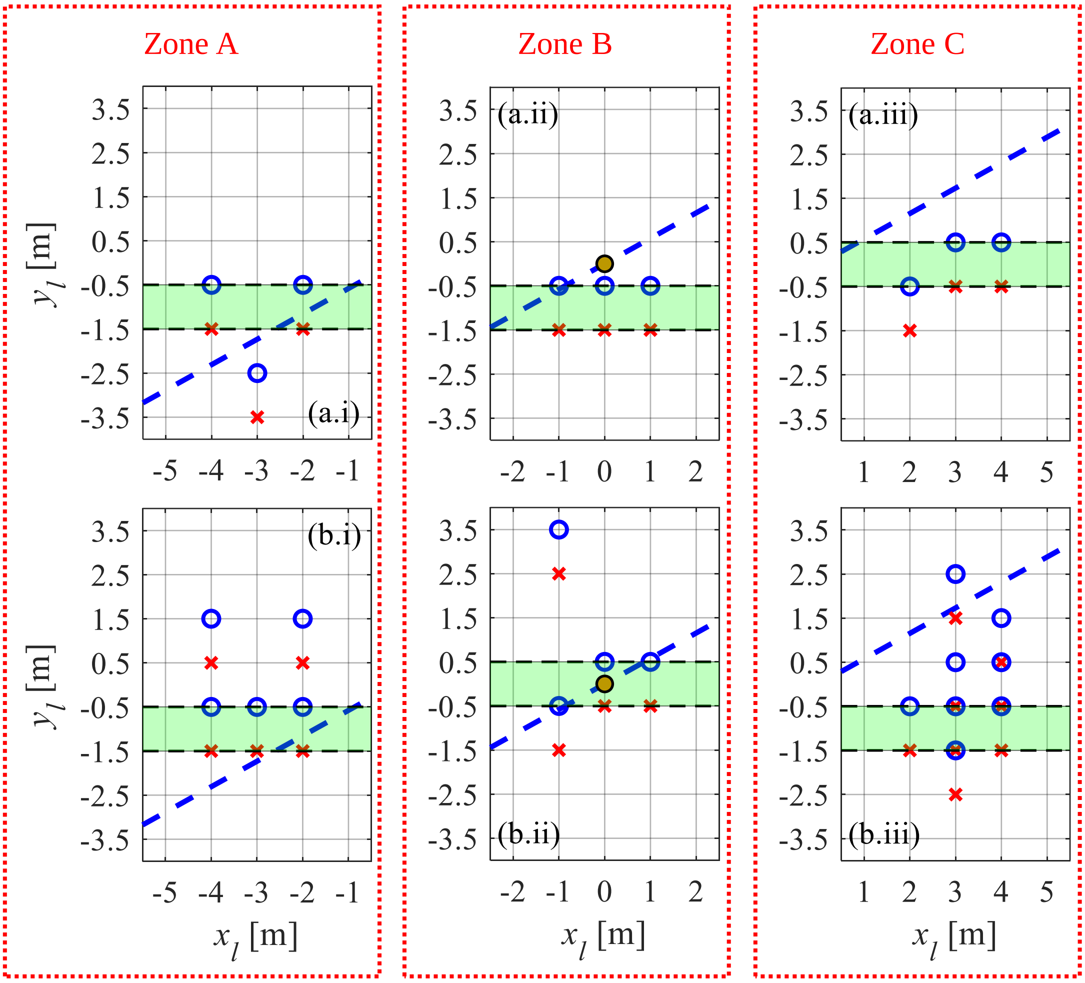

Source: elaborated by the author.

Therefore, it is evident that both localization techniques cannot locate the buried pipe of the Brazilian test rig if the misalignment angle between measurement lines and pipe direction is higher than 30°, as shown by the results of Fig. 69, or if the measurement lines are positioned farther than 2 m from the leak position, as shown by the results obtained for zone A and C of Figs. 67 and 68. Note that this behavior differs from the one observed on the results obtained for the experimental data of the British test rig, in which the two-sensor technique successfully located the pipe position on the ground surface for much longer distances in relation to the leak.

Figure 69 - Results for pipe localization with (a) one-sensor and (b) two-sensor techniques applied on the measurement grid with 60° misalignment in relation to the pipe direction. The dashed blue lines correspond to the buried pipe and the dark yellow dots correspond to the leak position.

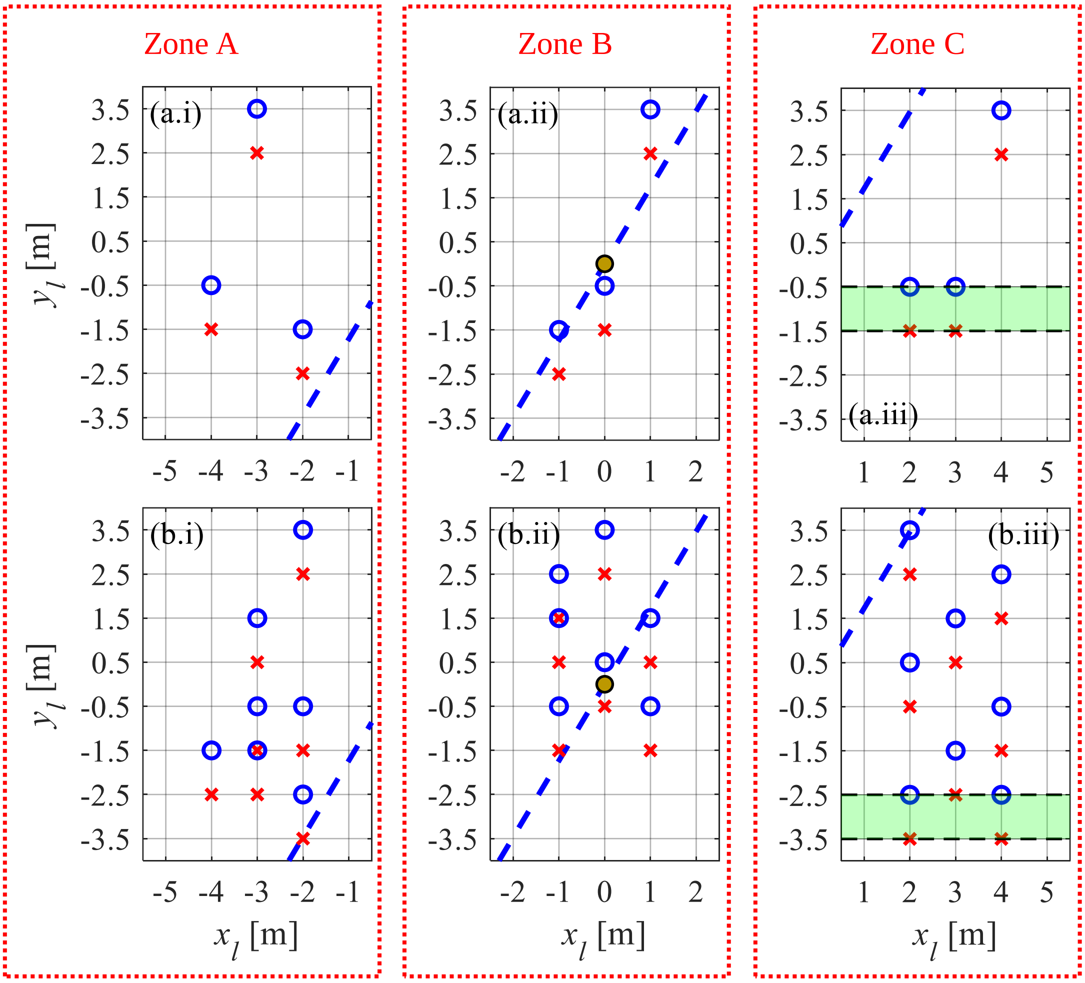

Source: elaborated by the author.

As the respective regions were correctly determined by the two-sensor technique for zone B of the measurement grids with 0° and 30° misalignment, the same localization technique is applied along them to circumscribe the leak region on the ground surface. The results for leak localization on zone B of the measurement grids with 0° and 30° misalignment are shown in Figs. 70 and 71, respectively. By comparing the coherences for the same position in relation to the leak along the region, the coherence also decreases and the leak noise bandwidth also gets narrower with the increase of angle of misalignment, as observed on previous results for pipe localization with the two-sensor technique applied on the measurement grids with different misalignment angles.

Figure 70 - Leak localization with the two-sensor technique applied on zone B of the measurement grid with 0° misalignment. (a.i-ii) 1st and 2nd positions of the pair of sensors, (b.i-ii) coherence $\gamma_{1,2}^{2}(\omega)$ for 1st and 2nd positions, (c.i-iii) unwrapped phase $\phi_{1,2}(\omega)$ (solid black line) and approximated line $\hat{\phi}_{1,2}(\omega)$ (dashed red line) for 1st and 2nd positions, and (a.iii) estimate of leak localization. The dashed blue lines correspond to the buried pipe and the dark yellow dots correspond to the leak position.

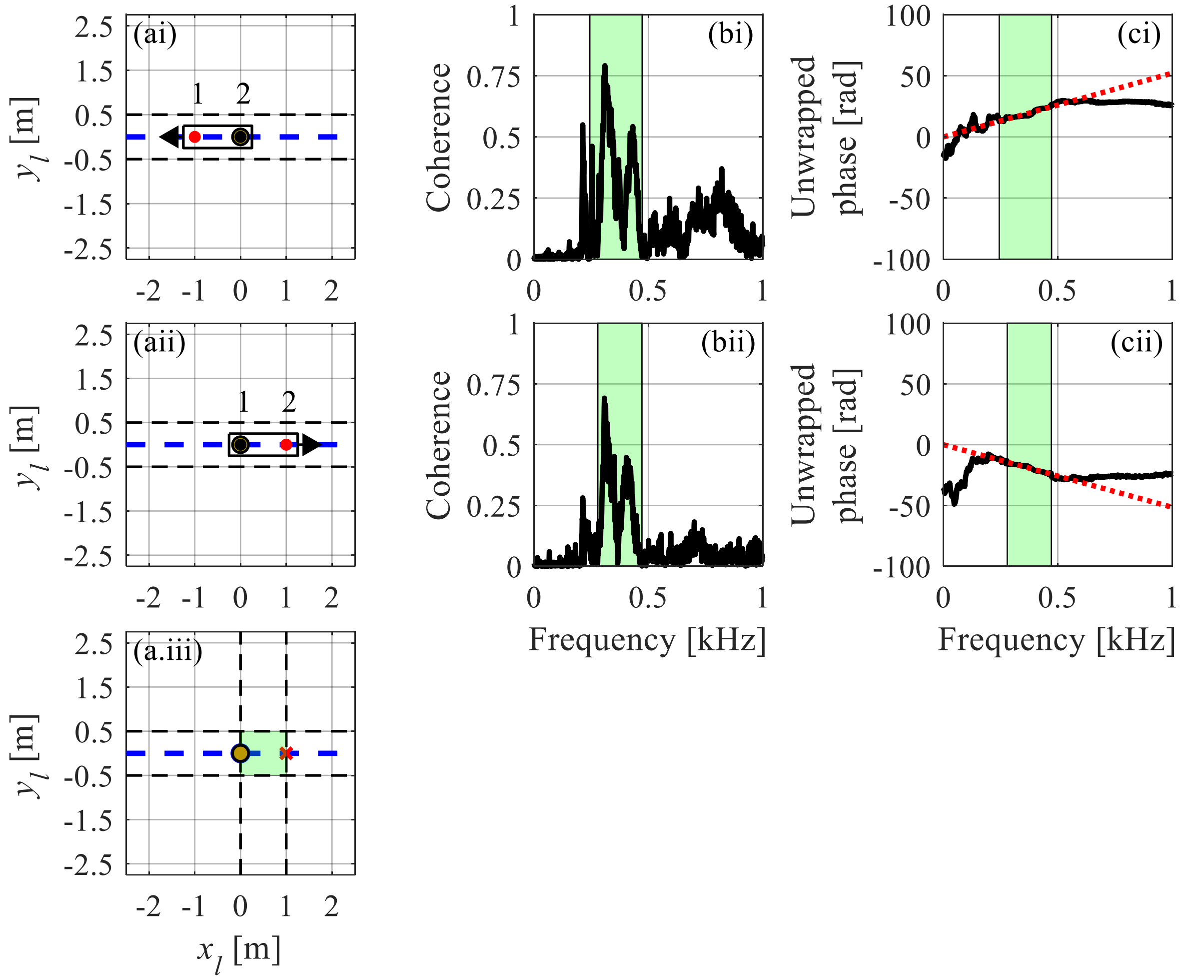

Source: elaborated by the author.

Figure 71 - Leak localization with the two-sensor technique applied on zone B for the measurement grid with 30° misalignment. (a.i-ii) 1st and 2nd positions of the pair of sensors, (b.i-ii) coherence $\gamma_{1,2}^{2}(\omega)$ for 1st and 2nd positions, (c.i-iii) unwrapped phase $\phi_{1,2}(\omega)$ (solid black line) and approximated line $\hat{\phi}_{1,2}(\omega)$ (dashed red line) for 1st and 2nd positions, and (a.iii) estimate of leak localization. The dashed blue lines correspond to the buried pipe and the dark yellow dots correspond to the leak position.

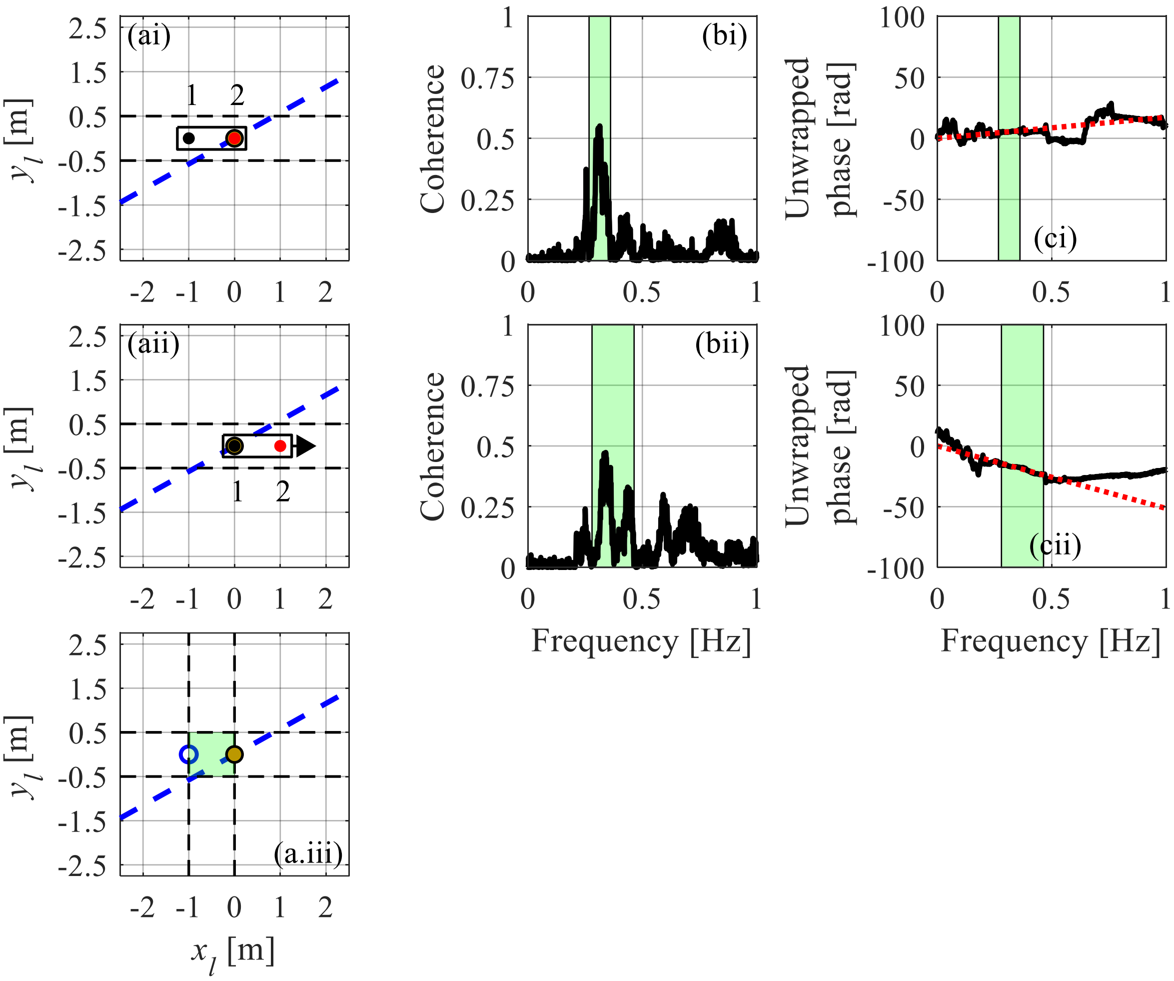

Source: elaborated by the author.

6.3 FEASIBILITY STUDY ON APPLICATION OF GEOPHONES TOGETHER WITH THE TWO-SENSOR TECHNIQUE

From the application of both localization techniques presented in Chapter 5, it can be seen that the one-sensor technique is more sensitive to environmental noise than the two-sensor technique if measurements are carried out on ground surface relatively far from the leak along the pipe, as discussed for the results of the British test rig, and the two-sensor technique is more suitable for an environment with a high-level source of noise than the one-sensor technique, as discussed for the results of the first experiment in the Brazilian test rig. The application of both localization techniques presented previously in this chapter highlights that the two-sensor technique can locate a pipe and a leak on the ground surface, even if the measurement lines are not perpendicular to pipe direction, but they must be as close as possible to 90° as discussed in Chapter 3. Although the aforementioned results indicate a promising performance of the two-sensor technique in relation to the one-sensor technique, some important limitations were also observed. The first limitation is the poor coherence and phase unwrapping for positions relatively far from the buried pipe along the measurement line. The second limitation is the poor coherence and phase unwrapping for positions relatively far from the leak along the pipe, which is a kind of behavior that was not observed for the experimental data acquired in the British test rig.

It is evident that one of the most important considerations to locate a buried pipe and a leak using measurements of ground surface vibration is the type of sensor, whose SNR must be as high as possible to sense properly low-level vibration on the ground surface. Geophones, for example, are sensors commonly used to measure low-level ground vibration caused by earthquakes (LIU *et al*., 2017; HANSEN, SCHMANDT, 2015; SHENG *et al*., 2021), underground blasts (MILEV *et al*., 2001; RAMULU; CHAKRABORTY; SITHARAM, 2009; MURPHY *et al*., 2012), moving trains (PRIEST; POWRIE, 2009; CRESPO-CHACÓN; GARCÍA-DE-LA-OLIVA; SANTIAGO-RECUERDA, 2016; HE *et al*., 2020), traffic roads (ZHAO; RECTOR, 2010; RIAHI; GERSTOFT, 2015; LIU *et al*.; 2017), etc., and also to measure ground vibration due to a buried leaking pipe (WANG *et al*., 2017; CHENG *et al*., 2018; YAN *et al*., 2020; XERRI *et al*., 2022). The application of geophones on works correlated to one presented in this thesis and their satisfactory performance on the British test rig, presented in Chapter 5, motivate a feasibility study on the application of such a type of sensor with the two-sensor technique on the Brazilian test rig, to verify if their combination can overcome the limitations found in the previous results.

6.3.1 Results for the application of two-sensor technique with geophones

The same measurement grid illustrated in Fig. 64(a) was elaborated for the feasibility study, and 8 SM-24 geophones were used to acquire vertical ground surface velocities along each measurement line of zones A, B and C. The LMS SCADAS data acquisition system was also used to store the measurements, which consist of 60 s long velocity time histories sampled at a frequency of 12.8 kHz. Note that the experiment with geophones was not carried out simultaneously with the one with accelerometers, due to the limited number of channels of the data acquisition system.

Before applying the localization technique, the experimental data were passed through a bandpass filter with cutoff frequencies of 130 Hz and 1,000 Hz, to remove low-frequency noise and to prevent aliasing. Harmonics at integer multiples of 60 Hz were observed during the analysis of the experimental data as shown in Fig. 72, which presents the spectral density for the geophone positioned at the origin of the measurement grid. This phenomenon is probably caused by ground loops because the geophones were not electrically isolated during experiments and were attached to a structure (in this case, the ground surface) that has a different electrical potential than the data acquisition. So, a portion of the current flows through the cable ground shield and connectors, resulting in harmonics at integer multiples of line frequency captured by the measurement system (O'CONNELL, 2001).

Figure 72 - Spectral density for the geophone positioned at the origin of measurement grid.

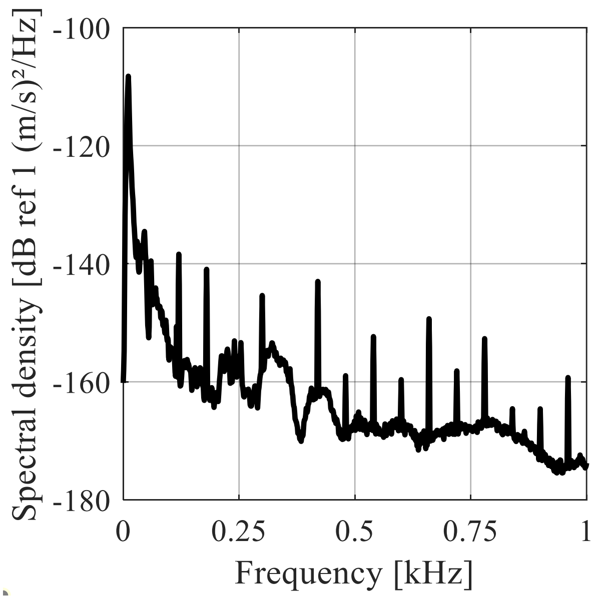

Source: elaborated by the author.

To prevent the interference of such spurious signals on the application of two-sensor technique, the experimental data were also passed through a comb filter to remove the integer multiples of the line frequency. Then, the cross-spectral density and coherence were calculated via Eqs. (5.1) and (5.2), respectively, for each pair of positions along each measurement line shown in Fig. 64(a). Both functions were determined by averaging the time-series using segment averaging (SHIN; HAMMOND, 2008) with 64 averages, 12,800-point fast Fourier transform and a Hanning window with 50% overlap, resulting in a frequency resolution of 1 Hz. The modified tracking algorithm of the two-sensor technique is then applied to estimate the limits of the leak noise bandwidth, and to calculate the approximate slope of unwrapped phase for each pair of positions. As explained previously, a great amount of results is generated when the two-sensor technique is applied because coherence and unwrapped phase are calculated for each pair of position along each measurement line. Therefore, only the results for the 2^{nd} measurement line of zone B are presented to provide a detailed discussion without extending unnecessarily.

The results for pipe localization with the two-sensor technique applied on the 2^{nd} measurement line of zone B are presented in Figs. 73 and 74, where the dashed blue lines correspond to the buried pipe and the dark yellow dots correspond to the leak position. By analyzing Figs. 65(b.i-iv), 66(b.i-iii), 73(b.i-iv) and 74(b.i-iii), it can be seen that the coherences resulted for the application with geophones contain higher values at low frequencies than the coherences resulted for the application with accelerometers. This difference is consistent with the theory discussed in Appendix C, in which the geophones are more sensitive than the accelerometers for frequencies below about 92 Hz. Note also that the coherences resulted for the application with geophones also contain higher values at high frequencies, than the coherences resulted for the application with accelerometers. This difference, however, is not consistent with the theory presented in Appendix C, where it is expected that the accelerometers would perform better than the geophones at high frequencies, and the respective reasons are still unknown. A new investigation in which both sensors are tested simultaneously needs to be carried out under controlled conditions, to check experimentally their sensitivity and spectral noise to properly understand which sensor is more suitable for such an application. Once this is done, the performance for both sensors with the two-sensor technique can be properly compared by elaborating a set of geophones and a set of accelerometers on the test rig.

Figure 73 - Pipe localization with the two-sensor technique applied on 2nd measurement line of zone B for the measurement grid with geophones - Part 1. (a.i-iv) 1st, 2nd, 3rd and 4th positions of the pair of sensors, (b.i-iv) coherence $\gamma_{1,2}^{2}(\omega)$, (c.i-iii) unwrapped phase $\phi_{1,2}(\omega)$ (solid black line) and approximated line $\hat{\phi}_{1,2}(\omega)$ (dashed red line) for 1st, 2nd, 3rd and 4th positions.

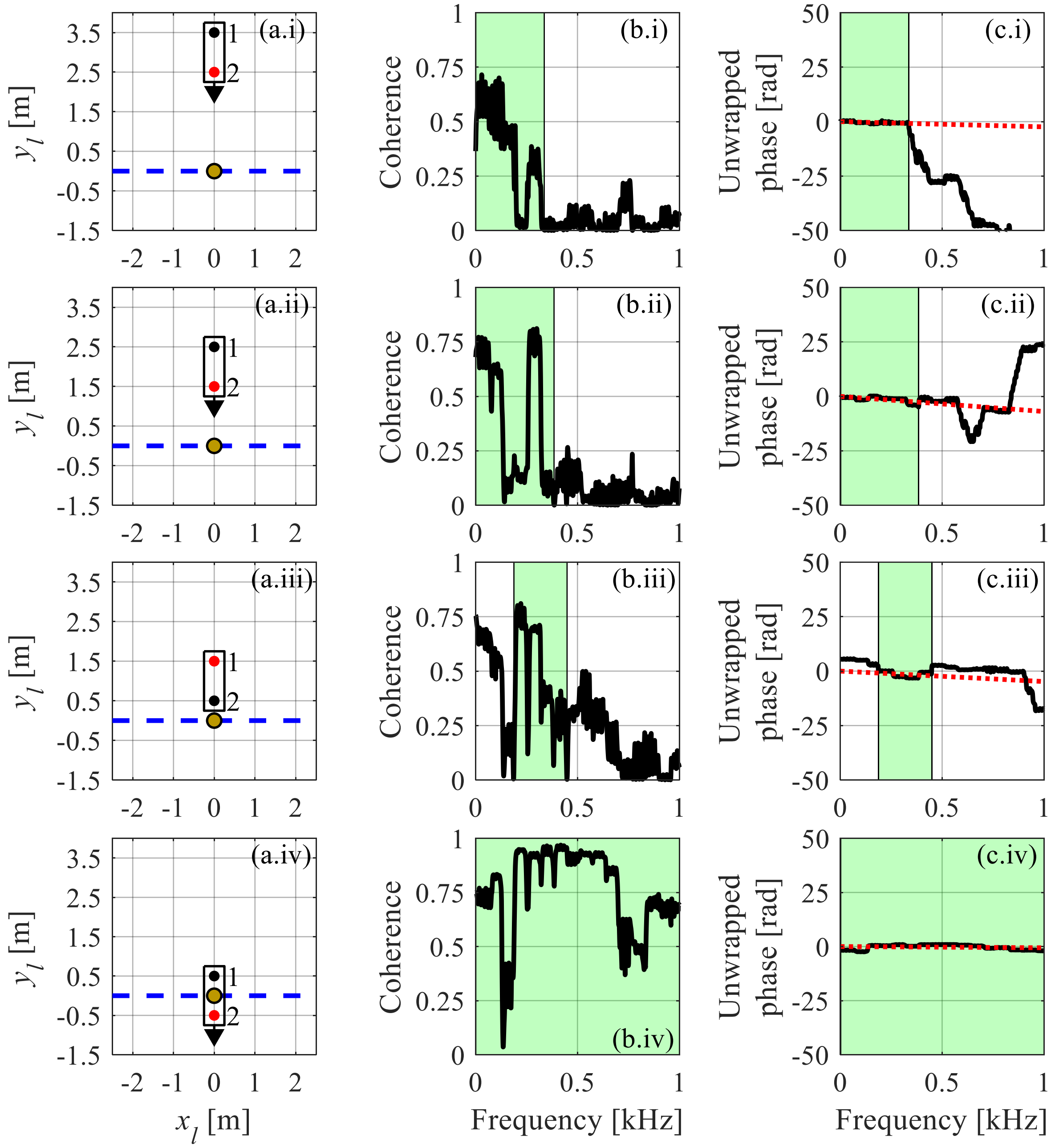

Source: elaborated by the author.

Figure 74 - Pipe localization with the two-sensor technique applied on 2nd measurement line of zone B for the measurement grid with geophones - Part 2. (a.i-iv) 5th, 6th and 7th positions of the pair of sensors, (b.i-iv) coherence $\gamma_{1,2}^{2}(\omega)$, (c.i-iii) unwrapped phase $\phi_{1,2}(\omega)$ (solid black line) and approximated line $\hat{\phi}_{1,2}(\omega)$ (dashed red line) for 5th, 6th and 7th, and (a.iv) estimate of pipe localization.

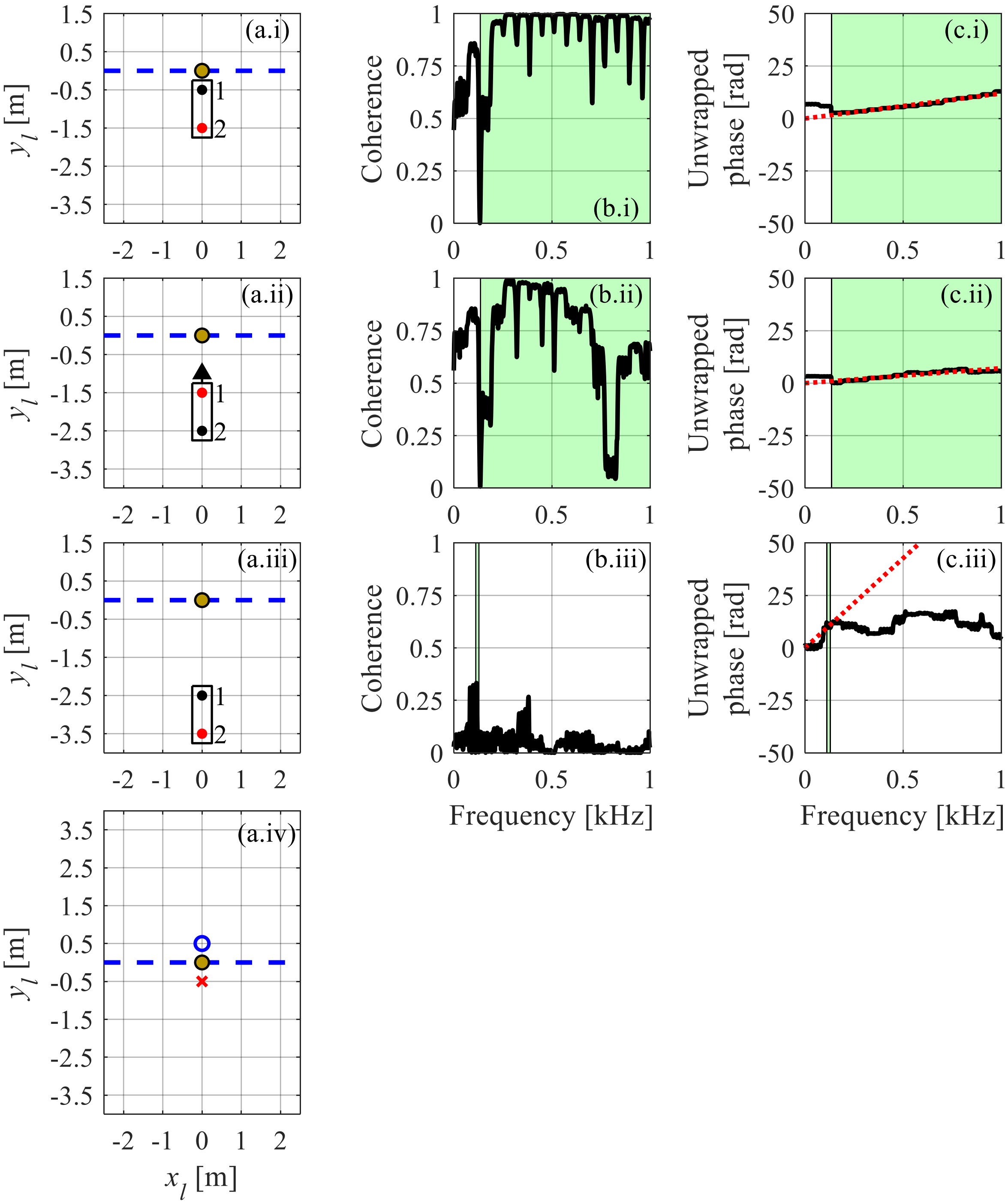

Source: elaborated by the author.

By analyzing Figs. 73(c.i-iv) and 74(c.i-iii), it can be seen that the phase is unwrapped adequately within the limits of leak noise bandwidth, and the modified tracking algorithm successfully captures the corresponding slope by approximating the line $\hat{\phi}_{1,2}(\omega)$. By comparing Figs. 65(c.i-iv) and 66(c.i-iii) with Figs. 73(c.i-iv) and 74(c.i-iii), it can be seen that the phase measured by the geophones presents a more evident slope than the phase measured by the accelerometers, for positions farther than 1.5 m from the leak position along the measurement line. These results suggest that the geophones improve the chances of the two-sensor technique to track the pipe for farther distances on ground surface, though a side-by-side comparison is still necessary to comprehend their limitations.

6.3.2 Comparison between the performances of two-sensor technique using geophones and accelerometers

The results for pipe localization with the two-sensor technique applied on each zone of the measurement grid with geophones are presented in Fig. 75. To evaluate qualitatively the performance of the geophones in relation to the accelerometers, the results of Figs. 67(b.i), 67(b.ii) and 67(b.iii) are compared with the ones of Figs. 75(a), 75(b) and 75(c), respectively, since their grids are the same but the measurements with both type of sensors were not carried out simultaneously. Note that the two-sensor technique only located the pipe position for zone B using accelerometers, while the same technique located the pipe position for zones A and B using geophones. Also note that, for the same zone of Figs. 67(b.i-iii) and 75(a-c), that the amount of wrong estimates for pipe localization on each measurement line is less using geophones than using accelerometers, due to a better phase unwrapping resulted from the measurements with geophones. These two results demonstrate that the geophones improve the chances of the two-sensor technique to locate the pipe position, when measurements of ground surface vibration are carried out far from the buried pipe, which can also be confirmed by the results of Figs. 73 and 74.

Figure 75 - Results for pipe localization with two-sensor techniques applied on (a) zone A, (b) zone B and (c) zone C of the measurement grid with geophones. The dashed blue lines correspond to the buried pipe and the dark yellow dots correspond to the leak position.

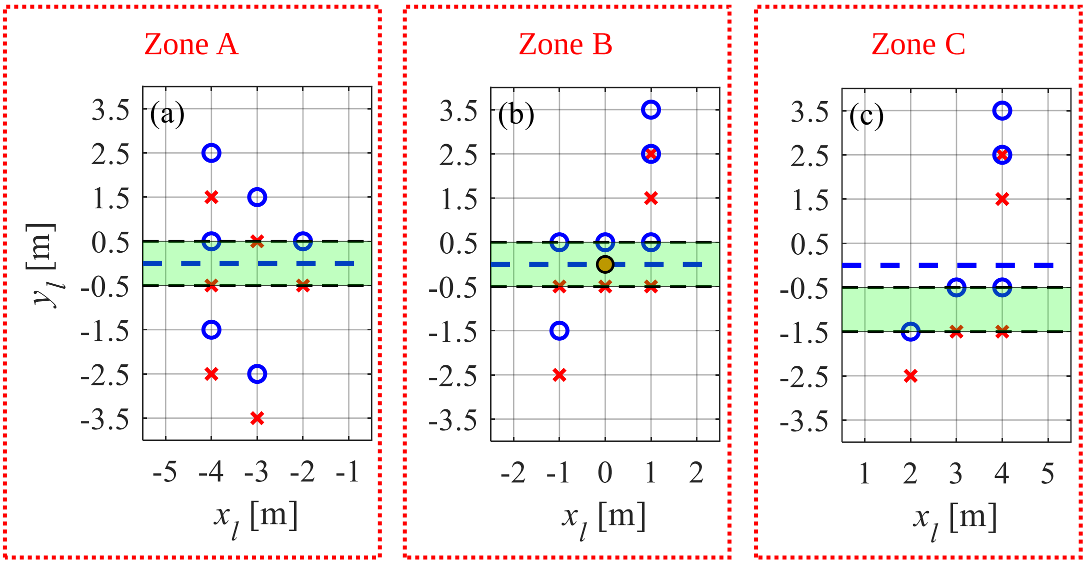

Source: elaborated by the author.

Once the buried pipe is located, the two-sensor technique is applied along the pipe region elaborated for zone B to circumscribe the leak region on ground surface, whose results are shown in Fig. 76. By comparing Figs. 70(b.i-ii) and 76(b.i-ii), it can be seen that the coherences when using geophones contain higher values than the coherences when using accelerometers for frequencies higher than 92 Hz.

By analyzing Figs. 76(c.i-ii), it can be seen that the phase is unwrapped adequately within the limits estimated for the leak noise bandwidth. By comparing Figs. 70(c.i-ii) and 76(c.i-ii), the phase measured by the geophones presents a more evident slope for a broader bandwidth, than the phase measured by the accelerometers. Note that this not expected because the accelerometers are more sensitive than the geophones for frequencies higher than 92 Hz, as explained in Appendix C. Note also by comparing Figs. 70(c.i-ii) and 76(c.i-ii), that the corresponding unwrapped phases contain different slopes, in which the results for the accelerometers contain greater slopes than the results for the geophones. This indicates that one of the experiments captured an extra wave propagating on the ground surface with a different speed. Furthermore, the signs of the corresponding slopes are also different, in which they change from positive to negative in Figs. 70(c.i-ii) and from negative to positive in Figs. 76(c.i-ii), which also suggests that that one of experiments captured an extra wave.

Figure 76 - Leak localization with two-sensor technique applied on zone B for the measurement grid with geophones. (a.i-ii) 1st and 2nd positions of the pair of sensors, (b.i-ii) coherence $\gamma_{1,2}^2(\omega)$, (c.i-iii) unwrapped phase $\phi_{1,2}(\omega)$ (solid black line) and approximated line $\hat{\phi}_{1,2}(\omega)$ (dashed red line) for 1st and 2nd positions, and (a.iii) estimate of leak localization.

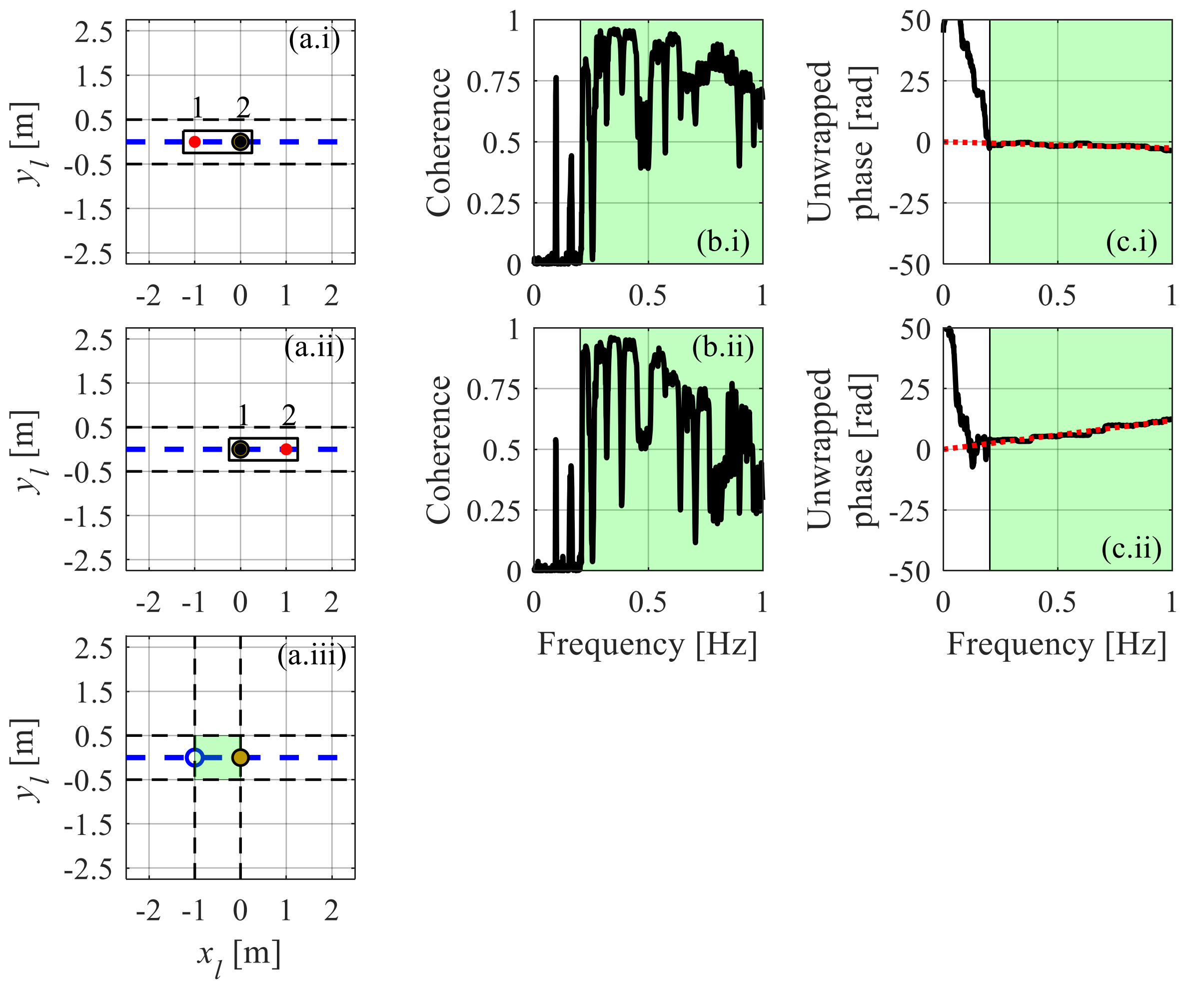

Source: elaborated by the author.

6.4 CONCLUSIONS

This chapter has presented the results for an experimental investigation to check possible limitations that might occur during the practical application of both location techniques. The first limitation assumed for the investigation was the distance between the buried pipe and the measurement positions, and the second limitation was to assume that the measurement lines are misaligned in relation to pipe direction. To investigate such limitations, a second experiment was carried out on the Brazilian test rig, in which much wider measurement grids with 0°, 30° and 60° misalignment angle were elaborated on the ground surface to measure ground surface vibration with accelerometers.

The first limitation was checked by analyzing the results for the measurement grid with 0° misalignment, which is similar to the first experiment performed on the Brazilian test rig but using longer measurement lines. Although the results for such an investigation suggest that the two-sensor technique has a better performance than the one-sensor technique, the coherences are poor, the estimates for leak noise bandwidth are narrow, and the phases are inadequately unwrapped for measurement positions on the ground surface farther than 2.5 m from the pipe. This indicates that the accelerometers cannot sense the ground surface vibration due to the waves radiating from the main pipe and the leak for such distances. The second limitation was checked by comparing the final results for the measurement grids with 0°, 30° and 60° misalignment. The results for such an investigation show that the two-sensor technique has a better performance than the one-sensor technique, in which the two-sensor technique can locate a leak on the ground surface even when the measurement lines are not perpendicular to the pipe direction. However, as discussed in Chapter 3, this is only valid if the misalignment angle is not too great, and the distance of the measurement positions in relation to the buried pipe is not greater than 2.5 m when using accelerometers. A third limitation was also discovered during the analysis of the results, in which both localization techniques cannot locate the buried pipe for distances longer than 2 m in relation to the leak position, along x_l-axis of the measurement grid.

A third experiment was performed to investigate if the application of geophones would improve the performance of the two-sensor technique, as they usually have higher sensitivity for low frequencies than accelerometers. To carry out such an experiment, the same measurement grid with 0° misalignment was elaborated using geophones, rather than accelerometers. The results for pipe localization obtained for the experiment with geophones were compared with the ones obtained for the experiment with accelerometers. The comparison shows that the coherences contain higher values, the estimates for leak noise bandwidth are broader, and the phases are adequately unwrapped for much higher frequencies when using geophones rather than accelerometers. Then, the final results obtained for the experiment with geophones were compared with the ones obtained for the experiment with accelerometers. The comparison shows that the amount of wrong estimates for pipe localization on each measurement line is less when using geophones than using accelerometers. This indicates that the geophones can improve the chances of the two-sensor technique to locate the pipe position, when measurements are carried out on the ground surface far from the pipe.

7 FINAL REMARKS

7.1 SUMMARY OF THE THESIS

The main objective of the research presented in this thesis was to investigate a novel leak localization technique based on measurement of ground surface vibration. It is able to locate an approximate position for the pipe and the leak on the ground surface considering the propagation of multiple waves in the soil and the interference of background noise on the measurements. Based on the research conducted by Muggleton, Brennan and Gao (2011), the unwrapped phase between a pair of sensors on the ground surface has been investigated to extract an indication of the pipe and the leak, due to its robustness to uncorrelated noise. The content of this thesis is summarized as follows.

In Chapter 1, the available leak localization technologies are briefly introduced. It is found that single-sensor roving devices are commonly used to pinpoint the leak position, by measuring ground surface vibration when access to the buried pipe is not possible. Although these devices are able to locate a leak when the amplitude of the noise measured on the ground surface is high in relation to background noise, there are some situations commonly found in the practice that limit their performance, such as when the amplitude of leak noise is low in relation to background noise, or when a high-level external source of noise is situated close to the measurement site. The state-of-the-art research for acoustic source localization techniques was introduced to investigate potential solutions for the limitations of the localization technique used by single-sensor roving devices. However, implementing such techniques to locate leaks in buried pipes might be quite challenging, as they rely on a precise estimation for the wave speed, and multiples waves can propagate in the soil simultaneously. The limitations of single-sensor roving devices and the limitations of current acoustic source localization techniques available in the literature are the main motivation of the research presented in this thesis.

Chapter 2 briefly introduces the theoretical model for wave propagation in a buried pipe system proposed by Muggleton *et al*. (2023), to explain the physics behind the vibration captured by sensors on the ground surface when there is a buried leaking pipe. Such a model assumes that the predominantly fluid-borne axisymmetric wave is the only propagating in the pipe, no reflections occur in the system, and the surrounding soil is an elastic medium where shear and compressional waves can propagate. It is explained with the theoretical model that one or more waves can radiate from the pipe depending on the type of soil where the measurements are carried out, as the speed of the compressional and shear conical waves depends on the soil properties. So, if the speed of the wave propagating in the pipe is greater than the speed of a wave in the soil, then a conical wave radiates from the pipe into the soil. Otherwise, the wave radiating from the pipe is evanescent and, hence, does not propagate towards the ground surface. Once a conical wave or a combined conical wave reaches the surface, an approximate hyperbola of constant phase is perceived by the sensors. A numerical model for the buried pipe system and an experiment are used to extract ground surface vibration data to validate the theoretical model.

The technique on which single-sensor roving devices are based on, named the one-sensor technique, is introduced in Chapter 3 to provide a baseline for the technique proposed in this research, named the two-sensor technique, introduced in Chapter 3 as well. The one-sensor technique is based on the amplitude difference for different positions on the ground surface, in which the position that contains the highest amplitude corresponds to the leak position. The two-sensor technique is explained using the shape and direction of propagation of the lines of constant phase that travel on the ground surface. Such a technique marks on the ground surface the pipe position when the sign of slope of unwrapped phase changes along a measurement line, and the leak position when the sign of slope of unwrapped phase changes along the pipe. The localization procedure of both techniques is divided into two stages, in which the first one is to locate the pipe position, named pipe localization, and the second one is to locate the leak position, named leak localization. The tracking algorithm is presented, which is an algorithm of the two-sensor technique that tracks the direction for the pair of sensors to cross the pipe, or the leak, on the ground surface. Then, the dependence of the two-sensor technique on the angle between the measurement lines and pipe direction is introduced as a theoretical background, to highlight the importance of setting the measurement lines as close as possible to 90° in relation to pipe direction when using the two-sensor technique. The data extracted from the theoretical and numerical models are used to illustrate the application of both localization techniques when the measurement lines are perpendicular to pipe direction, and when they are misaligned in relation to pipe direction.

Two important features for the practical application of the two-sensor technique are investigated in Chapter 4. The first feature investigated is the extraction of the indication for pipe location in the time and frequency domains, and the second feature investigated is the minimum distance between the pair of sensors on which the two-sensor technique can effectively extract such an indication. The experimental data acquired on the British test rig is used to carry out both investigations, where the two-sensor technique is applied to estimate the location of the respective buried pipe.

In Chapter 5, a modified version of the tracking algorithm is presented since the original version might not work properly for practical applications, due to interference of environmental noise and external sources of noise. In the modified version, the direction for the pair of sensors to cross the pipe, or the leak, on the ground surface is a result of the comparison between the direction informed by amplitude and the direction informed by phase. After introducing the modified tracking algorithm, the performance of the one-sensor and two-sensor techniques are evaluated by testing them on the experimental data collected in the British and Brazilian test rigs.

Chapter 6 presents the comparison between the performances of the one-sensor and two-sensor techniques for complex situations, where the measurement positions on the ground surface are farther from the buried pipe, and the measurement lines are misaligned to the pipe direction. To conduct such an investigation, a second experiment was carried out in the Brazilian test rig, where wider measurement grids with different misalignment angles in relation to the pipe direction were deployed on the ground surface. Then, a feasibility study on the application of geophones with the two-sensors technique was carried out to evaluate if such a type of sensor can improve the technique performance in relation to accelerometers, since geophones are usually more sensitive than accelerometers at low frequencies.

The thesis is summarized in Chapter 7, and then the main conclusions are presented with some recommendations for further work.

7.2 MAIN CONCLUSIONS

Some important conclusions can be extracted for each investigation conducted in this thesis, emphasizing the contributions for the state-of-the-art research on leak localization in buried water pipes and providing suggestions for future research. For ease of reference, the main conclusions are given for each chapter as follows:

- Chapter 2: the comparison between the contour maps for amplitude and spatially unwrapped phase indicates that the theoretical model for a buried pipe system, proposed by Muggleton *et al*. (2023), can replicate properly the lines of constant phase that travel on the ground surface due to the waves that radiate from a leaking buried pipe. The same model, however, cannot replicate faithfully the amplitude of ground surface vibration as it does not consider the waves radiating from the leak (source), neither the reflections of incident waves on the ground surface.

- Chapter 3: the leak localization technique proposed in this research is based on the unwrapped phase of a roving pair of sensors, positioned on the ground surface in relation to the buried pipe. The main advantages of the proposed technique are that it has a simple setup, as it only requires two synchronized sensors on the ground surface, and it does not depend on knowing the wave speed for the localization procedure, as most of the acoustic source localization techniques available in the literature. Note that estimating such a speed in the soil might be quite complex, since more than one type of wave can propagate depending on the type of soil. However, the main disadvantages of the proposed technique are that it depends on an estimate for the pipe direction, so the measurement lines can be set as close as possible to 90° in relation to it, and multiple measurements must be carried out until the roving pair of sensors crosses the pipe, or the leak, on the ground surface.

- Chapter 4: the results for the first investigation have shown that extracting the indication for pipe location in the frequency domain is more suitable for practical applications of the two-sensor technique, than extracting it in the time domain. This is because the proposed technique estimates a slope by approximating a line for the values of unwrapped phase, within the bandwidth in which the pair of signals are well coherent. It was discovered that such a procedure is more robust than finding the maximum absolute cross-correlation for the pair of positions, because the approximate line compensates for the phase changes caused by external phenomena. The results for the second investigation have shown that the minimum distance between the pair of sensors must not be less than 1 m for the two-sensor technique, otherwise the phase changes caused by external phenomena become dominant and, consequently, the chances of the technique of resulting a wrong estimate for pipe location increases.

- Chapter 5: the preliminary analysis of the experimental data has shown that the waves radiating from a flexible pipe, which collects the water that escapes through a leak in the main pipe, have a profound effect on the experiment carried out in the Brazilian test rig. Since the main pipe is the one that effectively contains the leak in the test rig, the investigation is carried out assuming that the flexible pipe is a high-level source of noise in the experiment, and both techniques are applied to locate the leak in the main pipe. Then, the one-sensor and two-sensor techniques are applied to locate the main pipe of the British test rig, and to locate the main pipe and the leak of the Brazilian test rig. For both applications, the measurement lines are arranged on the ground surface perpendicular to the main pipe. The results for the British test rig have shown that the two-sensor technique can locate the pipe for much longer distances than the one-sensor technique. This is because the sensors are still able to capture the approximate hyperbolas of constant phase that travel on the ground surface due to a leaking buried pipe, though the amplitude of the respective waves is heavily attenuated with the distance relative to the leak. The results for the Brazilian test rig have shown that the two-sensor technique is more robust to the interference of an external source of noise than the one-sensor technique. This is because the sensors are still able to capture the approximate circles of constant phase that travel on the ground surface due to the leak in the main pipe, though the amplitude of the waves that radiate from the flexible pipe is much higher than the amplitude of the waves that radiate from the leak in the main pipe.

- Chapter 6: a second experiment was carried out in the Brazilian test rig to evaluate the performance of the two-sensor technique in relation to the one-sensor technique, when the measurement positions are much farther from the pipe, and when the measurement lines are misaligned to the pipe direction. The results have shown that the proposed technique still can locate the pipe, and the leak afterwards, when such a condition is not attended. However, the misalignment angle must be as close as possible to 90° in relation to pipe direction, otherwise the technique performance decreases considerably. The results for the feasibility study have shown that, for the experiment with geophones, the coherences are greater and contain a broader bandwidth for farther positions in relation to the pipe, and to the leak, than for the experiment with accelerometers. The results have also shown that, for the experiment with geophones, the phases are properly unwrapped within a broader bandwidth for farther positions in relation to the pipe, and to the leak, than for the experiment with accelerometers. The results of such an investigation suggests that geophones can improve the technique performance in relation to accelerometers when the measurement positions are distant from the pipe, or the leak, on the ground surface.

7.3 RECOMMENDATIONS FOR FURTHER WORK

The main objective of this thesis was to propose a leak localization technique for buried water pipes based on measurements of ground surface vibration, which is robust to the interference of environmental noise and other external sources of noise, and does not require knowing the wave speeds for the localization procedure. The conclusions provided in the previous section state the main contributions and gaps of the research conducted by the author, his supervisors, and colleagues, paving the way for further work as follows:

- The vibration sensed on the ground surface is due to a portion of the compressional and shear waves that is transmitted, since another portion is reflected back to soil when they reach the ground surface (GAO *et al*., 2017). When a second layer is added between the sensors and the ground surface, such as asphalt or concrete, the waves reflect at least twice because they travel at different speeds in the soil and in the second layer (GRAFF, 1975). Hence, the vibration sensed on the ground surface in even lower. Therefore, it is recommended to investigate the influence of different types of layers on the wave propagation in a soil medium, and then evaluate the performance of the proposed technique for each of them.

- As it was discussed in Chapter 3, the performance of two-sensor technique depends on the angle between the measurement lines and the pipe direction. It is recommended to develop an analytical model to predict with more precision the critical value for this angle, on which the algorithm of the two-sensor still can perceive that the pair of sensors has crossed the pipe on the ground surface.

- As a sensor can only measure vibration on the ground surface depending on the level of pipe excitation and the attenuation in the soil, it is recommended to investigate the performance of the proposed technique for different leak sizes and different pipe burial depths.

- As interferences of ground loops and external sources were observed on the comparison between the application of geophones and accelerometers, a new investigation is necessary to decide which sensor is more suitable for the two-sensor technique. Therefore, it is recommended to carry out an experiment where the geophones and the accelerometers are used simultaneously to measure vibration in an indoor environment, to avoid the interference of external sources of noise when estimating the SNR for each sensor. It is also recommended to isolate the sensors and assure that there is no voltage difference between them to avoid ground loops.

- It is recommended to extend the theoretical model proposed by Muggleton *et al.* (2023), considering the waves radiating from the leak into the soil and also the reflection of their incident waves on the ground surface, to check if it can replicate faithfully amplitude of ground surface vibration and the lines of constant phase close to the leak position.

- As it was discussed in Chapter 5, the leak mechanism can have a profound effect on measurements carried out on the ground surface. To guarantee that a test rig simulates properly a buried pipe with a real leak, it is necessary to choose a mechanism that can replicate faithfully the pipe excitation resulted by a real leak. Therefore, investigating different types of leak mechanisms, such as valves, connections, and some types of standpipes, is recommended to verify which one is more suitable for this kind of application.

REFERENCES

ABDULLAH, A Z. **Smartphones, floating balls and monitoring sensors**: how Singapore is going high-tech in detecting water leaks. CNA, 2020. Available in: https://www.channelnewsasia.com/singapore/high-tech-detecting-water-leaks-533736. Accessed on: 6 Jan. 2022.

ABOUHAMAD, M.; ZAYED, T.; MOSELHI, O. Leak detection in buried pipes using ground penetrating radar – A comparative study. **Pipelines 2016**: Out of Sight, Out of Mind, Not Out of Risk, p. 417-424, 2016. Available in: https://doi.org/10.1061%2F9780784479957.039. Accessed on: 12 Dec. 2022.

ADS. **Eureka2R leak noise correlator user manual**. [*S. l.*], 2010. Available in: https://www.adsenv.com/sites/default/files/manuals/adseureka2rusermanuala1.pdf. Accessed on: 6 Jan. 2023.

ALKASSEH, J. M. A.; ADLAN, M. N.; ABUSTAN, I.; AZIZ, H. A.; HANIF, A. B. M. Applying minimum night flow to estimate water loss using statistical modeling: A case study in Kinta Valley, Malaysia. **Water Resour Manage**, [*s. l.*], v. 27, p. 1439-1455, 2013. Available in: https://doi.org/10.1007/s11269-012-0247-2. Accessed on: 6 Jan. 2023.

AL QAHTANI, T.; YAAKOB, M. S.; YIDRIS, N.; SULAIMAN, S.; AHMAD, K. A. A review on water leakage detection method in the water distribution network. **Journal of Advanced Research in Fluid Mechanics and Thermal Sciences**, v. 68, n. 2, p. 152-163, 2020. Available in: https://akademiabaru.com/submit/index.php/arfmts/article/view/2880. Accessed on: 17 Jan. 2023.

ALMEIDA, F. C. L. **Improved acoustic methods for leak detection in buried plastic water distribution pipes**. 2013. 240 f. Thesis (PhD in Mechanical Engineering) – University of Southampton, Southampton, 2013.

ALMEIDA, F. C. L.; BRENNAN, M. J.; JOSEPH, P. F.; GAO, Y.; PASCHOALINI, A. T. The effects of resonances on time delay estimation for water leak detection in plastic pipes. **Journal of Sound and Vibration**, London, v. 420, p. 315-329, 2018. Available in: https://doi.org/10.1016/j.jsv.2017.06.025. Accessed on: 17 Jan. 2023.

ALMEIDA, F. C. L.; BRENNAN, M. J.; LIMA, F. K.; IWANAGA, M. K.; SCUSSEL, O. Using a geophone as an actuator to estimate the velocity of leak noise propagation in buried water pipes. **Applied Acoustics**, Oxford, v. 184, n. 108251, 2021. Available in: https://doi.org/10.1016/j.apacoust.2021.108251. Accessed on: 6 Jan. 2023.

AQUASAVE. **Leak detection**. [*S. l.*], 2015. Available in: http://www.aquasave.mk/en-GB/Home/ServiceDetails/15. Accessed on: 24 Jan. 2023.

ATKINS, P. South West Water leak detectors reveals the quirky tricks of his trade. **Cornwall Live**. [*S. l.*], 2022. Available in: https://www.cornwalllive.com/special-features/south-west-water-leak-detector-7324226. Accessed on: 6 Jan. 2022.

AZO SENSORS. **What is a hydrophone?** [*S. l.*], 2012. Available in: https://www.azosensors.com/article.aspx?ArticleID=13. Accessed on: 6 Jan. 2023.

BAVITECH CORPORATION. **Water leak detection services.** [*S. l.*], 2023. Available in: https://bavitech.com/service/water-leak-detection-services/. Accessed on: 24 Jan. 2023.

BRENNAN, M. J.; KARIMI, M.; ALMEIDA, F. C. L.; LIMA, F. K.; AYALA, P. C.; OBATA, D.; PASCHOALINI, A. T.; KESSISSOGLOU, N. On the role of vibro-acoustics in leak detection for plastic water distribution pipes. **Procedia Engineering**, Amsterdam, v. 199, p. 1350-1355, 2017. Available in: https://doi.org/10.1016/j.proeng.2017.09.350. Accessed on: 16 Jan. 2023.

BRENNAN, M. J.; KARIMI, M.; MUGGLETON, J. M.; ALMEIDA, F. C. L.; LIMA, F. K.; AYALA, P. C.; OBATA, D.; PASCHOALINI, A. T.; KESSISSOGLOU, N. On the effects of soil properties on leak noise propagation in plastic water distribution pipes. **Journal of Sound and Vibration**, London, v. 427, p. 120-133, 2018. Available in: https://doi.org/10.1016/j.jsv.2018.03.027. Accessed on: 16 Jan. 2023.

BROWN, M. E.; FUNK, C. C. Food security under climate change. **Science**, v. 319, n. 5863, p. 580-581, 2008. Available in: https://doi.org/10.1126/science.1154102. Accessed on: 3 Jan. 2023.

BUREK, P.; SATOH, Y.; FISCHER, G.; KAHIL, M. T.; SCHERZER, A.; TRAMBEREND, S.; NAVA, L. F.; WADA, Y.; EISNER, S.; FLÖRKE, M.; HANASAKI, N.; MAGNUSZEWSKI, P.; COSGROVE, B.; WIBERG, D. **Water futures and solution**: fast track initiative. Technical Report – International Institute for Applied Systems Analysis, Laxenburg, 2016. Available in: https://pure.iiasa.ac.at/id/eprint/13008/. Accessed on: 5 Jan. 2023.

BURN, S.; DESILVA, D.; EISWIRTH, M.; HUNAIDI, O.; SPEERS, A.; THORNTON, J. **Pipe leakage – Future challenges and solutions**. [*S. l.*], 1999. Available in: https://www.researchgate.net/publication/44055423_Pipe_Leakage_-_Future_Challenges_and_Solutions. Accessed on: 7 Jan. 2023.

CATALDO, A.; PERSICO, R.; LEUCCI, G.; DE BENEDETTO, E.; CANNAZZA, G.; MATERA, L.; DE GIORGI, L. Time domain reflectometry, ground penetrating radar and electrical resistivity tomography: A comparative analysis of alternative approaches for leak detection in underground pipes. **NDT & E International**, London, v. 62, p. 14-28, 2014. Available in: https://doi.org/10.1016/j.ndteint.2013.10.007. Accessed on: 16 Dec. 2022.

CHEN, J. C.; YAO, K.; HUDSON, R. E. Acoustic source localization and beamforming: Theory and practice. **EURASIP Journal on Applied Signal Processing.** [*S. l.*], 2003. Available in: https://doi.org/10.1155/S1110865703212038. Accessed on: 17 Jan. 2022.

CHATZIGEORGIOU, D. M.; YOUCEF-TOUMI, K; KHALIFA, A. E.; BEN-MANSOUR, R. Analysis and design of an in-pipe system for water leak detection. *In:* DESIGN AUTOMATION CONFERENCE, PARTS A AND B, 37., 2011, Washington. **Proceedings of the ASME 2011 International Design Engineering Technical Conferences and Computers and Information in Engineering Conference**. ASME, 2012, p. 1007-1016.

CHENG, F.; LIU, J.; WANG, J.; YANG, Z.; ABBASI, S. S.; TIAN, Z.; XU, H. Locating leaking buried pipes based on ground microseismic records in 3D space. **Surveys in Geophysics**, Dordrecht, v. 39, p. 993-1007, 2018. Available in: https://doi.org/10.1007/s10712-018-9479-x. Accessed on: 7 Jan. 2023.

COBOS, M.; ANTONACCI, F.; ALEXANDRIDIS, A.; MOUCHTARIS, A.; LEE, B. A survey of sound source localization methods in wireless acoustic sensor networks. **Wireless Communications and Mobile Computing.** [*S. l.*], 2017. Available in: https://doi.org/10.1155/2017/3956282. Accessed on: 28 Nov. 2022.

CRESPO-CHACÓN, I.; GARCÍA-DE-LA-OLIVA, J. L.; SANTIAGO-RECUERDA, E. On the use of geophones in the low-frequency regime to study rail vibrations. **Procedia Engineering**, Amsterdam, v. 143, p. 782-794, 2016. Available in: https://doi.org/10.1016/j.proeng.2016.06.126. Accessed on: 23 Jan. 2023.

DATAMATIC. **Permalog+ leak noise loggers**. [*S. l.*], 2023. Available in: https://www.environmental-expert.com/products/permalog-leak-noise-loggers-122138. Accessed on: 24 Jan. 2023.

EARTH SCIENCES. **The geophone:** how we listen to the Earth. [*S. l.*], 2021. Available in: https://www.essearth.com/the-geophone-how-we-listen-to-the-earth/. Accessed on: 6 Jan. 2022.

ELIASSON, J. The rising pressure of global water shortages. **Nature**, London, v. 517, p. 6, 2015. Available in: https://doi.org/10.1038/517006a. Accessed on: 4 Dec. 2022.

EL-ZAHAB, S.; ASAAD, S.; MOHAMMED ABDELKADER, E.; ZAYED, T. Collective thinking approach for improving leak detection systems. **Smart Water**, v. 2, 2016. Available in: https://doi.org/10.1186/s40713-017-0007-9. Accessed on: 7 Dec. 2022.

EL-ZAHAB, S.; MOHAMMED ABDELKADER, E.; ZAYED, T. An accelerometer-based leak detection system. **Mechanical Systems and Signal Processing**, v. 108, p. 276-291, 2018. Available in: https://doi.org/10.1016/j.ymssp.2018.02.030. Accessed on: 7 Dec. 2022.

EL-ZAHAB, S.; ZAYED, T. Leak detection in water distribution networks: an introductory overview. **Smart Water**, Heidelberg, v. 4, n. 5, 2019. Available in: https://doi.org/10.1186/s40713-019-0017-x. Accessed on: 6 Jan. 2023.

ENVIROTECH ONLINE. **Pocket-sized electronic listening stick for acoustic leak detection**. Hertfordshire: International Labmate Limited, 2013. Available in: https://www.envirotech-online.com/news/portable-field-testing/43/hwm-water-ltd/pocket-sized-electronic-listening-stick-for-acoustic-leak-detection/26136. Accessed on: 6 Jan. 2022.

ESDERS. **Automated leak detection**. [*S. l.*], 2020. Available in: https://www.esders.com/2020/05/automated-leak-detection/. Accessed on: 5 Jan. 2022.

FAHMY, M.; MOSELHI, O. Detecting and locating leaks in underground water mains using thermography. *In*: INTERNATIONAL SYMPOSIUM ON AUTOMATION AND ROBOTICS IN CONSTRUCTION, 26., 2009, Austin. **Proceedings of the 26th ISARC**. IAARC, 2009, p. 61-67. Available in: https://www.iaarc.org/publications/fulltext/Detecting_and_Locating_Leaks_in_Underground_Water_Mains_Using_Thermography.pdf. Accessed on: 6 Jan. 2022.

FLOMEC. **QS200 Turf irrigation flow sensor**. [*S. l.*], 2023. Available in: https://flomecmeters.com/flomec-products/qs200-turf-irrigation-flow-sensor/. Accessed on: 24 Jan. 2023.

FOTI, S.; LAI, C. G.; RIX, G. J.; STROBBIA, C. **Surface wave methods for near-surface site characterization**. Oxford: CRC Press, 2014.

FRAUENDORFER, R.; LIEMBERGER, R. **The issues and challenges of reducing non-revenue water.** Mandaluyong City: Asian Development Bank, 2010.

FUCHS, H. V.; RIEHLE, R. Ten years of experience with leak detection by acoustic signal analysis. **Applied Acoustics**, Oxford, v. 33, n. 1, p. 1-19, 1991. Available in: https://doi.org/10.1016/0003-682X(91)90062-J. Accessed on: 6 Jan. 2023.

FUJI TECOM. **Fuji non-metallic pipe locator NPL-100**. [*S. l.*], 2022. Available in: https://www.fujitecom.com/products/pcl.html. Accessed on: 24 Jan. 2023.

GAO, Y.; BRENNAN, M. J.; JOSEPH, P. F. On the effects of reflections on time delay estimation for leak detection in buried plastic water pipes. **Journal of Sound and Vibration**, London, v. 325, 649-663, 2009. Available in: https://doi.org/10.1016/j.jsv.2009.03.037. Accessed on: 17 Jan. 2023.

GAO, Y.; BRENNAN, M. J.; JOSEPH, P. F.; MUGGLETON, J. M.; HUNAIDI, O. A model of the correlation function of leak noise in buried plastic pipes. **Journal of Sound and Vibration**, London, v. 277, n. 1-2, p. 133-148, 2004. Available in: https://doi.org/10.1016/j.jsv.2003.08.045. Accessed on: 6 Jan. 2023.

GAO, Y.; BRENNAN, M. J.; JOSEPH, P. F.; MUGGLETON, J. M.; HUNAIDI, O. On the selection of acoustic/vibration sensors for leak detection in plastic water pipes. **Journal of Sound and Vibration**, London, v. 283, n. 3-5, p. 927-941, 2005. Available in: https://doi.org/10.1016/j.jsv.2004.05.004. Accessed on: 6 Jan. 2023.

GAO, Y., LIU, Y.; MUGGLETON, J. M. Axisymmetric fluid-dominated wave in fluid-filled plastic pipes: loading effects of surrounding elastic medium. **Applied Acoustics**, Oxford, v. 116, p. 43-49, 2017. Available in: https://doi.org/10.1016/j.apacoust.2016.09.016. Accessed on: 26 Jan. 2023.

GAO, Y.; MUGGLETON, J. M.; LIU, Y.; RUSTIGHI, E. An analytical model of ground surface vibration due to axisymmetric wave motion in buried fluid-filled pipes. **Journal of Sound and Vibration**, London, v. 395, p.142-159, 2017. Available in: https://doi.org/10.1016/j.jsv.2017.02.022. Accessed on: 11 Jan. 2023.

GAO, Y.; SUI, F.; MUGGLETON, J.M.; YANG, J. Simplified dispersion relationships for fluid-dominated axisymmetric wave motion in buried fluid-filled pipes. **Journal of Sound and Vibration**, London, v. 375, p. 386-402, 2016. Available in: https://doi.org/10.1016/j.jsv.2016.04.012. Accessed on: 13 Jan. 2023.

GAUTAM, J.; CHAKRABARTI, A.; AGARWAL, S.; SINGH, A.; GUPTA, S.; SINGH, J. Monitoring and forecasting water consumption and detecting leakage using an IoT system. **Water Supply**, London, v. 20, n. 3, p. 1103-1113, 2020. Available in: https://doi.org/10.2166/ws.2020.035. Accessed on: 7 Dec. 2022.

GEOSCAN. **Ground Penetrating Radar (GPR)**. [*S. l.*], 2023. Available in: https://www.geoscan.ca/methods/ground-penetrating-radar-gpr/. Accessed on: 24 Jan. 2023.

GLEGG, S.; DEVENPORT, W. Chapter 12 - Phased arrays. *In*: GLEGG, S.; DEVENPORT, W. **Aeroacoustics of Low Mach Number Flows**. New York: Academic Press, 2017. p. 299-323. Available in: https://doi.org/10.1016/B978-0-12-809651-2.00012-6. Accessed on: 25 Jan. 2023.

GLENTIS, G. O.; ANGELOPOULOS, K. Leakage detection using leak noise correlation techniques – Overview and implementation aspects. *In:* PAN-HELLENIC CONFERENCE ON INFORMATICS, 23., 2019, Nicosia. **Proceedings of the 23rd Pan-Hellenic Conference on Informatics**. New York: Association for Computing Machinery, 2019, p. 50-57.

GRAFF, K. F. **Wave motion in elastic solids**. New York: Dover Publications, 1975.

GUIDELINE GEO. **What do I need to know about geophones?**, 2021. Available in: https://www.guidelinegeo.com/help-articles/what-do-i-need-to-know-about-geophones/. Accessed on: 6 Jan. 2022.

GUTERMANN. **MULTISCAN multi-point correlator**. [*S. l.*], 2023. Available in: https://en.gutermann-water.com/product/multiscan-multi-point-correlator/. Accessed on: 24 Jan. 2023.

HAMILTON, S.; CHARALAMBOUS, B. **Leak detection:** technology and implementation. London: IWA Publishing, 2020.

HANJRA, M. A.; QURESHI, M. E. Global water crisis and future food security in an era of climate change. **Food Policy**, Oxford, v. 35, n. 5, p. 365-377, 2010. Available in: https://doi.org/10.1016/j.foodpol.2010.05.006. Accessed on: 4 Dec. 2022.

HANSEN, S. M.; SCHMANDT, B. Automated detection and location of microseismicity at Mount St. Helens with a large-N geophone array. **Geophysical Research Letters**, Hoboken, v. 42, n. 18, p. 7390-7397, 2015. Available in: https://doi.org/10.1002/2015GL064848. Accessed on: 23 Jan. 2023.

HE, W.; SHI, W.; LE, J.; LI, H.; MA, R. Geophone-based energy harvesting approach for railway wagon monitoring sensor with high reliability and simple structure. **IEEE Access**, Piscataway, v. 8, p. 35882-35891, 2020. Available in: https://doi.org/10.1109/ACCESS.2020.2968089. Accessed on: 23 Jan. 2023.

HEATH CONSULTANTS. **Aqua-Scope user manual**. [*S. l.*], 2001. Available in: https://heathus.com/assets/uploads/aqua_scope_manual.pdf. Accessed on: 6 Jan. 2022.

HERRÁEZ, M. A., BURTON, D.R., LALOR, M. J., GDEISAT, M. A. Fast two-dimensional phase-unwrapping algorithm based on sorting by reliability following a noncontinuous path. **Applied Optics**, Washington, v. 41, n. 35, p. 7437-7444, 2002. Available in: https://doi.org/10.1364/AO.41.007437. Accessed on: 16 Jan. 2023.

HUNAIDI, O. **Detecting leaks in water-distribution pipes**. Ottawa: Institute for Research in Construction, National Research Council of Canada, 2000. Available in: https://publications.gc.ca/collections/collection_2008/nrc-cnrc/NR25-2-40E.pdf. Accessed on: 6 Jan. 2022.

HUNAIDI, O.; CHU, W.; WANG, A.; GUAN, W. Detecting leaks in plastic pipes. **American Water Works Association**, Oxford, v. 92, n. 2, p. 82-94, 2000. Available in: http://www.jstor.org/stable/41296929. Accessed on: 6 Jan. 2023.

HWM. **ST20 listening stick**. [*S. l.*], 2023. Available in: https://www.hwmglobal.com/st20-listening-stick/. Accessed on: 24 Jan. 2023.

INFRATEC. **Leak detection.** [*S. l.*], 2023. Available in: https://www.infratec.eu/thermography/service-support/glossary/leak-detection/. Accessed on: 24 Jan. 2022.

INTELLIGENZA INTUITIVA. **La semplicitá è la suprema sofisticazione**. [*S. l.*], 2023. Available in: https://www.intelligenzaintuitiva.com/la-semplicita-e-la-suprema-sofisticazione/. Accessed on: 28 Jan. 2023.

ISLAM, M. T.; ASLAN, S. Leak detection and location pinpointing in water pipeline systems using a wireless sensor network. *In*: IEEE INTERNATIONAL SYMPOSIUM ON CIRCUITS AND SYSTEMS, 2021. **Proceedings of the IEEE International Symposium on Circuits and Systems**, p. 1-7, 2021. Available in: https://doi.org/10.1109/ISCAS51556.2021.9401106. Accessed on: 7 Dec. 2022.

ISLAM, M. R.; AZAM, S.; SHANMUGAM, B.; MATHUR, D. A review on current technologies and future direction of water leakage detection in water distribution network. **IEEE Access**, Piscataway, v. 10, p. 107177-107201, 2022. Available in: https://doi.org/10.1109/ACCESS.2022.3212769. Accessed on: 7 Dec. 2022.

IWANAGA, M. K.; BRENNAN, M. J.; SCUSSEL, O.; ALMEIDA, F. C. L.; KARIMI, M. On the pipe localization based on the unwrapped phase of ground surface vibration between a roving pair of sensors. *In.*: DIMITROVOVÁ, Z.; BISWAS, P.; GONÇALVES, R.; SILVA, T. (org.). **Recent Trends in Wave Mechanics and Vibrations**. WMVC 2022. Mechanics and Machine Science, v. 125. Springer, Cham, 2023. Available in: https://doi.org/10.1007/978-3-031-15758-5_110. Accessed on: 16 Jan. 2023.

JETTE, A. N.; PARKER, J. G. Surface displacements accompanying the propagation of acoustic waves within an underground pipe. **Journal of Sound and Vibration**, London, v. 69, n. 2, p. 265-274, 1980. Available in: https://doi.org/10.1016/0022-460X(80)90611-2. Accessed on: 6 Jan. 2023.

JONGMANS, D.; DEMANET, D. The importance of surface waves in vibration study and the use of Rayleigh waves for estimating the dynamic characteristics of soils. **Engineering Geology**, Amsterdam, v. 34, p. 105-113, 1993. Available in: https://doi.org/10.1016/0013-7952(93)90046-F. Accessed on: 17 Jan. 2023.

JOODE, A. Pipeline leak detection technologies. **Engineer Live**. [*S. l.*], 2021. Available in: https://www.engineerlive.com/content/pipeline-leak-detection-technologies. Accessed on: 10 Dec. 2022.

KATZ, A.; KARAA, F.; NIVER, E. **Innovative and effective techniques for locating underground conduits**. Technical report – New Jersey Institute of Technology, Newark, 2011. Available in: https://www.nj.gov/transportation/business/research/reports/FHWA-NJ-2011-001.pdf. Accessed on: 6 Jan. 2023.

KELLER. **Pressure sensors on water pipelines.** [*S. l.*], 2023. Available in: https://keller-druck.com/en/industries/water-and-environment/pressure-sensors-on-water-pipelines. Accessed on: 24 Jan. 2023.

KIM, Y. **Sound propagation: An impedance based approach**. Singapore: Wiley, 2010.

KVS. **Leak detection with tracer gas methods**. [*S. l.*], 2023. Available in: http://www.leakdetection-technology.com/science/leak-detection-with-tracer-gas-methods.html. Accessed on: 24 Jan. 2023.

KOLES, S.; JALILIAN, E.; HULL, J. Overcoming the challenges and increasing value in fiber optic monitoring. **Pipeline Technology Journal**, [*s. l.*], n. 3, p. 26, 2020. Available in: https://www.pipeline-journal.net/ejournal/ptj-3-2020/. Accessed on: 6 Jan. 2023.

KUNDU, T. Acoustic source localization. **Ultrasonics**, Amsterdam, v. 54, p. 25-38, 2014. Available in: http://dx.doi.org/10.1016/j.ultras.2013.06.009. Accessed on: 17 Jan. 2023.

LIEMBERGER, R.; WYATT, A. Quantifying the global non-revenue water problem. **Water Supply**, London, v. 19, n. 3, p. 831-837, 2019. Available in: https://doi.org/10.2166/ws.2018.129. Accessed on: 4 Dec. 2022.

LIU, J.; CHEN, C.; WU, T.; CHEN, H.; HATTORI, K.; YANG, I.; BLEIER, T.; KAPPLER, K.; XIA, Y.; CHEN, W.; LIU, Z. Co-seismic signatures in magnetometer, geophone, and infrasound data during the Meinong Earthquake. **TAO: Terrestrial, Atmospheric and Oceanic Sciences Journal**, Taiwan, v. 28, p. 683-692, 2017. Available in: https://doi.org/10.3319/TAO.2017.03.05.01. Accessed on: 23 Jan. 2023.

LIU, Y.; HABIBI, D.; CHAI, D.; WANG, X.; CHEN, H.; GAO, Y.; LI, S. A comprehensive review of acoustic methods for locating underground pipelines. **Applied Sciences**, Bucharest, v. 10, n. 3, 2020. Available in: https://doi.org/10.3390/app10031031. Accessed on: 6 Jan. 2022.

LIU, P.; OTTO, F.; WANG, D.; OESER, M.; BALCK, H. Measurement and evaluation on deterioration of asphalt pavements by geophones. **Measurement**, Amsterdam, v. 109, p. 223-232, 2017. Available in: https://doi.org/10.1016/j.measurement.2017.05.066. Accessed on: 23 Jan. 2023.

METJE, N.; ATKINS, P. R.; BRENNAN, M. J.; CHAPMAN, D. N.; LIM, H. M.; MACHELL, J.; MUGGLETON, J. M.; PENNOCK, S.; RATCLIFFE, J.; REDFERN, M.; ROGERS, C. D. F.; SAUL, A. J.; SHAN, Q.; SWINGLER, S.; THOMAS, A. M. Mapping the underworld – State-of-the-art review. **Tunnelling and Underground Space Technology**, Oxford, v. 22, n. 5-6, p. 568-586, 2007. Available in: https://doi.org/10.1016/j.tust.2007.04.002. Accessed on: 16 Dec. 2022.

MILEV, G. V.; SPOTTSWOODE, A. M.; RORKE, S. M.; FINNIE, A.J. Seismic monitoring of a simulated rockburst on a wall of an underground tunnel. **Journal of the Southern African Institute of Mining and Metallurgy**, Marshalltown, v. 101, n. 5, p. 253-260, 2001. Available in: https://www.saimm.co.za/Journal/v101n05p253.pdf. Accessed on: 23 Jan. 2023.

MOHAMED, A. B. J. S.; VENUSAMY, K.; SANGEETHA, S. V. T.; AL RAWAHI, A. S. A.; AL BALUSHI, A. S. M. Leak detection and corrosion identification in water tubes, gas pipes by mobile robot. *In:* INTERNATIONAL CONFERENCE ON SMART ELECTRONICS AND COMMUNICATIONS, 2., 2021, Trichy. IEEE, 2021. p. 1-6.

MUGGLETON, J. M.; BRENNAN, M. J.; GAO, Y. Determining the location of buried plastic water pipes from measurements of ground surface vibration. **Journal of Applied Geophysics**, Amsterdam, v. 75, p. 54-61, 2011. Available in: https://doi.org/10.1016/j.jappgeo.2011.06.030. Accessed on: 6 Jan. 2023.

MUGGLETON, J. M.; BRENNAN, M. J.; LINFORD, P. W. Axisymmetric wave propagation in fluid-filled pipes: wavenumber measurements in in vacuo and buried pipes. **Journal of Sound and Vibration**, London, v. 270, n. 1-2, p. 171-190, 2004. Available in: https://doi.org/10.1016/S0022-460X(03)00489-9. Accessed on: 6 Jan. 2023.

MUGGLETON, J. M.; BRENNAN, M. J.; PINNINGTON, R. J. Wavenumber prediction of waves in buried pipes for water leak detection. **Journal of Sound and Vibration**, London, v. 249, n. 5, p. 939-954, 2002. Available in: https://doi.org/10.1006/jsvi.2001.3881. Accessed on: 6 Jan. 2023.

MUGGLETON, J. M.; BRENNAN, M. J.; ROGERS, C. D. F. Point vibration measurements for the detection of shallow-buried objects. **Tunneling and Underground Space Technology**, Oxford, v. 39, p. 27-33, 2014. Available in: https://doi.org/10.1016/j.tust.2012.02.006. Accessed on: 7 Jan. 2023.

MUGGLETON, J. M.; SCUSSEL, O.; RUSTIGHI, E.; BRENNAN, M. J.; ALMEIDA, F.; KARIMI, M.; JOSEPH, P. F. A simplified model of the ground surface vibration from a leaking pipe. *In.*: DIMITROVOVÁ, Z.; BISWAS, P.; GONÇALVES, R.; SILVA, T. (org.). **Recent Trends in Wave Mechanics and Vibrations**. WMVC 2022. Mechanics and Machine Science, v. 125. Springer, Cham, 2023. Available in: https://doi.org/10.1007/978-3-031-15758-5_105. Accessed on: 15 Jan. 2023.

MUGGLETON, J. M.; PAPANDREOU, B. A shear wave ground surface vibration technique for the detection of buried pipes. **Journal of Applied Geophysics**, Amsterdam, v. 106, p. 164-172, 2014. Available in: http://dx.doi.org/10.1016/j.jappgeo.2014.04.021. Accessed on: 6 Jan. 2023.

MUGGLETON, J. M.; RUSTIGHI, E. 'Mapping the Underworld': recent developments in vibro-acoustic techniques to locate buried infrastructure. **Géotechnique Letters**, [*s. l.*], v. 3, n. 3, p. 137-141, 2013. Available in: https://doi.org/10.1680/geolett.13.00032. Accessed on: 6 Jan. 2022.

MURPHY, M. M.; WESTMAN, E. C.; IANNACCHIONE, A.; BARCZAK, T. M. Relationship between radiated seismic energy and explosive pressure for controlled methane and coal dust explosions in an underground mine. **Tunnelling and Underground Space Technology**, Oxford, v. 28, p. 278-286, 2012. Available in: https:/doi.org/10.1016/j.tust.2011.12.002. Accessed on: 23 Jan. 2023.

NIKLES, M.; VOGEL, B.; BRIFFOD, F.; GROSSWIG, S.; SAUSER, F.; LUEBBECKE, S.; BALS, A; PFEIFFER, T. Leakage detection using fiber optics distributed temperature monitoring. **Proceedings of the 11th SPIE Annual International Symposium on Smart Structures and Materials**, p. 18-25, 2004. Available in: https://www.researchgate.net/publication/228756063_Leakage_detection_using_fiber_optics_distributed_temperature_monitoring. Accessed on: 10 Dec. 2022.

O'CONNELL, K. Seismic instruments, environmental factors. *In*.: BRAUN, S. **Encyclopedia of Vibration**. Lodon: Elsevier, 2001. p. 1121-1134.

PAPANDREOU, B.; BRENNAN, M. J.; RUSTIGHI, E. On the detection of objects buried at a shallow depth using seismic wave reflections. **The Journal of the Acoustical Society of America**, Melville, v. 129, p. 1366-1374, 2011. Available in: http://dx.doi.org/10.1121/1.3552878. Accessed on: 6 Jan. 2023.

PCB PIEZOTRONICS. **Model 333B40 operational manual.** [*S. l.*], 2002a. Available in: https://www.pcb.com/contentStore/docs/pcb_corporate/vibration/products/manuals/333b40.pdf. Accessed on: 23 Jan. 2023.

PCB PIEZOTRONICS. **Model 356A17 operational manual**. [*S. l.*], 2002b. Available in: https://www.pcb.com/contentStore/docs/pcb_corporate/vibration/products/manuals/356a17.pdf. Accessed on: 23 Jan. 2023.

PINNINGTON, R. J.; BRISCOE, A. R. Externally applied sensor for axisymmetric waves in a fluid filled pipe. **Journal of Sound and Vibration**, London, v. 173, n. 4, p. 503-516, 1994. Available in: https://doi.org/10.1006/jsvi.1994.1243. Accessed on: 13 Jan. 2023.

PHILLIPS, C.; CASCANTE, G.; HUTCHINSON, J. Detection of underground voids with surface waves. **Proceedings of the 13th EEGS Symposium on the Application of Geophysics to Engineering and Environmental Problems**, 2000. Available in: https://doi.org/10.4133/1.2922756. Accessed on: 6 Jan. 2023.

PRIEST, J. A.; POWRIE, W. Determination of dynamic track modulus from measurement of track velocity during train passage. **Journal of Geotechnical and Geoenvironmental Engineering**, Reston, v. 135, n. 11, p. 1732-1740, 2009. Available in: https://doi.org/10.1061/(ASCE)GT.1943-5606.0000130. Accessed on: 23 Jan. 2023.

PRIMAYER. **Enigma3hyQ**. [*S. l.*], 2020. Available in: https://www.primayer.com/products/enigma3hyq/. Accessed on: 24 Jan. 2023.

PROVAC AUSTRALIA PTY LTD. **What is ground penetrating radar?**. [*S. l.*], 2021. Available in: https://www.provac.net.au/what-is-ground-penetrating-radar/. Accessed on: 24 Jan. 2023.

RABEEK. S. M.; BEIBEI, H.; CHAI, K. T. C. Design of wireless IoT sensor node & platform for water pipeline leak detection. *In*: IEEE ASIAN-PACIFIC MICROWAVE CONFERENCE, 2019. **Proceedings of the IEEE Asian-Pacific Microwave Conference**, p. 1328-1330, 2019. Available in: https://doi.org/10.1109/APMC46564.2019.9038809. Accessed on: 7 Dec. 2022.

RADIODETECTION. **RD500 plastic water pipe locator.** [*S. l.*], 2023. Available in: https://www.radiodetection.com/en-gb/products/plastic-water-pipe-locator/rd500. Accessed on: 24 Jan. 2023.

RAGAB, R.; PRUDHOMME, C. SW – Soil and water: Climate change and water resources management in arid and semi-arid regions: Prospective and challenges for the 21st century. **Biosystems Engineering**, London, v. 81, n. 1, p. 3-34, 2002. Available in: https://doi.org/10.1006/bioe.2001.0013. Accessed on: 3 Jan. 2023.

RAMULU, M.; CHAKRABORTY, A. K.; SITHARAM, T. G. Damage assessment of basaltic rock mass due to repeated blasting in a railway tunnelling project – A case study. **Tunnelling and Underground Space Technology**, Oxford, v. 24, p. 208-221, 2009. Available in: https://doi.org/10.1016/j.tust.2008.08.002. Accessed on: 23 Jan. 2023.

RIAHI, N.; GERSTOFT, P. The seismic traffic footprint: Tracking trains, aircraft, and cars seismically. **Geophysical Research Letters**, Hoboken, v. 42, n. 8, p. 2674-2681, 2015. Available in: https://doi.org/10.1002/2015GL063558. Accessed on: 23 Jan. 2023.

RUSSELL, D. A. **Plane waves and evanescent waves**. [*S. l.*], 2014. Available in: https://www.acs.psu.edu/drussell/Demos/EvanescentWaves/EvanescentWaves.html. Accessed on: 15 Jan. 2023.

SCUSSEL, O.; BRENNAN, M. J.; MUGGLETON, J. M.; ALMEIDA, F. C. L.; PASCHOALINI, A. T. On the dynamic loading effects of soil on plastic water distribution pipes and its significances for leak detection using acoustics. *In*: PROCEEDINGS OF ASME 2018 INTERNATIONAL MECHANICAL ENGINEERING CONGRESS AND EXPOSITION, 2018, Pittsburgh. **Proceedings of the** […] Pittsburgh: ASME, 2018. 7 p. Available in: https://www.researchgate.net/publication/330403970_On_the_Dynamic_Loading_Effects_of_Soil_on_Plastic_Water_Distribution_Pipes_and_its_Significance_for_Leak_Detection_Using_Acoustics. Accessed on: 16 Jan 2023.

SCUSSEL, O.; BRENNAN, M. J.; MUGGLETON, J. M.; ALMEIDA, F. C. L.; PASCHOALINI, A. T. Estimation of the bulk and shear moduli of soil surrounding a plastic water pipe using measurements of the predominantly fluid wave in the pipe. **Journal of Applied Geophysics**, Amsterdam, v. 164, p. 237-246, 2019. Available in: https://doi.org/10.1016/j.jappgeo.2019.01.010. Accessed on: 16 Jan 2023.

SEBAKMT. **PAM HYDRO 3 Hydrophone for trunk mains and plastic pipes.** [*S. l.*], 2023. Available in: https://www.sebakmt.com/detail/PAM-HYDRO-3_US.html. Accessed on: 24 Jan. 2023.

SEWERIN. **Leak detection in water distribution networks by correlation sound velocity as a possible source of error**. [*S. l.*], 2023a. Available in: https://www.sewerin.com/us/info-center/publications/leak-detection-in-drinking-water-distribution-networks. Accessed on: 24 Jan. 2023.

SEWERIN. **Water leak noise loggers for the early recognition and detection of leaks in water supply networks.** [*S. l.*], 2023b. Available in: https://www.sewerin.co.uk/products/water-leak-location/sepem/. Accessed on: 24 Jan. 2023.

SHENG, Y.; ELLSWORTH, W. L.; LELLOUCH, A.; BEROZA, G. C. Depth constraints on coseismic velocity changes from frequency-dependent measurements of repeating earthquake waveforms. **Journal of Geophysical Research: Solid Earth**, Hoboken, v. 126, n. 2, 2021. Available in: https://doi.org/10.1029/2020JB020421. Accessed on: 23 Jan. 2023.

SHI, N.; BAI, L.; MA, Y.; LI, L.; CAO, J. Field experimental research on application of strain special optical cable and parallel optical cable. **IOP Conference Series: Earth and Environmental Science**, Bristol, v. 687, p. 012147, 2021. Available in: https://doi.org/10.1088/1755-1315/687/1/012147. Access on: 10 Dec. 2022.

SHIN, K.; HAMMOND, J. K. **Fundamentals of signal processing for sound and vibration engineers**. Chichester: Wiley, 2008.

SPARKFUN. **SM-24 geophone datasheet.** [*S. l.*], 2006. Available in: http://cdn.sparkfun.com/datasheets/Sensors/Accelerometers/SM-24%20Brochure.pdf. Accessed on: 23 Jan. 2023.

STERLING, R.; ANSPACH, J. H.; ALLOUCHE, E. N.; SIMICEVIC, J.; ROGERS, C. D.; WESTON, K. E.; HAYES, K. **Encouraging innovation in locating and characterizing underground utilities**. Technical report – The National Academies Press, Washington, 2009. Available in: https://doi.org/10.17226/22994. Access on: 6 Jan. 2023.

TELFORD, W. M.; GELDART, L. P.; SHERIFF, R. E. **Applied Geophysics**. Cambridge: Cambridge University Press, 1990.

XERRI, W.; SARACCO, G.; RIBODETTI, A.; ZOMERO, L.; PICON, P. Three-dimensional localization of buried polyethylene pipes using acoustic method. **Sensors**, Basel, v. 22, n. 23, p. 9433, 2022. Available in: https://doi.org/10.3390/s22239433. Accessed on: 29 Jan. 2023.

XYLEM. **Pure Technologies SmartBall® inline free-swimming inspection platform**. [*S. l.*], 2023a. Available in: https://www.xylem.com/en-us/products--services/pipeline-assessment/smartball-inline-free-swimming-inspection-platform/. Accessed on: 24 Jan. 2023.

XYLEM. **Pure Technologies Sahara® inline tethered inspection platform**. [*S. l.*], 2023b. Available in: https://www.xylem.com/en-us/products--services/pipeline-assessment/sahara-inline-tethered-inspection-platform/. Accessed on: 24 Jan. 2023.

YAN, S.; YUAN, H.; GAO, Y.; JIN, B.; MUGGLETON, J. M.; DENG, L. On image fusion of ground surface vibration for mapping and locating underground pipeline leakage: An experimental investigation. **Sensors**, Basel, v. 20, n. 7, p. 1896, 2020. Available in: https://doi.org/10.3390/s20071896. Accessed on: 7 Jan. 2023.

YANG, L.; GUO, Y.; GAO, S. Multi-leak detection in pipeline based on optical fiber detection. **Optik**, Jena, v. 220, p. 164996, 2020. Available in: https://doi.org/10.1016/j.ijleo.2020.164996. Accessed on: 10 Dec. 2022.

WALEED, D.; MUSTAFA, S. H.; MUKHOPADHYAY, S.; ABDEL-HAFEZ, M. F.; JARADAT, M. A. K.; DIAS, K. R.; ARIF. F.; AHMED, J. I. An in-pipe leak detection robot with a neural-network-based leak verification system. **IEEE Sensors Journal**, Piscataway, v. 19, n. 3, p. 1153-1165, 2019. Available in: https://ieeexplore.ieee.org/document/8519788. Accessed on: 6 Jan. 2023.

WANG, J.; LIU, J.; LIU, H.; TIAN, Z.; CHENG, F. Modeling and locating underground water pipe leak with microseismic data. **Journal of Applied Geophysics**, Amsterdam, v. 136, p. 1-8, 2017. Available in: http://dx.doi.org/10.1016/j.jappgeo.2016.10.030. Accessed on: 7 Jan. 2023.

ZAMAN, D.; TIWARI, M. J.; GUPTA, A. K.; SEN, D. A review of leakage detection strategies for pressurized pipeline in steady-state. **Engineering Failure Analysis**, Oxford, v. 109, p. 104264, 2020. Available in: https://doi.org/10.1016/j.engfailanal.2019.104264. Accessed on: 17 Jan. 2023.

ZHANG, P.; HE, J.; HUANG, W.; YUAN, Y.; WU, C.; ZHANG, J.; YUAN, Y.; WANG, P.; YANG, B.; CHENG, K.; CUI, H.; ZHANG, L. Ground vibration analysis of leak signals from buried liquid-filled pipes: An experimental investigation. **Applied Acoustics**, Oxford, v. 200, 2022. Available in: https://doi.org/10.1016/j.apacoust.2022.109054. Accessed on: 7 Jan. 2023.

ZHAO, Y.; RECTOR, J. W. Using seismic surface waves generated by motor vehicles to find voids: field results. **SEG Technical Program Expanded Abstracts**, Tulsa, p. 2029-2033, 2010. Available in: https://doi.org/10.1190/1.3513243. Accessed on: 23 Jan. 2023.

ZOU, W.; SUN, D.; TONG, X.; LI, X.; SHU, W. Some developments and new insights for microseismic/acoustic emission source localization. **Shock and Vibration**, London, v. 2019, 2019. Available in: https://doi.org/10.1155/2019/9732606. Accessed on: 17 Jan. 2023.

APPENDIX A – WAVENUMBER OF THE PREDOMINANTLY FLUID-BORNE AXISYMMETRIC WAVE

A.1 INTRODUCTION

A leak in a buried pipe generates noise in the form of waves that travel in the pipe, and waves that radiate into the surrounding soil. The frequency regimes for the waves that propagate in a fluid-filled pipe are separated by the pipe ring frequency, which is the frequency at which a compressional wavelength is equal to the pipe circumference (PINNINGTON; BRISCOE, 1994; GAO *et al*., 2016, 2017). Well below the pipe ring frequency, the predominantly fluid-borne axisymmetric wave is one of the main responsible for leak noise propagation in water-filled plastic pipes (PINNINGTON; BRISCOE, 1994; GAO *et al*., 2016, 2017). The wavenumber for the predominantly fluid-borne axisymmetric wave is obtained from the relation of stresses and displacements at the interface between the pipe-wall and the soil, when only free waves exist in the system (GAO *et al*., 2016, 2017; GAO; LIU; MUGGLETON, 2017). This appendix presents an analytical model for the wavenumber of the predominantly fluid-borne axisymmetric wave, based on that described by Gao, Liu and Muggleton (2017) and using the concept of wave dynamic stiffness to conveniently point out the physical contribution of each component (pipe-wall, water inside the pipe, and surrounding soil) on the wave propagation, as performed by Brennan *et al*. (2018) and Scussel *et al*. (2018).

A.2 ANALYTICAL MODEL FOR THE WAVENUMBER OF THE PREDOMINANTLY FLUID-BORNE AXISYMMETRIC WAVE

A schematic diagram for the wave propagation in a buried pipe system, which includes the pipe-wall, the water inside the pipe and the surrounding soil is illustrated in Fig. 77. The pipe has a mean radius a and wall-thickness b. The axial and radial coordinates are given by x and r, respectively. The pipe and the soil are assumed to be under compact contact (also known as “no-slip” boundary condition), in which the stresses and displacements of the pipe-wall are equal to the stresses and displacements of the soil at the interface (JETTE; PARKER, 1980; GAO *et al*., 2016, 2017). The shear and compressional stresses acting at the interface $\left(r=a\right)$ are given by τ_a and σ_a, respectively, and the axial and radial displacements at the interface $\left(r=a\right)$ are given by u_a and w_a, respectively. In the derivation of the analytical model, the following simplifying assumptions are considered:

- The pipe and surrounding soil are of infinite extent in the axial direction, and the surrounding soil is also of infinite extent in the radial direction.
- The predominantly fluid-borne axisymmetric wave is the only wave propagating in the pipe and is responsible for the leak noise propagation.
- The surrounding soil is an elastic medium where shear and compressional waves can propagate.
- The frequency range of interest is well below the pipe ring frequency, so that bending in the pipe-wall can be neglected.
- The frequency range of interest is such that an acoustic wavelength in water is much greater than the diameter of the pipe.
- The multiple internal reflections of the predominantly fluid-borne axisymmetric wave due to discontinuities are neglected for simplicity.

Figure 77 - Schematic diagram for the wave propagation in a buried pipe system.

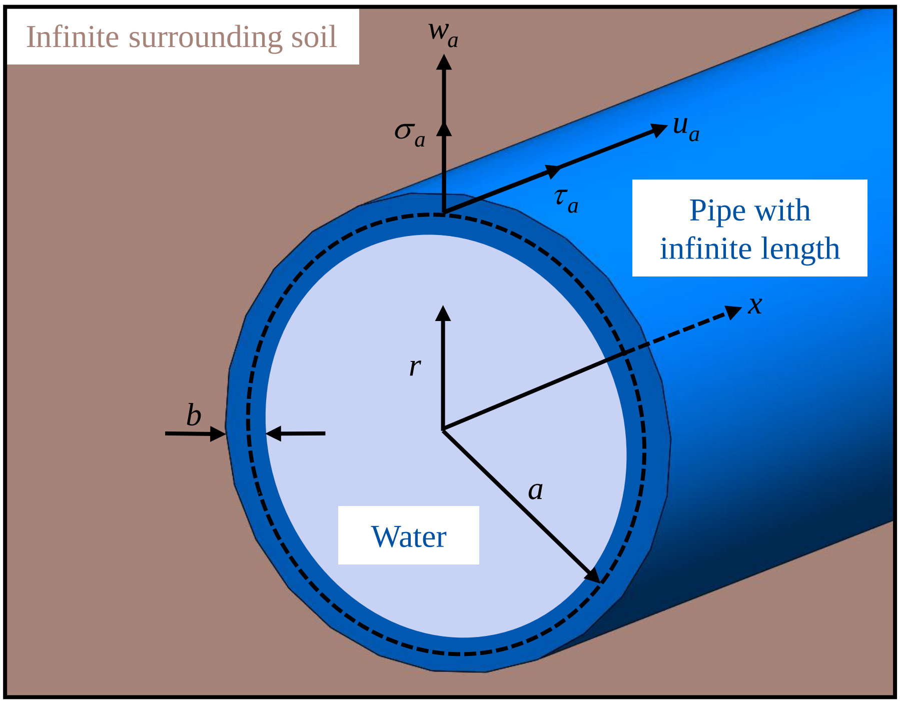

Source: elaborated by the author.

The axial and radial stresses acting on the pipe-wall and soil, and the axial and radial displacements of the pipe-wall and the soil are assumed to be harmonic in both space and time, so that the stresses τ_a and σ_a, and the displacements u_a and w_a can be respectively described by

$$\tau_a = \mathrm{T}_a e^{\mathrm{j}\left(\omega t - k_f x\right)},\ \sigma_a = \Phi_a e^{\mathrm{j}\left(\omega t - k_f x\right)},\ u_a = U_a e^{\mathrm{j}\left(\omega t - k_f x\right)} \text{ and } w_a = W_a e^{\mathrm{j}\left(\omega t - k_f x\right)}. \qquad \text{(14a,b,c,d)}$$

The amplitudes of the axial and radial stresses, T_a and Φ_a, are related to the complex amplitudes of the axial and radial displacements, U_a and W_a, by

$$\boldsymbol{\sigma}_a = \left[\mathbf{K}^{(\text{pipe})} + \mathbf{K}^{(\text{water})} + \mathbf{K}^{(\text{soil})}\right]\mathbf{u}_a, \qquad (15)$$

where $\boldsymbol{\sigma}_a = \left\{\mathrm{T}_a \quad \Phi_a\right\}^T$ and $\mathrm{u}_a = \left\{U_a \quad W_a\right\}^T$, in which the superscript T denotes the transpose. The wave dynamic stiffness matrix for the pipe-wall $\mathbf{K}^{(\text{pipe})}$ is given by

$$\mathbf{K}^{(\text{pipe})} = \begin{bmatrix} K_{11}^{(\text{pipe})} & K_{12}^{(\text{pipe})} \\ K_{21}^{(\text{pipe})} & K_{22}^{(\text{pipe})} \end{bmatrix} = \begin{bmatrix} \left(k_f a\right)^2 \tilde{K}^{(\text{pipe})} - \omega^2 \rho_{\text{pipe}} b & \mathrm{j}\,\nu_{\text{pipe}}\left(k_f a\right)\tilde{K}^{(\text{pipe})} \\ -\mathrm{j}\,\nu_{\text{pipe}}\left(k_f a\right)\tilde{K}^{(\text{pipe})} & \tilde{K}^{(\text{pipe})} - \omega^2 \rho_{\text{pipe}} b \end{bmatrix}, \qquad (16)$$

in which $\tilde{K}^{(\text{pipe})} = E_{\text{pipe}}^{*} b \Big/ \left[a^2\left(1 - \nu_{\text{pipe}}^2\right)\right]$. The term $E_{\text{pipe}}^{*} = E_{\text{pipe}}\left(1 + \mathrm{j}\,\eta_{\text{pipe}}\right)$ is the complex Young's modulus of the pipe, where E_{pipe}, η_{pipe}, ρ_{pipe} and ν_{pipe} are the Young's modulus, the loss factor, the density, and the Poisson's ratio of the pipe-wall respectively. The wave dynamic stiffness matrix for the water inside the pipe $\mathbf{K}^{(\text{water})}$ is given by

$$\mathbf{K}^{(\text{water})} = \begin{bmatrix} 0 & 0 \\ 0 & -K^{(\text{water})} \end{bmatrix} = \begin{bmatrix} 0 & 0 \\ 0 & \dfrac{-\omega^2 \rho_{\text{water}}}{k_{\text{water}}^R} \dfrac{J_0\left(k_{\text{water}}^R a\right)}{J_0'\left(k_{\text{water}}^R a\right)} \end{bmatrix}, \qquad (17)$$

where $J_0(\bullet)$ is a Bessel function of the first kind of zero order. The term $k_{\text{water}}^R = \sqrt{k_{\text{water}}^2 - k_f^2}$ is the component of the wavenumber in the radial direction, in which $k_{\text{water}} = \omega / c_{\text{water}}$ is the wavenumber for the water and c_{water} is the wave speed in an infinite homogeneous body of water, which is approximately 1,500 m/s. At low frequencies, where the acoustic wavelength in water is much greater than the diameter of the pipe, $J_0\left(k_{\text{water}}^R a\right) / J_0'\left(k_{\text{water}}^R a\right) \approx -2 / k_{\text{water}}^R a$. Noting that $k_{\text{water}}^2 = \omega^2 \rho_{\text{water}} / B_{\text{water}}$, then

$$K^{(\text{water})} \approx \frac{\tilde{K}^{(\text{water})}}{\left(\dfrac{k_f^2}{k_{\text{water}}^2} - 1 \right)}, \tag{18}$$

in which $\tilde{K}^{(\text{water})} = 2B_{\text{water}} / a$ and B_{water} is the bulk modulus of water. The wave dynamic stiffness matrix for the surrounding soil is given by

$$\mathbf{K}^{(\text{soil})} = G_{\text{soil}}^* \begin{bmatrix} -\alpha k_d^R & \mathrm{j}\left(2 - \alpha \bar{H}_d\right) k_f \\ -\mathrm{j}\left(2 - \alpha \bar{H}_d\right) k_f & \dfrac{2}{a} + \alpha \dfrac{k_s^R}{k_d^R} \bar{H}_s \bar{H}_d k_d^R \end{bmatrix}, \tag{19}$$

where $\alpha = k_s^2 / \left(k_d^R k_s^R \bar{H}_s + k_f^2 \bar{H}_d \right)$, $\bar{H}_s = H_0\left(k_s^R r\right) / H_0'\left(k_s^R r\right)$ and $\bar{H}_d = H_0\left(k_d^R r\right) / H_0'\left(k_d^R r\right)$, in which $H_0(\bullet)$ is a Hankel function of the second kind of zero order; $k_s^R = \sqrt{k_s^2 - k_f^2}$, in which $k_s = \omega / c_s$ is the shear wavenumber for the soil and $c_s = \sqrt{G_{\text{soil}}^* / \rho_{\text{soil}}}$ is the shear wave speed in the soil, where $G_{\text{soil}}^* = G_{\text{soil}}\left(1 + \mathrm{j}\,\eta_s\right)$ is the complex shear modulus of the soil, in which G_{soil} and η_s are the shear modulus and the shear loss factor of the soil respectively; $k_d^R = \sqrt{k_d^2 - k_f^2}$, in which $k_d = \omega / c_d$ is the compressional wavenumber for the soil and $c_d = \sqrt{\left(B_{\text{soil}}^* + 4G_{\text{soil}}^* / 3 \right) / \rho_{\text{soil}}}$ is the compressional wave speed in the soil, where $B_{\text{soil}}^* = B_{\text{soil}}\left(1 + \mathrm{j}\,\eta_d\right)$ is the complex bulk modulus of the soil, in which B_{soil} and η_d are the bulk modulus and the bulk loss factor of the soil respectively.

Assuming that there are only free waves in the buried pipe system, so that $\mathrm{T}_a = \Phi_a = 0$, and noting that $K_{21}^{(\text{pipe})} = -K_{12}^{(\text{pipe})}$ and $K_{21}^{(\text{soil})} = -K_{12}^{(\text{soil})}$, Eq. (15) can be rearranged to give an expression for the wavenumber of the predominantly fluid-borne axisymmetric wave, k_f, which is given by

$$k_f = k_{\text{water}} \left(1 + \frac{\tilde{K}^{(\text{water})}}{K^{(\text{pipe})} + K^{(\text{pipe\_soil})} + K^{(\text{soil})}} \right)^{\frac{1}{2}} \tag{20}$$

where $K^{(\text{pipe})} = K_{22}^{(\text{pipe})}$, $K^{(\text{pipe\_soil})} = \left(K_{12}^{(\text{pipe})} + K_{12}^{(\text{soil})} \right)^2 \Big/ K_{11}^{(\text{pipe})} + K_{11}^{(\text{soil})}$ and $K^{(\text{soil})} = K_{22}^{(\text{soil})}$. Note that the wavenumber is a function of the wave dynamic stiffnesses. One of these is related to the water in the pipe $\tilde{K}^{(\text{water})}$, one to the pipe alone $K^{(\text{pipe})}$, one to the soil alone $K^{(\text{soil})}$, and one that is related to the interaction between the soil and the pipe $K^{(\text{pipe\_soil})}$. Note, however, that the wave dynamic stiffnesses in Eq. (20) are functions of k_f, so Eq. (20) is recursive.

APPENDIX B - COMPLEMENTARY RESULTS FOR TWO-SENSOR TECHNIQUE

Figure 78 - Pipe localization with the two-sensor technique applied on 1st measurement line of zone A of the British test rig. (a.i-iii) 1st, 2nd and 3rd positions of the pair of sensors, (b.i-iii) coherence $\gamma_{1,2}^{2}(\omega)$ for 1st, 2nd and 3rd positions, (c.i-iii) unwrapped phase $\phi_{1,2}(\omega)$ (solid black line) and approximated line $\hat{\phi}_{1,2}(\omega)$ (dashed red line) for 1st, 2nd and 3rd positions, and (a.iv) estimate of pipe localization. The dashed blue lines correspond to the buried pipe.

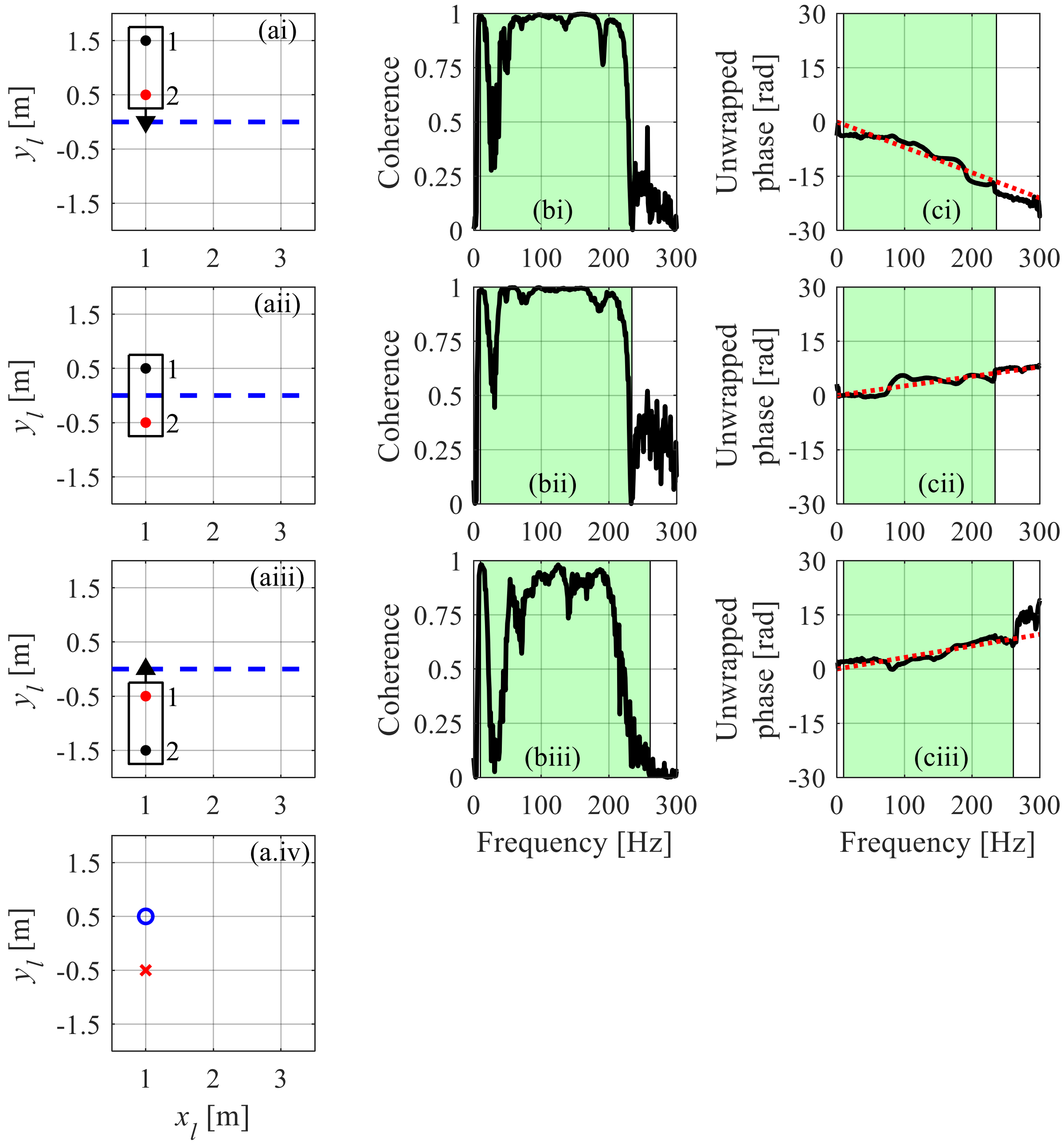

Source: elaborated by the author.

Figure 79 - Pipe localization with the two-sensor technique applied on 2nd measurement line of zone A of the British test rig. (a.i-iii) 1st, 2nd and 3rd positions of the pair of sensors, (b.i-iii) coherence $\gamma_{1,2}^2(\omega)$ for 1st, 2nd and 3rd positions, (c.i-iii) unwrapped phase $\phi_{1,2}(\omega)$ (solid black line) and approximated line $\hat{\phi}_{1,2}(\omega)$ (dashed red line) for 1st, 2nd and 3rd positions, and (a.iv) estimate of pipe localization. The dashed blue lines correspond to the buried pipe.

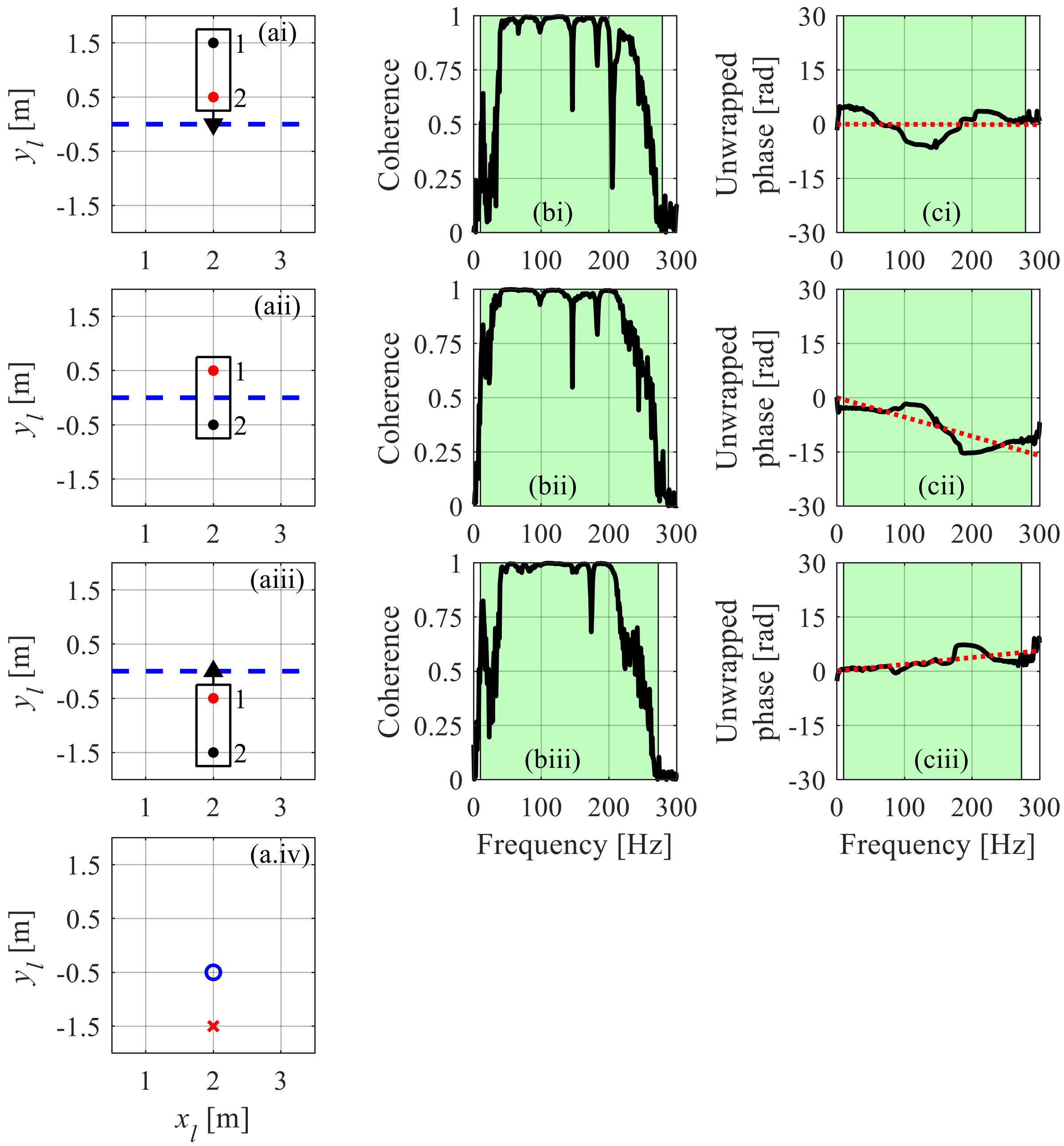

Source: elaborated by the author.

Figure 80 - Pipe localization with the two-sensor technique applied on 3rd measurement line of zone A of the British test rig. (a.i-iii) 1st, 2nd and 3rd positions of the pair of sensors, (b.i-iii) coherence $\gamma_{1,2}^{2}\left(\omega\right)$ for 1st, 2nd and 3rd positions, (c.i-iii) unwrapped phase $\phi_{1,2}\left(\omega\right)$ (solid black line) and approximated line $\hat{\phi}_{1,2}\left(\omega\right)$ (dashed red line) for 1st, 2nd and 3rd positions, and (a.iv) estimate of pipe localization. The dashed blue lines correspond to the buried pipe.

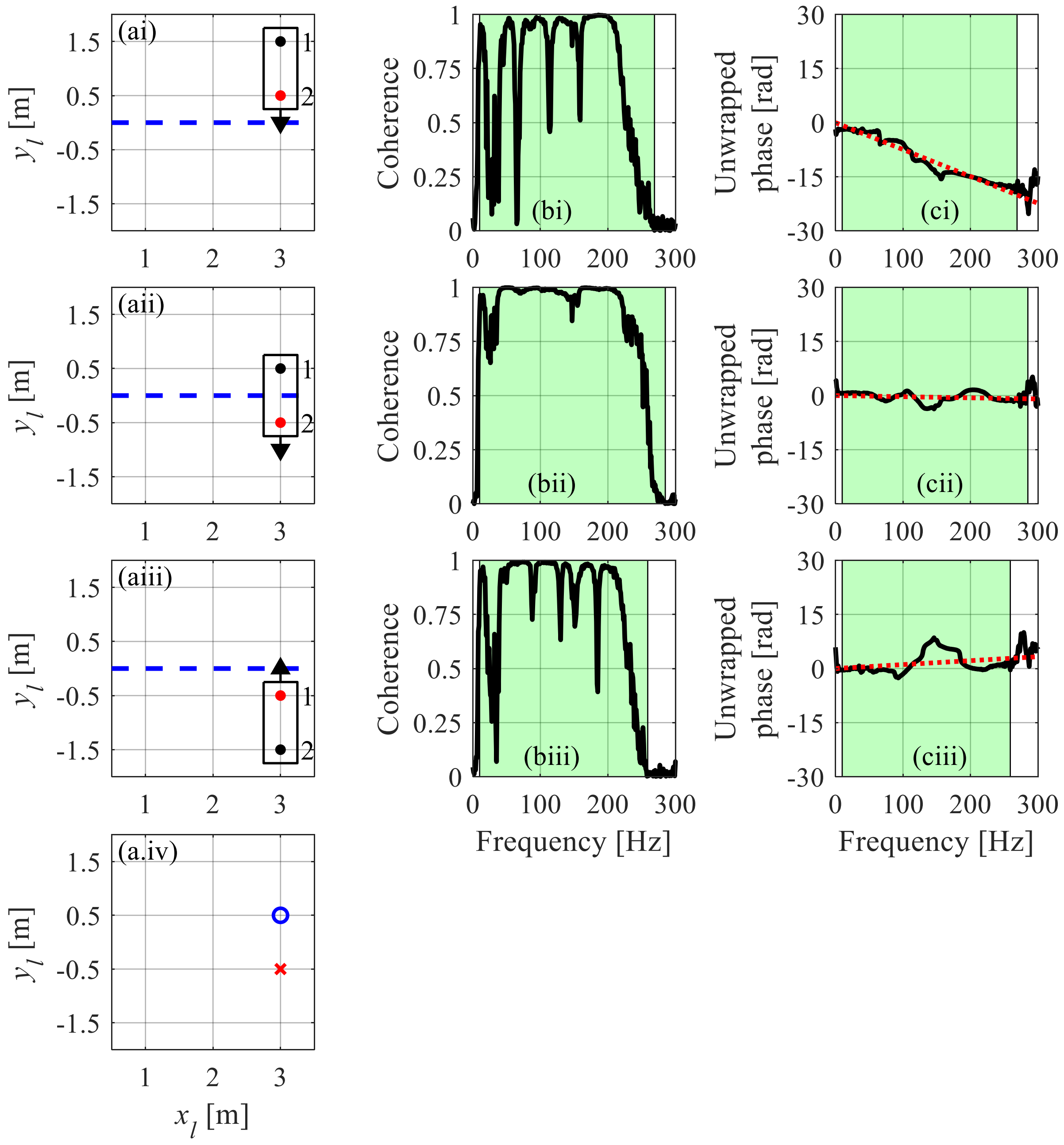

Source: elaborated by the author.

Figure 81 - Pipe localization with the two-sensor technique applied on 1st measurement line of zone B of the British test rig. (a.i-iii) 1st, 2nd and 3rd positions of the pair of sensors, (b.i-iii) coherence $\gamma_{1,2}^{2}(\omega)$ for 1st, 2nd and 3rd positions, (c.i-iii) unwrapped phase $\phi_{1,2}(\omega)$ (solid black line) and approximated line $\hat{\phi}_{1,2}(\omega)$ (dashed red line) for 1st, 2nd and 3rd positions, and (a.iv) estimate of pipe localization. The dashed blue lines correspond to the buried pipe.

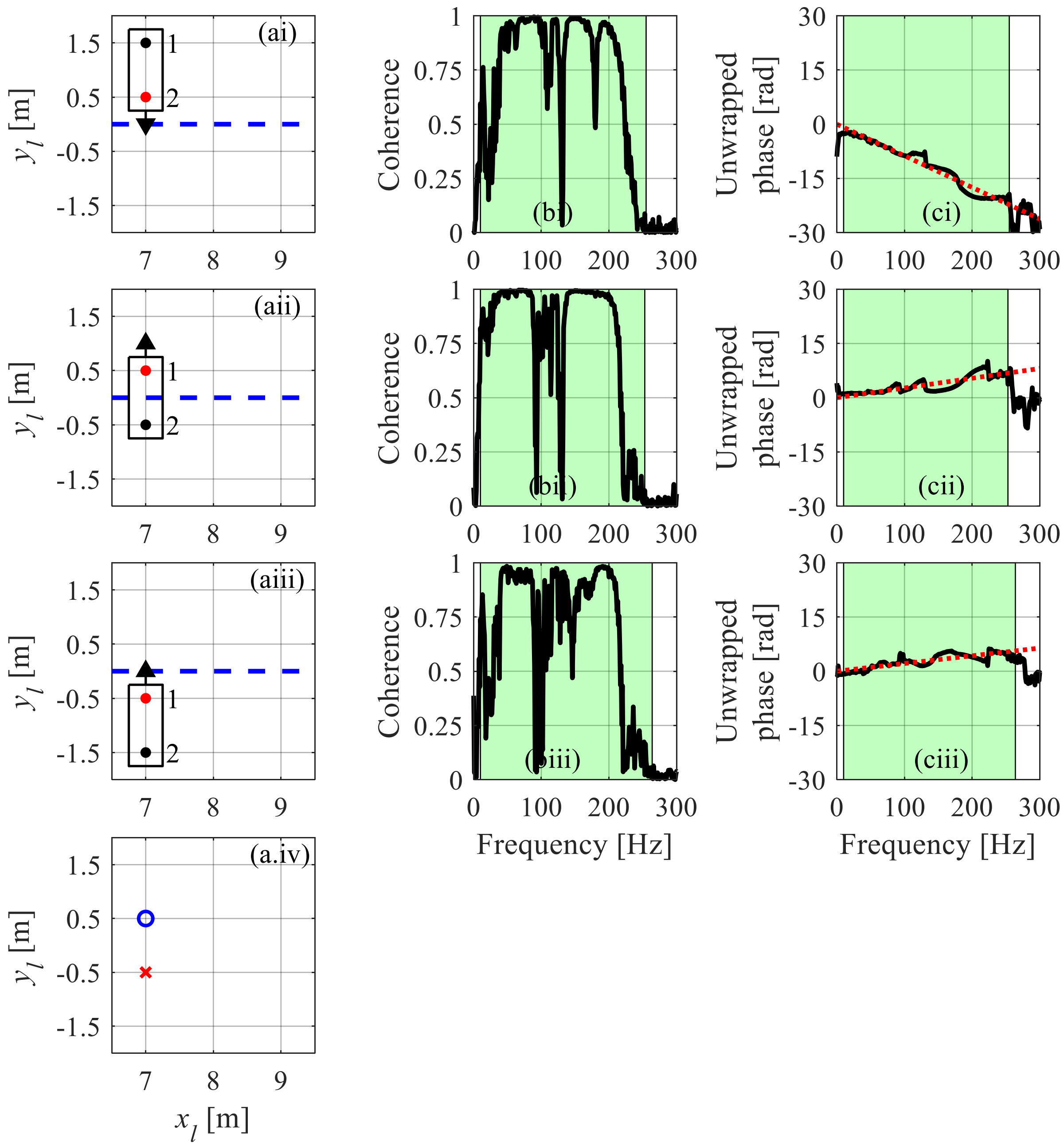

Source: elaborated by the author.

Figure 82 - Pipe localization with the two-sensor technique applied on 2nd measurement line of zone B of the British test rig. (a.i-iii) 1st, 2nd and 3rd positions of the pair of sensors, (b.i-iii) coherence $\gamma_{1,2}^2(\omega)$ for 1st, 2nd and 3rd positions, (c.i-iii) unwrapped phase $\phi_{1,2}(\omega)$ (solid black line) and approximated line $\hat{\phi}_{1,2}(\omega)$ (dashed red line) for 1st, 2nd and 3rd positions, and (a.iv) estimate of pipe localization. The dashed blue lines correspond to the buried pipe.

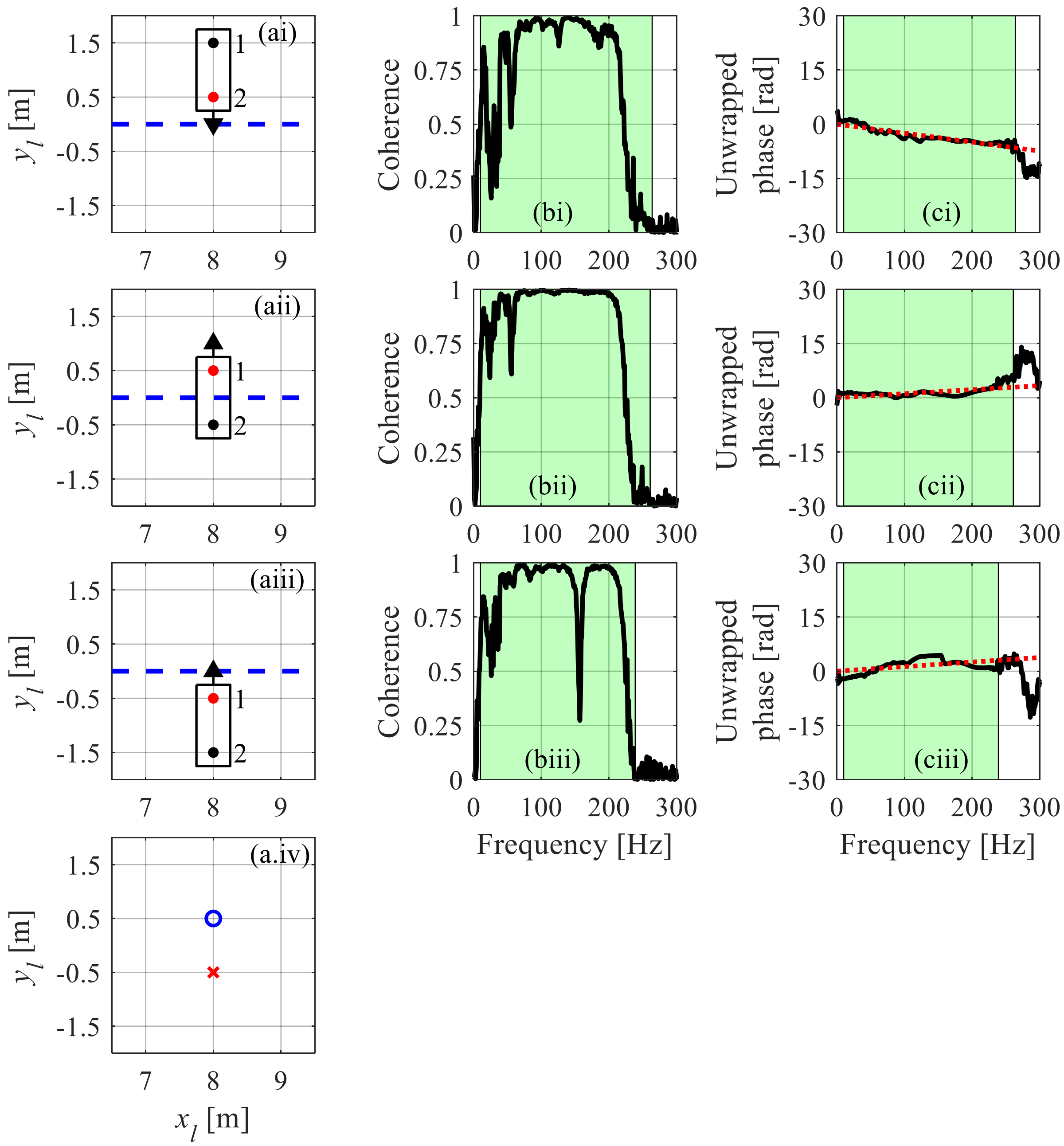

Source: elaborated by the author.

Figure 83 - Pipe localization with the two-sensor technique applied on 3rd measurement line of zone B of the British test rig. (a.i-iii) 1st, 2nd and 3rd positions of the pair of sensors, (b.i-iii) coherence $\gamma_{1,2}^{2}(\omega)$ for 1st, 2nd and 3rd positions, (c.i-iii) unwrapped phase $\phi_{1,2}(\omega)$ (solid black line) and approximated line $\hat{\phi}_{1,2}(\omega)$ (dashed red line) for 1st, 2nd and 3rd positions, and (a.iv) estimate of pipe localization. The dashed blue lines correspond to the buried pipe.

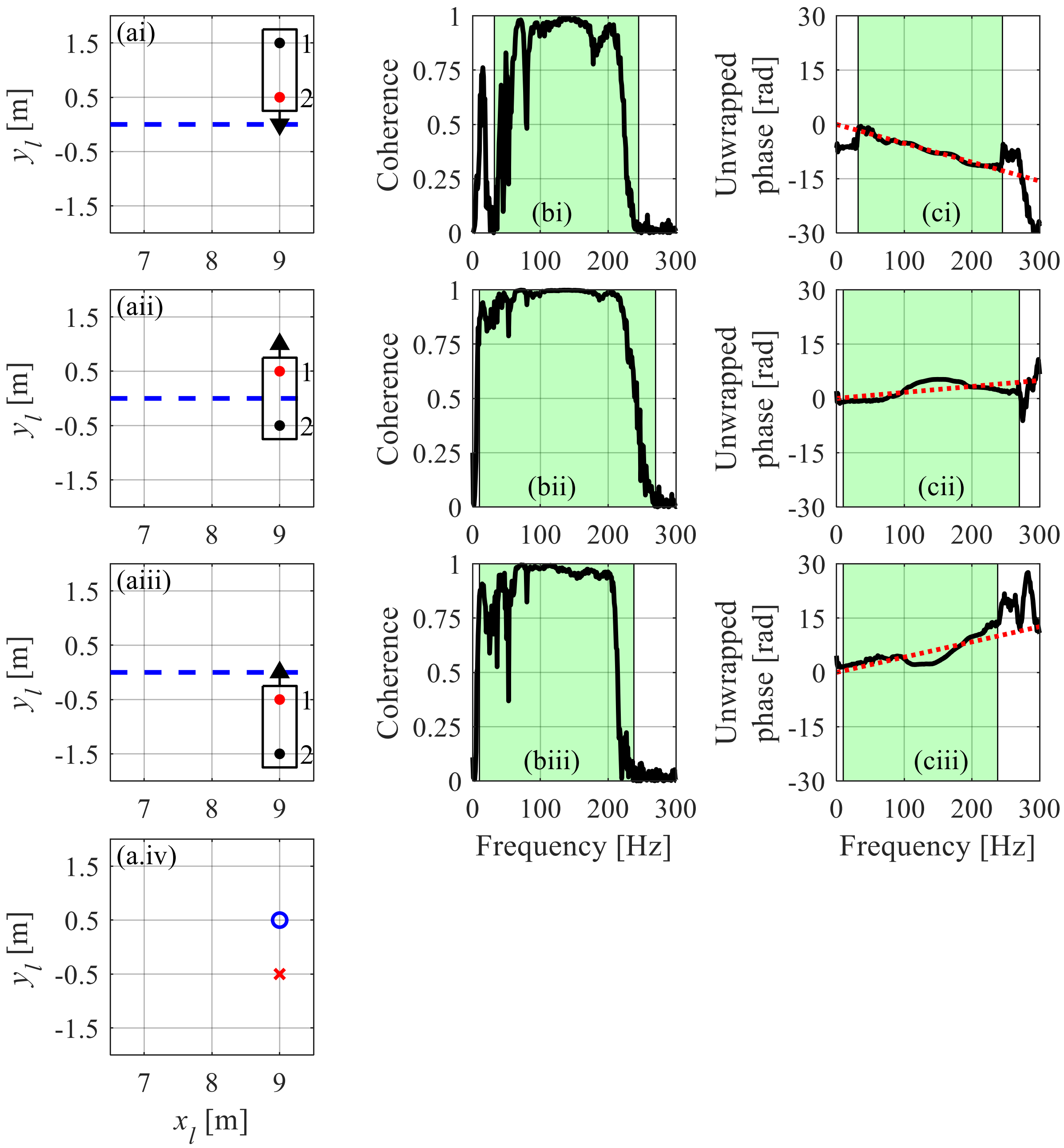

Source: elaborated by the author.

Figure 84 - Pipe localization with the two-sensor technique applied on 2nd measurement line of zone B of the measurement grid with 30° misalignment, arranged in the Brazilian test rig with accelerometers - Part 1. (a.i-iv) 1st, 2nd, 3rd and 4th positions of the pair of sensors, (b.i-iv) coherence $\gamma_{1,2}^{2}(\omega)$, (c.i-iii) unwrapped phase $\phi_{1,2}(\omega)$ (solid black line) and approximated line $\hat{\phi}_{1,2}(\omega)$ (dashed red line) for 1st, 2nd, 3rd and 4th positions.

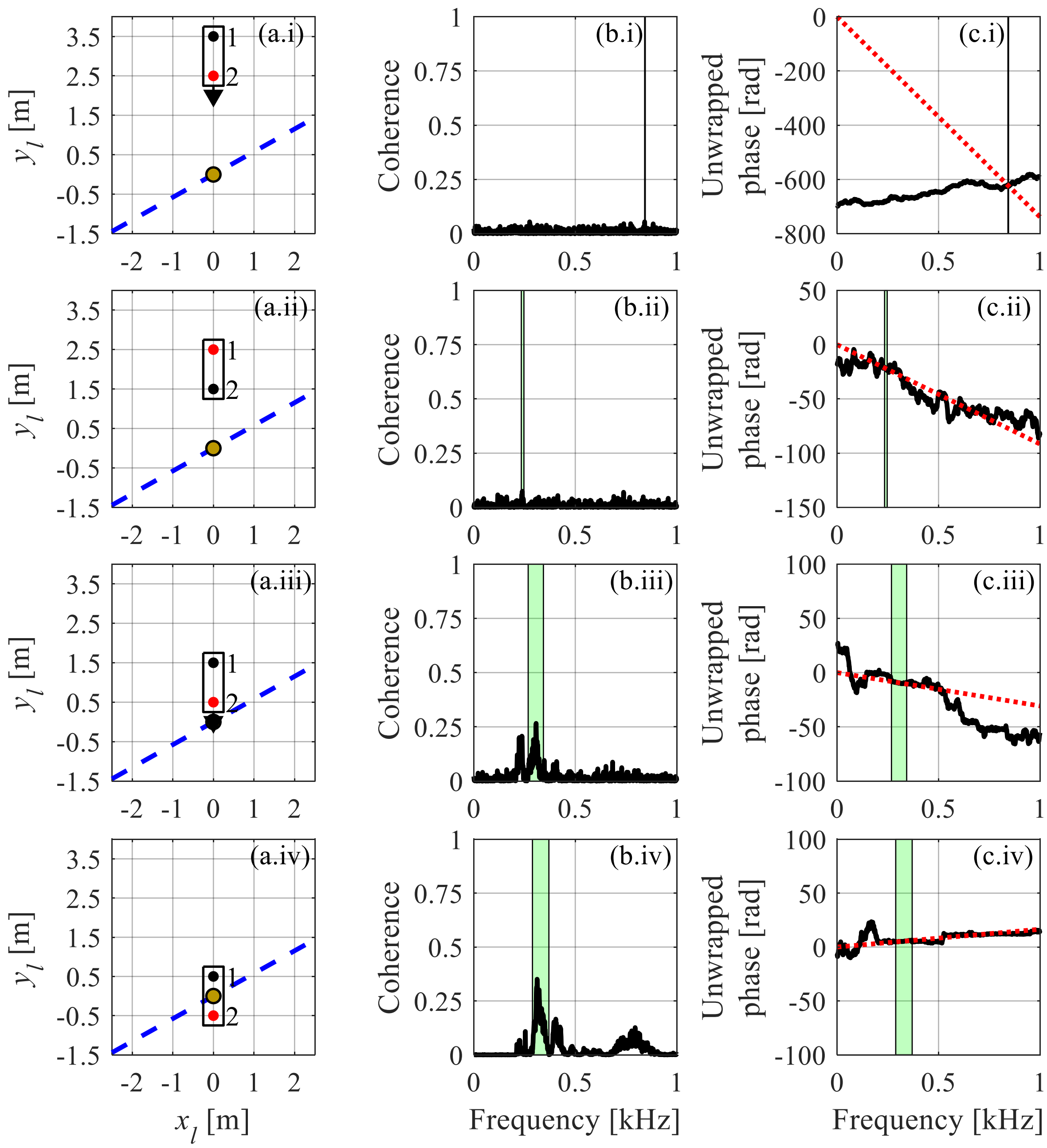

Source: elaborated by the author.

Figure 85 - Pipe localization with the two-sensor technique applied on 2nd measurement line of zone B for the measurement grid with 30° misalignment, arranged in the Brazilian test rig with accelerometers - Part 2. (a.i-iv) 5th, 6th and 7th positions of the pair of sensors, (b.i-iv) coherence $\gamma_{1,2}^2(\omega)$, (c.i-iii) unwrapped phase $\phi_{1,2}(\omega)$ (solid black line) and approximated line $\hat{\phi}_{1,2}(\omega)$ (dashed red line) for 5th, 6th and 7th, and (a.iv) estimate of pipe localization.

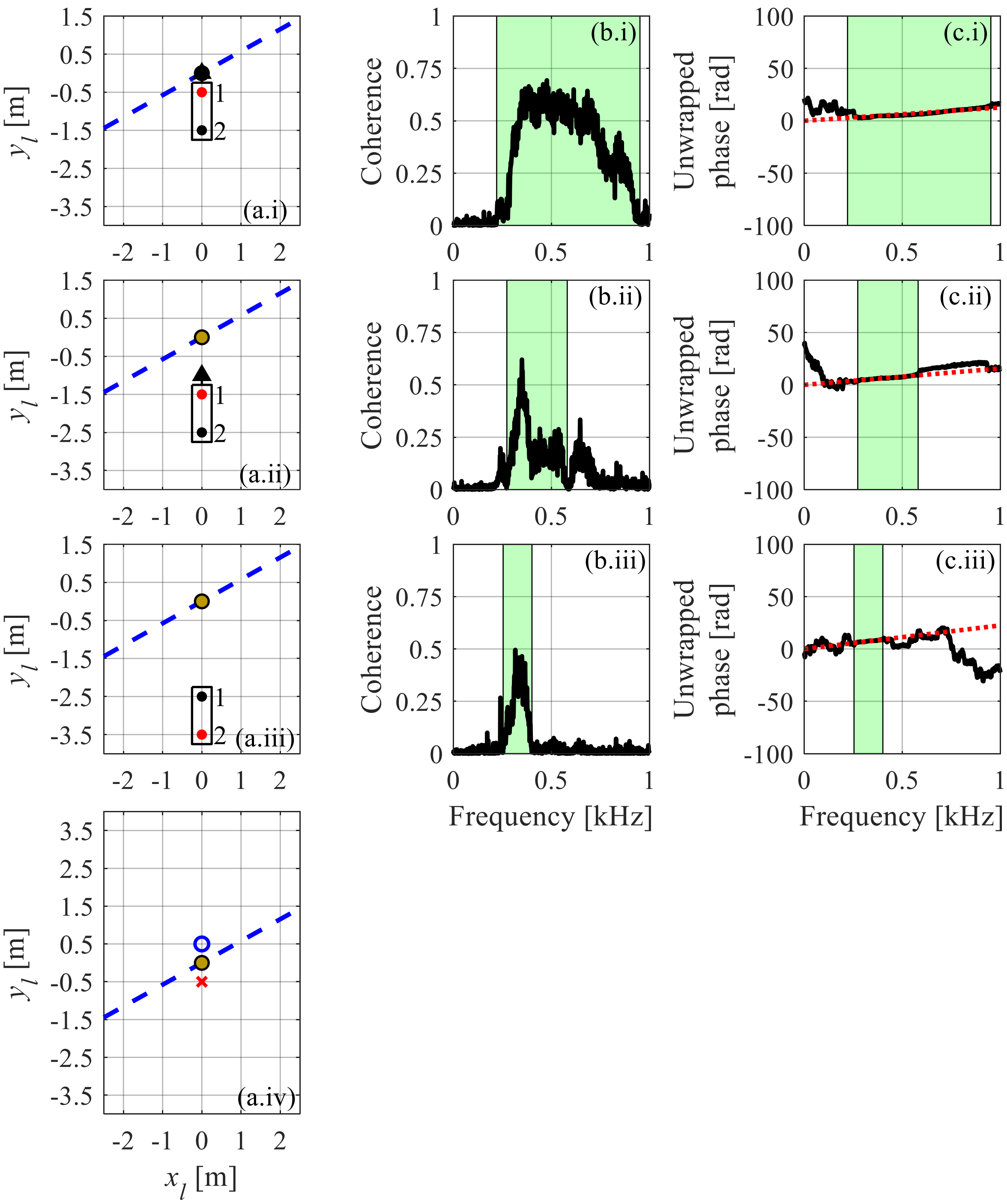

Source: elaborated by the author.

Figure 86 - Pipe localization with the two-sensor technique applied on 2nd measurement line of zone B for the measurement grid with 60° misalignment, arranged in the Brazilian test rig with accelerometers - Part 1. (a.i-iv) 1st, 2nd, 3rd and 4th positions of the pair of sensors, (b.i-iv) coherence $\gamma_{1,2}^2(\omega)$, (c.i-iii) unwrapped phase $\phi_{1,2}(\omega)$ (solid black line) and approximated line $\hat{\phi}_{1,2}(\omega)$ (dashed red line) for 1st, 2nd, 3rd and 4th positions.

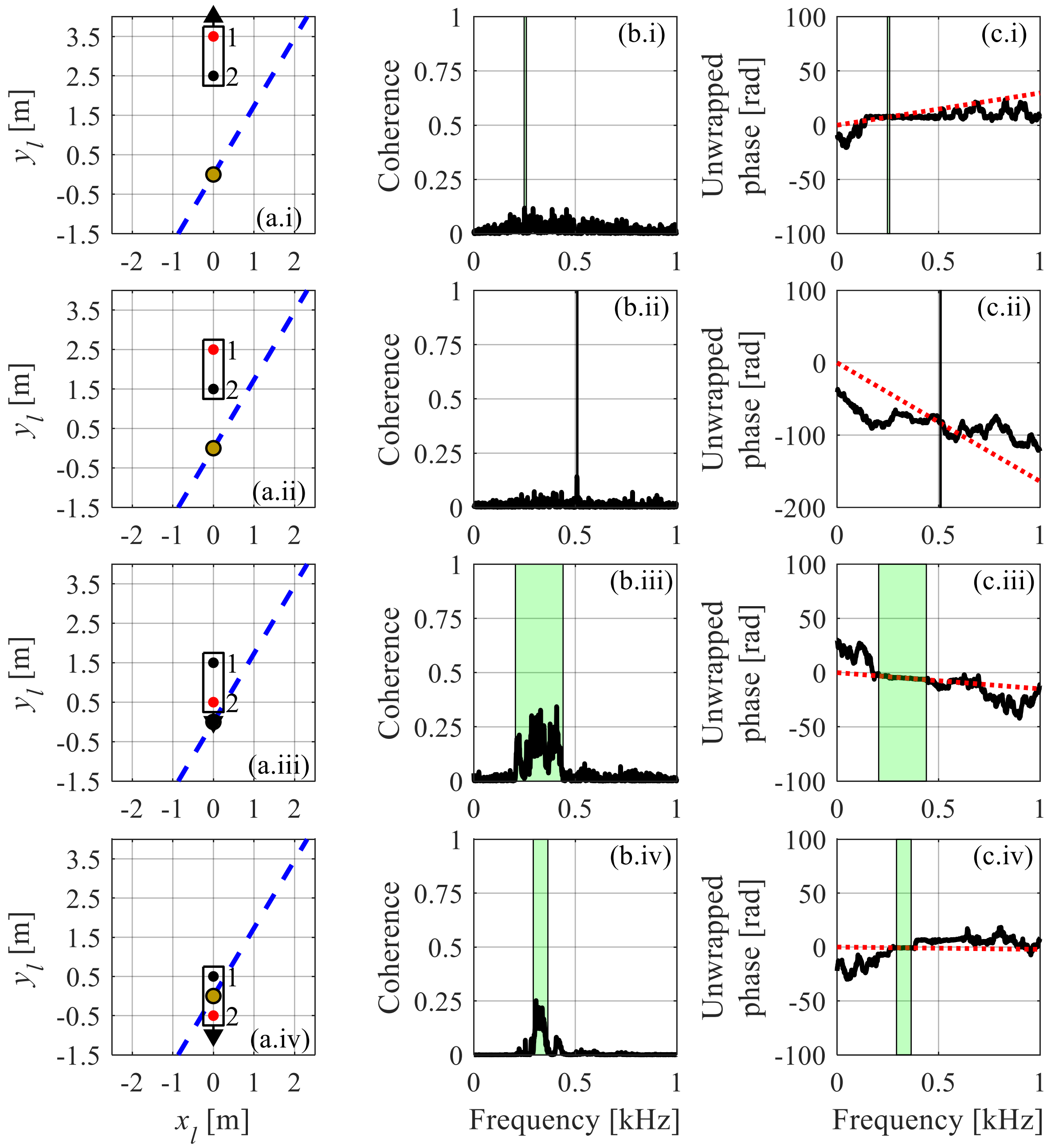

Source: elaborated by the author.

Figure 87 - Pipe localization with the two-sensor technique applied on 2nd measurement line of zone B for the measurement grid with 60° misalignment, arranged in the Brazilian test rig with accelerometers - Part 2. (a.i-iv) 5th, 6th and 7th positions of the pair of sensors, (b.i-iv) coherence $\gamma_{1,2}^{2}(\omega)$, (c.i-iii) unwrapped phase $\phi_{1,2}(\omega)$ (solid black line) and approximated line $\hat{\phi}_{1,2}(\omega)$ (dashed red line) for 5th, 6th and 7th, and (a.iv) estimate of pipe localization.

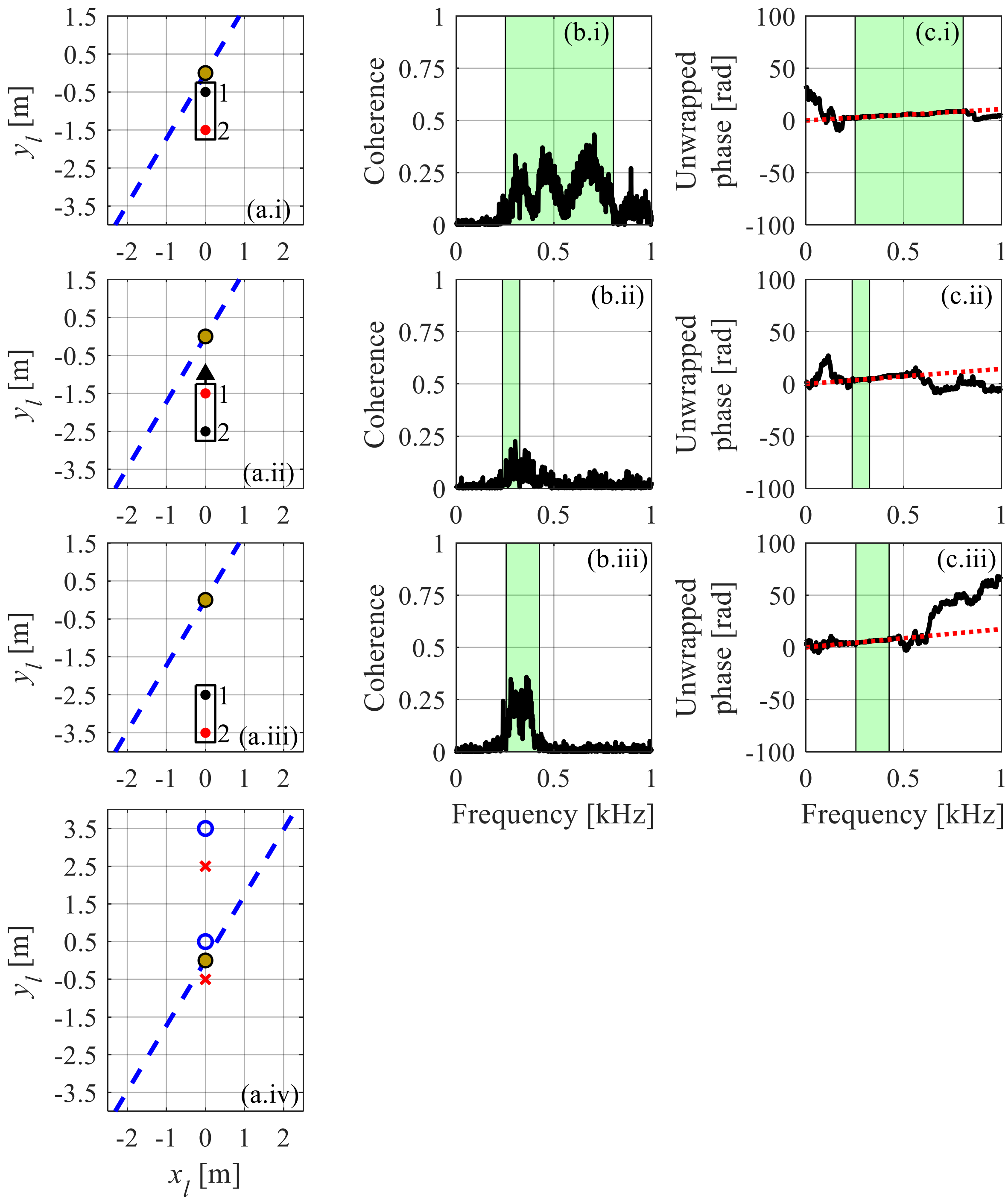

Source: elaborated by the author.

APPENDIX C - COMPARISON BETWEEN THE SENSITIVITIES OF GEOPHONES AND ACCELEROMETERS

To do a proper comparison between the sensitivities of geophones and accelerometers, it is necessary to describe the relationship between the quantities measured by both sensors. The voltage $v_g(t)$ generated by geophones is proportional to the velocity $\dot{x}(t)$ of the structure, and the voltage $v_a(t)$ generated by accelerometers is proportional to the acceleration $\ddot{x}(t)$ of the structure. Assuming that the response of both sensors is linear, the relationship between $v_g(t)$ and $\dot{x}(t)$, and the relationship between $v_a(t)$ and $\ddot{x}(t)$ are given by

$$v_g(t) = \alpha_g \dot{x}(t),\ v_a(t) = \alpha_a \ddot{x}(t), \tag{21a,b}$$

respectively, where α_g and α_a are constants that describe the sensitivities of a geophone in [V/(m/s)] and an accelerometer in [V/(m/s²)], respectively. Applying the Fourier transform on Eqs. (C.1a,b), the corresponding relationships can be written in the frequency domain as

$$V_g(\omega) = \mathrm{j}\alpha_g \omega X(\omega),\ V_a(\omega) = -\alpha_a \omega^2 X(\omega), \tag{22a,b}$$

where $V_g(\omega) = F\{v_g(t)\}$, $V_a(\omega) = F\{v_a(t)\}$, and $X(\omega) = F\{x(t)\}$, in which $F\{\bullet\}$ denotes Fourier transform and $x(t)$ is the displacement of the structure. The combination of Eqs. (C.2a) and (C.2b) provides the relationship between the voltages $V_a(\omega)$ and $V_g(\omega)$, given by

$$\frac{V_a(\omega)}{V_g(\omega)} = \mathrm{j}\omega \frac{\alpha_a}{\alpha_g}. \tag{23}$$

By analysing Eq. (23), the amplitude of the voltage $V_a(\omega)$, provided by an accelerometer, is equal to the amplitude of the voltage $V_g(\omega)$, provided by a geophone, scaled by a factor of $\omega \alpha_a / \alpha_g$ and the voltage $V_a(\omega)$ is also 90° advanced in relation to the voltage $V_g(\omega)$.

For the specific types of geophone and accelerometers used in the experiments described in Chapter 6, $\alpha_a = 0.05$ V/(m/s²) and $\alpha_g = 28.8$ V/(m/s) according to their respective datasheets (PCB, 2002a, 2002b; SPARKFUN, 2006). By combining such values with Eq. (23), it can be concluded that, for a given acceleration amplitude, the geophone provides the same voltage amplitude in relation to the accelerometer for a frequency of approximately 92 Hz. For frequencies below this value the geophone provides a voltage amplitude higher than the accelerometer, and for frequencies above this value the accelerometer provides a voltage amplitude higher than the geophone, for a given acceleration amplitude. Therefore, it can be concluded for the sensors used in the experiments described in Chapter 6, that the geophones are more sensitive than the accelerometers for frequencies below than 92 Hz, and that the accelerometers are more sensitive than the geophones for frequencies higher than 92 Hz.